

AD-A250 409

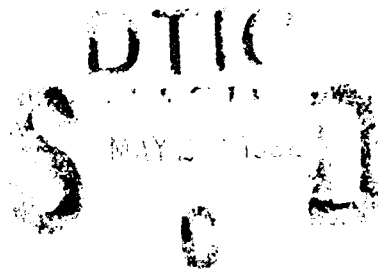


AD-A250 409 8

2

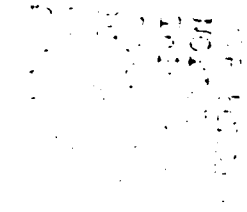
INTERACTION OF ISOTROPIC TURBULENCE WITH A SHOCK WAVE

By
S. Lee, P. Moin
and S. K. Lele



Prepared with the support of the
Air Force Office of Scientific Research
under AFOSR Grant No. [REDACTED]

AFOSR-89-0249



Report No. TF-52

Thermosciences Division
Department of Mechanical Engineering
Stanford University
Stanford, California 94305

March 1992

92-13271



REPORT DOCUMENTATION PAGE

Form Approved
OMB No. 0704-0188

Public reporting burden for this collection of information is estimated to average 1 hour per response, including the time for reviewing instructions, searching existing data sources, gathering and maintaining the data needed, and completing and reviewing the collection of information. Send comments regarding this burden estimate or any other aspect of this collection of information, including suggestions for reducing this burden, to Washington Headquarters Services, Directorate for Information Operations and Reports, 1215 Jefferson Davis Highway, Suite 1204, Arlington, VA 22202-4302, and to the Office of Management and Budget, Paperwork Reduction Project (0704-0188), Washington, DC 20503.

1. AGENCY USE ONLY (Leave blank)		2. REPORT DATE March 1992		3. REPORT TYPE AND DATES COVERED Final 01 JAN 89 - 31 Dec 91	
4. TITLE AND SUBTITLE Interaction of isotropic Turbulence with a Shock Wave				5. FUNDING NUMBERS AFOSR- 89-0249 2307/AS	
6. AUTHOR(S) S. Lee, P. Moin and S. Lele					
7. PERFORMING ORGANIZATION NAME(S) AND ADDRESS(ES) Stanford University STANFORD, CA 94305				8. PERFORMING ORGANIZATION REPORT NUMBER TF-52	
9. SPONSORING / MONITORING AGENCY NAME(S) AND ADDRESS(ES) AIR FORCE OFFICE OF SCIENTIFIC RESEARCH DIRECTORATE OF AEROSPACE SCIENCES BOLLING AFB, DC 20332-6448				10. SPONSORING / MONITORING AGENCY REPORT NUMBER AFOSR 89-0249	
11. SUPPLEMENTARY NOTES					
12a. DISTRIBUTION / AVAILABILITY STATEMENT APPROVED FOR PUBLIC RELEASE DISTRIBUTION IS UNLIMITED				12b. DISTRIBUTION CODE	
13. ABSTRACT (Maximum 200 words) As a first step to understand the compressibility effects, interaction of isotropic quasi-incompressible turbulence with a weak shock wave was studied by three-dimensional time-dependent direct numerical simulations. In addition, linear analysis was used to study interaction of isotropic turbulence with shock waves of a wide range of strengths. The effects of the fluctuation Mach number M_t and the average Mach number M_1^U of the upstream turbulence on turbulence statistics were investigated. Both numerical simulations and linear analyses of the interaction show that turbulence is enhanced during the interaction with a shock wave. ----					
14. SUBJECT TERMS Turbulence, Direct Numerical Simulation, Shock Wave				15. NUMBER OF PAGES 225	
				16. PRICE CODE	
17. SECURITY CLASSIFICATION OF REPORT UNCLASSIFIED	18. SECURITY CLASSIFICATION OF THIS PAGE UNCLASSIFIED	19. SECURITY CLASSIFICATION OF ABSTRACT UNCLASSIFIED	20. LIMITATION OF ABSTRACT		

ABSTRACT

As a first step to understand the compressibility effects, interaction of isotropic quasi-incompressible turbulence with a weak shock wave was studied by three-dimensional time-dependent direct numerical simulations. In addition, linear analysis was used to study interaction of isotropic turbulence with shock waves of a wide range of strengths. The effects of the fluctuation Mach number M_t and the average Mach number M_1^U of the upstream turbulence on turbulence statistics were investigated.

Both numerical simulations and linear analyses of the interaction show that turbulence is enhanced during the interaction with a shock wave. Turbulent kinetic energy (TKE) and transverse vorticity components are amplified, and turbulent length scales are decreased. The predictions of the linear analyses compare favorably with simulation results for flows with $M_t < M_1^U - 1$, which suggests that the amplification mechanism is mainly linear.

Rapid evolution of TKE just downstream of the shock was not, however, reproduced by the linear analysis. Investigation of the budget of the TKE transport equation shows that this behavior of TKE is manifested in the pressure transport term $(\overline{p''u_i''})_{,i}$, which is nonlinear. The budgets of enstrophy components $\overline{\omega_i'^2}$ show that their amplifications through the shock are mainly caused by the distortion due to the mean flow compression, and that effect of baroclinic torque is not significant.

Shock waves were found to be distorted by the upstream turbulence, but still have a well-defined shock front for $M_t < M_1^U - 1$. In this regime, the statistics of the displacement and inclination of the shock front compare favorably with the linear analysis predictions. For flows with $M_t > M_1^U - 1$, shock waves no longer have well-defined fronts: shock wave thickness and strength vary widely in the transverse directions. Multiple peaks in pressure are found along the mean streamline where the local thickness of the shock wave has increased significantly.

Acknowledgements

The authors would like to acknowledge the financial support from the Air Force Office of Scientific Research under Grant No. 88-NA-322 with Dr. Leonidas Sakell as the technical monitor. The use of the computer facilities at NASA-Ames research center is also greatly appreciated.

We are grateful for useful discussions with Professor Dean R. Chapman, Professor Gregory Blaisdell, and Mr. Krishnan Mahesh. Helpful comments on a draft of this report by Professor Peter Bradshaw are warmly acknowledged.

The first author wishes to thank the Korean government for financially supporting him at the initial stage of his Ph.D. program.

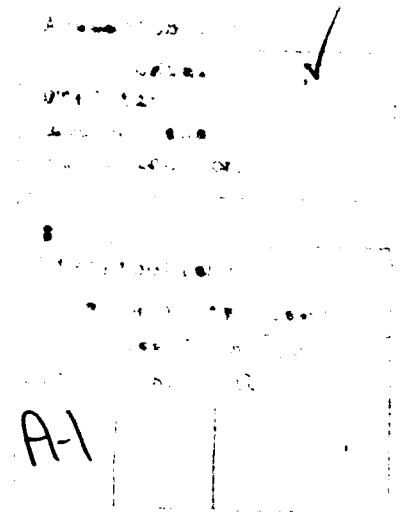


Table of Contents

	Page
Abstract	iv
Acknowledgement	v
Table of Contents	vi
List of Tables/Figures	ix
Nomenclature	xiv
 Chapter	
1. Introduction	1
1.1 Motivation	1
1.2 Survey of Previous Work	1
1.2.1 Linear Analysis	2
1.2.2 Experiments	3
1.2.3 Numerical Simulation	5
1.3 Objectives and Overview	6
2. Linear Analysis	9
2.1 Turbulence Statistics	10
2.2 Statistics of the Shock Front	18
3. Numerical Schemes	35
3.1 Governing Equations	35
3.2 Numerical Schemes	38
3.2.1 Time Advancement	38
3.2.2 Evaluation of Spatial Derivatives	39
3.2.3 Nonlinear Numerical Stability	41
3.2.4 Inflow/Outflow Boundary Conditions	42
3.2.5 Initial Conditions	46
3.2.6 Statistical Averages	46
3.3 Validations	47
3.3.1 Laminar Shock Wave	48
3.3.2 Thermal Inhomogeneity Interacting with a Shock Wave	50

4. Direct Numerical Simulation	63
4.1 Modification of Turbulence	64
4.1.1 Preliminary Considerations	64
4.1.2 Evolution of Turbulent Kinetic Energy	67
4.1.3 Dilatation and Vorticity	70
4.1.4 Turbulence Length Scales	74
4.1.5 Thermodynamic Properties	75
4.1.6 Modeling Issues	78
4.2 Modification of a Shock Wave	82
4.2.1 Statistics of a Shock Wave	82
4.2.2 Instantaneous Fields	84
5. Conclusions and Recommendations	133

Appendix

A. Rapid Distortion Theory	139
B. Linear Interaction Theory	147
B.1 Description of LIA— Ribner's Analysis	147
B.1.1 Formulation of the Boundary-Value Problem	147
B.1.2 Solutions to the Problem	154
B.1.3 Summary and Discussion	157
B.2 Application of LIA to Shock-Turbulence Interaction	161
B.2.1 Turbulence Modification	161
B.2.2 Shock Front Distortion	168
C. Removal of Aliasing Errors in Simulation of Compressible Flows	175
D. Direct Numerical Simulations of Spatially Evolving Turbulence	177
D.1 Method of Generating Inflow Turbulence	177
D.2 Simulation of Spatially Decaying Turbulence	178
D.2.1 Comparison with Temporal Simulation Results	178
D.2.2 Comparison with Experimental Data	180
E. Parameter Limitations in Direct Numerical Simulation of Shock-Turbulence Interaction	191
E.1 Requirements for Resolution and Sample Size	191
E.2 Limitations of the Physical Parameters: Re_λ, M_1^U, M_t	195
F. Turbulence Statistics in Kinematic Oscillation	

of a Plane Shock Wave	197
G. Effect of a Refined Outflow Boundary Condition	203
G.1 Description of Giles' Boundary Condition	203
G.2 Comparison of Turbulence Statistics	208
H. Drift in the Shock Position and the Outflow Condition	215
References	219

List of Tables and Figures

Table	Page
4.1 Parameters for the simulations of shock-turbulence interaction.....	64
Figure	Page
2.1 The coordinate system used in the linear analyses.	21
2.2 Predictions of transverse vorticity amplification: (a) $1 \leq M_1^U \leq 10$, (b) $1 \leq M_1^U \leq 2$	22
2.3 Predictions of velocity component amplification: (a) $1 \leq M_1^U \leq 10$, (b) $1 \leq M_1^U \leq 2$	23
2.4 Predictions of velocity component amplification at near-field.....	24
2.5 Decay of velocity components behind the shock wave for exponential fall-off upstream spectrum (2.1), with $M_1^U = 1.2$	25
2.6 Decay of streamwise velocity fluctuation behind the shock wave for exponential fall-off upstream spectrum (2.1).....	26
2.7 Decay of streamwise velocity fluctuation behind the shock wave for a von Kármán upstream spectrum (2.2).	27
2.8 Frequency spectrum amplification ration for a von Kármán upstream spectrum (2.2): (a) RDT, (b) LIA.....	28
2.9 Wave number spectrum amplification ratio for a von Kármán upstream spectrum (2.2): (a) RDT, (b) LIA.....	29
2.10 Predictions of changes in Taylor microscales: (a) $1 \leq M_1^U \leq 10$, (b) $1 \leq M_1^U \leq 2$...	30
2.11 Acoustic pressure fluctuation downstream of the shock wave: (a) normalized with the downstream mean pressure, (b) normalized with the upstream mean pressure...	31
2.12 Shock front statistics for exponential fall-off upstream spectrum, (2.1).	32
2.13 Comparison of local upstream velocity fluctuation and the local shock front speed for various angles of incidence.....	33
2.14 Predictions of <i>rms</i> shock front speed by LIA: (a) $1 \leq M_1^U \leq 10$, (b) $1 \leq M_1^U \leq 2$...	34
3.1 The schematic plot of the computational domain.	52

3.2	The transfer function of filtering in the Fourier space.....	53
3.3	Laminar shock wave profiles: (a) streamwise velocity, (b) pressure, (c) temperature, (d) dilatation, (e) entropy, (f) entropy budget.....	54,55,56
3.4	Temperature fields from passage of a thermal inhomogeneity through a shock.....	57
3.5	Vorticity fields from passage of a thermal inhomogeneity through a shock.....	58
3.6	Evolution of the circulation in the upper half plane from passage of a thermal inhomogeneity through a shock.	59
3.7	Vorticity field at $t = 16.6$ from passage of a thermal inhomogeneity through a shock.....	60
3.8	Pressure fields from passage of a thermal inhomogeneity through a shock.	61
4.1	Evolution of mean quantities across the shock wave for case A: (a) streamwise velocity, (b) pressure, (c) temperature.	86
4.2	Evolution of velocity derivative skewness for case C.....	87
4.3	One dimensional power spectra upstream of the shock wave for case C at $k_0 x_1 = 15.8$	88
4.4	Evolution of the energy spectra of (a) streamwise velocity, (b) transverse velocity, and (c) density fluctuation for case C.....	89,90,91
4.5	Two point correlations upstream of the shock wave ($k_0 x_1 = 9.07$) for case A where the mean shock position is $k_0 x_1 = 12.6$	92
4.6	Evolution of the normal components of the Reynolds stress tensor, $R_{\alpha\alpha}$ for case C.....	93
4.7	Budget of terms in the turbulent kinetic energy transport equation for case C (a) near the shock wave and (b) in the entire domain.....	94
4.8	Decomposition of the pressure work term for case C (a) near the shock wave and (b) in the entire domain.	95
4.9	Budget of terms in the transport equation of Reynolds stresses, (a) R_{11} and (b) R_{22} , for case C in the entire domain.....	96
4.10	Approximation of the viscous term for case C.....	97
4.11	Variances of dilatation and vorticity for case C.....	98
4.12	Evolution of components of vorticity for case C ($Re_T = 84.8$).....	99
4.13	Evolution of a transverse component of vorticity for different shock strengths.	100

4.14	Evolution of vorticity for different turbulence Reynolds numbers: (a) $Re_T = 240$, (b) $Re_T = 133$, (c) $Re_T = 240$ (resolution effect).....	101,102
4.15	Budget of terms in the transport equation of $\overline{\omega'^2_2}$ for case A.....	103
4.16	Production of vorticity by the mean and turbulent strain in the transport equation of $\overline{\omega'^2_2}$ for case A.....	104
4.17	Individual (a) and total effects (b) of nonlinear terms in the transport equation of $\overline{\omega'^2_2}$ for case A.....	105
4.18	Budget of terms in the transport equation of $\overline{\omega'^2_1}$ for case A, $Re_T = 240$	106
4.19	Budget of terms in the transport equation of (a) $\overline{\omega'^2_1}$ ($Re_T = 240$), (b) $\overline{\omega'^2_2}$ ($Re_T = 240$), (c) $\overline{\omega'^2_1}$ ($Re_T = 84.8$), (d) $\overline{\omega'^2_2}$ ($Re_T = 84.8$).....	107,108
4.20	Approximation of the viscous terms by the homogeneous dissipation in the transport equations of $\overline{\omega'^2_1}$ and $\overline{\omega'^2_2}$ for case A.....	109
4.21	Evolution of integral scales defined in (4.7) for case A.....	110
4.22	Evolution of the turbulence length scale defined in (4.17) for case C.....	111
4.23	Evolution of Taylor microscales for case C.....	112
4.24	Comparison of Taylor microscale change across the shock wave with linear predictions.....	113
4.25	Evolutions of (a) <i>rms</i> values of thermodynamic properties and (b) the polytropic exponent [†] n_1 for case A.....	114
4.26	Budget of terms in the transport equation of $\overline{\rho'^2}$ for case A (a) in the shock zone, (b) in the entire domain.....	115
4.27	Joint probability function of scaled pressure and density fluctuations for case C...	116
4.28	Evolution of the correlation coefficient $c_{\rho T}$ between density and temperature fluctuations for case A.....	117
4.29	Evaluation of Durbin and Zeman's [1991] model for $\overline{p'u''_{i,i}}$ (a) near the shock and (b) in the entire domain for case C.....	118
4.30	Evaluation of the model for $\overline{p'^2}$ transport for case C.....	119
4.31	Evaluation of the models (4.27) for $-(\overline{p'u''_1})_1$ in case C: (a) approximation in terms of $\overline{\rho'u''_1}$, (b) transport of $\overline{\rho'u''_1}$	120
4.32	Unscaled (a) and scaled (b) turbulent mass fluxes.....	121

4.33	Contour plot for the peak negative dilatation inside the shock wave along the mean streamlines for case C.....	122
4.34	Probability density function for the peak negative dilatation in (a) linear-linear and (b) linear-logarithmic coordinates for case C.	123
4.35	Contour plot for the shock front distortion based on (a) the pressure half-rise and (b) the density half-rise point for case C.	124,125
4.36	Comparison of scaled <i>rms</i> displacement of the shock front from different simulations with LIA predictions with spectrum (2.1).	126
4.37	Comparison of scaled <i>rms</i> shock front slopes from different simulations with LIA predictions	127
4.38	Instantaneous density fields in typical x_1x_2 -planes for (a) case D and (b) case F...128	
4.39	Profiles of dilatation along the mean streamlines for (a) case D and (b) case F....	129
4.40	Profiles of pressure along the mean streamlines for (a) case D and (b) case F.....	130
4.41	Contour plot for the streamwise Mach number for case A.....	131
B.1	Convection of plane oblique sinusoidal shear wave through the shock wave.....	172
B.2	Symbols and coordinate systems used in LIA.....	173
B.3	Geometrical relations across the shock, with and without perturbation σ in the shock inclination angle.....	174
D.1	Schematic plot of randomized temporal dependence of phases.....	183
D.2	Approximation of the spectrum by signals with time-dependent random phases...184	
D.3	Time history of turbulence signals at the inflow.....	185
D.4	Evolutions of velocity derivative skewness.....	186
D.5	Comparison of one-dimensional spectra of (a) vorticity and (b) dilatation at $t/\tau_t = 0.67$	187
D.6	Comparison of turbulent kinetic energy evolution.....	188
D.7	Comparison of the normalized energy spectrum of Ling and Huang given by (D.4) and the energy spectra obtained in the simulation at five different positions.....	189
D.8	Comparison of turbulent kinetic energy decay with (D.5).....	190
F.1	Effects of kinematic shock wave oscillation on turbulence statistics.....	199
F.2	Effects of kinematic shock wave oscillation on the budget of terms in the transport equation for R_{11}	200

F.3 Effects of kinematic shock wave oscillation on the pressure-work term decomposition.	201
G.1 Effect of boundary condition on the evolution of the vorticity variance $\overline{\omega'_i \omega'_i}$ for case A.	210
G.2 Effect of boundary conditions on the evolution of R_{11} for case A.	211
G.3 Effect of boundary conditions on the evolution of the pressure-work $-\overline{p'_i u''_i}$ for case A.	212
G.4 Effect of boundary conditions on the evolution of the dilatation variance $\overline{\theta'^2}$ for case A.	213
H.1 Mass flowrate across the shock wave for case A.	217
H.2 Time history of the mean exit pressure for case of A.	218

NOMENCLATURE

Roman Symbols

a_1, a_2, a_3	Parameters in differentiation and filtering schemes
a_S, b_S	Shock front displacement factor
a_T, b_T	Parameters for temperature inhomogeneity
A	Jacobian $\partial F/\partial Q$
b_1, c_1	Grid stretching parameters
b^s	Parameter for initial shock wave profile
c	Speed of sound
c_i	One-dimensional characteristic variable
c_d	Model constant $c_d = (5 - 3\gamma)/12$
c_v, c_p	Specific heats at constant volume and pressure
$c_{\rho T}$	Correlation between density and temperature fluctuations
CFL	Courant-Friedrichs-Lewy number
e	Internal energy
e_i	Total strain component
\tilde{e}_i	Reduced total strain component
e_i^*	Incompressible total strain component
\mathbf{e}_i	Unit vector in x_i -direction
e_o	Dilatational total strain
E	Three-dimensional energy spectrum
E_{ij}	Energy spectrum tensor component
E_i	One-dimensional energy spectrum of u_i'
E_T	Total energy
f	RHS of a differential equation
F	Flux vector in the x_1 -direction
F_{ij}	Generalized energy spectrum tensor
h', h''	Metric quantities for the grid stretching
h_T	Total enthalpy
H	System matrix

H_{ij}	Vorticity spectrum tensor in deforming coordinate
J	Jacobian ρ^U / ρ^D
k	Thermal conductivity
k	Magnitude of a wave number, $\mathbf{k} = (k_1, k_2, k_3)$
k_h	Magnitude of transverse wave number vector $\mathbf{k}_h = (k_2, k_3)$
k_i	Wave number component
k_o	Energy peak wave number
k^*	Normalized wave number, k/k_o
l	Turbulence length scale
L_i	Computational box size
m	Density jump ratio across the shock wave
M_1	Mean Mach number in the streamwise direction
M_t	Fluctuation Mach number $M_t = q/c$
M^*	Dimensionless velocity
n, n_1, n_2	Polytropic exponents
n_T	Parameter for temperature inhomogeneity
N_t	Number of total time steps
p	Pressure
p_C	Pressure corresponding to dilatational motion
p_e	Equilibrium pressure fluctuation
Pr	Prandtl number
q	Velocity scale
q_I, q_C	Incompressible and compressible velocity scales
Q	Conservative flow variable vector
Q_i	Heat flux vector
$Q_{ff,i}$	Two-point correlation of f' in x_i -direction
r	Radial coordinate in a cylindrical coordinate
R	Flow variable Jacobian
Re	Computational Reynolds number
Re_λ	Reynolds number based on Taylor microscale
Re_T	Turbulent Reynolds number
R_{ij}	Reynolds stress tensor
s	Entropy, Section 3.3.1
s_{ij}	Strain rate tensor, Section 4.1

S	Equivalent mean strain rate $(S_{ij}S_{ij}/2)^{1/2}$
S_i	Velocity derivative skewness
S_{ij}	Mean strain rate tensor
S_{ij}^*	Deviatoric component of mean strain rate tensor
S^{k_1}	1D wave number spectrum amplification
S^ω	1D frequency spectrum amplification
t	Time
t_T	Parameter for temperature inhomogeneity
T	Temperature
T	Diagonalizing matrix
T_t	Total temperature
u_i	Velocity component
u^R	Eigenvector of H
U	Non-conservative flow variable vector
U_1	Mean streamwise velocity
U_s	Mean shock drift speed
v	Specific volume
v^L	Eigenvector of H^T
V_{ij}	Vorticity correlation tensor $\overline{\omega_i\omega_j}$
\mathbf{x}	Spatial coordinate vector $\mathbf{x} = (x_1, x_2, x_3)$
x_i	Spatial coordinate component
x_1^s	Parameter for initial shock wave profile
y	Dependent variable
y^i, y^{ii}	Intermediate solutions of time advance scheme
y^n	Solution at time level t^n
Z	Amplitude amplification of a wave in LIA

Greek Symbols

α, β	Parameters in the expression for p_e^2
γ	Specific heat ratio
Γ	Circulation
Γ_i	Mean strain rate component in principal coordinates

$\tilde{\Gamma}_i$	Reduced strain rate component in principal coordinates
δ_{ij}	Kronecker delta; 1 for $i = j$, 0 for $i \neq j$
δ_s	Shock thickness
δ_{sh}	Phase shift of the shock front displacement
Δt	Time step
Δx_i	Grid spacing
ϵ	TKE dissipation rate
ϵ^I, ϵ^C	Incompressible and compressible TKE dissipation rate
ϵ_{ijk}	Permutation tensor
θ	Dilatation
θ	Wave incident angle, Circumferential angle
θ_{cr}	Critical angle of wave incidence
κ_i	Shock front curvature
κ_i	Wave number component in deforming coordinate system
λ, λ_i	Taylor microscale
Λ	Eigenvalue of the system matrix
$\Lambda_{ff,i}$	Length scale based on $Q_{ff,i}$
μ	Molecular viscosity
ν	Kinematic viscosity
P_i	Amplitude of acoustic velocity fluctuations
ρ	Density
σ_i	Shock front inclination angle in the x_i -direction
τ, τ_t	Turbulence time scale
τ	Time in deforming coordinate system
τ_a	Acoustic time scale
τ_{ij}	Shear stress tensor
ξ	Shock front displacement
ξ_i	Coordinate in deforming coordinate
ϕ	Azimuthal angle in a spherical coordinate
ϕ_r	Random phase
Φ_i	Viscous term in vorticity variance transport equation
Φ_i^H	Homogeneous part of Φ_i
χ	Modified wave number
χ^θ	Ratio of dilatation and vorticity variances

ω	Frequency
ω_i	Vorticity component

Other Symbols

$()^*$	Complex conjugate also Dimensional quantity
$()_o$	Reference quantity
$()_{in}$	Mean inflow quantity
$()^D$	Downstream quantity
$()_L$	Laminar quantity
$()^T$	Transpose matrix
$()^U$	Upstream quantity
$\hat{()}$	Fourier transform
$\overline{()}$	Ensemble average
$\tilde{()}$	Favre average
$()'$	Reynolds fluctuating quantity
$()''$	Mass weighted fluctuating quantity

Abbreviations

<i>CFL</i>	Courant-Friedrichs-Lewy number
DNS	Direct numerical simulation
LES	Large-eddy simulation
LHS	Left hand side
LIA	Linear interaction analysis
PDF	Probability density function
RDT	Rapid distortion theory
RHS	Right hand side
<i>rms</i>	Root mean square
TKE	Turbulent kinetic energy

CHAPTER 1

INTRODUCTION

1.1 Motivation

A fundamental understanding of compressible turbulence is necessary for the development of supersonic transport aircraft. Compressibility effects on turbulence were found significant when the energy associated with the dilatational fluctuations is large or when the mean flow is significantly distorted— expanded or compressed. The presence of shock waves is an important feature that distinguishes high-speed flows from low-speed ones. Understanding the mechanisms of isotropic turbulence interacting with a shock wave is not only of generic interest, but also of fundamental importance in understanding the interactions of turbulent boundary layers with shock waves which occur in many practical engineering applications: the flow inside a high speed compressor or a gas turbine, the flow over wings in supersonic aircrafts, and the intake flow to a supersonic ramjet (scramjet).

The numerical simulation using turbulence models is becoming a standard tool in aerospace technology. Most current models of compressible turbulence are, however, based on incompressible turbulence models. A better understanding of the underlying physics could lead to improvements to turbulence models, leading to more efficient designs. There is, therefore, a need to assess our understanding of compressible turbulence.

The present work is a fundamental study of the interactions of a shock wave with turbulence. We investigate the interaction of isotropic turbulence with a shock wave using direct numerical simulation and linear analyses.

1.2 Survey of Previous Work

Studies of the interaction of turbulence with a shock wave were initiated using linear theories in the early 1950's. Twenty years later, there was a resurgence of research interest in this area through experiments on the interaction of isotropic

turbulence and turbulent boundary layer with a shock wave. However, direct numerical simulation of the interaction of "true" turbulence with a shock wave has never been attempted.

1.2.1 Linear Analysis

Using his general theory of aerodynamic sound generation, Lighthill [1953] estimated the acoustic energy scattered from the interaction of turbulence with sound and shock waves. Most of the analytical studies of shock-turbulence interaction [Ribner 1953, Moore 1953, Kerrebrock 1956, Chang 1957, McKenzie, and Westphal 1968] are based on the linear theories of three-dimensional disturbances interacting with a shock wave. These disturbances were waves of vorticity, entropy, or sound. Kovasznay [1953] pointed out that they are linearly independent in weak turbulence. Any one such wave interacting with the shock wave generates all three kinds of fluctuations downstream of the shock wave. The linear theories developed by various researchers followed procedures that are mathematically different but physically equivalent and are, therefore, mutually consistent: inviscid linear equations for the disturbances are solved downstream of the shock, and the boundary conditions at the downstream side of the shock front are expressed in terms of the upstream disturbances by the use of Rankine-Hugoniot relations. Ribner [1953] investigated the passage of a single vorticity wave through a plane shock and the modification of the vorticity wave with simultaneous generation of an acoustically intense sound wave *in a reference frame fixed on the shock wave*. He later extended this analysis to study turbulence amplification due to a shock wave [1954] and the flux of acoustic energy emanating on the downstream side of the shock [1969]. He also used it to predict the one-dimensional power spectra of various fluctuations downstream of the shock [1987]. Moore [1953] analyzed the flow field produced by the oblique impingement of weak plane disturbances on a normal shock wave *in a reference frame fixed on the mean upstream flow*. Chang [1955] investigated the interaction of a plane shock and oblique plane disturbances with special reference to entropy waves. McKenzie and Westphal [1968] investigated the effect of a stationary plane shock on the travelling waves of vorticity, entropy, and sound. Anyiwo and Bushnell [1982] revisited the analysis of McKenzie and Westphal [1968] to identify primary

mechanisms of turbulence enhancement— amplification of vorticity mode, generation of vorticity mode from the interaction of acoustic and entropy modes with a shock wave, and turbulence “pumping” by shock oscillations.

Debieve, Gouin, and Gaviglio [1982a, 1982b] analyzed turbulence evolution through the shock using the Reynolds stress transport equation. They were able to separate the effects of the specific turbulent sources from the effects of the mean motion— convection and production. Their prediction of the longitudinal velocity fluctuation showed good comparison with the experimental result.

1.2.2 Experiments

There has been a significant accumulation of experimental data on the shock turbulence interaction during the last decade. Debieve, Gouin, and Gaviglio [1982a, 1982b] performed an experiment on the turbulent boundary layer interacting with a shock wave. They measured the mean and turbulent fields in an adiabatic compression ramp, where the mean upstream Mach number was $M_1^U = 2.32$, with a corner angle of 6° . They found amplifications of turbulence intensity $\overline{u_1'^2}$, the structure parameter $-\overline{u_1' u_2'} / \overline{u_1'^2}$, and the temperature fluctuation inside the boundary layer.

Dolling and Or [1985] measured wall pressure fluctuations upstream of the corner in flows with $M_1^U = 3.0$ over compression ramps with corner angles of 8° , 12° , 16° , and 20° . They found that the shock wave structure is unsteady in both separated and attached downstream flows, resulting in a region in which the wall pressure signal is intermittent.

Andreopoulos and Muck [1987] investigated the wall pressure fluctuations in the shock-wave/boundary-layer interactions over two-dimensional ramps, and found that the frequency of the shock-wave unsteadiness is of the same order as the bursting frequency of the upstream boundary layer and independent of the downstream separated flow.

Smits and Muck [1987] performed experiments to study the effects of different compression corners with angles of 8° , 16° , and 20° on a compressible turbulent boundary layer with $M_1^U = 2.9$. They found that the interaction significantly amplifies the turbulent stresses, and that the amplification increases with increasing

the effective normal Mach number. The structure parameter $-\overline{u'_1 u'_2} / \overline{u'^2_1}$ also increased significantly, which was attributed mainly to the unsteady oscillation of the shock system.

Kuntz, Amatucci, and Addy [1987] conducted an experimental investigation of the interaction between a shock wave and a turbulent boundary layer. Compression corners were used to generate an oblique shock wave in the flow field with $M_1^U = 2.94$. Ramp angles of $8^\circ, 12^\circ, 16^\circ, 20^\circ$, and 24° were used to produce a range of possible flow fields, including flows with no separation, incipient separation, and significant separation. They found that the boundary layer after the interactions showed an acceleration of the mean flow near the wall as the boundary layers began to return to equilibrium, and that the mean streamwise velocity profiles downstream of the separated compression corner were wavy due to the redeveloping boundary layer which had a velocity profile with inflection at reattachment.

There are a number of additional experimental studies of the interaction of turbulent boundary layers with an oblique shock [Settles, Fitzpatrick, and Bogdonoff 1979, Dussauge, Muck, and Andreopoulos 1986, Jayaram, Taylor, and Smits 1987, Selig, Andreopoulos, Muck, Dussauge, and Smits 1989]. A general finding from these experiments is that Reynolds shear stress and turbulence intensities are amplified across the shock wave. The studies of oblique shock wave/turbulent boundary layer interaction included several additional phenomena which complicated the flow behavior. These phenomena are: (a) oscillation of the shock wave in the longitudinal direction, (b) flow separation downstream of the shock, (c) streamline curvature, and (d) wall effects which result in high turbulence intensity and high flow anisotropy. Because of these complications, it was impossible to identify the sole effect of a shock wave on turbulence.

In order to isolate the effects of a shock wave on turbulence, several experiments on the interaction between the shock wave and grid-generated turbulence have been performed. Debieve and Lacharme [1986] experimentally investigated a shock-wave/free turbulence interaction at $M_1^U = 2.3$ over a ramp with a corner angle of 6° . They measured velocity and temperature spectra upstream and downstream of the shock wave and concluded that turbulent fluctuations are amplified and the Taylor microscales *increase* during the interaction. An intermittency effect due to unsteady shock wave distortion on turbulence statistics was also clearly described.

Keller and Merzkirch [1990] performed an experiment on the interaction of grid generated turbulence with a shock inside a shock tube. They verified amplification of the turbulence intensity quantitatively, showing that amplification was restricted to the lower wave numbers in the spectrum. This was consistent with the conclusion of length scale increase made by Debieve and Lacherme [1986], but it contradicts the intuitive reasoning that mean flow compression decreases the relevant turbulence length scales. Our results (Sec. 2.1 and Subsection 4.1.4) show that the Taylor microscale actually decreases in passing through the shock.

Honkan and Andreopoulos [1990] examined the interaction of a normal shock wave with homogeneous grid-generated turbulence. They found that turbulence is considerably amplified during the interaction, and that the amplification ratio of turbulence is not the same for different length scales and different turbulence intensities.

Jacquín, Blin and Geffroy [1991] investigated the interactions of a normal shock wave with grid-generated turbulence and a turbulent jet, and compared turbulence amplifications with the predictions by a linear analysis. They observed that turbulence amplification was not significant during the interaction, and that the decay of turbulent kinetic energy was accelerated downstream of the shock wave.

The aforementioned experiments treated the interaction of a shock with quasi-incompressible turbulence where fluctuations in pressure and density are not significant. A comprehensive experiment on the interaction of weak shocks ($M_1^U = 1.007, 1.03, \text{ and } 1.1$) with a random medium of density inhomogeneity was performed by Hesselink and Sturtevant [1988]. They observed that the pressure histories of the distorted shock waves were both peaked and rounded. In the rounded case, they found the perturbed shock was made up of a succession of weak, slightly curved fronts, and the total effective shock thickness was significantly greater than the classical Taylor thickness. They concluded that the observed distortions of the shock can best be explained in terms of the focusing/defocusing of its front due to inhomogeneity of the medium.

1.2.3 Numerical Simulation

Zang *et al.* [1984] simulated the interaction of a shock wave with a single wave using two-dimensional Euler equations. The interaction of a shock wave with an

isolated flow inhomogeneity was computed by Hussaini *et al.* [1986] and Meadows *et al.* [1991], and with two-dimensional turbulence by Rotman [1991] and Lee, Lele, and Moin [1991a].

Rotman [1991] numerically calculated the change in a turbulent flow caused by the passage of a travelling shock wave. He found that the shock causes an increase in the turbulent kinetic energy and that the length scale of the turbulent field behind the shock is smaller than that in front. He also found that increasing the initial turbulent kinetic energy caused a straight shock wave to evolve into a distorted front.

Lee, Lele, and Moin [1991a] found that vorticity amplification in the numerical simulation compared well with the predictions of the linear analyses, but that turbulent kinetic energy evolution behind the shock showed significant nonlinear effects. The energy spectrum was found to be enhanced more at small scales, leading to an overall length scale decrease.

Zang *et al.* [1984] examined various effects pertinent to the amplification and generation of turbulence in shock/turbulent boundary layer interaction and placed limits on the range of validity of linear theory. Hussaini *et al.* [1986] numerically investigated the effects of upstream eddy motion and temperature inhomogeneity on the enhancement and production of turbulence. Meadows *et al.* [1991] computed two-dimensional shock-vortex interaction using a shock capturing scheme. They qualitatively evaluated the effects of upstream vortex strength on both the flow field and acoustic field generated by the interaction.

1.3 Objectives and Overview

The primary objective of this work is to investigate the physics of the interaction of isotropic turbulence with shock waves using direct numerical simulations and linear analyses. The simulations and linear analyses provide statistical information for testing of turbulence models. Instantaneous flow fields from the simulations contribute to our understanding of the physical nature of the interaction.

The principal contributions and findings of this work are as follows:

- A numerical scheme to generate turbulence at the inflow boundary was developed and the simulation of spatially evolving grid-generated turbulence was conducted.
- The linear mechanisms involved in the shock/turbulence interaction enhance the amplitude of turbulent fluctuations and decrease the relevant turbulence length scales.
- Linear analysis predicts the corrugation of the shock front caused by upstream turbulence fluctuations. The distortion of the shock front is scaled with the upstream turbulence intensity and length scales.
- Isotropic upstream turbulence becomes axisymmetric after the interaction. All the components of turbulent kinetic energy are amplified across the shock wave. The streamwise intensity is amplified more than the transverse components. Fluctuations in pressure, density, and temperature are significantly enhanced.
- Power spectra of turbulent fluctuations are more amplified at small scales than at large scales. The integral turbulence length scale and Taylor microscales decrease during the interaction.
- Transverse components of vorticity are enhanced because of the mean flow compression, but the component normal to the shock remains unchanged. Baroclinic torque has a negligible contribution to the production of vorticity in the shock/quasi-incompressible turbulence interaction.
- Rapid evolution of turbulent kinetic energy found downstream of the shock wave is caused by the nonlinear pressure work. Decomposition of the pressure work term shows that the inhomogeneous pressure transport is the main cause of the rapid evolution.
- Isentropic relations hold between normalized fluctuations in pressure, density, and temperature throughout the flow field.
- Shock waves are found to be distorted by the upstream turbulence. Instantaneous shock wave structure depends on the upstream fluctuation Mach number and the mean shock strength. For flows with small fluctuation Mach numbers,

shock waves have a well-defined front. In this regime, the statistics of the distorted shock front compare favorably with the linear analysis predictions. For flows with large fluctuation Mach numbers, multiple peaks in pressure are found along the mean streamline where the local thickness of a shock wave has increased significantly.

This report is organized as follows. In Chapter 2 linear analyses of shock-isotropic turbulence interaction are conducted. The governing equations and the numerical method chosen are discussed in Chapter 3. Chapter 4 describes the numerical simulations of shock-turbulence interaction and their results. Conclusions and recommendations for future work are given in Chapter 5. The appendices include brief descriptions of the linear analyses (Appendix A and B), a proposal for an alias-free compressible turbulence simulation (Appendix C), development and validation of a numerical method for the simulations of spatially evolving turbulence (Appendix D), the limitations on the physical parameters for direct numerical simulation of shock-turbulence interaction (Appendix E), the effect of the shock oscillation on turbulence statistics (Appendix F), the effect of outflow boundary conditions (Appendix G), and the drift in the mean shock position and the outflow condition (Appendix H).

CHAPTER 2

LINEAR ANALYSIS

Two different linear approaches are used to investigate the interaction of isotropic turbulence with a normal shock wave. The first approach is the rapid distortion theory (RDT). The second is the compressible linear interaction analysis (LIA). Both analyses are for inviscid flows. The assumptions and main features of these analyses are discussed in Appendices A and B. The main effect of a shock wave on turbulence is the mean flow compression in the direction normal to the shock wave. The secondary effects are the vorticity generation due to shock front curvature and turbulent kinetic energy generation caused by the unsteady movement of the shock front. RDT accounts for the effect of the mean flow compression, while LIA includes all three effects.

For proper applications of the linear analyses, upstream Mach number variation may be considered as a small perturbation from the mean Mach number. Furthermore, time required for turbulence to pass through the shock wave may be considered small compared to a turbulence time scale, so that turbulence has no time to redistribute energy into different scales through nonlinear processes.

In the following, interaction of isotropic turbulence with a normal shock wave is discussed. Because LIA is more comprehensive, its results are mentioned in detail, and those from RDT are introduced for comparison when needed. Turbulence before the interaction is considered to be purely vortical, that is, upstream turbulence has no fluctuations in density and entropy. The fluid is assumed to be ideal gas with the specific heat ratio $\gamma = 1.40$.

The coordinate system used in the analysis is Cartesian, as shown in Figure 2.1. The streamwise direction x_1 is aligned with the direction normal to the mean shock plane. The reference frame is fixed on the mean shock plane. In this system, upstream flow approaches the shock with a supersonic speed, and downstream flow leaves with a subsonic speed.

2.1 Turbulence Statistics

Figure 2.2 presents amplifications of the transverse vorticity components predicted by LIA and RDT. The streamwise vorticity component is unchanged through the linear interaction. As the strength of the shock wave increases (higher mean Mach number), the ratio of downstream to upstream vorticity also increases. We find that the asymptotic value of the amplification factor for mean square vorticity for a shock wave with very large Mach number is about 20 in LIA and 36 in RDT. The ratio of the vorticity amplification by RDT is simply the ratio of downstream to upstream density, which is explained as an enhancement of vorticity due to the shrinking of the cross section of a transversely-oriented vortex tube by the mean flow compression. The predictions by LIA and RDT agree very well for weak shock waves but do not compare as well for stronger shock waves. This implies that effects of shock front curvature and shock front unsteadiness are negligible for weak shock waves, while these secondary effects become more significant for stronger shock waves. Prediction of lower amplification by LIA suggests that secondary mechanisms have adverse effects on enhancement of vorticity fluctuations.

Figure 2.3 shows the amplification of solenoidal turbulent kinetic energy by LIA and RDT. Both approaches predict more enhanced streamwise fluctuations than spanwise fluctuations for shock waves with the mean upstream Mach number $M_1^U < 2.0$. However, this trend is reversed for stronger shock waves in LIA predictions. In fact, the predictions by LIA and RDT are close only for very weak shocks, differing significantly for $M_1^U = 1.5$.

Through interaction of vortical waves with a shock wave, acoustic waves are generated downstream of the shock wave. These acoustic waves accompany the purely dilatational velocity fluctuations, which also contribute to the total turbulent kinetic energy. LIA can also predict the acoustic energy generated downstream of the shock. Figure 2.4 presents the amplification of turbulent kinetic energy, including both solenoidal (or vortical, incompressible) and dilatational (or acoustic, compressible) velocity fluctuations. Since part of the acoustic energy undergoes an *inviscid* decay (ref. Appendix B), turbulence behind the shock is not homogeneous in the streamwise direction. Figure 2.4 presents velocity fluctuation levels at both immediate downstream (near-field) and far downstream (far-field) of the

shock. Streamwise velocity fluctuation is always larger than that of the spanwise velocity fluctuations in the near-field. The far-field velocity fluctuations are composed mostly of the solenoidal velocity fluctuations: the acoustic waves contribute less than 2% of the *far-field* turbulent kinetic energy for $M_1^U = 1.2$.

According to LIA, the vorticity waves incident at angles beyond a critical angle $\theta_{cr} = \theta_{cr}(M_1^U)$ generate acoustic waves which decay exponentially as they propagate downstream. This leads to an inviscid decay of the compressible part of velocity fluctuations. The decays of velocity fluctuations are shown in Figure 2.5 for upstream turbulence with a spectrum of

$$E(k) \sim \left(\frac{k}{k_o}\right)^4 \exp\left[-2\left(\frac{k}{k_o}\right)^2\right], \quad (2.1)$$

where k_o is the characteristic wave number corresponding to the energy peak. This is the form of the inflow turbulence spectrum used in the direct numerical simulation of shock turbulence interaction in Chapter 3. Significant but monotonic decay occurs just downstream of a shock wave which is caused by the inviscid decay of acoustic waves.

Decays of velocity fluctuations for different shock strengths are shown in Figure 2.6. The decay in the downstream velocity fluctuation is monotonic for all shock strengths.

We also investigated the effect of upstream spectrum shape on the decay, as shown in Figure 2.7. In addition to the spectrum described in (2.1), we used the von Kármán spectrum

$$E(k) \sim \frac{(k/k_o)^4}{[1 + (k/k_o)^2]^{17/6}}. \quad (2.2)$$

This is a good approximation for the high Reynolds number turbulence, where the slope is k^4 at small k and $k^{-5/3}$ for the inertial subrange at large k . Monotonic decay of turbulent kinetic energy is reproduced. However, the decay rate is faster compared to that of (2.1) (see Figure 2.5), since the von Kármán spectrum has more small scale content, thus causing faster decay.

Experimental studies [Debieve *et al.* 1986, Keller *et al.* 1990] have reported that large scale turbulent motions are enhanced more than small scale motions as turbulence passes through a shock wave, leading to the overall increase of turbulence length scales. In order to check whether turbulence length scales do indeed increase, we investigate the amplification of the one-dimensional velocity spectrum $E_1(k_1)$, which is defined as

$$E_1(k_1) = \int_{-\infty}^{+\infty} \int_{-\infty}^{+\infty} E_{11}(\mathbf{k}) dk_2 dk_3, \quad (2.3)$$

where $\mathbf{k} = (k_1, k_2, k_3)$ is the wave number vector. The velocity spectrum tensor $E_{ij}(\mathbf{k})$ is defined as

$$E_{ij}(\mathbf{k}) = \overline{\widehat{u}_i \widehat{u}_j^*}, \quad (2.4a)$$

where $\widehat{(\cdot)}$ denotes the Fourier transform, the superscript $*$ denotes complex conjugate, and $\overline{(\cdot)}$ indicates the ensemble average. For incompressible isotropic turbulence

$$E_{ij}(\mathbf{k}) = \frac{E(k)}{4\pi k^2} (\delta_{ij} - \frac{k_i k_j}{k^2}), \quad (2.4b)$$

where $k = |\mathbf{k}|$, and $E(k)$ is the energy spectrum function.

In the following analysis, we consider only contributions from the vorticity waves to the upstream and downstream velocity fluctuations. A velocity fluctuation \mathbf{u} associated with a vorticity wave in the homogeneous field can be represented as

$$\mathbf{u} = \widehat{\mathbf{u}}(\omega, k_2, k_3; U_1) \exp[i(\mathbf{k} \cdot \mathbf{x} - \omega t)], \quad (2.5)$$

where $\mathbf{k} \cdot \widehat{\mathbf{u}} = 0$ for a solenoidal wave. Assuming that vorticity fluctuations are simply advected by the mean flow, we obtain the following dispersion relation

$$\omega - U_1 k_1 = 0. \quad (2.6)$$

In this approximation, the turbulence fields upstream and downstream of the shock are considered homogeneous and frozen with respect to the corresponding mean

flow. From Appendices A and B, the Fourier coefficient of the streamwise velocity fluctuation after the interaction can be expressed in terms of that before the interaction. The transfer function $Z(\omega, k_2, k_3)$ is defined as

$$Z(\omega, k_2, k_3; M_1^U) = \frac{\hat{u}_1^D(\omega, k_2, k_3; U_1^D)}{\hat{u}_1^U(\omega, k_2, k_3; U_1^U)}, \quad (2.7)$$

where the superscripts U and D refer to upstream and downstream states.

If there is no generation or destruction of waves inside the shock wave, the frequency ω of a vorticity wave remains *unchanged* by the interaction, while the associated wave number k_1 *changes* to satisfy the dispersion relation (2.6). The one-dimensional frequency spectrum $E_1(\omega)$ is defined as

$$E_1(\omega) = \int \int F_{11}(\omega, k_2, k_3; U_1) dk_2 dk_3, \quad (2.8a)$$

where the limits of the integrations are $(-\infty, +\infty)$ for both k_2 and k_3 . In the above expression, F_{11} is

$$F_{11}(\omega, k_2, k_3; U_1) = \overline{\hat{u}_1(\omega, k_2, k_3; U_1) \hat{u}_1^*(\omega, k_2, k_3; U_1)}. \quad (2.8b)$$

Amplification of the one-dimensional frequency spectrum is described by the ratio of the frequency spectra before and after the interaction $S^\omega(\omega; M_1^U)$, which is

$$\begin{aligned} S^\omega(\omega; M_1^U) &= \frac{\int \int F_{11}^D(\omega, k_2, k_3; U_1^D) dk_2 dk_3}{\int \int F_{11}^U(\omega, k_2, k_3; U_1^U) dk_2 dk_3} \\ &= \frac{\int \int |Z(\omega, k_2, k_3; M_1^U)|^2 F_{11}(\omega, k_2, k_3; U_1^U) dk_2 dk_3}{\int \int F_{11}(\omega, k_2, k_3; U_1^D) dk_2 dk_3}. \end{aligned} \quad (2.9)$$

Spectral amplification ratio is dependent on the special form of the upstream spectrum shapes. We choose a von Kármán spectrum (2.2) for the energy spectrum in the following analyses.

The amplification ratios of the one-dimensional frequency spectra for different shock strengths are shown in Figures 2.8: the results from RDT and LIA are presented in Figures 2.8(a) and 2.8(b), respectively. The results from RDT and LIA are qualitatively the same: the spectrum amplification ratio is larger for a wave with small ω , which is consistent with the results of Ribner [1987]. Some researchers interpret this fact as evidence of turbulence length scale increase through the interaction, but this conclusion does not necessarily follow, for the change in frequency spectra reflects a change in time scale, not in length scale. More amplification at the small frequency part of the spectrum implies that turbulence time scale increases through the interaction.

To investigate the length scale change, one should evaluate the amplification of wave number spectrum rather than that of frequency spectrum. Amplifications of these two spectra are not the same: as a wave passes through the shock, the relation between wave number and frequency changes due to the mean flow deceleration (see (2.6)). The one-dimensional wave number spectrum is obtained by replacing ω with $U_1 k_1$ in (2.8b). Streamwise velocity fluctuations upstream and downstream of the shock can be represented as

$$\overline{u_1^U{}^2} = \int \left[\int \int F_{11}^U(U_1^U k_1, k_2, k_3; U_1^U) dk_2 dk_3 \right] dk_1^U, \quad (2.10a)$$

$$\overline{u_1^D{}^2} = \int \left[\int \int F_{11}^D(U_1^D k_1, k_2, k_3; U_1^D) dk_2 dk_3 \right] dk_1^D. \quad (2.10b)$$

Downstream velocity fluctuation can also be expressed in terms of the upstream spectrum F_{11}^U and its amplification ratio at the same wave number across the shock wave $S^{k_1}(k_1; M_1^U)$ as

$$\begin{aligned} \overline{u_1^D{}^2} &= \int S^{k_1}(k_1; M_1^U) \left[\int \int F_{11}^U(U_1^U k_1, k_2, k_3; U_1^U) dk_2 dk_3 \right] dk_1^U \\ &= \int S^{k_1}(k_1; M_1^U) \left[\int \int F_{11}^U(U_1^U k_1, k_2, k_3; U_1^U) dk_2 dk_3 \right] (J dk_1^D), \end{aligned} \quad (2.11a)$$

where

$$S^{k_1}(k_1; M_1^U) = \frac{\int \int F_{11}^D(U_1^D k_1, k_2, k_3; U_1^D) dk_2 dk_3}{\int \int F_{11}^U(U_1^U k_1, k_2, k_3; U_1^U) dk_2 dk_3}. \quad (2.11b)$$

Here J is the Jacobian of the transformation from the upstream to the downstream wave number defined as $J = \rho^U / \rho^D < 1$. (The upstream wave number interval dk_1^U corresponds to the downstream wave number interval $dk_1^D = J^{-1} dk_1^U$.) Comparing the terms in (2.10b) and (2.11a), we have the amplification ratio of the one-dimensional wave number spectrum $JS^{k_1}(k_1; M_1^U)$ as

$$\begin{aligned} JS^{k_1}(k_1; M_1^U) &= J \times \frac{\int \int F_{11}^D(U_1^D k_1, k_2, k_3; U_1^D) dk_2 dk_3}{\int \int F_{11}^U(JU_1^U k_1, k_2, k_3; U_1^U) dk_2 dk_3} \times \frac{\int \int F_{11}^U(JU_1^U k_1, k_2, k_3; U_1^U) dk_2 dk_3}{\int \int F_{11}^U(U_1^U k_1, k_2, k_3; U_1^U) dk_2 dk_3} \\ &= J \times S^\omega(\omega; M_1^U) \times \frac{E_1^U(\omega)}{E_1^U(\omega/J)}, \end{aligned} \quad (2.12)$$

where $\omega = U_1^D k_1 = JU_1^U k_1$. The wave number spectrum amplification factor is, therefore, the product of the Jacobian, the frequency spectrum amplification and the ratio of the upstream frequency spectra at two different frequencies. The resultant wave number spectrum amplifications for different shock strengths predicted by RDT and LIA are presented in Figures 2.9(a) and (b), respectively. These predictions are qualitatively consistent: the spectral density increases more at large wave numbers, even though it increases more at small frequencies (see Figure 2.8). LIA predicts a suppression of the spectrum at small wave numbers for large upstream Mach numbers, while RDT predicts an amplification at all wave numbers irrespective of the shock strength. Larger amplification at large wave numbers is more pronounced for stronger shock waves.

It is, therefore, erroneous to infer an increase in the length scale in shock turbulence interaction by appealing to Ribner's analysis (akin to Figures 2.8) as Keller *et al.* [1990] have done. Investigation of the spectrum amplification leads to the conclusion that turbulence time scale increases through the interaction, while turbulence length scale decreases.

The experimental results by Debieve *et al.* [1986] are consistent with the present predictions. However, they compared the upstream frequency spectrum to that on the shock and concluded an increase in the length scale. The spectrum on the shock is contaminated by the intermittency effect due to the unsteady shock front distortion. The characteristic length scale of the distortion is scaled with the upstream turbulence length scale (see Section 2.2 for LIA and Section 4.2 for DNS) to yield an apparent amplification of the spectrum on the shock at an energetic (or large) scale. This enhancement does not necessarily imply the amplification of the turbulent motion of that scale. In order to investigate length scale change, one has to transform frequency spectra into wave number spectra and compare the upstream spectrum with the downstream spectrum. Proper comparison of wave number spectra shows more amplification at small scales rather than at large scales, leading to an overall scale decrease. Direct numerical simulations confirm that turbulence length scales do decrease through the shock-turbulence interaction (see Section 4.2).

Since linear analyses predict the change of the Fourier coefficients of the velocity components across the shock wave (see (2.7)), the changes in turbulence length scales can also be calculated. The change in the Taylor microscale λ_α defined as

$$\lambda_\alpha^2 = \frac{\overline{u_\alpha^2}}{\overline{u_{\alpha,\alpha}^2}}, \quad (2.13)$$

across the shock wave is independent of the shape of the three-dimensional energy spectrum for isotropic upstream turbulence, since the contributions to the integral involving the wave number magnitude k (see (A.25)) are cancelled out in the evaluation of the ratios of $\overline{u_\alpha^2}$ and $\overline{u_{\alpha,\alpha}^2}$ across the shock wave. The denominator in (2.13), $\overline{u_{\alpha,\alpha}^2}$, can be evaluated using

$$\overline{u_{\alpha,\alpha}^2} = \int \int \int k_\alpha^2 E_{\alpha\alpha} dk_1 dk_2 dk_3. \quad (2.14)$$

Figures 2.10(a) and (b) show the change in the Taylor microscales across the shock wave predicted by LIA and RDT. (In LIA prediction, only the solenoidal velocity component is included because the contribution from the dilatational component

becomes negligible after a short distance from the shock wave. See Figures 2.4, 2.5 and 2.6.) All the length scales are found to decrease through the interaction: the streamwise scale decreases more than the transverse scale. LIA predicts more reduction in the streamwise scale and less reduction in the transverse scale than RDT does. For weak shock waves, however, the predictions by LIA and RDT are in good agreement.

Shock/turbulence interaction leads to noise generation behind the shock wave in the form of fluctuating pressure, p' . Using (B.55) and (B.56) and from the isotropy relations (2.4) for upstream velocity fluctuations (see also (B.61) - (B.64)),

$$\begin{aligned}
 \frac{\overline{p'^2}}{p^D{}^2} &= \frac{1}{U_1^2} \left(\frac{2\gamma m}{(\gamma+1)m - (\gamma-1)} \right)^2 \int \frac{\Pi^2}{\cos^2 \theta \cos^2 \theta'} \overline{\hat{u}_1 \hat{u}_1^*} dk \\
 &= \frac{1}{4U_1^2} \left(\frac{2\gamma m}{(\gamma+1)m - (\gamma-1)} \right)^2 \int_0^\infty E(k) dk \int_0^{2\pi} \frac{\Pi^2 \cos \theta}{\cos^2 \theta'} d\theta \\
 &= \frac{3}{8} \frac{u_o^2}{U_1^2} \left(\frac{2\gamma m}{(\gamma+1)m - (\gamma-1)} \right)^2 \int_0^{2\pi} \frac{\Pi^2 \cos \theta}{\cos^2 \theta'} d\theta, \tag{2.15}
 \end{aligned}$$

where p^D is the downstream mean pressure and

$$\theta' = \tan^{-1}(m \tan \theta). \tag{B.5c}$$

Figures 2.11(a) and (b) show the pressure fluctuation for various shock strengths both at the immediate downstream and far downstream of the shock wave normalized by the downstream mean pressure and upstream mean pressure, respectively. Note that for normalization we have also used the upstream turbulence intensity, because pressure fluctuations scale with the upstream turbulence intensity independent of the shape of the spectrum. Near field noise scaled with the downstream mean pressure peaks around $M_1^U = 1.3$, and far field noise reaches its asymptotically maximum strength for very large Mach numbers. Note that acoustic energy decays by an order of magnitude from the near field to the far field. Even though

the near- and far-field pressure intensities scaled with the downstream mean pressure tend to asymptotic values for an infinite strength shock wave, their absolute amplitudes increase indefinitely as the shock strength increases (see Figure 2.11(b)).

2.2 Statistics of the Shock Front

Using LIA, we can estimate the level of fluctuations of the shock front caused by the action of turbulence. The details for calculating the variances of a local shock front displacement ξ , its inclination angle σ_2 , and its curvature κ_2 are shown in Appendix B. The nondimensionalized variances of those quantities are $k_o^2 \overline{\xi^2}$, $\overline{\sigma_2^2}$, and $k_o^{-2} \overline{\kappa_2^2}$, where k_o is the wave number corresponding to the energy peak in the spectrum.

The dimensionless variance of the shock front displacement (see (B.68)) can be expressed as

$$\begin{aligned} k_o^2 \overline{\xi^2} &= \frac{1}{U_1^2} \int_0^\infty \left(\frac{k}{k_o} \right)^{-2} E(k) dk \int_0^{\pi/2} (a_S^2 + b_S^2) \cos \theta d\theta \\ &= \frac{3}{2} \left(\frac{u_o}{U_1} \right)^2 \frac{\int_0^\infty E(k^*)/k^{*2} dk^*}{\int_0^\infty E(k^*) dk^*} \int_0^{\pi/2} (a_S^2 + b_S^2) \cos \theta d\theta, \end{aligned} \quad (2.16)$$

where $k^* = k/k_o$, and u_o is the rms fluctuation velocity in one direction. (Definitions of a_S and b_S are given in (B.18) and (B.21).) Likewise, the dimensionless variance of the shock front curvature (see (B.69)) can be written as

$$k_o^{-2} \overline{\kappa_2^2} = \frac{9}{32} \left(\frac{u_o}{U_1} \right)^2 \frac{\int_0^\infty k^{*2} E(k^*) dk^*}{\int_0^\infty E(k^*) dk^*} \int_0^{\pi/2} (a_S^2 + b_S^2) \cos^5 \theta d\theta. \quad (2.17)$$

As seen in (2.16) and (2.17), the statistics of shock front displacement and its curvature are dependent on the shape of the upstream spectrum, $E(k^*)$. The shock wave displacement has significant contributions from large scale turbulence,

while its curvature is scaled with the inverse of upstream turbulence microscale ($\overline{\kappa_2^2} \sim \int k^2 E(k) dk / \int E(k) dk \simeq 1/\lambda^2$).

Statistics of shock front distortion are obtained by numerically integrating (B.65), (2.16) and (2.17) using the energy spectrum in (2.1). Figure 2.12 presents the *rms* values of

$$\left(\frac{U_1}{u_o}\right) k_o \xi, \quad \left(\frac{U_1}{u_o}\right) \sigma_2, \quad \text{and} \quad \left(\frac{U_1}{u_o}\right) \frac{\kappa_2}{k_o}.$$

Note that the statistics of the shock front distortions are scaled with the upstream turbulence intensity. As the mean upstream Mach number increases, the scaled *rms* values are found to decrease.

Considering the time dependence of the upstream velocity fluctuations at a fixed point, LIA can predict the local fluctuating shock front speed, $\xi_{,t}$. Expression (B.27) can be rewritten as

$$du_i = d\hat{u}_i \exp[i(k_1(x_1 - U_1 t) + k_2 x_2 + k_3 x_3)]. \quad (2.18)$$

Since the velocity fluctuations at the shock front ($x_1 = 0$) vary not only in the transverse direction but also in time, the argument of the exponential function in (2.18) becomes $i(-k_1 U_1 t + k_2 x_2 + k_3 x_3)$ with $x_1 = 0$. Therefore, expression (B.66) for the local shock displacement can be rewritten as

$$\xi = \frac{1}{ik_h} \hat{\sigma} \exp[i(\mathbf{k}_h \cdot \mathbf{x}_h - k_1 U_1 t + \delta_{sh})], \quad (2.19)$$

where k_h is the magnitude of $\mathbf{k}_h = (k_2, k_3)$, and $\mathbf{x}_h = (x_2, x_3)$. From (2.19), one obtains the relation between the local fluctuating shock front speed, $\xi_{,t}$, and the local shock front inclination angle in the transverse direction (x_2 direction), $\sigma_2 = \xi_{,2}$, as

$$\xi_{,t} = -\frac{k_1 U_1}{k_2} \sigma_2. \quad (2.20)$$

Using (B.57) and (B.58), (2.20) can be expressed as

$$\xi_{,t} = -\frac{k_1}{|\mathbf{k}_h|} \hat{u}_1 \sqrt{a_S^2 + b_S^2} \exp[i(\mathbf{k}_h \cdot \mathbf{x}_h - k_1 U_1 t + \delta_{sh})]. \quad (2.21)$$

Figure 2.13 compares the local upstream velocity fluctuation and the local shock front speed for upstream waves incident on a shock wave of $M_1^U = 1.2$ at different angles. The magnitude of the shock speed is comparable to the upstream fluctuation velocity. For waves whose incident angles are smaller than the critical angle of incidence, $\theta_{cr} = 36.4^\circ$, the local shock front speed lags by a phase angle between 0 to 90° with respect to the upstream velocity fluctuation; for waves whose incident angles are larger than the critical angle, the shock front speed is in phase with the velocity fluctuation. The local shock front speed which is in phase with the upstream fluctuation velocity attenuates the fluctuations in the effective upstream Mach number, $M_1 = (U_1 + u_1 - \xi_{,t})/c$.

Figures 2.14(a) and (b) show the dependence of the *rms* fluctuating shock front speed on the mean upstream Mach number. The shock front speed exceeds the upstream fluctuation velocity for $M_1^U < 1.25$. For weak shock waves, the shock front speed is close to the upstream fluctuation velocity resulting in approximately uniform effective upstream Mach number.

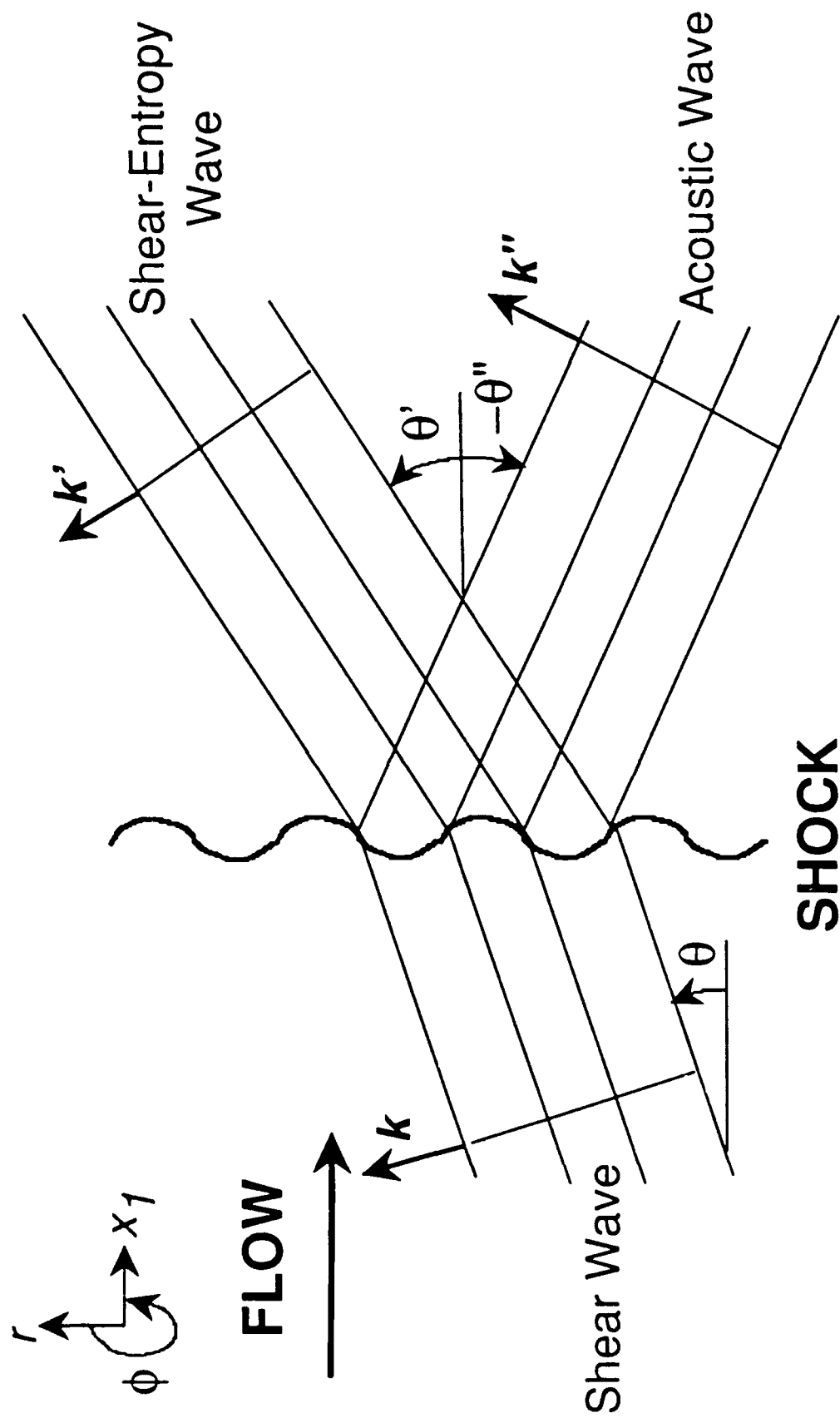


FIGURE 2.1. the coordinate system used in the linear analyses.

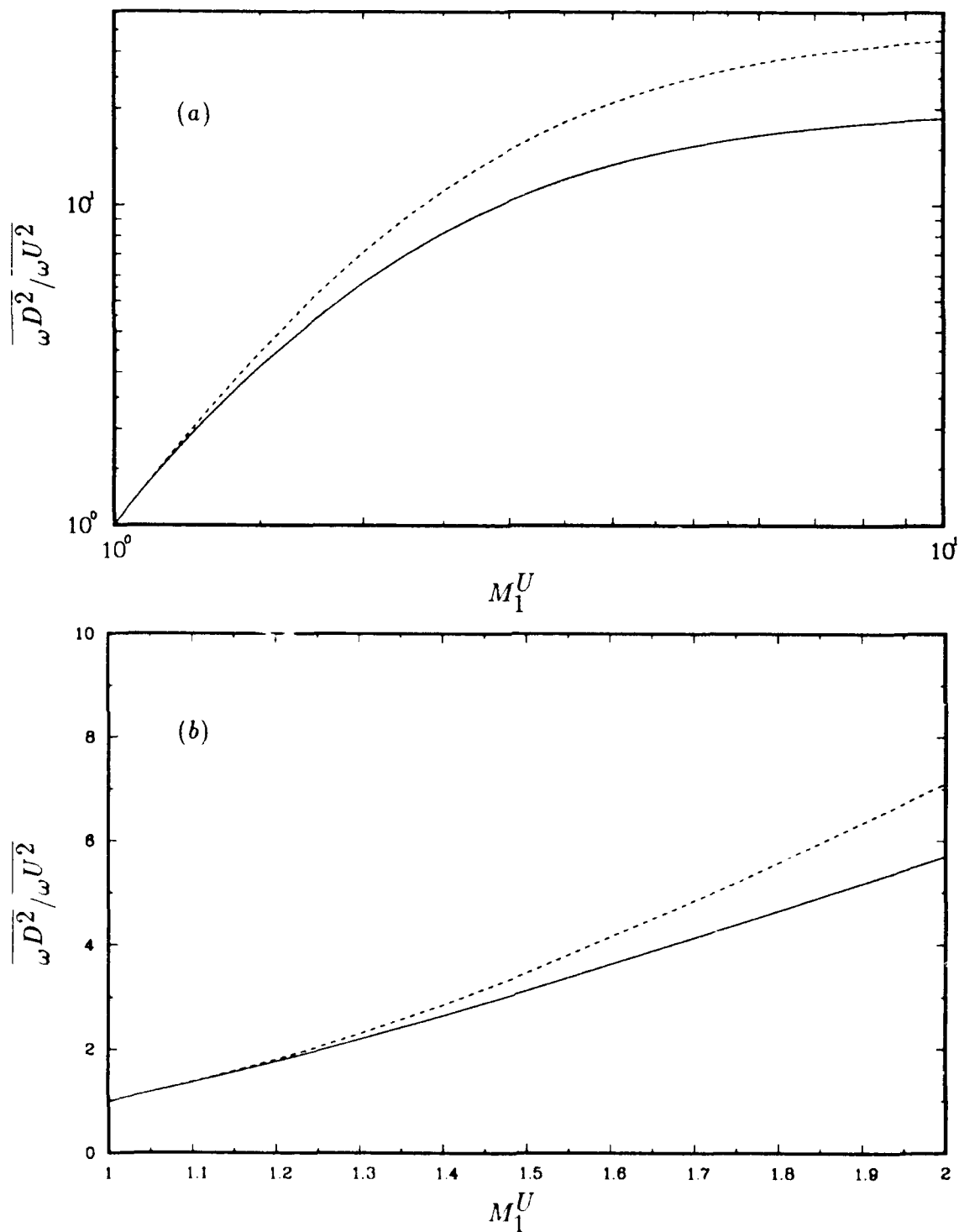


FIGURE 2.2. Predictions of transverse vorticity amplification: (a) $1 \leq M_1^U \leq 10$, (b) $1 \leq M_1^U \leq 2$. — LIA, ---- RDT.

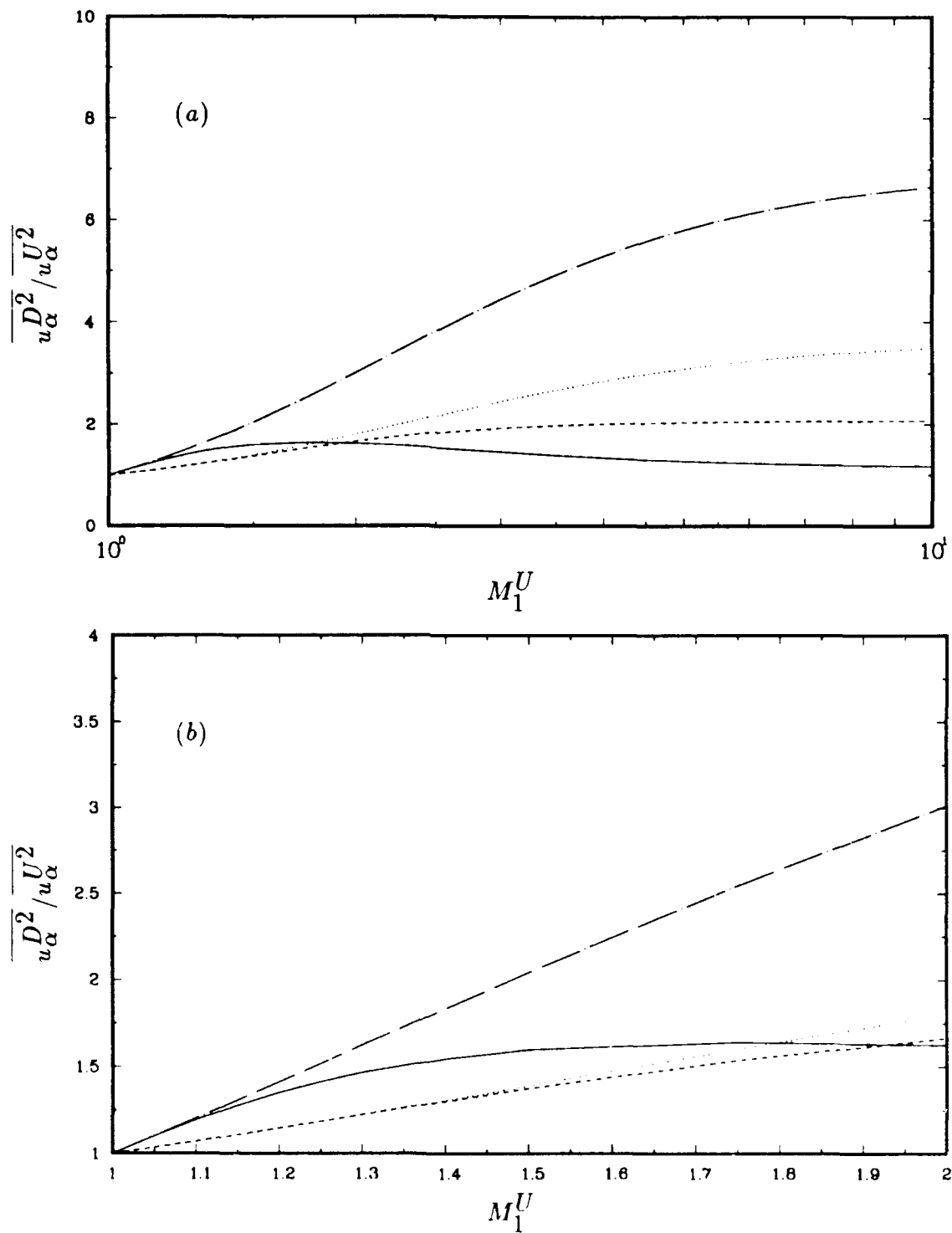


FIGURE 2.3. Predictions of solenoidal velocity component amplification: (a) $1 \leq M_1^U \leq 10$, (b) $1 \leq M_1^U \leq 2$. — u_1 (LIA), ---- $u_2 \& u_3$ (LIA), — u_1 (RDT), $u_2 \& u_3$ (RDT).

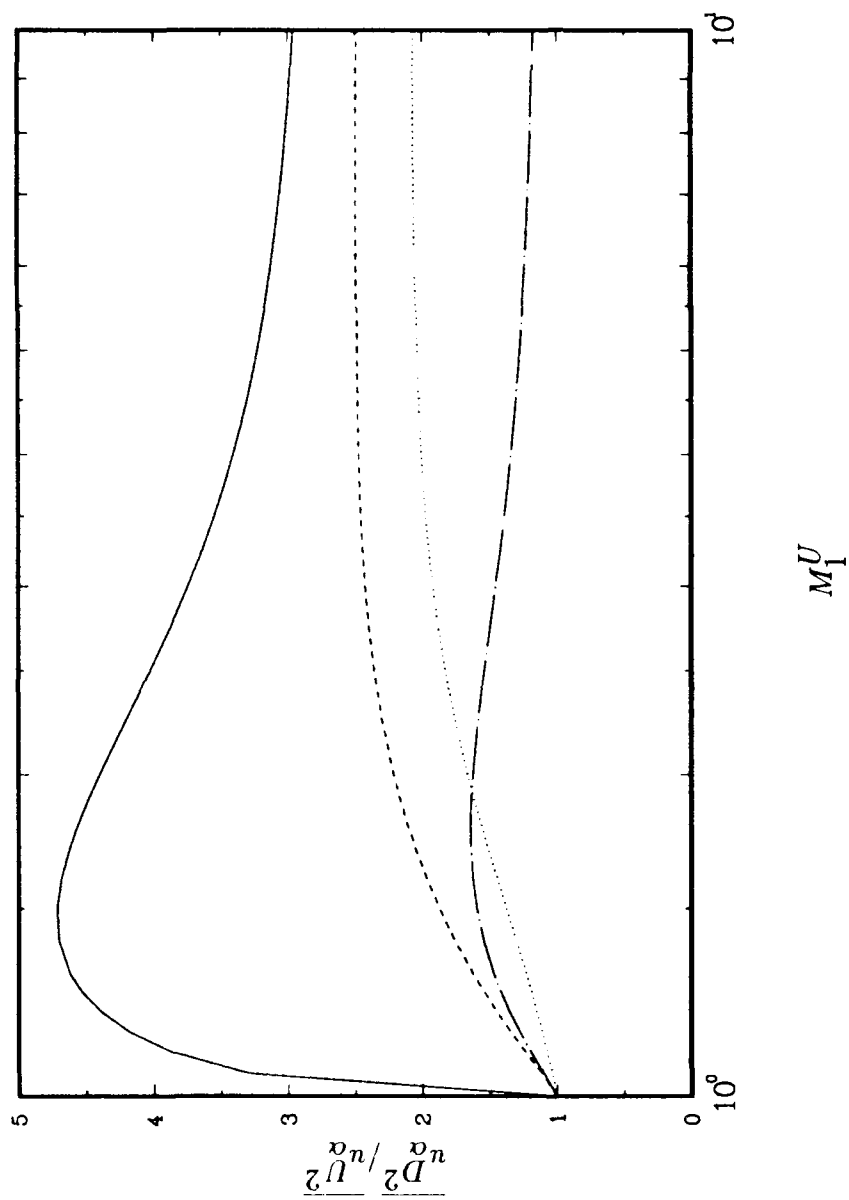


FIGURE 2.4. Predictions of velocity component amplification at near-field and far-field: — $u_1(\text{near})$, --- $u_2 \& u_3(\text{near})$, $u_1(\text{far})$, - · - · - $u_2 \& u_3(\text{far})$.

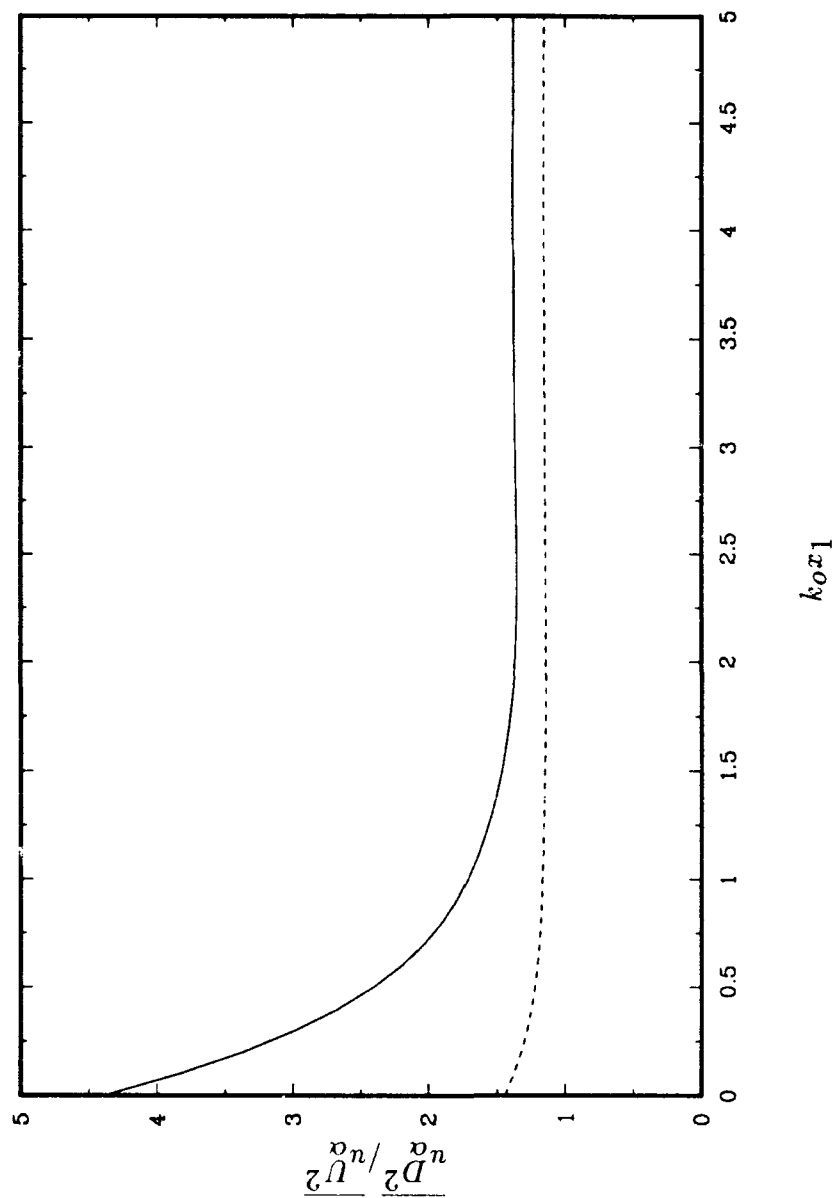


FIGURE 2.5. Decay of velocity components behind the shock wave for exponential fall-off upstream spectrum (2.1), with $M_1^U = 1.2$: — u_1 , ---- u_2/u_3 .

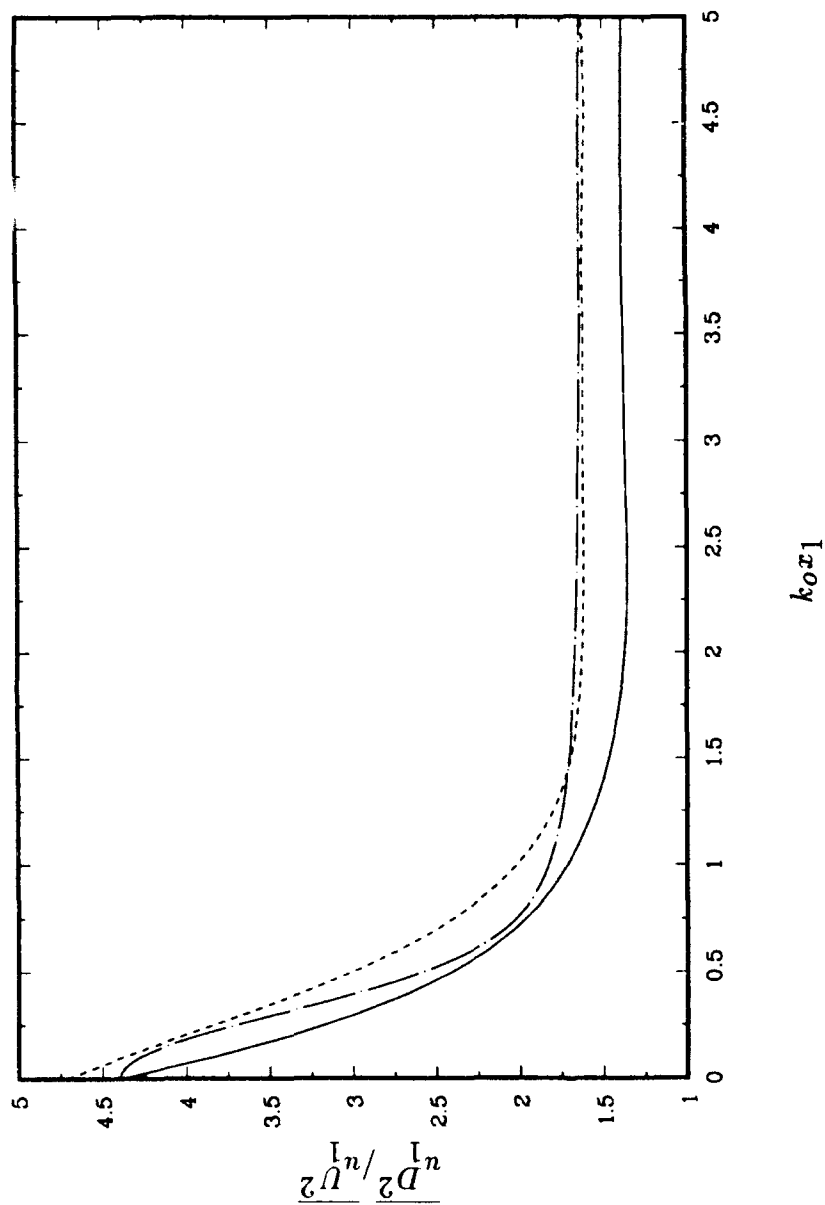


FIGURE 2.6. Decay of streamwise velocity fluctuation behind the shock wave for exponential fall-off upstream spectrum, (2.1): — $M_1^U = 1.2$, --- $M_1^U = 1.5$, - · - $M_1^U = 2.0$.

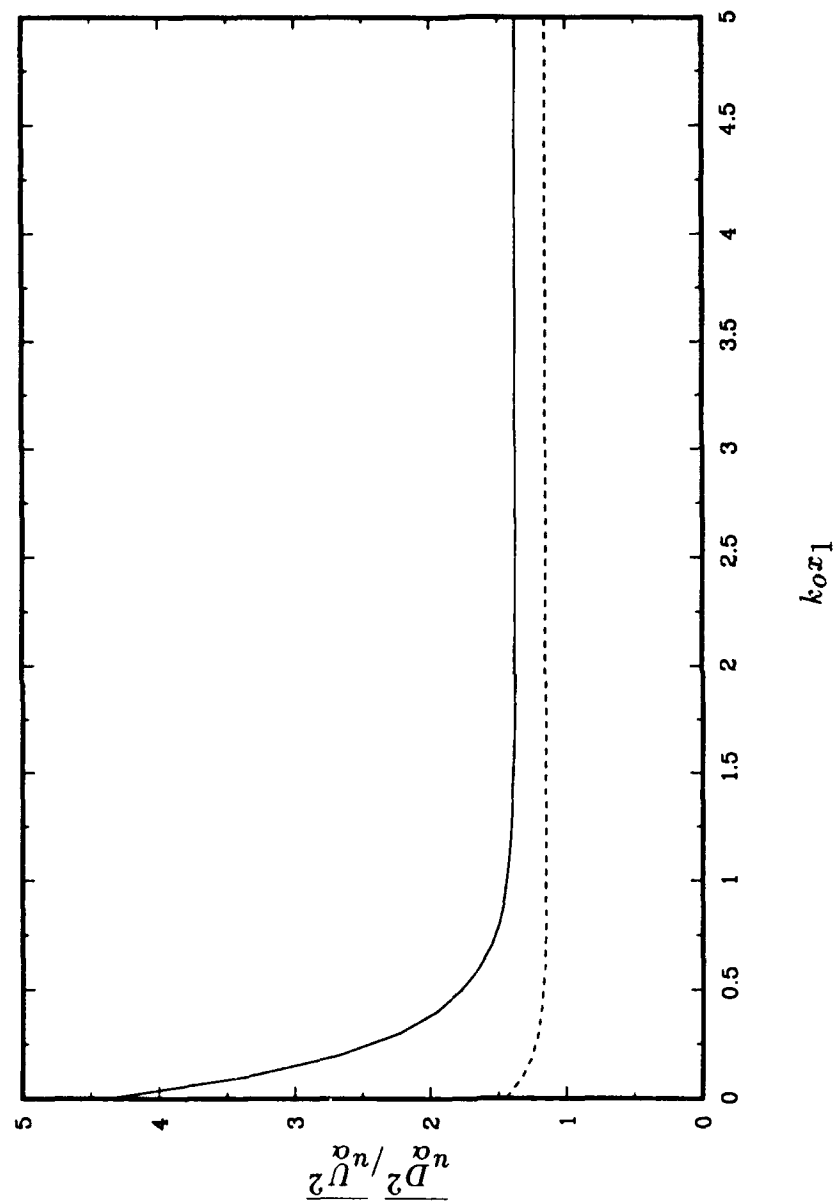


FIGURE 2.7. Decay of streamwise velocity fluctuation behind the shock wave for a von Kármán upstream spectrum (2.2), with $M_1^U = 1.2$: — u_1 , --- $u_2 u_3$.

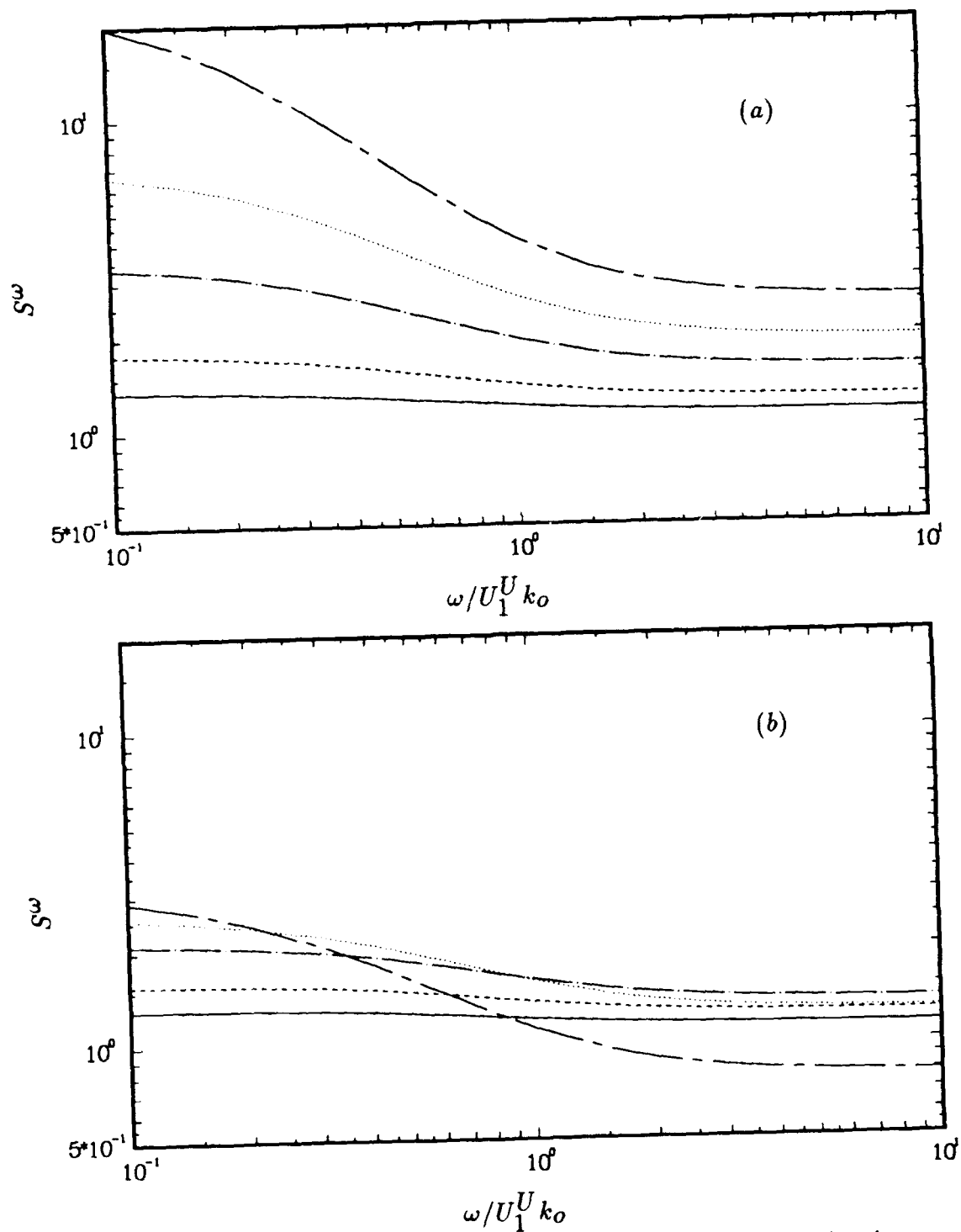


FIGURE 2.8. Frequency spectrum amplification ratio for a von Kármán upstream spectrum, (2.2): (a) RDT, (b) LIA. — $M_1^U = 1.1$, ---- $M_1^U = 1.2$, — — — $M_1^U = 1.5$, $M_1^U = 2.0$, - · - · - $M_1^U = 5.0$.

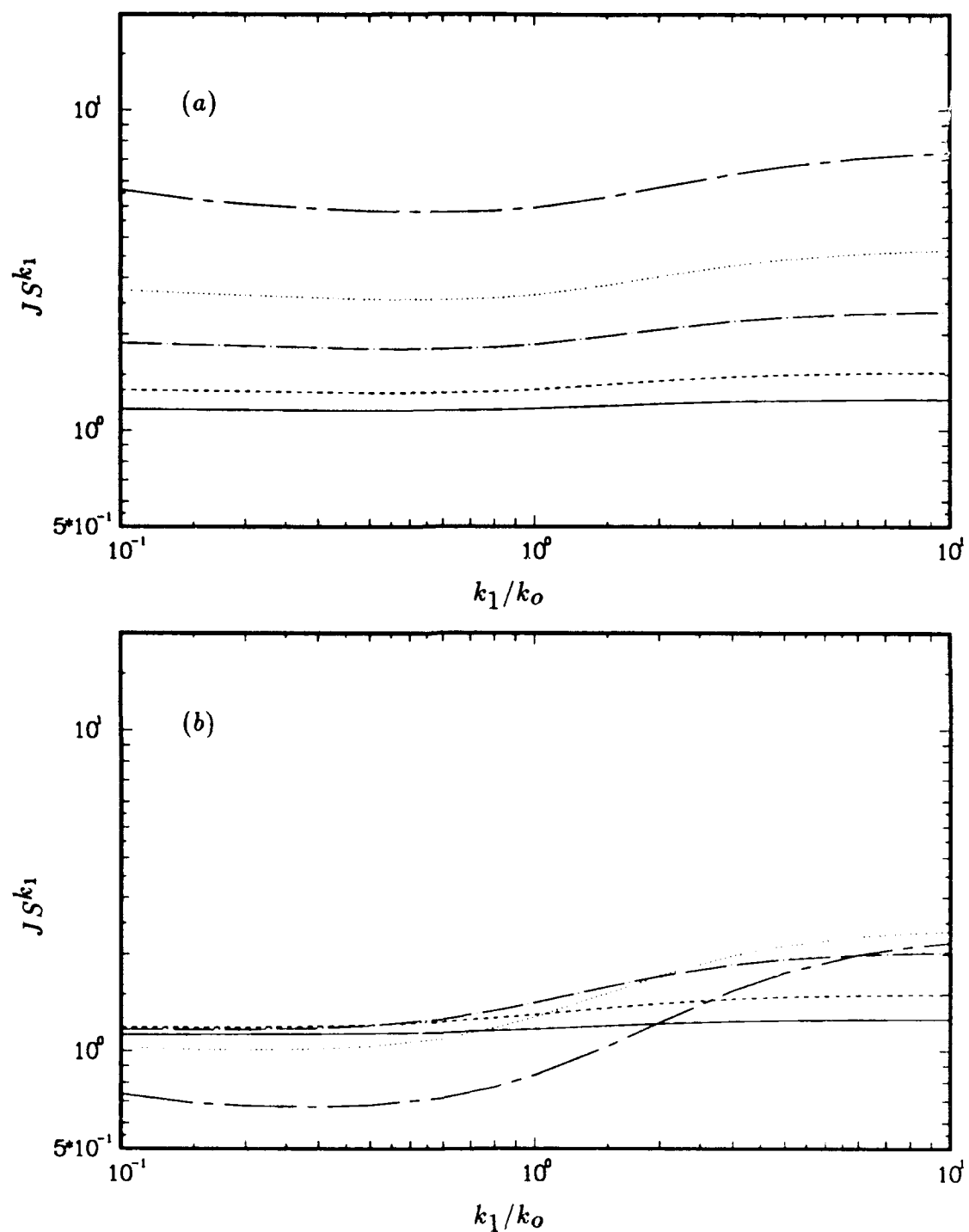


FIGURE 2.9. Wave number spectrum amplification ratio for a von Kármán upstream spectrum, (2.2): (a) RDT, (b) LIA. — $M_1^U = 1.1$, ---- $M_1^U = 1.2$, — · — $M_1^U = 1.5$, $M_1^U = 2.0$, --- $M_1^U = 5.0$.

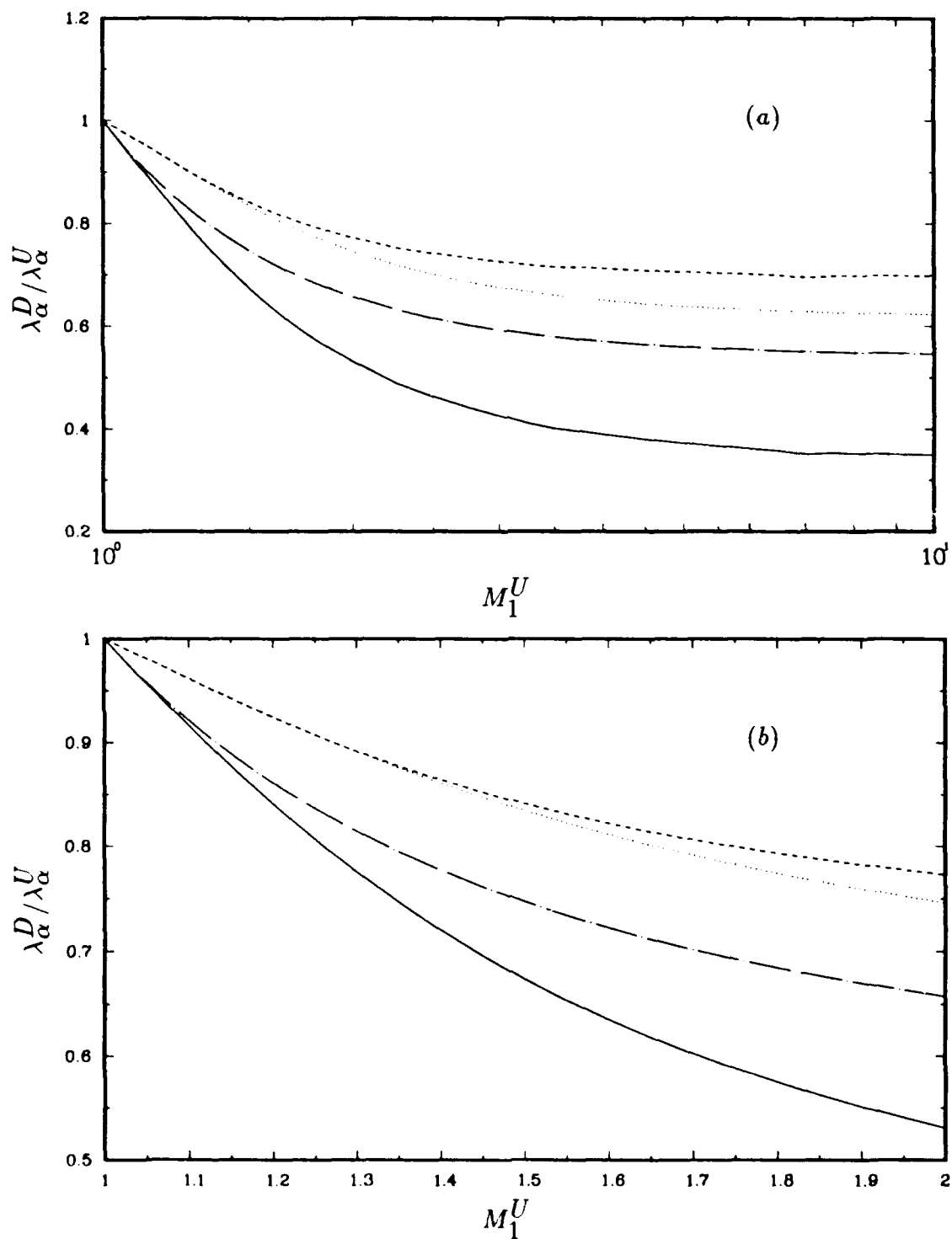


FIGURE 2.10. Predictions of changes in Taylor microscale: (a) $1 \leq M_1^U \leq 10$, (b) $1 \leq M_1^U \leq 2$. — $\lambda_1(\text{LIA})$, ---- $\lambda_2 \& \lambda_3(\text{LIA})$, — — $\lambda_1(\text{RDT})$, $\lambda_2 \& \lambda_3(\text{RDT})$.

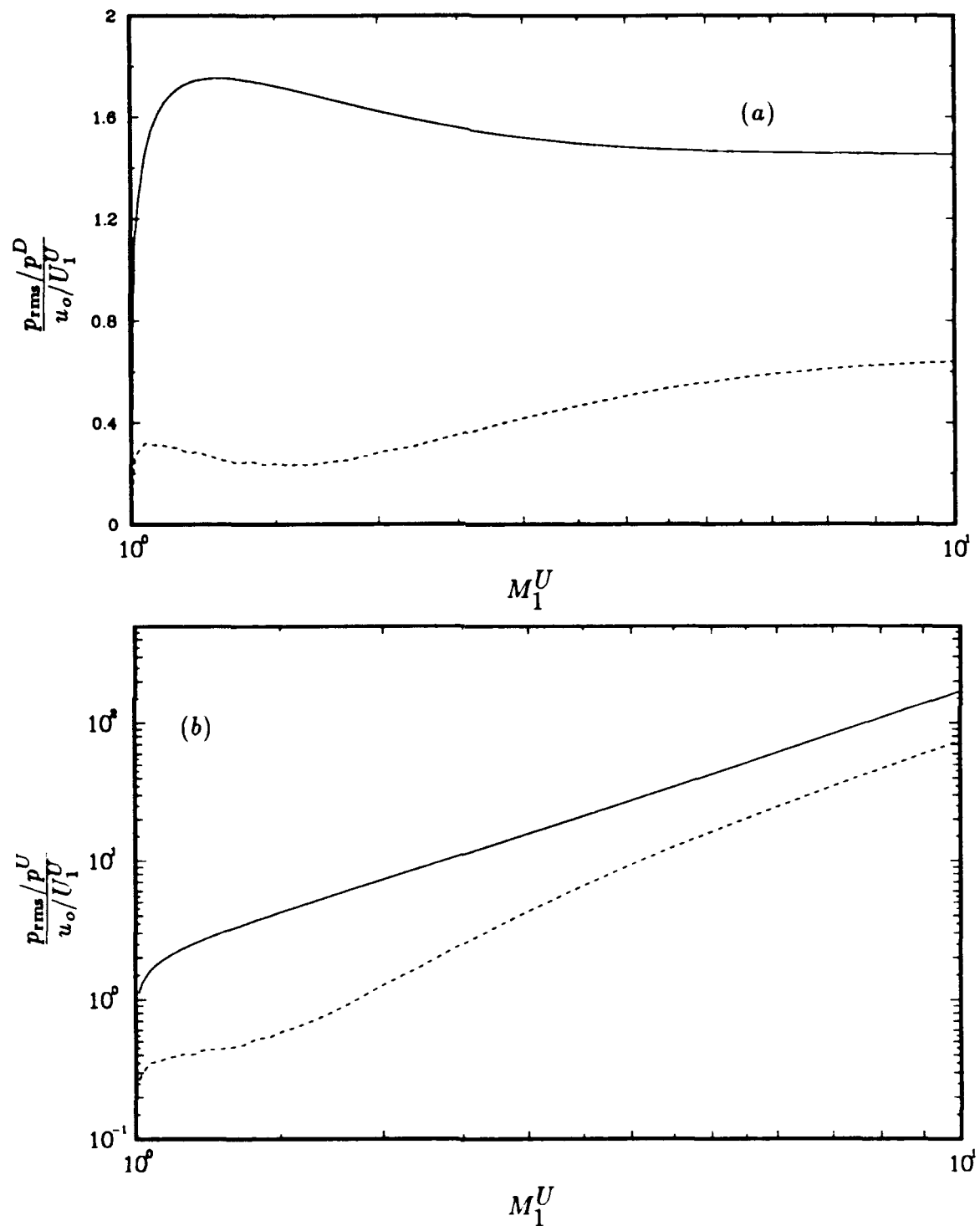


FIGURE 2.11. Acoustic pressure fluctuation downstream of the shock wave: (a) normalized with the downstream mean pressure, (b) normalized with the upstream mean pressure. — near field, ---- far field.

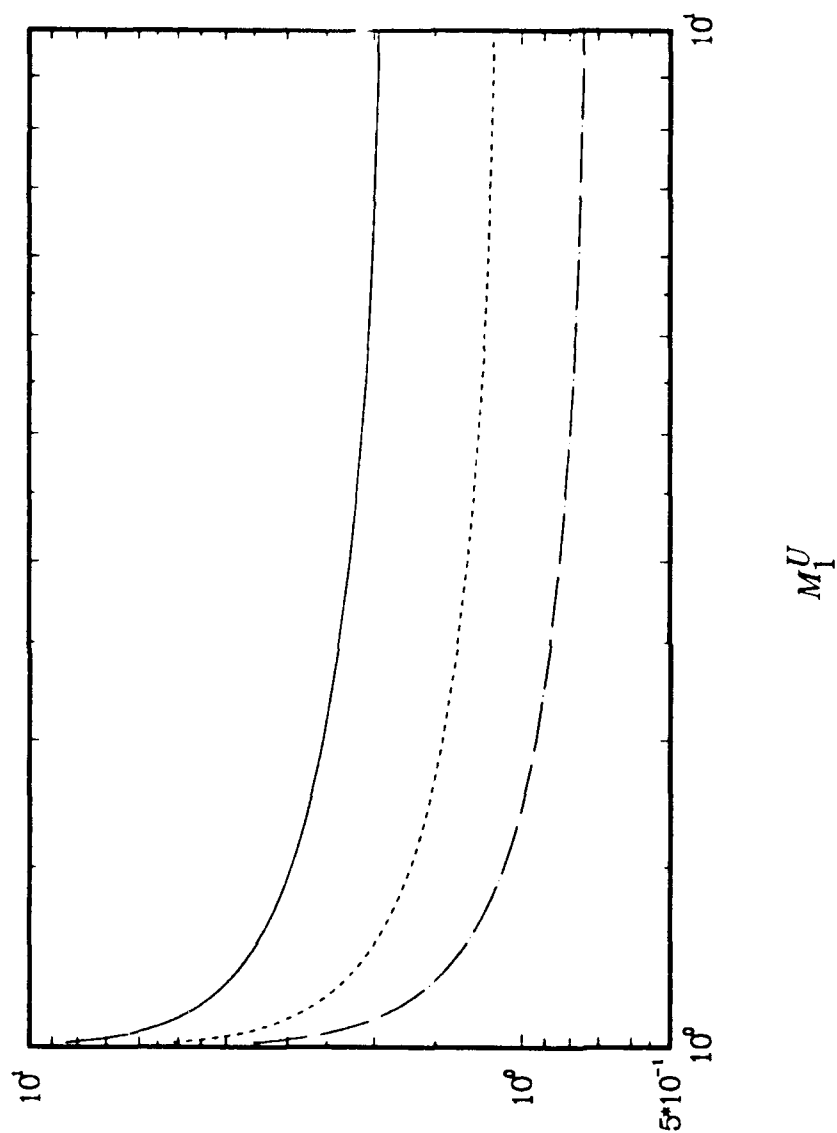
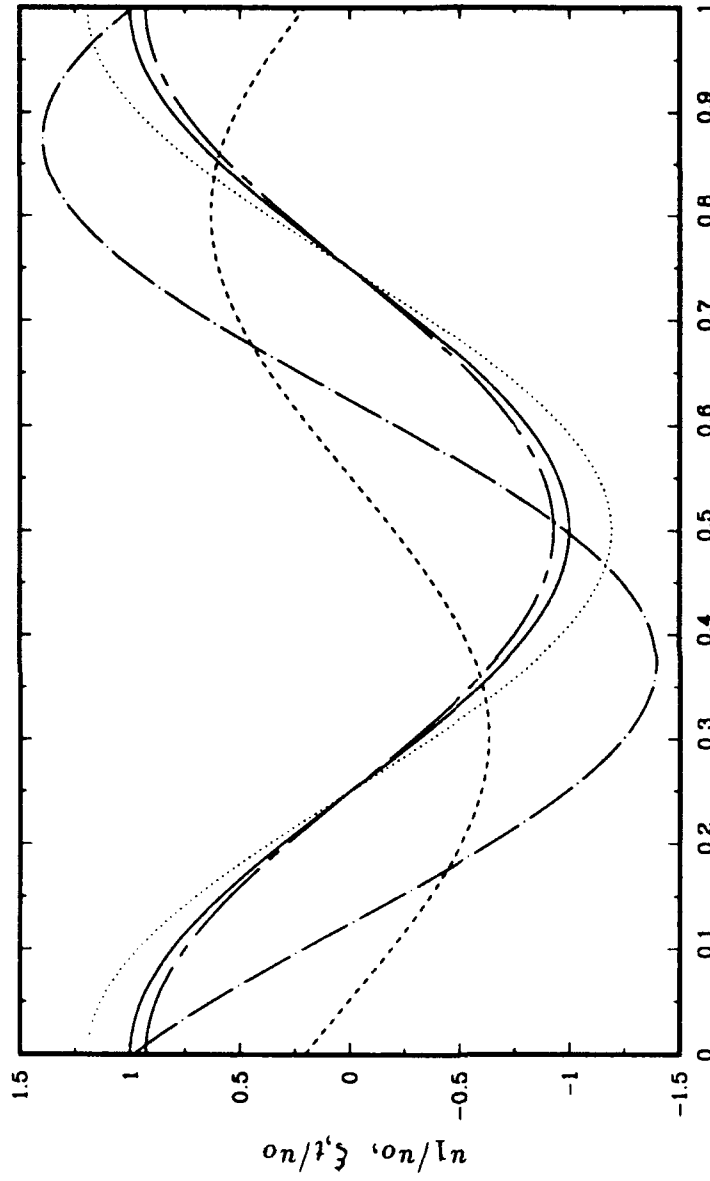


FIGURE 2.12. Shock front statistics for exponential fall-off upstream spectrum, (2.1): — $(U_1^U k_0 / u_0) \xi_{\text{rms}}$,
 ---- $(U_1^U / u_0) (\sigma_2)_{\text{rms}}$, - · - $(U_1^U / k_0 u_0) (\kappa_2)_{\text{rms}}$.



$$(k_2x_2 + k_3x_3 - k_1U_1t)/2\pi$$

FIGURE 2.13. Comparison of local upstream velocity fluctuation and the local shock front speed for various angles of incidence (ref. (2.18)): — u_1 , --- $\xi_t(\theta = 15^\circ)$, - - - $\xi_t(\theta = 30^\circ)$, $\xi_t(\theta = 45^\circ)$, - · - · $\xi_t(\theta = 60^\circ)$.

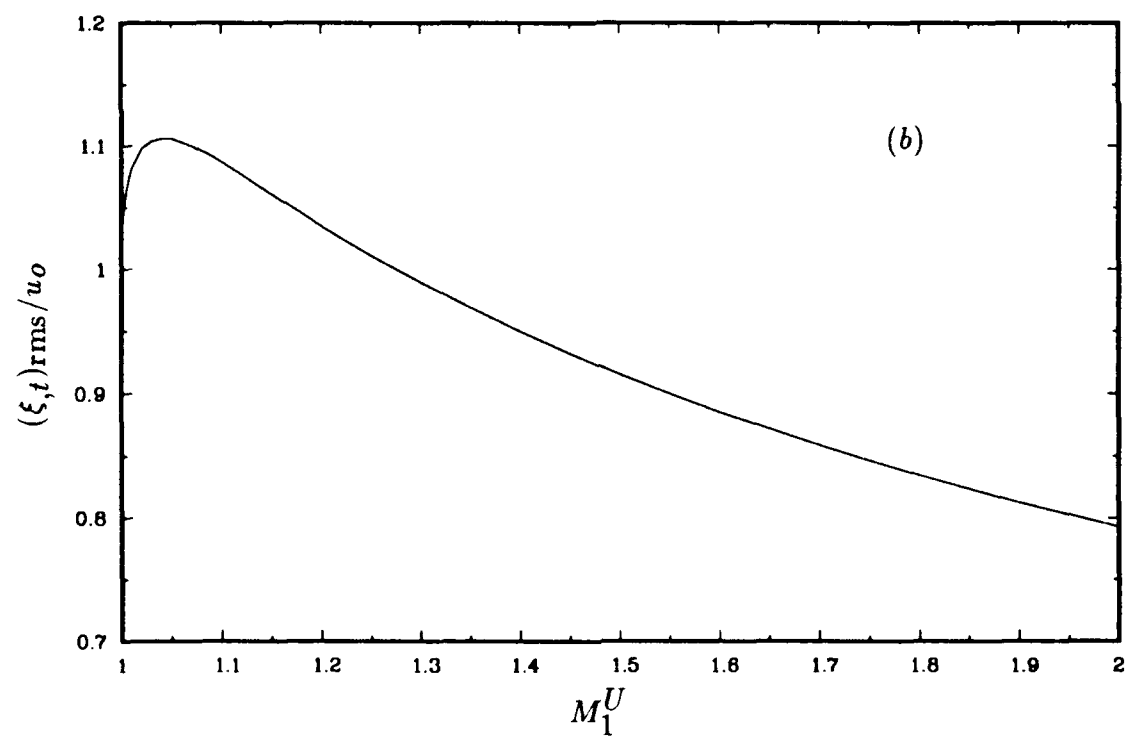
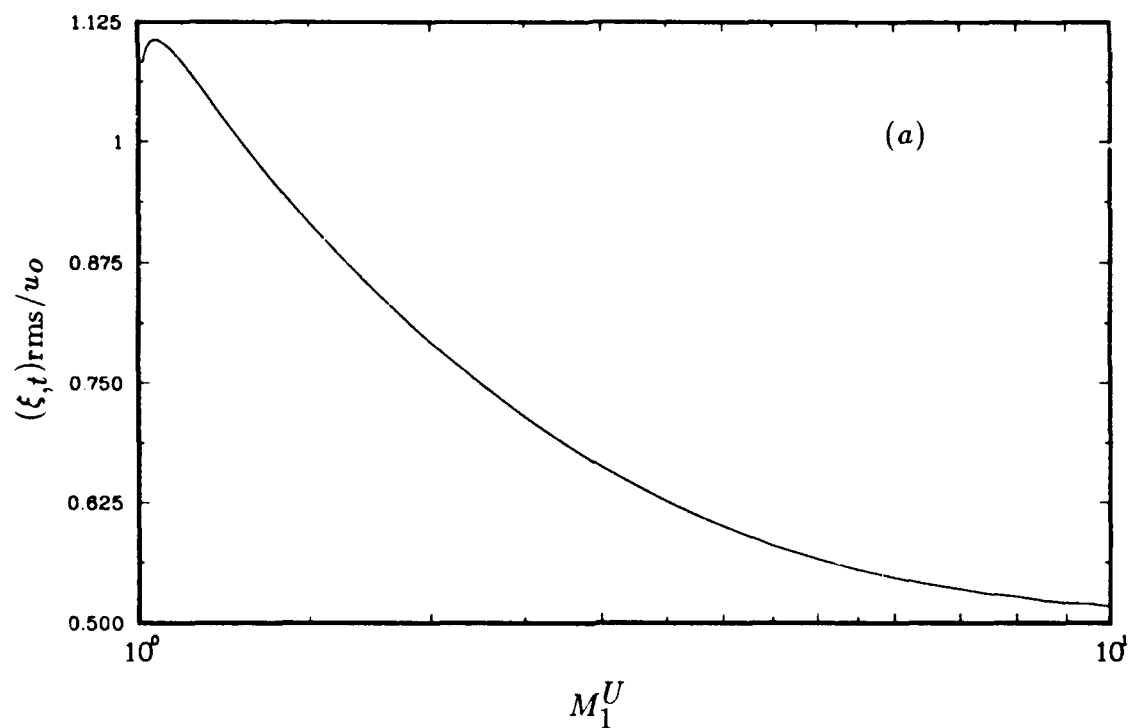


FIGURE 2.14. Predictions of *rms* shock front speed by LIA: (a) $1 \leq M_1^U \leq 10$, (b) $1 \leq M_1^U \leq 2$.

CHAPTER 3

NUMERICAL METHOD

The time-dependent Navier-Stokes equations for a compressible fluid were solved directly. All the relevant turbulence scales are resolved without a turbulence model, and the shock wave structure is resolved as a solution of the Navier-Stokes equations without introducing the techniques of shock-fitting or shock-capturing. The shock structure is adequately represented by the Navier-Stokes equations for Mach numbers M_1^U less than 2.0 [Sherman 1955]. Except for monatomic gases, however, the thickness of the shock wave as a solution of the Navier-Stokes equations is underpredicted even for $M_1^U \leq 2.0$, because the rotational energy mode is not in equilibrium inside the shock wave [Lumpkin 1990]. This chapter describes the governing equations and the numerical method used to simulate shock/turbulence interaction, where the flow is assumed to be periodic in transverse directions (x_2 and x_3). This chapter also includes validations of our numerical schemes. The code is written in the VECTORAL language [Wray 1988] and implemented on a Cray Y-MP/832 at NASA-Ames Research Center.

3.1 Governing Equations

The conservation laws for mass, momentum, and energy are [Anderson, Tannehill and Pletcher 1984]:

$$\frac{\partial \rho^*}{\partial t^*} + \frac{\partial(\rho^* u_i^*)}{\partial x_i^*} = 0 \quad (3.1)$$

$$\frac{\partial(\rho^* u_i^*)}{\partial t^*} + \frac{\partial(\rho^* u_i^* u_j^* + p^* \delta_{ij})}{\partial x_j^*} = \frac{\partial \tau_{ij}^*}{\partial x_j^*} \quad (3.2)$$

$$\frac{\partial E_T^*}{\partial t^*} + \frac{\partial[(E_T^* + p^*) u_i^*]}{\partial x_i^*} = -\frac{\partial Q_i^*}{\partial x_i^*} + \frac{\partial(u_j^* \tau_{ij}^*)}{\partial x_j^*}, \quad (3.3)$$

where superscript $*$ indicates a dimensional quantity, ρ^* is the density, u_i^* the velocity components, p^* the pressure, τ_{ij}^* the shear stress tensor, and Q_i^* is the heat flux vector. E_T^* is the total energy, defined by:

$$E_T^* = \rho^* \left(e^* + \frac{u_i^* u_i^*}{2} \right), \quad (3.4)$$

where e^* is the internal energy per unit mass.

We assume the fluid to be a perfect gas satisfying

$$p^* = \rho^* R^* T^*, \quad (3.5)$$

where R^* is the gas constant and T^* the temperature. We assume a Newtonian fluid and use Stokes hypothesis and Fourier law of heat conduction, so that the constitutive equations for τ_{ij}^* and Q_i^* are:

$$\tau_{ij}^* = \mu^* \left(\frac{\partial u_i^*}{\partial x_j^*} + \frac{\partial u_j^*}{\partial x_i^*} - \frac{2}{3} \frac{\partial u_k^*}{\partial x_k^*} \delta_{ij} \right) \quad (3.6)$$

$$Q_i^* = -k^* \frac{\partial T^*}{\partial x_i^*}, \quad (3.7)$$

where μ^* is the molecular viscosity and k^* the thermal conductivity.

The flow variables are non-dimensionalized as follows

$$u_i = \frac{u_i^*}{c_o^*} \quad \rho = \frac{\rho^*}{\rho_o^*} \quad p = \frac{p^*}{\rho_o^* c_o^{*2}} \quad T = \frac{T^*}{(\gamma - 1) T_o^*} \quad (3.8a)$$

$$\mu = \frac{\mu^*}{\mu_o^*} \quad e = \frac{e^*}{c_o^{*2}} \quad t = \frac{t^* c_o^*}{L_o^*} \quad x_i = \frac{x_i^*}{L_o^*}, \quad (3.8b)$$

where subscript o represents the mean upstream value, c^* is the speed of sound, and L_o^* is an arbitrary reference length scale. The value of the specific heat ratio γ defined as

$$\gamma = c_p^* / c_v^* \quad (3.9)$$

is taken as 1.40 in this work.

The non-dimensional equations for continuity, momentum, and energy are

$$\frac{\partial \rho}{\partial t} = - \frac{\partial (\rho u_i)}{\partial x_i} \quad (3.10)$$

$$\frac{\partial(\rho u_i)}{\partial t} = -\frac{\partial(\rho u_i u_j + p \delta_{ij})}{\partial x_j} + \frac{\partial \tau_{ij}}{\partial x_j} \quad (3.11)$$

$$\frac{\partial E_T}{\partial t} = -\frac{\partial[(E_T + p)u_i]}{\partial x_i} - \frac{\partial Q_i}{\partial x_i} + \frac{\partial u_i \tau_{ij}}{\partial x_j}, \quad (3.12)$$

with constitutive relations

$$\tau_{ij} = \frac{\mu}{Re} \left(\frac{\partial u_i}{\partial x_j} + \frac{\partial u_j}{\partial x_i} - \frac{2}{3} \frac{\partial u_k}{\partial x_k} \delta_{ij} \right), \quad (3.13)$$

$$Q_i = -\frac{\mu}{Pr Re} \frac{\partial T}{\partial x_i} \quad (3.14)$$

where Re and Pr are defined as

$$Re = \frac{\rho_o^* c_o^* L_o^*}{\mu_o^*} \quad (3.15a)$$

$$Pr = \frac{c_p^* \mu^*}{k^*}. \quad (3.15b)$$

We assume the Prandtl number to be constant equal to 0.70 and assume the viscosity to follow the power law:

$$\left(\frac{\mu^*}{\mu_o^*} \right) = \left(\frac{T^*}{T_o^*} \right)^n, \quad \text{or} \quad \mu = [(\gamma - 1)T]^n, \quad (3.16)$$

where $n = 0.76$.

If we assume constant specific heats and set $e^* = 0$ at $T^* = 0$, we can write $e^* = c_v^* T^*$. The non-dimensional form of the perfect gas law is

$$p = \frac{(\gamma - 1)}{\gamma} \rho T. \quad (3.17)$$

3.2 Numerical Schemes

This section describes the numerical schemes used: time advancement scheme, approximation of spatial derivatives, special treatment of convective terms for numerical stability, method of generating inflow turbulence, and initial and boundary conditions.

3.2.1 Time Advancement

An explicit time-advancement method is used. The variables $(\rho, \rho u_i, E_T)$ are advanced using a three-step compact-storage third-order Runge-Kutta scheme [Wray 1986]. This scheme, when applied to $dy/dt = f(y, t)$, has the following three sub-steps:

$$y^i = y^n + \frac{8}{15} f(y^n, t^n) \Delta t \quad (3.18a)$$

$$y^{ii} = y^n + \frac{1}{4} f(y^n, t^n) \Delta t + \frac{5}{12} f(y^i, t^i) \Delta t \quad (3.18b)$$

$$y^{n+1} = y^n + \frac{1}{4} f(y^n, t^n) \Delta t + \frac{3}{4} f(y^{ii}, t^{ii}) \Delta t, \quad (3.18c)$$

where $t^i = t^n + \frac{8}{15} \Delta t$ and $t^{ii} = t^n + \frac{2}{3} \Delta t$.

The time step is computed from the following formula:

$$\Delta t = \frac{(CFL)}{|\Lambda|_{\max}}, \quad (3.19)$$

where CFL is the Courant-Friedrichs-Lewy number. The subscript \max refers to the maximum over all grid points. The maximum CFL number for stability is fixed by the time-advance method. For linear equations the limit is $\sqrt{3}$ for the third-order Runge-Kutta method described above. For the three-dimensional Navier-Stokes equations, we have used:

$$|\Lambda|_{\max} = \left(\frac{|u_1| + c}{\Delta x_1} + \frac{|u_2| + c}{\Delta x_2} + \frac{|u_3| + c}{\Delta x_3} \right)_{\max}, \quad (3.20)$$

where $|u_i|$ is the absolute velocity in the i^{th} direction and Δx_i is the grid spacing.

3.2.2 Evaluation of Spatial Derivatives

A family of high-order modified Padé schemes has been derived by Lele [1990] with spectral-like resolution characteristics as well as high-order formal accuracy. In this work, we used such a scheme for both the first and second derivatives.

The first derivative is given by:

$$y'_{j-1} + a_1 y'_j + y'_{j+1} = a_2 \frac{y_{j+1} - y_{j-1}}{2\Delta x} + a_3 \frac{y_{j+2} - y_{j-2}}{4\Delta x}. \quad (3.21a)$$

We can obtain y'_j by solving a tridiagonal system of equations. A family of fourth order schemes is obtained if we choose

$$a_2 = \frac{2 + 4a_1}{3} \quad a_3 = \frac{4 - a_1}{3}. \quad (3.21b)$$

For $a_1 = 4$, the conventional Padé scheme is recovered, while with $a_1 = 3$ and (3.21b) we have a sixth-order scheme. Similarly, we can write for the second derivative:

$$y''_{j-1} + a_1 y''_j + y''_{j+1} = a_2 \frac{y_{j+1} - 2y_j + y_{j-1}}{\Delta x^2} + a_3 \frac{y_{j+2} - 2y_j + y_{j-2}}{4\Delta x^2} \quad (3.22a)$$

$$a_2 = \frac{4a_1 - 4}{3} \quad a_3 = \frac{10 - a_1}{3}. \quad (3.22b)$$

The choice of $a_1 = 10$ recovers the usual Padé scheme, and for $a_1 = 11/2$ with (3.22b) it is sixth-order accurate.

In this work, we used the sixth-order schemes both for the first and second derivatives. The resolution characteristics of the conventional Padé scheme are improved with negligible increase of operations.

The diffusion terms in the governing equations require evaluation of successive derivatives, for example

$$\frac{\partial}{\partial x_1} \left(\mu \frac{\partial u_1}{\partial x_1} \right). \quad (3.23)$$

When a spectral method is used, there is no loss of accuracy when these are computed by two applications of a first-derivative operator. With finite difference methods, however, two applications of a first derivative results in a less accurate representation of the derivative at high wave numbers as compared to one application of a second-derivative operator, for the modified wave number goes to zero for the first derivative at high wave numbers [Lele 1990]. To eliminate this inaccuracy, we expanded all diffusion terms into two terms (non-conservative formulation):

$$\mu \frac{\partial^2 u_1}{\partial x_1^2} + \frac{\partial \mu}{\partial x_1} \frac{\partial u_1}{\partial x_1}, \quad (3.24)$$

and use the formulae (3.21) and (3.22) to approximate the first and the second derivatives, respectively.

To simulate shock/turbulence interaction, a shock wave is placed near the center of the computational domain (Figure 3.1) and numerical simulations are performed in a frame moving with the shock wave. Since the resolution requirements for a shock wave are far more restrictive than those for turbulence, a non-uniform grid is used in the streamwise (or x_1) direction to resolve the shock wave structure. The following mapping from the uniform computational grid to the non-uniform physical grid is used to concentrate points near the region occupied by the shock wave:

$$x_1 = L_1 \frac{s - \frac{\sqrt{\pi}}{2} \frac{b_1}{c_1} \operatorname{erf}(c_1 s)}{1 - \sqrt{\pi} \frac{b_1}{c_1} \operatorname{erf}(c_1/2)}, \quad (3.25)$$

where L_1 is the length of the computational box in the streamwise direction, s is the coordinate in the computational grid ranging between $(-\frac{1}{2}, \frac{1}{2})$, and b_1 and c_1 are the stretching parameters controlling grid stretching ratio and the grid stretching rate respectively. The grid stretching ratio, $(\Delta x_1)_{\max}/(\Delta x_1)_{\min} \simeq 1/(1 - b_1)$, was chosen to be between 5 and 20. Higher grid stretching is required for a larger separation between the shock wave thickness and turbulence length scales. With larger c_1 , the rate of grid stretching is faster. In this work c_1 is chosen to be 5. If we define the metric quantities:

$$h' = \frac{dx_1}{ds} = L_1 \frac{1 - b_1 \exp(-c_1^2 s^2)}{1 - \frac{b_1}{c_1} \sqrt{\pi} \operatorname{erf}(c_1/2)}, \quad (3.26)$$

$$h'' = \frac{d^2 x_1}{ds^2} = L_1 \frac{2b_1 c_1^2 s \exp(-c_1^2 s^2)}{1 - \frac{b_1}{c_1} \sqrt{\pi} \operatorname{erf}(c_1/2)}, \quad (3.27)$$

the first and second derivatives of a function y can be computed in the computational space as follows:

$$\frac{\partial y}{\partial x_1} = \frac{1}{h'} \frac{\partial y}{\partial s} \quad (3.28)$$

$$\frac{\partial^2 y}{\partial x_1^2} = \frac{1}{h'^2} \frac{\partial^2 y}{\partial s^2} - \frac{h''}{h'^2} \frac{\partial y}{\partial s}. \quad (3.29)$$

3.2.3 Nonlinear Numerical Stability

Compressible flow simulations with conservative formulation are especially prone to aliasing errors because evaluations of velocity and temperature from the conservative variables involve the division operation which has no clear interpretation in the Fourier space. A possible way of conducting alias-free simulation of compressible turbulence is to solve for the specific volume in a mass conservation equation. We discuss this alternative in Appendix C.

Feiereisen *et al.* [1981] have noted that the use of a special form of the convection term with a symmetric differencing in space ensures conservation of total energy in the inviscid limit. Blaisdell *et al.* [1990] have explicitly shown that this special form helps to control aliasing errors. For the numerical stability, we evaluate the convection term in the momentum equations in the following special form:

$$\frac{\partial \rho u_i u_j}{\partial x_j} = \frac{1}{2} \left[\frac{\partial \rho u_i u_j}{\partial x_j} + \rho u_j \frac{\partial u_i}{\partial x_j} + u_i \frac{\partial \rho u_j}{\partial x_j} \right]. \quad (3.30)$$

In a spatially evolving simulation, spurious numerical waves are generated at the inflow as soon as disturbances encounter the outflow boundary [Buell and Huerre, 1988]. These numerical waves have a wave length of twice the grid size and continue to grow in time. To remove these spurious waves, localized filtering near the inflow plane is performed using the following scheme:

$$y_{i-1}^f + a_1 y_i^f + y_{i+1}^f = a_2 (y_{i-1} + 2y_i + y_{i+1}) + a_3 (y_{i-2} - 2y_i + y_{i+2}), \quad (3.31)$$

where y and y^f are the unfiltered and the filtered quantities respectively. We choose

$$a_2 = \frac{a_1 + 2}{4}, \quad a_3 = \frac{2 - a_1}{16}.$$

The unfiltered quantity is recovered for $a_1 = 2$. This filtering operation exactly removes waves of twice the grid size. The filter transfer function in the Fourier space, defined as the ratio of the Fourier transforms of y^f and y , is shown in Figure 3.2. For a_1 close to 2, filtering operation is more localized at high wave numbers. Since the spurious numerical waves travel mainly in the streamwise direction, appearing first at the inflow boundary with wave length of twice the grid size, the filtering operation is performed only in the streamwise direction near the inflow boundary over less than a tenth of the computational domain with $a_1 = 2.01$.

3.2.4 Inflow/Outflow Boundary Conditions

Many of the existing boundary conditions for the compressible Navier-Stokes equations are based on the concept of the characteristics along which information travels. The number of boundary conditions required at a point on a boundary varies with the flow conditions at that point: in general, the number of boundary conditions which must be specified at a point on a boundary is equal to the number of incoming waves (from outside of the domain) at that point [Thompson 1987].

In this work, the inflow is kept supersonic so that we can specify all the flow variables. This is because supersonic inflow guarantees all the information to be incoming. Mean values of velocity, pressure, and density are set to be constant over the inflow plane. The turbulence velocity signal generated at the inflow boundary is designed to be isotropic with a prescribed spectrum with no fluctuations in

pressure and density. Appendix D gives a detailed description and validations of the procedure for generation of inflow turbulence.

To generate inflow turbulence, we use the following three-dimensional energy spectrum function:

$$E(k) = 16 \sqrt{\frac{2}{\pi}} \frac{u_o^2}{k_o} \left(\frac{k}{k_o}\right)^4 \exp \left[-2 \left(\frac{k}{k_o}\right)^2\right], \quad (3.32)$$

where u_o is the *rms* turbulence intensity and k_o is the most energetic wave number. This spectrum has the following properties:

$$\frac{q^2}{2} = \int_0^\infty E(k) dk = \frac{3}{2} u_o^2 \quad (3.33)$$

$$\epsilon = 2\mu \int_0^\infty k^2 E(k) dk = \frac{15}{4} \mu u_o^2 k_o^2 \quad (3.34)$$

$$Re_\lambda = \frac{u_o \lambda}{\nu} = 2 \frac{u_o}{\nu k_o}, \quad (3.35)$$

where ν is the kinematic viscosity, and λ is the longitudinal Taylor microscale.

Outflow is subsonic in the mean sense, which requires special attention in applying boundary conditions, since one of the characteristics is incoming (from outside). We can determine what information the outgoing characteristics carry from the solution inside the computational domain. But difficulty arises in determining contributions from the incoming characteristics. Since we are limited to the information inside the computational domain, the information that can be used to determine the effect of incoming characteristics is incomplete, and we need to make some assumptions.

Thompson's boundary condition [1987] is derived from the assumption that the unknown incoming data have no effect on the flow variables at the boundaries. Poinso *et al.* [1990] extended Thompson's boundary condition to include viscous effects at the boundaries. Giles' [1990] boundary condition is designed in the Fourier

space so that small amplitude waves may leave the computational domain without reflection.

In this work, we tested the boundary conditions by Thompson [1987], Poinso *et al.* [1990], and Giles [1990]. We found that they were comparable in suppressing numerical reflections at the boundary, with Giles' boundary condition being superior to the other two. However, this improvement had virtually no effect on the turbulence statistics downstream of the shock wave (for details, see Appendix G). For simplicity of implementation, we used Thompson's method in most of this work. In the remaining part of this subsection, we show the derivation and application of Thompson's boundary condition.

The basic idea is to consider the characteristic form of the Euler equations at the outflow boundary. Outgoing characteristics use information from within the computational domain, and can be computed with no difficulty. Incoming characteristics are handled by setting the time derivative of their amplitude equal to zero, thus ensuring that no waves enter the domain during the simulation, giving the boundary conditions a non-reflecting character.

We begin by writing the Euler equations in terms of the conservative variables $Q = (\rho, \rho u_1, \rho u_2, \rho u_3, E_T)^T$:

$$\frac{\partial Q}{\partial t} + \frac{\partial F}{\partial x_1} = (\text{RHS}), \quad (3.36)$$

where

$$F = (\rho u_1, \rho u_1^2 + p, \rho u_1 u_2, \rho u_1 u_3, (E_T + p)u_1)^T. \quad (3.37)$$

We are concerned here only with the derivatives in the x_1 direction. Derivatives in x_2 and x_3 , and viscous terms, are evaluated at the boundary using information from the previous substep, and are included in the right hand side (RHS). The flux Jacobian of F is more easily derived if we work with the non-conservative flow variables $U = (\rho, u_1, u_2, u_3, p)^T$. Setting $A = \partial F / \partial Q$ (i.e. $A_{ij} = \partial F_i / \partial Q_j$) and $R = \partial Q / \partial U$, we have

$$\frac{\partial U}{\partial t} + A \frac{\partial U}{\partial x_1} = R^{-1} (\text{RHS}) \quad (3.38)$$

and

$$\frac{\partial F}{\partial x_1} = RA \frac{\partial U}{\partial x_1}. \quad (3.39)$$

Now A can be diagonalized, $A = T^{-1}\Lambda T$, where the elements of the diagonal matrix Λ are $(u_1 - c, u_1 + c, u_1, u_1, u_1)$. Equation (3.39) can now be written as

$$\frac{\partial F}{\partial x_1} = RT^{-1}(\Lambda T \frac{\partial U}{\partial x_1}). \quad (3.40)$$

This is the relation that is imposed at the boundary to calculate $\partial F/\partial x_1$ in (3.36).

The quantity in the parenthesis in (3.40) is a vector. The sign of each eigenvalue in Λ is used to determine the course of action for each element in the vector. If the characteristic velocity is directed out of the computational domain (positive eigenvalue at the outflow boundary), then the quantity is calculated as it stands using a one-sided difference. On the other hand, if the characteristic is directed inwards then the element is set to zero. This gives the non-reflecting character of the boundary condition for waves at close to normal incidence. The final step is to premultiply the vector by the matrices T^{-1} and R . The various matrices required in the computation are:

$$T = \begin{pmatrix} 0 & -\rho c & 0 & 0 & 1 \\ 0 & \rho c & 0 & 0 & 1 \\ c^2 & 0 & 0 & 0 & -1 \\ 0 & 0 & 1 & 0 & 0 \\ 0 & 0 & 0 & 1 & 0 \end{pmatrix}, \quad (3.41)$$

$$T^{-1} = \begin{pmatrix} \frac{1}{2c^2} & \frac{1}{c^2} & 0 & 0 & \frac{1}{2c^2} \\ -\frac{1}{2\rho c} & 0 & 0 & 0 & \frac{1}{2\rho c} \\ 0 & 0 & 1 & 0 & 0 \\ 0 & 0 & 0 & 1 & 0 \\ \frac{1}{2} & 0 & 0 & 0 & \frac{1}{2} \end{pmatrix}, \quad (3.42)$$

and

$$R = \begin{pmatrix} 1 & 0 & 0 & 0 & 0 \\ u_1 & \rho & 0 & 0 & 0 \\ u_2 & 0 & \rho & 0 & 0 \\ u_3 & 0 & 0 & \rho & 0 \\ \frac{u_k u_k}{2} & \rho u_1 & \rho u_2 & \rho u_3 & \frac{1}{\gamma-1} \end{pmatrix}. \quad (3.43)$$

3.2.5 Initial Conditions

To simulate shock turbulence interaction, we initialize the field by superposing isotropic homogeneous turbulence on the corresponding stationary laminar shock wave profile. This presumably reduces the time required for the shock wave and turbulence to reach statistically stationary state. The turbulence field used in the initial condition has the same energy spectrum as turbulence generated at the inflow boundary during the computation. Rogallo's scheme [1981] is used for turbulence initialization, and attention is given to ensure smoothness of turbulence signal at inflow boundary. We solved the Navier-Stokes equations to get a laminar shock wave, and used this solution to initialize a planar laminar shock wave in the computational domain.

3.2.6 Statistical Averages

Two different statistical averages are used: the conventional ensemble average and the Favre (or density-weighted) ensemble average. The ensemble average of a quantity $y(x_1, x_2, x_3, t)$, $\bar{y}(x_1)$, is defined as the average over time and over the (homogeneous) transverse directions. The ensemble-averaged equations in compressible turbulence are usually too complex. The averaged equations are simpler using density-weighted averages suggested by Favre [1965a, 1965b]. The density-weighted average $\tilde{y}(x_1)$ is defined as

$$\tilde{y}(x_1) = \frac{\overline{\rho y}}{\bar{\rho}}. \quad (3.44)$$

The fluctuations from the ensemble average and from the Favre average are defined as

$$y' = y - \bar{y}(x_1), \quad y'' = y - \tilde{y}(x_1).$$

The ensemble average of y'' is not zero; instead,

$$\begin{aligned}
 \overline{y''} &= \overline{y - \frac{\rho y}{\bar{\rho}}} \\
 &= \bar{y} - \frac{\overline{\rho y + \rho' y'}}{\bar{\rho}} \\
 &= -\frac{\overline{\rho' y'}}{\bar{\rho}}.
 \end{aligned} \tag{3.45}$$

3.3 Validations

In this section, we provide a validation of the computer code by separate computations of some of the components of the shock/turbulence interaction problem. For a direct numerical simulation of spatially evolving turbulence interacting with a shock wave, the shock wave needs to be well resolved, spatially evolving turbulence must be properly simulated, and the interaction of turbulence with a shock wave must be accurately predicted. For this purpose there are at least three independent categories to be validated: (1) simulation of spatially evolving turbulence (without a shock wave), (2) resolution of shock wave structure, and (3) interaction of flow inhomogeneity with a shock wave.

The validation of the first category is given in Appendix D by comparing the simulation results of spatially evolving turbulence with the experimental data.

Validations of the other two categories are performed in the present section. The capability of resolving the shock wave structure is validated by solving the one-dimensional Navier-Stokes equations, investigating the shock wave profile qualitatively and comparing the shock wave thickness with a theoretical prediction. Subsequently, interaction of a flow inhomogeneity with a shock wave is checked by investigating vorticity production through the baroclinic torque and comparing the resulting circulation with a theoretical prediction.

3.3.1 Laminar Shock Wave

The shock wave structure was resolved by solving the Navier-Stokes equations. Prediction of profiles across the shock wave was found reliable up to an upstream Mach number of 2.0 [Sherman 1955]. Beyond this Mach number, the thermal equilibrium assumption is no longer valid, preventing use of the Navier-Stokes equations to resolve the shock wave structure. Except for monatomic gases, however, the thickness of the shock wave as a solution of the Navier-Stokes equations is found to be underpredicted even for $M_1^U \leq 2.0$ [Lumpkin 1990].

In the following, we test the ability of our numerical scheme to resolve a normal shock wave in steady flow and estimate the number of grid points required across a shock wave to properly resolve its structure. We computed the normal shock wave for the upstream Mach number, $M_1^U = 1.2$, where superscript U denotes an upstream value. Calculations are performed in a frame fixed on the shock wave where the inflow is supersonic and the outflow subsonic with uniformly distributed 201 grid points.

The initial conditions of density, pressure, and velocity are given by the following expression, which satisfies the Rankine-Hugoniot relations across the shock wave:

$$y(x_1) = y^U + (y^D - y^U) \tanh\left(\frac{x_1 - x_1^s}{b^s}\right), \quad (3.36)$$

where superscript D represents a downstream value, y is one of the flow variables, and x_1^s and b^s represent the shock center position and the initial shock thickness parameter, respectively. The flow variables are fixed at the supersonic inflow and Thompson's non-reflecting boundary conditions are applied at the subsonic outflow boundary. As the Navier-Stokes equations are advanced, initial profiles relax or steepen into equilibrium profiles.

The profiles of velocity, pressure, temperature, dilatation, and entropy across the shock wave are shown in Figures 3.3(a-e). All the Rankine-Hugoniot conditions are satisfied without any spurious oscillations across the shock wave. The dilatation profile shows that the shock wave is well resolved without any numerical problems. The entropy profile shows a local peak inside the compression zone as well as a net increase across the zone. As flow passes through a shock wave, flow kinetic energy

is converted into internal energy by viscous dissipation, which leads to entropy production; the resulting temperature gradient leads to further irreversible entropy production and reversible entropy flux. Irreversibility from viscous dissipation and temperature gradient are responsible for the overall increase of entropy, while the reversible entropy flux leads to the peak inside the shock [Lagerstrom 1964]. Figure 3.3(f) shows the budget of terms in the entropy transport equation,

$$\underbrace{\rho u_1 \frac{ds}{dx_1}}_{(I)} = \underbrace{\frac{d}{dx_1} \left(\frac{k}{T} \frac{dT}{dx_1} \right)}_{(II)} + \underbrace{\frac{4\mu}{3T} \left(\frac{du_1}{dx_1} \right)^2}_{(III)} + \underbrace{\frac{k}{T^2} \left(\frac{dT}{dx_1} \right)^2}_{(IV)}$$

[Thompson 1984], where the convection (I) is balanced by the sum of the reversible entropy flux (II) and the entropy production by viscous dissipation (III) and irreversible heat transfer (IV). The figure verifies that the entropy decrease inside the shock wave is due to the reversible entropy flux (II). The primary source of the net entropy increase across the shock wave is found to be the viscous dissipation of the flow kinetic energy (III).

The shock wave thickness, δ_s , defined as

$$\delta_s = \frac{|U_1^U - U_1^D|}{|dU_1/dx_1|_{\max}} \quad (3.37)$$

is estimated to be

$$\delta_s \simeq \frac{4}{\gamma + 1} \left(\frac{4}{3} + \frac{\gamma - 1}{Pr} \right) \frac{1}{Re(M^* - 1)} \quad (3.38)$$

for very weak shocks [Shapiro 1953], where Re is defined as (3.15a) and

$$M^{*2} = \frac{\frac{\gamma+1}{2} M_1^{U^2}}{1 + \frac{\gamma-1}{2} M_1^{U^2}}.$$

The shock wave thickness in the simulation is within 7 percent of the estimate in (3.38) when the grid spacing in the shock zone is less than a third of the shock wave thickness, that is, $\Delta x_1 \leq \frac{1}{3}\delta_s$.

3.3.2 Thermal Inhomogeneity Interacting with a Shock Wave

A second validation study was performed to check the accuracy of the scheme in the prediction of the interaction of time-dependent disturbances with a shock wave. This study also provided an evaluation of Thompson's boundary conditions at the unsteady subsonic outflow boundary.

The interaction of a thermal inhomogeneity with a shock wave with $M_1^U = 1.20$ was simulated. Inhomogeneity at the inflow boundary had a circular shape in the $(t-x_2)$ plane as

$$T(x_2, t) = \frac{1}{\gamma - 1} \left(1 + a_T \exp \left[- \left(\frac{(U_1^U(t - t_T))^2 + x_2^2}{b_T^2} \right)^{n_T} \right] \right), \quad (3.39)$$

where a_T is the relative amplitude of the disturbance, t_T the time at which the center of the disturbance passes through the inflow plane, b_T the length scale of the disturbance, and n_T the parameter controlling the sharpness of the disturbance's edge. The simulation used 201×101 uniform meshes. The values used in the simulation are $a_T = 1/10$, $b_T = L_2/4$, and $n_T = 10$. (L_2 is the size of the computational box in the x_2 direction.) Pressure at the inflow plane is kept uniform and constant. Thompson's non-reflecting boundary condition is used at the outflow boundary and periodic boundary conditions are used in the transverse direction.

Figures 3.4(a-c) show a time sequence of the temperature field. Upstream of the shock wave the shape of the inhomogeneity is circular, and after the interaction the shape is changed into an ellipse. The predicted aspect ratio of this ellipse is within one percent of the exact value, equal to the density ratio across the shock wave, ρ^D/ρ^U . In Figures 3.5(a-c), a time sequence of the vorticity field is shown. Through the interaction of the thermal inhomogeneity with the shock wave, vorticity is produced by the baroclinic torque. Figure 3.5 clearly shows counter-rotating vortices generated during the interaction.

Picone *et al.* [1985] have derived an expression for the circulation of the vortices generated by the baroclinic torque, assuming the shock wave to be a planar discontinuity and the thermal inhomogeneity to be a circular discontinuity. Their expression for the circulation in the upper half plane is

$$\Gamma \simeq (U_1^U - U_1^D) \frac{U_1^U + U_1^D}{U_1^U} b_T \ln(1 + a_T). \quad (3.40)$$

In Figure 3.6, the history of circulation in the upper half plane is shown. We see that circulation peaks near the end of the interaction and decays through viscous diffusion as vortices flow downstream. This peak strength compares favorably with the estimation of (3.40) to within 5%, thus confirming the ability of the scheme to predict the shock/disturbance interaction correctly. More rapid decrease in circulation after $t = 20$ is due to the primary vortices leaving the domain. There are trailing vortices with circulations of opposite signs to the main vortices generated through the interaction (see Figure 3.7). The trailing vortices are produced by the relaxation of the curvature in the shock wave, and their strengths are an order of magnitude weaker than the main vortices.

To check the accuracy of Thompson's non-reflecting boundary condition in unsteady flows, we examined the pressure field at times of entrance, interaction, and exit of thermal inhomogeneity in Figures 3.8(a-c). The disturbance pressure at the outflow boundary is not noticed in these plots. The level of disturbance pressure after the exit of the inhomogeneity from the computational domain is about $O(10^{-3})$ compared to the mean pressure.

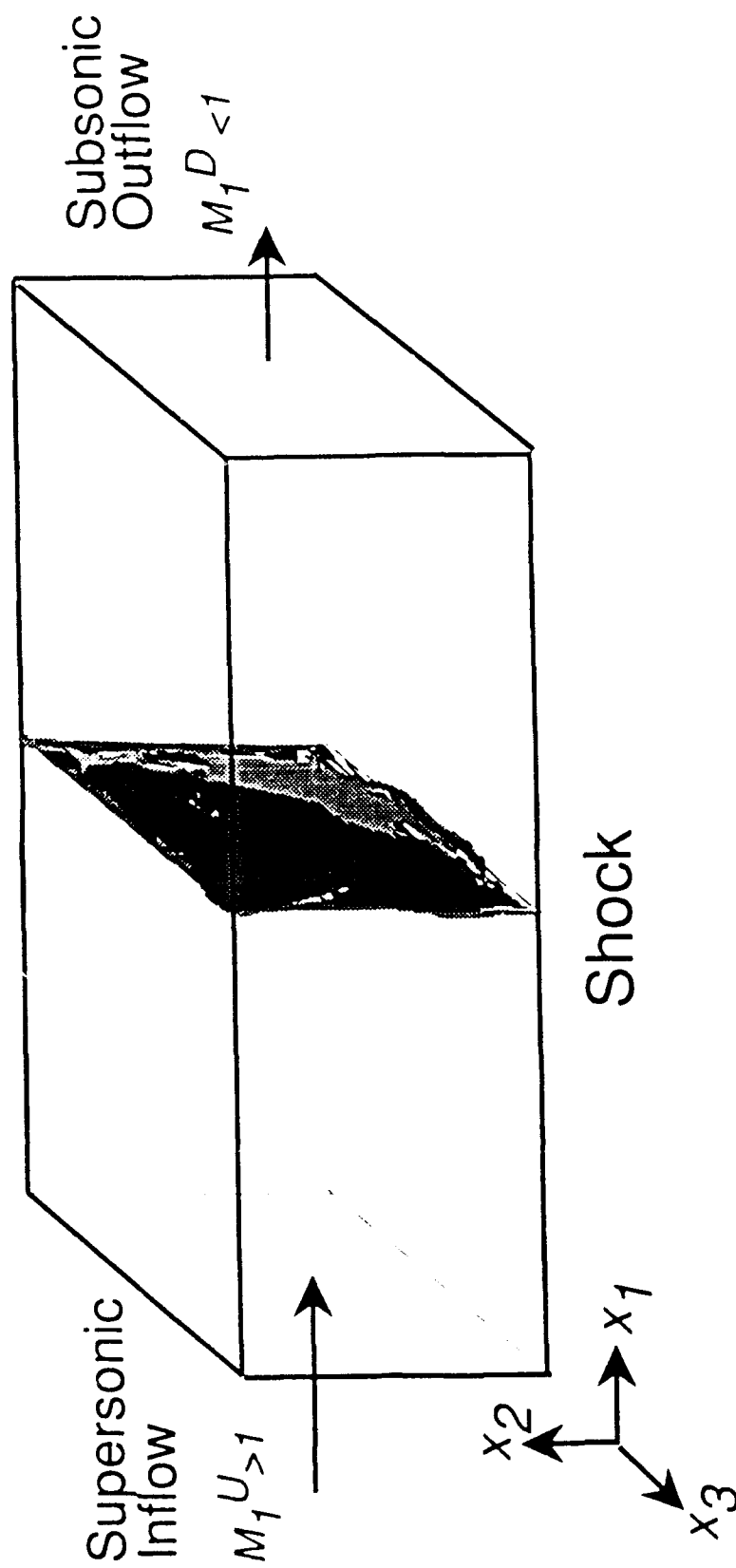


FIGURE 3.1. The schematic plot of the computational domain.

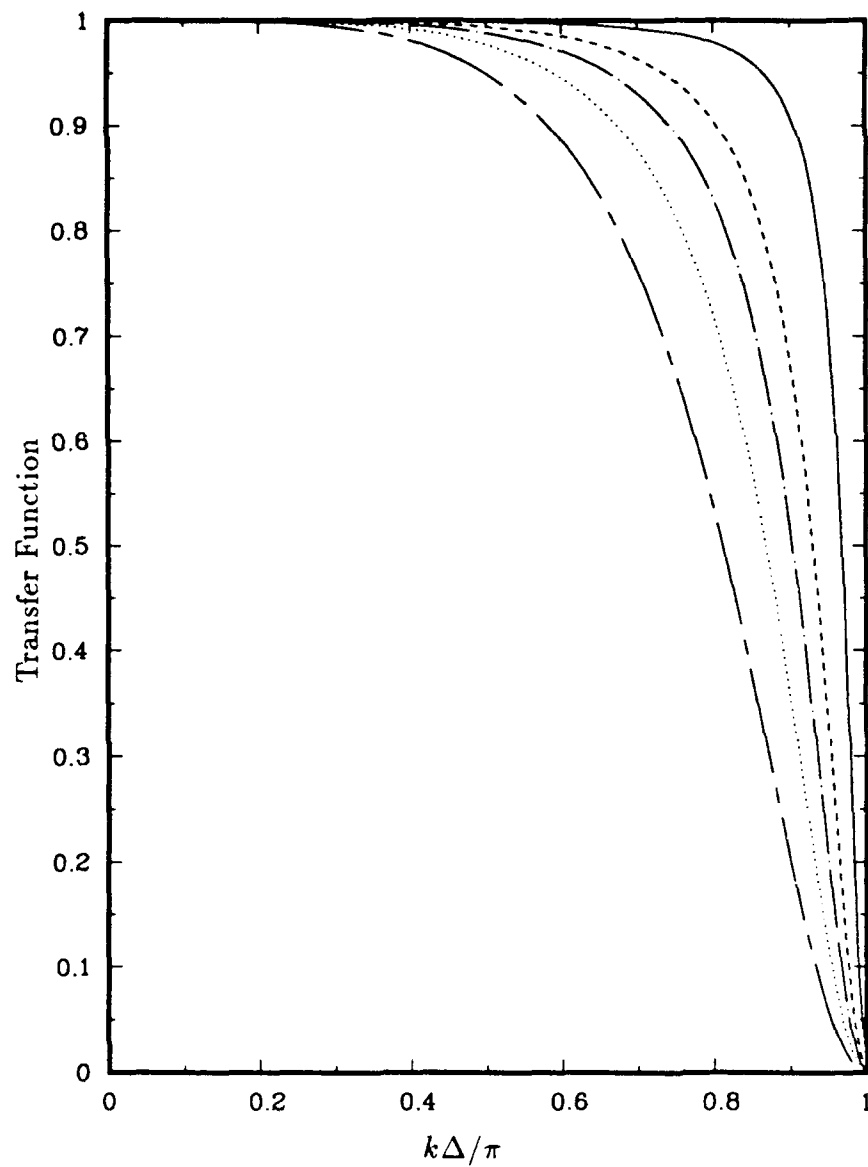


FIGURE 3.2. The transfer function of filtering in the Fourier space. — $a_1 = 2.01$; ---- $a_1 = 2.05$; — · — $a_1 = 2.10$; $a_1 = 2.20$; --- $a_1 = 2.50$.

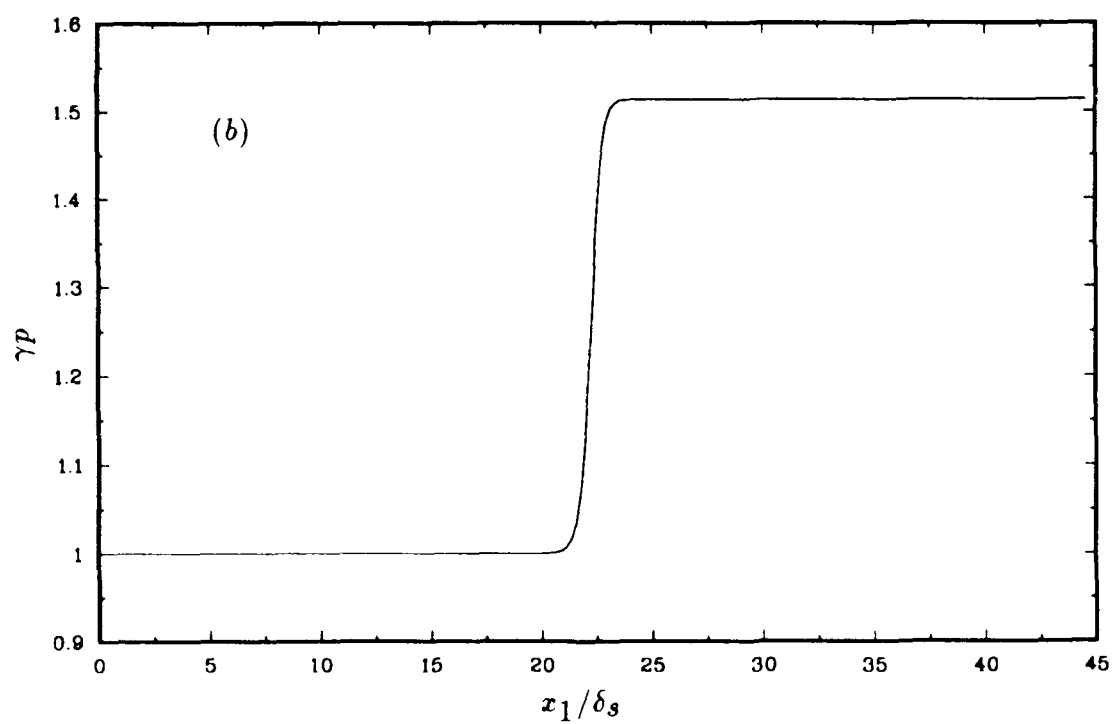
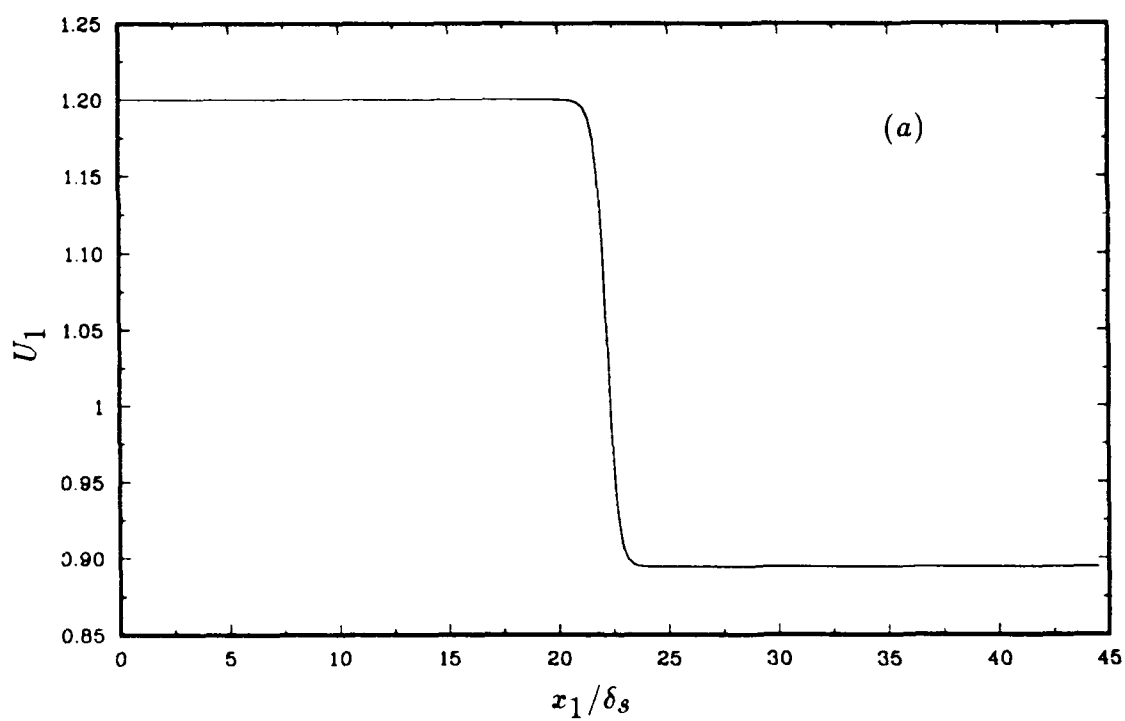


FIGURE 3.3. Laminar shock wave profiles: (a) streamwise velocity, (b) pressure, (c) temperature, (d) dilatation, (e) entropy, (f) entropy budget.

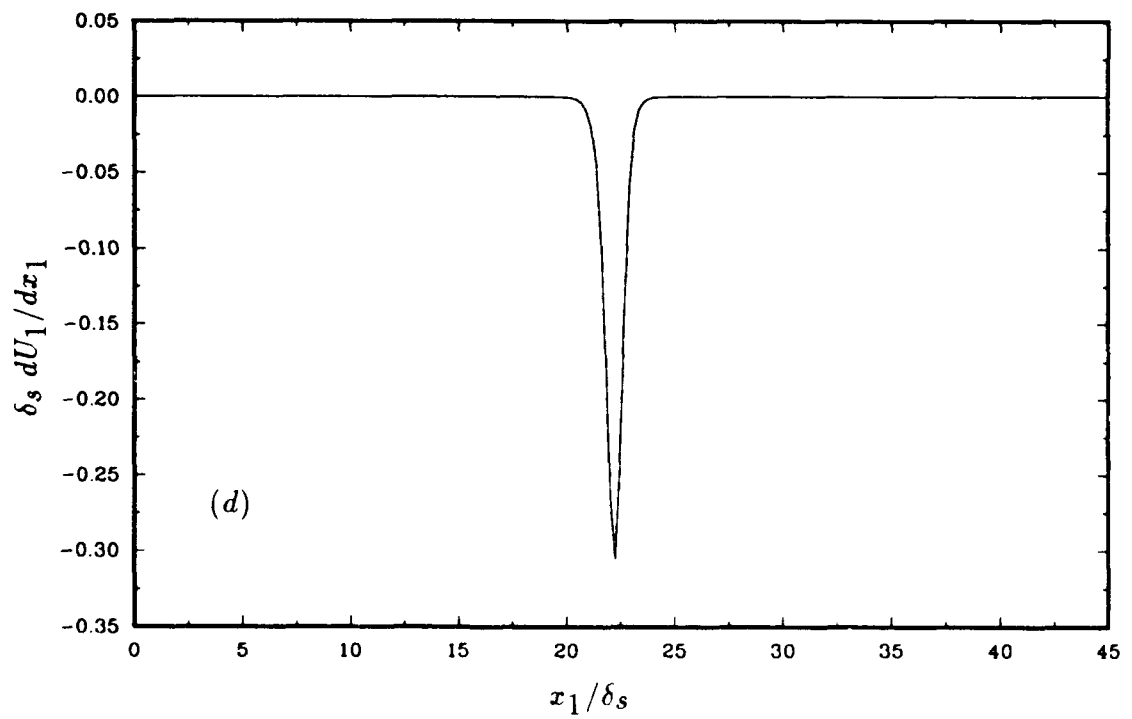
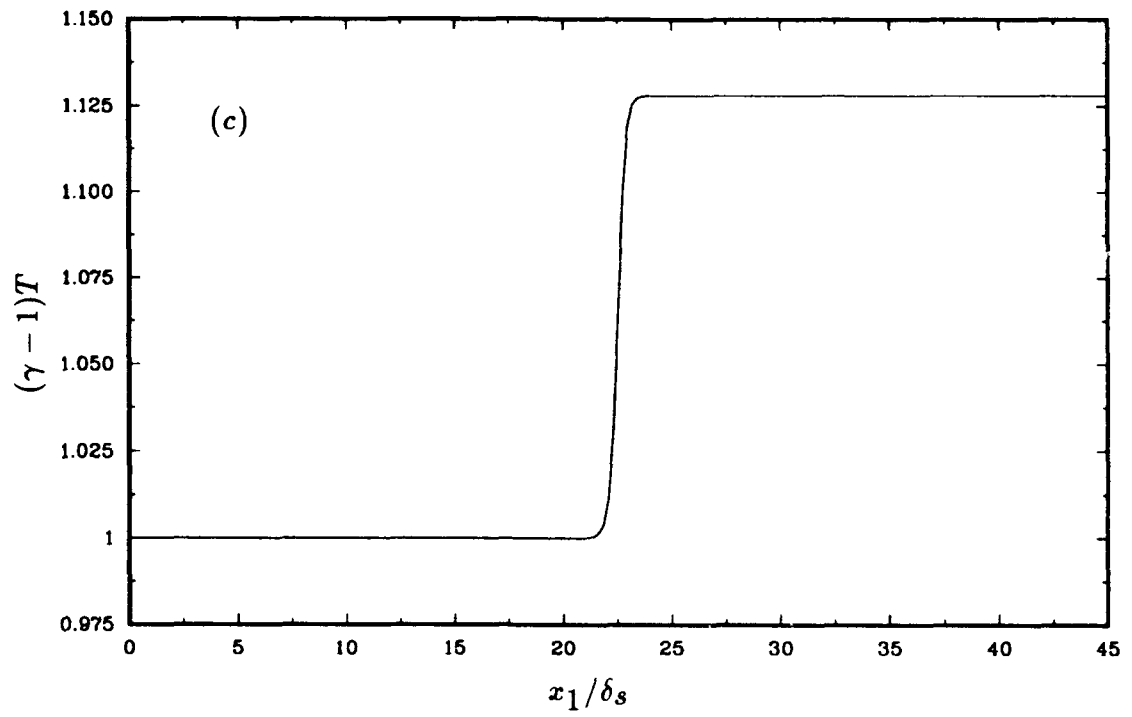


FIGURE 3.3. Continued.

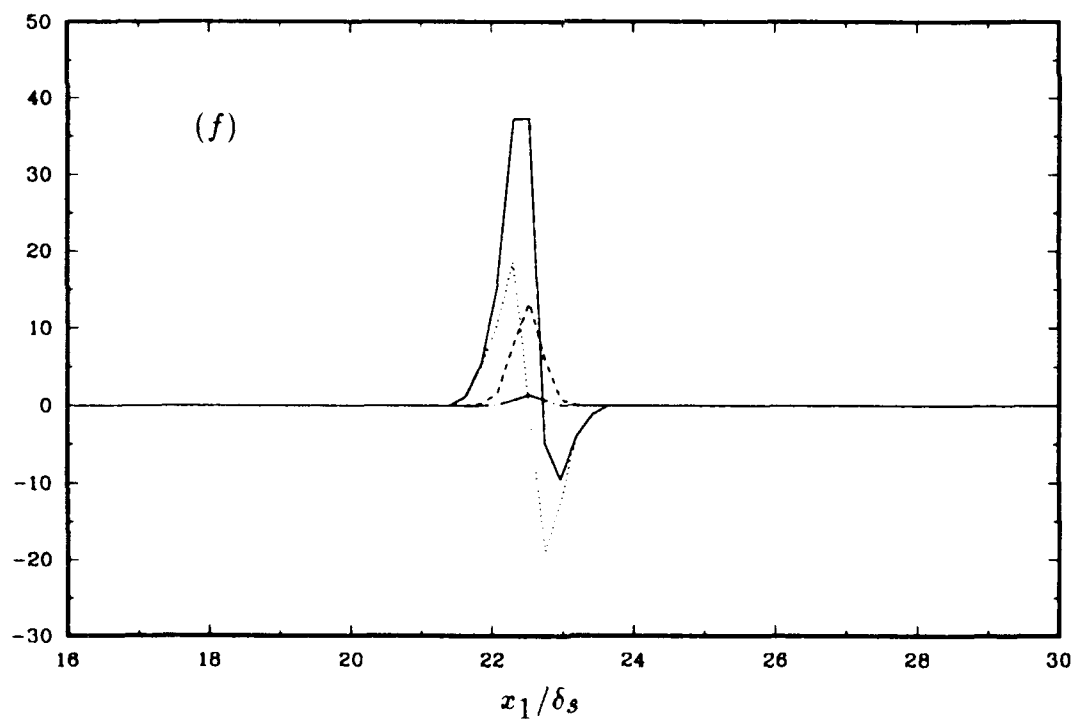
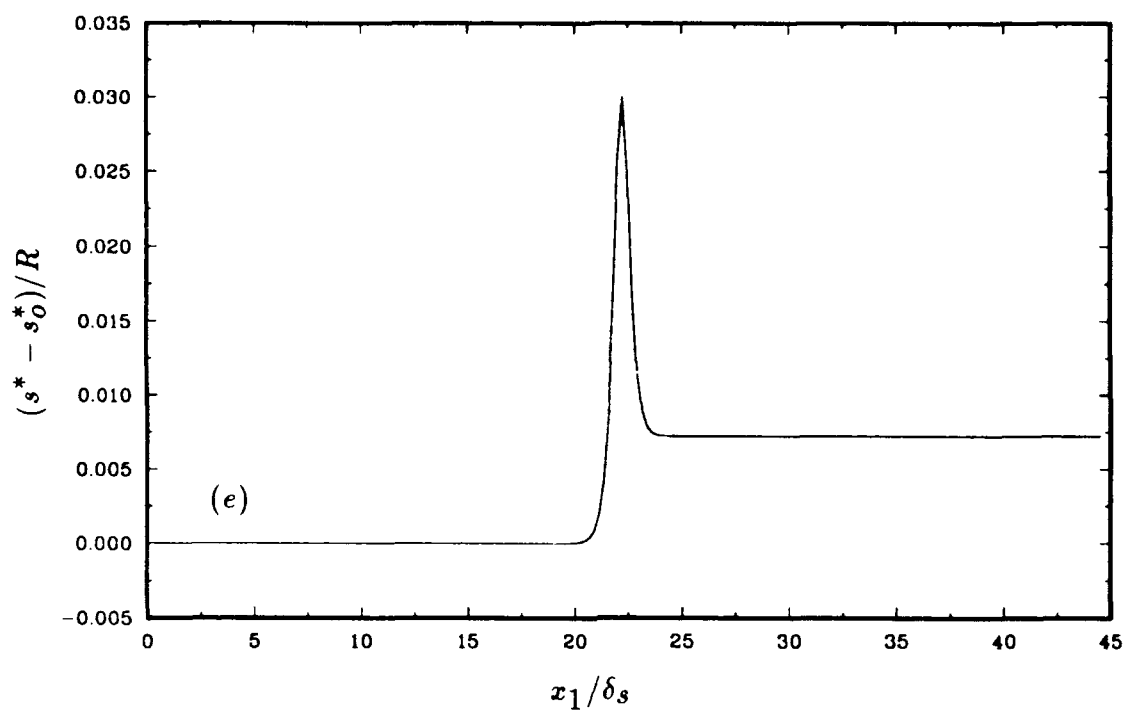


FIGURE 3.3. Continued. For Figure 3.3(f): — convection, entropy flux, ---- production by viscous dissipation, - - - production by irreversible heat transfer.

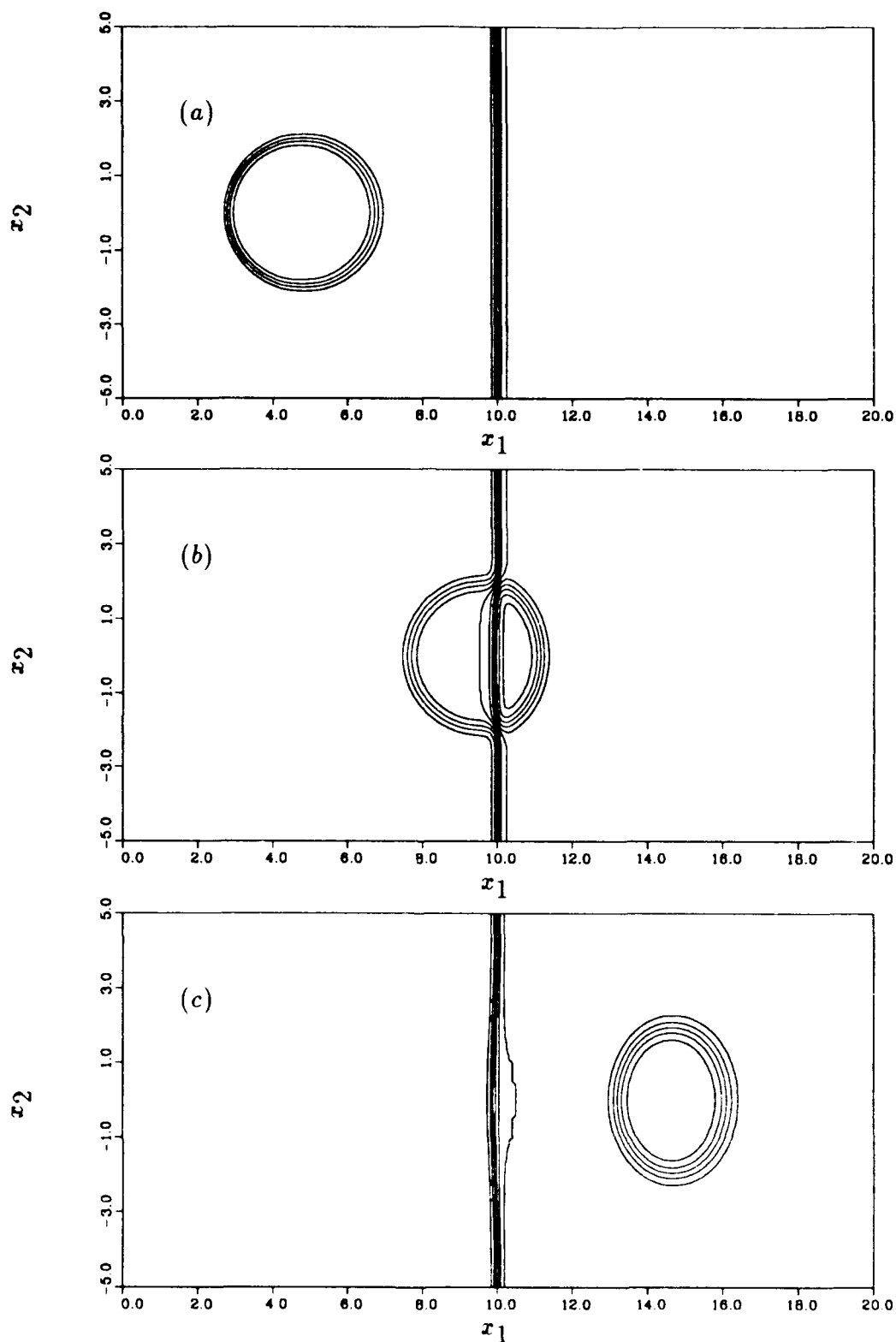


FIGURE 3.4. Temperature fields from passage of a thermal inhomogeneity through a shock (The contour increments are $(\gamma - 1)\Delta T = 0.02$ starting from the mean upstream temperature $(\gamma - 1)T = 1.0$). (a) $t = 7.0$, (b) $t = 11.0$, (c) $t = 16.6$.

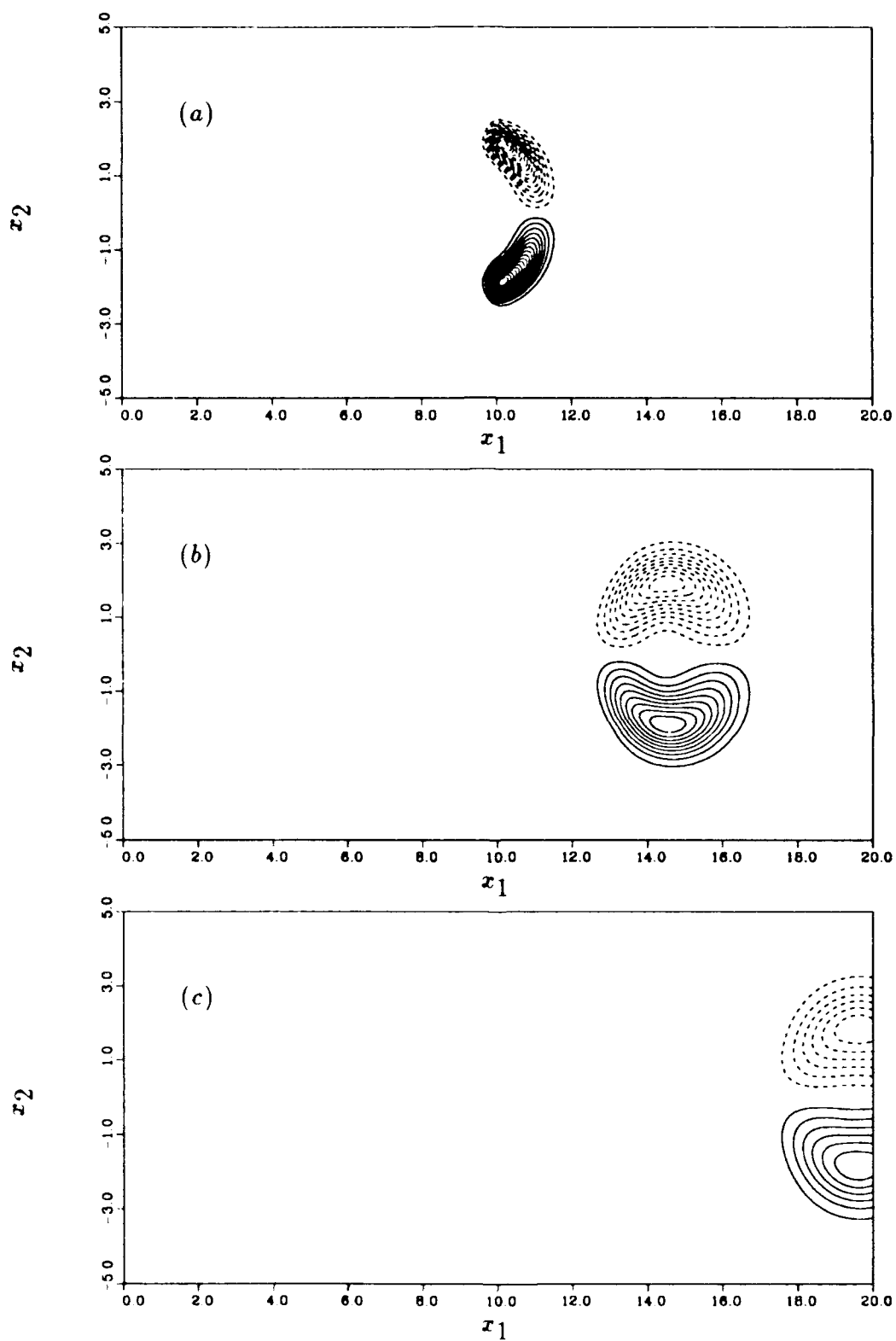


FIGURE 3.5. Vorticity fields from passage of a thermal inhomogeneity through a shock (The contour increments are $\Delta\omega_3 = 0.002$). Solid lines for $\omega_3 > 0$, dashed lines for $\omega_3 < 0$. (a) $t = 11.0$, (b) $t = 16.6$, (c) $t = 22.2$.

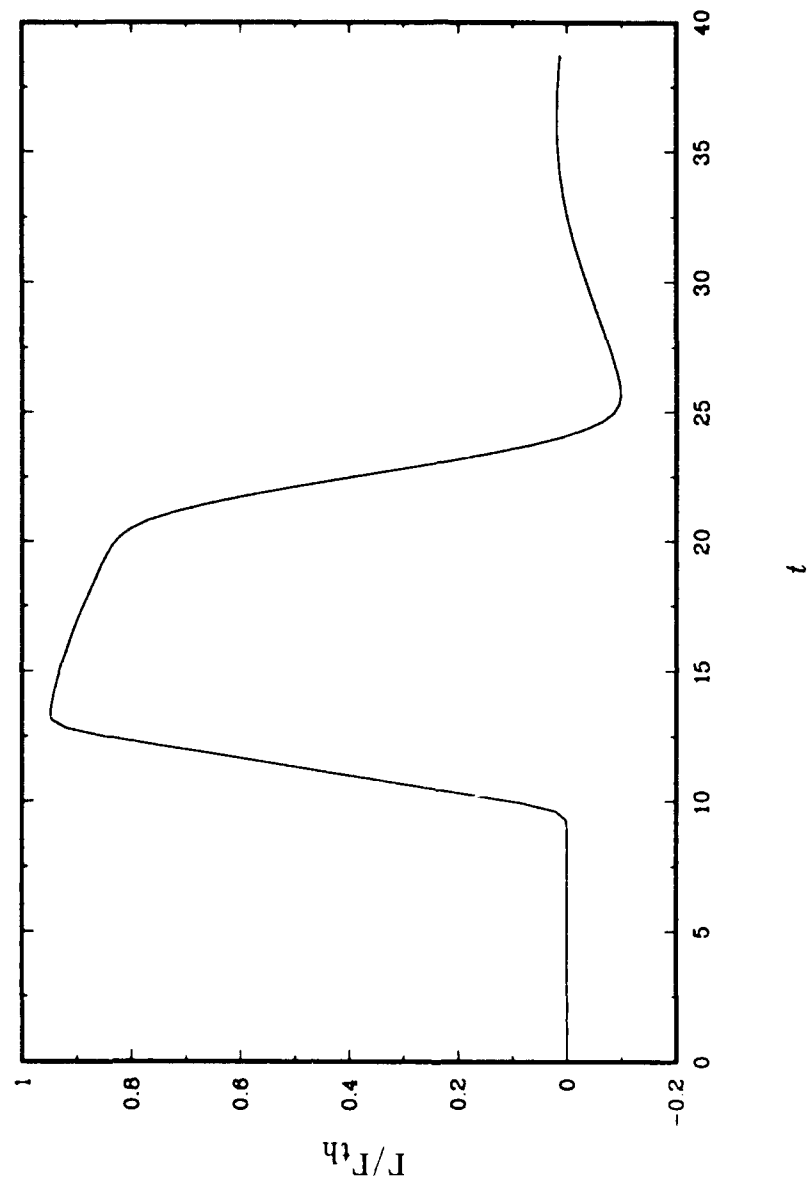


FIGURE 3.6. Evolution of the circulation in the upper half plane from passage of a thermal inhomogeneity through a shock. Γ_{th} is a theoretical estimation given in (3.40).

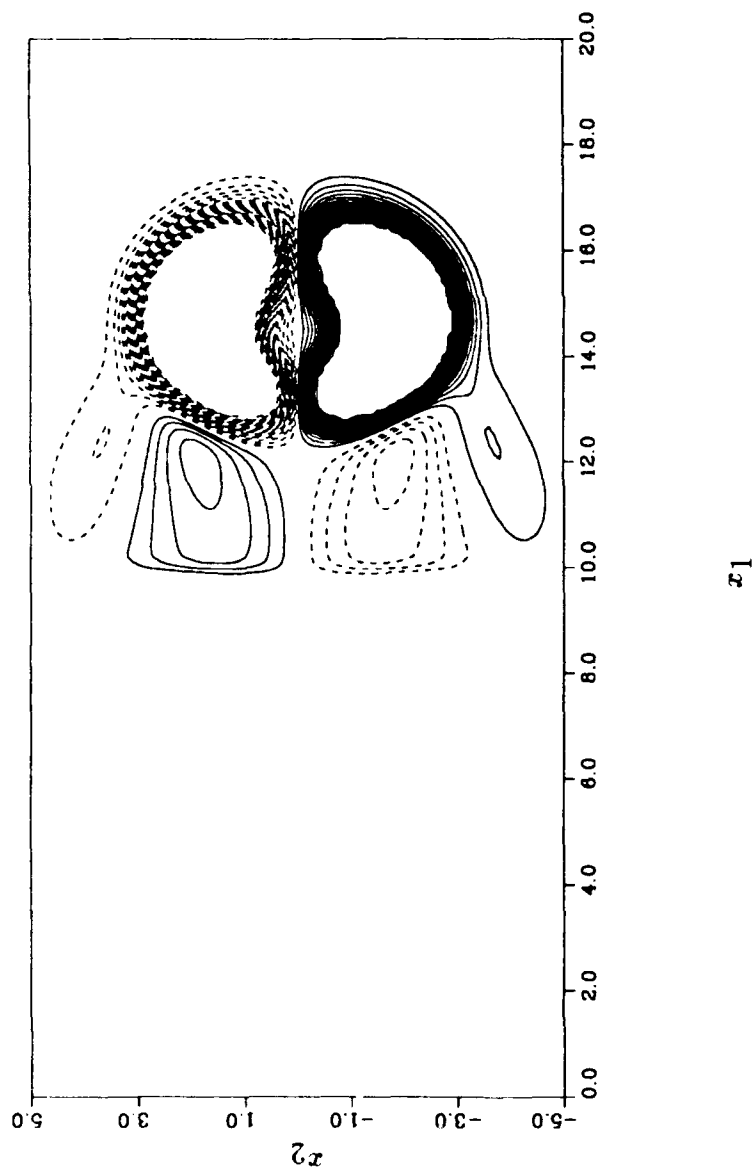


FIGURE 3.7. Vorticity field at $t = 16.6$ from passage of a thermal inhomogeneity through a shock. (The contour increments are $\Delta\omega_3 = 0.0002$). Solid lines for $\omega_3 > 0$, dashed lines for $\omega_3 < 0$.

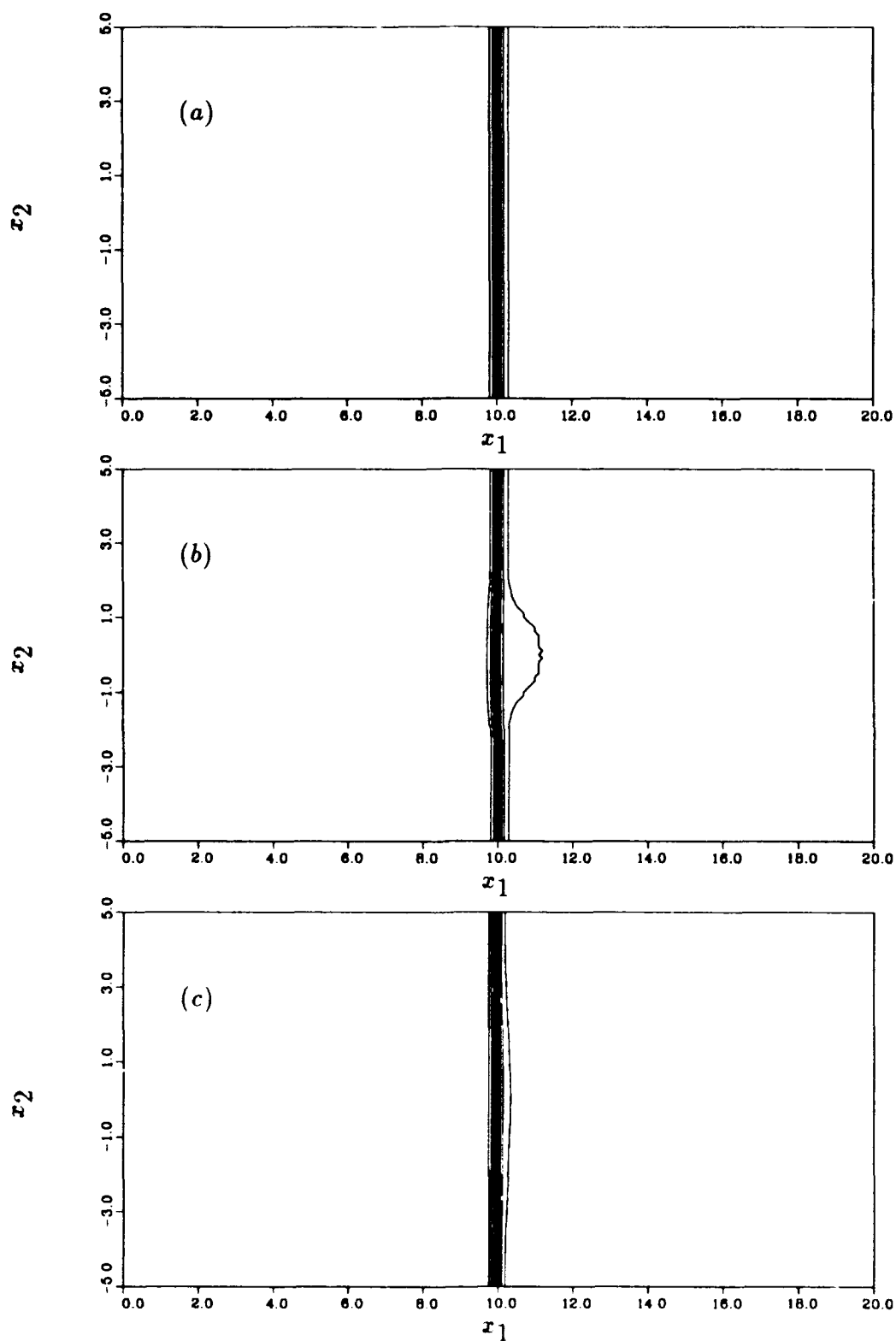


FIGURE 3.8. Pressure fields from passage of a thermal inhomogeneity through a shock (The contour increments are $\gamma\Delta p = 0.05$ starting from the mean upstream pressure $\gamma p = 1.0$). (a) $t = 3.00$, (b) $t = 11.0$, (c) $t = 22.2$.

CHAPTER 4

DIRECT NUMERICAL SIMULATION

In this chapter we discuss the results from direct numerical simulations of the interaction between isotropic turbulence and a normal shock wave.

The simulations are conducted in a reference frame fixed with respect to the mean shock position so that long-time statistical averages of turbulence quantities could be obtained. In this frame of reference, the mean flow approaches the shock wave with a supersonic speed and leaves with a subsonic speed. Inflow turbulence is generated using the method described in Appendix D, and the pressure and density are kept constant and uniform in the inflow plane. Fluctuations in pressure and density naturally evolve as the flow approaches the shock wave. The parameters of the simulations are the mean Mach number M_1^U , fluctuation Mach number $M_t = q/c$, and turbulent Reynolds number Re_λ . As described in Appendix E, resolution requirements limit the range of the parameters in the simulation.

Resolution of the shock wave structure limits the range of shock wave strengths; mean upstream Mach number in this work was in the range $1.05 \leq M_1^U \leq 1.20$.

Upstream of the shock wave, turbulence is weakly compressible and isotropic with $M_t < 0.2$, where compressibility effects are negligible [Lee *et al.* 1991b]. The range of M_t studied in this work is $0.057 \leq M_t \leq 0.110$.

The resolution requirement of turbulence length scales limits the range of turbulent Reynolds numbers. Here we define two turbulent Reynolds numbers,

$$Re_T = \frac{(\overline{\rho u_i'' u_i''})^2}{\bar{\mu} \epsilon} \quad \text{and} \quad Re_\lambda = \frac{\bar{\rho} u' \lambda_1}{\bar{\mu}}, \quad (4.1)$$

where $u' = (\overline{u_i' u_i'})^{1/2}$ and the rate of dissipation of turbulent kinetic energy per unit volume, ϵ , and the longitudinal Taylor microscale λ_α are defined as

$$\epsilon = \tau_{ij} \frac{\partial u_i''}{\partial x_j} \quad \text{and} \quad \lambda_\alpha^2 = \frac{\overline{u_\alpha'^2}}{u_{\alpha,\alpha}'^2}, \quad (4.2)$$

respectively. In incompressible isotropic turbulence, the two Reynolds numbers are related as $Re_T = \frac{3}{5} Re_\lambda^2$. The range of the turbulent Reynolds number in the simulation was $12 \leq Re_\lambda \leq 25$, corresponding to $80 \leq Re_T \leq 300$.

Thus, we have investigated interactions between weak shock waves and weakly compressible isotropic turbulence at low Reynolds numbers. Table 4.1 lists the simulation parameters. (The values of M_t , Re_T , and Re_λ are taken at the location just before the shock.) In this chapter, we discuss modification of turbulence by the shock wave (Section 4.1) and modification of the shock wave by turbulence (Section 4.2).

Table 4.1 Parameters for the simulations of shock-turbulence interaction

Case	A	B	C	D	E	F
Grid	129×64^2	129×64^2	193×64^2	129×64^2	129×64^2	129×64^2
M_t	1.20	1.20	1.20	1.20	1.10	1.05
M_t	0.110	0.102	.0953	.0567	.0762	0.100
Re_T	238	133	84.7	170	281	179
Re_λ	19.9	14.9	11.9	16.8	21.6	17.3
u_o^*	0.10	0.10	0.10	.050	.067	0.10
k_o^*	4	5	6	4	4	6
Re	500	500	500	667	750	750
b_1^\dagger	0.85	0.85	0.80	0.925	0.90	0.85

* defined in equation (3.32)

† defined in equation (3.25)

4.1 Modification of Turbulence

4.1.1 Preliminary Considerations

Figures 4.1(a-c) show the evolutions of mean flow quantities across the shock wave. The mean flow quantities undergo rapid jumps through the shock wave. The average downstream values of pressure and temperature are slightly higher than the values for the corresponding laminar shock wave. These higher mean values are caused by the irreversible energy transfer from turbulent kinetic energy to the internal energy by viscous dissipation. Mean pressure and temperature

undergo slight overshoots just behind the shock wave followed by relaxations due to nonequipartition of energy between fluctuations in pressure and velocity, as flow passes through the shock wave [Sarkar *et al.* 1991]. Suppose the total enthalpy of the flow $h_T^* = c_p^* T^* + u_i^* u_i^* / 2$ is constant behind the shock wave, then its fluctuation vanishes, so that

$$h_T^{*'} \sim c_p^* T^{*'} + U_1^* u_1^{*'} = 0.$$

The effect of temperature overshoot T' on the velocity fluctuation u_1' can be represented as

$$\begin{aligned} u_1' &= \frac{u_1^{*'}}{c_o^*} \\ &= - \frac{T^{*'}}{(\gamma - 1)T_o^*} \frac{c_o^*}{U_1^*} \\ &= -T'/M_1^D. \end{aligned} \quad (4.3)$$

Even though the magnitude of the overshoot is small (about 5%) compared to the jump across the shock wave with $M_1^{U'} = 1.20$, it contributes substantially to the level of the velocity fluctuations (about 20% for a flow with $M_t = 0.15$).

Velocity derivative skewness factor S_α is defined as

$$S_\alpha = \frac{\overline{u_{\alpha,\alpha}^3}}{(\overline{u_{\alpha,\alpha}^2})^{3/2}} \quad (4.4)$$

which has a value of about -0.4 to -0.6 in isotropic turbulence. This value varies with compressibility as well as with the turbulent Reynolds number [Tavoularis *et al.* 1978, Erlebacher *et al.* 1990]. Figure 4.2 shows the evolution of the velocity derivative skewnesses for case C. Turbulence at $k_o x_1 > 12$ may be regarded as realistic. Since the mean position of the shock wave is at $k_o x_1 = 18.8$, turbulence interacting with the shock wave is considered to be realistic.

One-dimensional power spectrum $E_f(k_2; x_1)$ of a fluctuation $f^l(x_1, x_2, x_3, t)$ from the average $\bar{f}(x_1)$ is defined by

$$E_f(k_2; x_1) = \overline{\hat{f}(x_1, k_2, x_3, t) \hat{f}^*(x_1, k_2, x_3, t)}, \quad (4.5)$$

where (\cdot) denotes averaging over the x_3 direction as well as in time, \hat{f} is the Fourier transform of f' in the x_2 direction, and \hat{f}^* is its complex conjugate. Figure 4.3 shows the one-dimensional power spectra of velocity components and density upstream of the shock wave for case C, where k_o/k_c is the largest (k_c is the cutoff, or the largest wave number represented in the simulation). The Kolmogorov wave number $k_K = (\epsilon/\bar{\rho}\nu^3)^{1/4}$ of the simulation was $k_K/k_o = 4.63$, or $k_K/k_c = 0.869$. So, the Kolmogorov scale is actually captured. The spectra decay at least three orders of magnitude, which shows that the flow field is well resolved. The spectra of E_1 and E_3 are in good agreement as expected of isotropic turbulence. The relation between the spectra $E_1(k_2)$ and $E_2(k_2)$ for isotropic turbulence,

$$E_1(k_2) = \frac{1}{2} \left[E_2(k_2) - k_2 \frac{\partial E_2(k_2)}{\partial k_2} \right], \quad (4.6)$$

[Hinze 1975] is also satisfied.

Figures 4.4(a-c) show the evolution of the one-dimensional power spectra of u'_1, u'_2 and density, respectively, throughout the computational domain. Across the shock wave, enhancement of the spectra can be noticed with more amplification at large wave numbers. As the flow evolves further downstream of the shock, the spectra drop over the entire range of the wave numbers. More amplification at large wave numbers across the shock wave leads to the decrease of the turbulence length scales, especially the Taylor microscale.

Two-point correlation $Q_{ff,\alpha}$ and the corresponding integral scale, $\Lambda_{ff,\alpha}$ are defined as

$$Q_{ff,\alpha}(r) = \frac{f'(\mathbf{x})f'(\mathbf{x} + r\mathbf{e}_\alpha)}{f'(\mathbf{x})f'(\mathbf{x})},$$

$$\Lambda_{ff,\alpha} = \int_0^\infty Q_{ff,\alpha}(r)dr, \quad (4.7)$$

respectively, where the direction of separation is indicated by $\alpha = 2, 3$. In order to check the adequacy of the computational box size in the transverse directions where periodic boundary conditions are used, we examine the two-point correlations of

three velocity components, density and pressure in the x_2 direction upstream of the shock for case A, where k_o/k_c is the smallest (Figure 4.5). The longitudinal velocity correlation $Q_{22,2}$ decays monotonically to zero as expected. Even with some problems in the sample size, the lateral velocity correlations, $Q_{11,2}$ and $Q_{33,2}$, show approximate isotropy especially for small separations. (Correlations are calculated by averaging over 65 saved fields which are separated in time by $\Delta t u' / \lambda_1 = 0.064$.) The correlations of pressure and density fluctuations are found to be identical. The size of the computational box in the transverse directions appears to be adequate.

4.1.2 Evolution of Turbulent Kinetic Energy

Figure 4.6 shows the evolution of the normal components of the Reynolds stress tensor R_{ij} defined by [Favre 1965a, 1965b]

$$R_{ij} = \frac{\overline{\rho u_i'' u_j''}}{\bar{\rho}}. \quad (4.8)$$

The off-diagonal components of R_{ij} stay close to zero over the entire flow field due to symmetry (isotropy upstream and axisymmetry downstream) in the velocity fluctuations. The statistics of the streamwise component in the shock zone contains the intermittency effects due to the oscillations of the shock. (The boundaries of the shock oscillations are defined as the locations where $\bar{u}_{1,1} = 0$.) The effect of kinematic oscillation of the plane shock wave on the statistics is investigated in Appendix F. All the velocity fluctuations are enhanced during the interaction as predicted by the linear analyses (RDT and LIA). Turbulent velocity fluctuations are anisotropic behind the shock wave. The return to isotropy is found to be negligible compared to the decay rate. The amplification in the variance of transverse velocity fluctuations, which is defined as the ratio of the downstream maximum value to the upstream minimum value, lies between the near-field and far-field predictions of LIA due to the oscillatory movement of the distorted shock front: for $M_1^U = 1.2$ (case C), the simulated amplification is 1.19, while the near-field LIA prediction is 1.45 and the far-field LIA prediction is 1.15. The streamwise component R_{11} undergoes rapid increase behind the shock wave: the linear analysis (LIA) predicts monotonic decay for all the velocity fluctuations (Figures 2.5-2.7). (Discussions

on the anomalous behavior of the statistics near the outflow boundary in Figures 4.6-4.9, 4.11, and 4.23 are given at the end of this section.)

In order to identify the mechanisms of amplification and rapid evolution of turbulent kinetic energy, the terms in the transport equation of the Reynolds stress tensor R_{ij} were computed. The transport equation for R_{ij} [Dussauge *et al.* 1987] is

$$\underbrace{\bar{\rho} \tilde{u}_k \frac{\partial R_{ij}}{\partial x_k}}_{(I)} = -\bar{\rho} \underbrace{\left(R_{ik} \frac{\partial \tilde{u}_j}{\partial x_k} + R_{jk} \frac{\partial \tilde{u}_i}{\partial x_k} \right)}_{(II)} - \underbrace{\left(\overline{u_i''} \frac{\partial \bar{p}}{\partial x_j} + \overline{u_j''} \frac{\partial \bar{p}}{\partial x_i} \right)}_{(III)} \\ - \underbrace{\left(u_i'' \frac{\partial p'}{\partial x_j} + u_j'' \frac{\partial p'}{\partial x_i} \right)}_{(IV)} - \underbrace{\frac{\partial \rho u_i'' u_j'' u_k''}{\partial x_k}}_{(V)} + \underbrace{\left(u_i'' \frac{\partial \tau_{jk}}{\partial x_k} + u_j'' \frac{\partial \tau_{ik}}{\partial x_k} \right)}_{(VI)}. \quad (4.9)$$

The convection (I) of the Reynolds stress tensor balances with the production by the mean strain field (II) and the production by the mass fluctuation (III), the pressure work (IV), the turbulent transport (V), and the viscous dissipation and transport (VI).

Figure 4.7 shows the TKE budget. The statistics of the flow variables inside the shock wave are contaminated by the intermittency effect caused by the unsteady distortion of the shock wave (Appendix F). Turbulence amplification mechanisms in shock-turbulence interaction cannot, therefore, be unambiguously identified by investigating the statistics of the numerical simulations inside the shock zone. Outside the shock wave, the viscous dissipation is the dominant term and the pressure work term just downstream of the shock is the only other term which has a comparable magnitude. The rapid evolution of TKE just downstream of the shock wave is due to pressure work.

The pressure work term which causes the rapid evolution of TKE downstream of the shock can be decomposed into two terms, the pressure dilatation $\overline{p' u_{i,i}''}$ and the pressure transport term $(\overline{p' u_i''})_{,i}$ as

$$\overline{p' u_{i,i}''} = \overline{p' u_{i,i}''} - (\overline{p' u_i''})_{,i}. \quad (4.10)$$

Positive pressure dilatation leads to reversible energy transfer from the mean internal energy to the turbulent kinetic energy, while the pressure transport is responsible for redistribution of TKE in the inhomogeneous direction. These decomposed terms are shown in Figures 4.8(a) and (b). The decomposition inside the shock wave is very similar to that in the kinematic oscillation of a plane shock wave (Appendix F), which suggests that the behavior of the profiles inside the shock wave are mainly due to its unsteady motion. The decomposition downstream of the shock wave, Figure 4.8(b), shows that the rapid evolution of TKE is caused by the pressure transport term and that the pressure dilatation acts mainly to convert the mean internal energy into turbulent kinetic energy.

Figures 4.9(a) and (b) show the budgets of R_{11} and R_{22} outside the shock wave. The effect of the pressure work term is quite pronounced in the R_{11} equation. The R_{22} equation has no pressure transport, since the flow is homogeneous (periodic numerically) in the x_2 direction. Therefore, the rapid evolution of TKE is mainly from the streamwise fluctuations.

In numerical simulations of two-dimensional inviscid turbulence interacting with a shock, Rotman [1991] found that turbulence is less amplified for the higher upstream turbulence level for the same mean shock strength. Here, comparison is made for the amplification ratios of transverse velocity fluctuations of cases B and D, both with the same shock strength, $M_1^U = 1.20$. Turbulent kinetic energy in case B is three times higher than that in case D, while turbulent Reynolds numbers are comparable. The amplification ratio is higher for the weaker upstream turbulence by about 8%: the amplification ratio is 1.19 for case B and 1.28 for case D. Even though Rotman's simulation had a stronger shock wave with $M_1^U = 2.07$, the reduction in amplification was about the same for the same change in the upstream turbulence intensity.

Application of Thompson's [1987] boundary condition at the outflow generated anomalous statistics of the streamwise velocity fluctuations in a region near the outflow (Figure 4.6), pressure work (Figures 4.7-4.9) and dilatation (Figure 4.11). These anomalies are due to an incomplete suppression of the acoustic wave reflections. In order to investigate whether these anomalous behaviors affect the overall evolution of the flow downstream of the shock wave, the more refined boundary conditions of Giles [1990] was implemented in the code. These numerical experiments verified that these undesirable behaviors were confined to only a small region

near the boundary. (The Giles boundary condition implemented is a first-order approximation for the free propagation of a wave through the boundary, whereas the Thompson boundary condition is a zeroth-order approximation.) A brief description of the Giles' boundary condition and a comparison of statistics are found in Appendix G.

4.1.3 Dilatation and Vorticity

Up to the turbulence Mach number M_t of about 0.5, the dissipation rate of turbulent kinetic energy ϵ can be approximated by neglecting the effect of viscosity variations, as [Lee, Lele, and Moin 1991b]

$$\begin{aligned}\epsilon &\simeq \bar{\mu} \left(\overline{\omega'_i \omega'_i} + \frac{4}{3} \overline{\theta'^2} \right) \\ &= \bar{\mu} \overline{\omega'_i \omega'_i} \left(1 + \frac{4}{3} \chi^\theta \right),\end{aligned}\tag{4.11}$$

where, $\theta = u_{i,i}$ is the dilatation and χ^θ is the ratio of the dilatation and vorticity variances defined by

$$\chi^\theta = \frac{\overline{\theta'^2}}{\overline{\omega'_i \omega'_i}}.\tag{4.12}$$

Therefore, the ratio χ^θ is a relative magnitude of the compressible dissipation rate to the incompressible dissipation rate.

The viscous term in the TKE transport equation, $\overline{u''_i \tau_{ik,k}}$, reduces to the expression (4.11) in homogeneous turbulence if property variations are neglected. This approximation is tested in Figure 4.10. The contributions of turbulence inhomogeneity and property variations to the viscous dissipation are found negligible outside the shock zone.

As noted in (4.11), variances of dilatation and vorticity contribute to the dissipation rate of turbulent kinetic energy. In the following, we investigate the effect of

a shock wave on the variances of dilatation and vorticity. The evolutions of dilatation variance and enstrophy are shown in Figure 4.11. The variance of fluctuating dilatation is enhanced by three orders of magnitude across the shock wave, and decays very rapidly behind the shock wave. Enstrophy is also amplified in passage through the shock.

Figure 4.12 shows the evolution of the components of vorticity across the shock wave for case C. Linear analyses predict that transverse components of vorticity are amplified whereas the streamwise component is unchanged. The simulation results shown in Figure 4.12 (and all other simulations) are consistent with the linear analysis prediction. Turbulence behind the shock wave becomes axisymmetric in vorticity fluctuations as well as in velocity fluctuations.

Figure 4.13 compares the amplifications of the transverse vorticity for different shock wave strengths. The amplification is smaller for the weaker shock. The amplifications of the transverse vorticity across the shock wave computed from the simulations compare favorably with the predictions of linear analyses: the maximum difference is 5% for case F with $M_1^U = 1.05$ and $M_t = 0.10$, where the local shock wave structure is significantly modified (see Sec. 4.2.2). The effect of turbulent Reynolds number on the vorticity amplification is found to be negligible.

Figures 4.14 (a) and (b) show the evolutions of vorticity for flows with different turbulent Reynolds numbers interacting with a shock wave of the same strength. Vorticity stays fairly constant upstream of the shock, and after the interaction transverse components decay whereas the streamwise component increases near the shock wave. In order to check if the increase of the streamwise vorticity component behind the shock (Figure 4.14 (a)) is caused by poor resolution of the simulation, a coarse grid simulation with $97 \times 48 \times 48$ points was performed. Figure 4.14 (c) compares the statistics of vorticity fluctuations with those from the original simulation with $129 \times 64 \times 64$ grid points. The variance of the streamwise vorticity fluctuation predicted by the coarse grid simulation is slightly less than that of the original simulation, thus, confirming that the increase of the variance of the streamwise vorticity behind the shock wave is not from a numerical artifact.

In order to identify the dominant mechanisms for the vorticity amplification and the Reynolds number effects on the evolution of vorticity, the transport equations for vorticity variances were examined. The fluctuating vorticity equation, which is obtained by taking the curl of $\rho^{-1} \times (3.11)$ is:

$$\frac{\partial \omega'_\alpha}{\partial t} + u_j \frac{\partial \omega'_\alpha}{\partial x_j} = \omega'_j s_{\alpha j} - \omega'_\alpha s_{jj} + \epsilon_{\alpha jk} \left[\left(\frac{1}{\rho} \tau_{kq,q} \right)_{,j} + \frac{\rho_{,j} p_{,k}}{\rho^2} \right], \quad (4.13)$$

where $s_{ij} = \frac{1}{2}(u_{i,j} + u_{j,i})$ is the strain rate. Multiplying (4.13) by $2\omega'_\alpha$ and taking the average over the homogeneous transverse directions and over time gives:

$$\begin{aligned} \underbrace{\overline{u_j \frac{\partial \omega'_\alpha \omega'_\alpha}{\partial x_j}}}_{(I)} &= \underbrace{2\overline{\omega'_\alpha \omega'_j s_{\alpha j}}}_{(II)} + \underbrace{2\overline{\omega'_\alpha \omega'_j s'_{\alpha j}}}_{(III)} - \underbrace{2\overline{\omega'_\alpha \omega'_\alpha s_{jj}}}_{(IV)} - \underbrace{\overline{\omega'_\alpha \omega'_\alpha s'_{jj}}}_{(V)} \\ &\quad + \underbrace{2\epsilon_{\alpha jk} \overline{\omega'_\alpha \rho_{,j} p_{,k} / \rho^2}}_{(VI)} - \underbrace{\overline{(\omega'_\alpha \omega'_\alpha u'_k)_{,k}}}_{(VII)} + \underbrace{\Phi_\alpha}_{(VIII)} \end{aligned} \quad (4.14)$$

[Blaisdell *et al.* 1990], where the repeated Greek indices are not summed. Here Φ_α is the viscous dissipation and transport, given by

$$\Phi_\alpha = 2\epsilon_{\alpha jk} \overline{\omega'_\alpha \left(\frac{1}{\rho} \tau_{kq,q} \right)_{,j}}. \quad (4.15)$$

The term on the left hand side of (4.14) represents the advection by the mean flow. The first and second terms on the right hand side represent vortex stretching by the mean and turbulent strain fields, respectively. The next two terms represent production (removal) by dilatation. The fifth is the vorticity production by the baroclinic torque, the sixth is the transport by the turbulent velocity field, and the last term is the viscous dissipation and transport.

The balance of the terms in (4.14) for the transverse vorticity, $\overline{\omega_2'^2}$ is shown in Figure 4.15. The averages are taken over the homogeneous directions, x_2 and x_3 , and over the 65 saved spatial fields for case A which are separated in time by $\Delta t u' / \lambda_1 = 0.064$. All the terms in (4.14) were evaluated independently, and the maximum imbalance, the difference between the LHS and the RHS, occurs outside

the shock zone and is about 10% of the largest terms, the viscous dissipation and turbulent vortex stretching. Inside the shock wave, the vorticity-dilatation (IV+V) is the dominant source for vorticity amplification. The viscous term (VIII) is balanced with the vortex stretching (II+III) beyond the shocked region. Baroclinic torque (VI) is less than 1% of the leading terms throughout the domain in all the simulations, including case F where the shock wave is strongly distorted. The effect of turbulent transport (VII) is also found to be negligible.

Figure 4.16 shows the vortex stretching and vorticity-compression by the mean and turbulent velocity fields, as they appear in (4.14). Even with the overestimation of turbulent strain rate in the shock wave due to intermittency, the vorticity-mean compression (IV) is much larger than the other terms inside the shock. The dominance of the vorticity-mean compression explains the good comparison of the simulation results with the predictions of the linear analyses.

Even though amplifications of the transverse components of vorticity obtained in the simulations are very close to the predictions of linear analyses, they are systematically lower than the linear predictions. The difference becomes larger for the higher upstream turbulence levels, or for the larger values of the ratio, $M_t/(M_1^U - 1)$. Figures 4.17 (a) and (b) show the balance between the nonlinear terms in the $\overline{\omega_2'^2}$ equation and their net effect on the $\overline{\omega_2'^2}$ amplification. The net effect of the nonlinear terms inside the shock wave acts against the amplification of vorticity. However, this nonlinear effects are negligible compared to the linear effects (Figure 4.15).

Figure 4.18 shows the balance of the terms in (4.14) for the streamwise vorticity $\overline{\omega_1'^2}$. Inside the shock wave, effects of vortex stretching (II+III) and vorticity-dilatation (IV+V) tend to cancel each other, resulting in no appreciable change in the streamwise vorticity.

As shown in Figures 4.12, 4.14(a) and (b), there are differences in the evolution of the streamwise vorticity for flows with different Reynolds numbers. To identify the effect of the turbulent Reynolds number on the evolution of vorticity, the vorticity budgets for flows with different Reynolds number are shown in Figures 4.19 (a-d). Outside the interaction zone, the dominating terms in (4.14) are the viscous dissipation (VIII) and the vortex stretching (II+III) — mainly by the turbulent strain rate. Both the stretching and dissipation increase by about the same amount with

the increase of the Reynolds number in the budget of the transverse vorticity component, resulting in no significant Reynolds-number dependence in the evolution of the transverse component. However, some Reynolds-number dependence was found in the budget of the streamwise vorticity evolution: the turbulent stretching overtakes the viscous dissipation behind the shock wave for the higher Reynolds number flow, resulting in a higher increase in the streamwise vorticity component behind the shock wave (Figure 4.14(a)).

For homogeneous turbulence with uniform density, the viscous dissipation and transport term Φ_α reduces to the homogeneous viscous dissipation Φ_α^H

$$\Phi_\alpha^H = -2\nu \overline{\omega'_{\alpha,j} \omega'_{\alpha,j}}. \quad (4.16)$$

The evolutions of Φ_α and Φ_α^H are provided in Figure 4.20. The effects of turbulence inhomogeneity and density variation on the viscous term are found to be negligible except for Φ_2 in the shock zone.

4.1.4 Turbulence Length Scales

Figure 4.21 shows the evolution of the integral scales defined in (4.7) — $\Lambda_{11,2}$, $\Lambda_{\rho\rho,2}$, and $\Lambda_{pp,2}$. Across the shock wave, the decrease in the transverse velocity integral scale $\Lambda_{22,2}$ is quite pronounced. The length scales of density and pressure fluctuations stay very close to each other throughout the domain. They grow upstream of the shock wave, decrease significantly across the shock, and recover to the upstream levels in a short distance downstream of the shock wave.

Figure 4.22 shows the evolution of the turbulence length scale l defined as

$$l = \frac{\rho q^3}{\epsilon}. \quad (4.17)$$

As the flow approaches the shock wave, this length scale decreases, probably because the energy spectrum becomes fuller at high wave numbers. (The inflow spectrum given in (3.32) has virtually no energy beyond $k/k_o > 2$.) The length scale decreases further across the shock wave, and rises rather rapidly over a short distance behind the shock wave. The length scale estimation inside the shock wave is significantly contaminated by the overestimation of $u_{1,j}^2$ due to the oscillation of the shock wave.

Another length scale of interest is the longitudinal Taylor microscale λ_α defined in (4.2). Figure 4.23 shows the evolution of the Taylor microscales throughout the computational domain. The evaluation of the streamwise microscale λ_1 inside the shock wave is also significantly contaminated due to the shock wave oscillation. Noticeable reductions of all the microscales are found across the shock wave.

Figure 4.24 compares the Taylor microscale reductions in a transverse direction from different cases with predictions by LIA and RDT. For the range of upstream Mach numbers simulated ($M_1^U = 1.05, 1.10, 1.20$), the predictions by LIA and RDT are virtually the same. Except for cases with strong upstream turbulence intensity, the simulation results compare favorably with the predictions by the linear theories. As the upstream turbulence intensity increases, the transverse Taylor microscales decrease more across the shock wave with the same M_1^U (compare cases A, B, and C). The streamwise Taylor microscale evolves rapidly downstream of the shock and it is difficult to identify its "downstream value."

4.1.5 Thermodynamic Properties

In Figure 4.25(a), we present evolutions of *rms* pressure, density, and temperature fluctuations (p_r, ρ_r , and T_r). As the flow passes through the shock wave, all the fluctuations are amplified, followed by a rapid decay. These fluctuations are virtually isentropic. The polytropic exponent $n_1(x_1)$ is defined as

$$n_1(x_1) = \frac{p_r(x_1)/\bar{p}(x_1)}{\rho_r(x_1)/\bar{\rho}(x_1)}, \quad (4.18)$$

which is equal to γ (1.40 here) for isentropic fluctuations. Figure 4.25(b) shows evolutions of the polytropic exponent. The polytropic exponent stays close to the isentropic value throughout the domain, varying between 1.35 and 1.40.

In order to identify the mechanisms of amplification and decay of the density fluctuation variance $\overline{\rho'^2}$, the budget for the density fluctuation variance [Taulbee *et al.* 1991] is investigated:

$$\underbrace{\tilde{u}_1 \frac{\partial \overline{\rho'^2}}{\partial x_1}}_{(I)} = \underbrace{-2\overline{\rho'^2} \frac{\partial \tilde{u}_1}{\partial x_1}}_{(II)} + \underbrace{-2\overline{\rho' u_1''} \frac{\partial \bar{\rho}}{\partial x_1}}_{(III)} + \underbrace{-2\bar{\rho} \rho' \frac{\partial u_1''}{\partial x_1}}_{(IV)} + \underbrace{-\rho'^2 \frac{\partial u_1''}{\partial x_1}}_{(V)} + \underbrace{-\frac{\partial \rho'^2 u_1''}{\partial x_1}}_{(VI)}. \quad (4.19)$$

The convection (I) is balanced by the productions by the mean compression (II) and the mean density gradient (III), density-dilatation correlations (IV+V), and turbulence transport (VI). Figures 4.26 (a) and (b) show the balance of the terms in (4.19) for the density fluctuation variance, $\overline{\rho'^2}$. The averages are taken over the homogeneous directions, x_2 and x_3 , and over the 65 saved spatial fields which are separated in time by $\Delta t u' / \lambda_1 = 0.064$ for case A. Across the shock wave, density fluctuations are enhanced mainly by the production due to the mean compression (II) and the mean density gradient (III). Density-fluctuating dilatation correlations (IV+V) are significantly overestimated inside the shock wave due to the shock front oscillation, but their net effect is the suppression of the density fluctuation during the interaction. Behind the shock wave, however, the evolution of $\overline{\rho'^2}$ is dominated by the density-fluctuating dilatation correlation (IV).

Figure 4.27 shows the joint probability density function of the instantaneous pressure versus instantaneous density scaled with their local mean values, $\bar{p}(x_1)$ and $\bar{\rho}(x_1)$. It is clear that the isentropic relations is satisfied for the instantaneous flow, even inside the shock wave. The local polytropic exponent $n_2(\mathbf{x})$ is defined as

$$n_2(\mathbf{x}) = \frac{p'(\mathbf{x})/\bar{p}(x_1)}{\rho'(\mathbf{x})/\bar{\rho}(x_1)}.$$

The average polytropic exponent \bar{n}_2 is obtained by averaging $n_2(\mathbf{x})$ over the flow field. (The states with $|\rho'(\mathbf{x})/\bar{\rho}(x_1)| < 10^{-3}$ were excluded in the averaging process to avoid large scatter.) The average polytropic exponent was found to be very close to the isentropic value ($\bar{n}_2/\gamma = 1.01$).

Examining a limited experimental data sets, Morkovin [1962] (see also Bradshaw [1977]) pointed out that in non-hypersonic boundary layers the acoustic mode is negligible and the entropy mode is very small for normal rates of heat transfer. He then deduced that

$$p'/\bar{p} \ll 1, \quad T''_o/\tilde{T}_o \ll 1$$

so that

$$\frac{\rho'}{\bar{\rho}} = -\frac{T''}{\tilde{T}} \sim (\gamma - 1) M_1^2 \frac{u''}{\tilde{u}_1}, \quad (4.20)$$

where the total temperature is $T_t = T + u_i u_i / 2c_p$. This is known as Morkovin's Strong Reynolds Analogy (the assumption of negligible total temperature fluctuations) and is widely used to correlate thermodynamic property fluctuations with velocity fluctuations in compressible turbulence closures. A more general correlation through the polytropic coefficient n is suggested by Rubesin [1976] as

$$\frac{p'}{\bar{p}} = n \frac{\rho'}{\bar{\rho}} = \frac{n}{n-1} \frac{T''}{\bar{T}}. \quad (4.21)$$

Morkovin's relation is a special case of (4.21) with $n = 0$.

Figure 4.28 shows the correlation between density and temperature fluctuations, $c_{\rho T}$, defined by

$$c_{\rho T} = \frac{\overline{\rho' T''}}{\bar{\rho}^2 \bar{T}},$$

which would be $n - 1$ if (4.21) were correct. Since the polytropic coefficient n was found to be close to the isentropic exponent ($\gamma = 1.40$), the validity of the Morkovin's analogy appears to be questionable (with wrong signs). The same conclusion was reached by Blaisdell *et al.* [1990] in their numerical simulation of homogeneous shear flow. Using Gibbs' equation and the equation of state of an ideal gas, the pressure fluctuations can be represented in terms of the fluctuations in density and entropy as

$$p' \simeq \left(\frac{\partial p}{\partial \rho} \right)_s \rho' + \left(\frac{\partial p}{\partial s} \right)_\rho s', \quad (4.22)$$

where s is the dimensionless entropy defined as $s = s^* / c_p^*$. When the temperature (or entropy) inhomogeneity in the flow is not significant, or

$$\left| \left(\frac{\partial p}{\partial \rho} \right)_s \rho' \right| \gg \left| \left(\frac{\partial p}{\partial s} \right)_\rho s' \right|,$$

then (4.22) reduces to the polytropic relations (4.21) with $n = \gamma$. This inequality can be translated into terms which can be estimated [Thompson 1984, p.144] as

$$|u_{i,i}| \gg \left| \frac{(\gamma - 1)}{\gamma p} [\epsilon + \kappa \nabla^2 T] \right|. \quad (4.23)$$

The RHS of (4.23) was found to be less than 5% of the dilatation in the present simulations, which verifies that the relations between thermodynamic property fluctuations are nearly isentropic.

Expression (4.21) reduces to the Strong Reynolds Analogy (4.20) if there exists an appreciable mean temperature gradient in the flow and the pressure fluctuations are negligible. The Strong Reynolds Analogy is, therefore, a good approximation in turbulent boundary layers where mean gradients of temperature and density normal to the wall are large.

4.1.6 Modeling Issues

In the k - ϵ formulation for compressible turbulence, the transport equation for turbulent kinetic energy (equation (4.9) with $i = j$) has more modeled terms than its incompressible counterpart. The additional terms are the compressible dissipation ϵ^C (included in $\overline{u_i'' \tau_{ik,k}}$), the pressure-dilatation correlation $\overline{p' u_{i,i}''}$ (included in $-\overline{u_i'' p'}$) and the average turbulent mass flux $\overline{u_i''}$. Zeman [1990] and Sarkar *et al.* [1991] proposed models which parametrize compressible dissipation in terms of incompressible dissipation ϵ^I , and the fluctuation Mach number M_t as $\epsilon^C = \epsilon^I f(M_t)$. Both models were successful in predicting the suppression of the spreading rate of compressible mixing layers at high convective Mach numbers. Coleman and Mansour [1991] proposed a modified turbulence model for the incompressible dissipation ϵ^I when turbulence is subject to mean compression.

Zeman [1991a] has identified the pressure-dilatation correlation with the rate of change of *compressible potential energy*, represented by the pressure fluctuation variance $\overline{p'^2}$, as

$$\overline{p' u_{i,i}''} = -\frac{1}{2} \frac{\tilde{u}_1}{\bar{\rho} \bar{c}^2} \frac{\partial \overline{p'^2}}{\partial x_1}. \quad (4.24a)$$

Zeman assumed that the rate of change of $\overline{p'^2}$ is governed by a nonlinear relaxation mechanism which drives $\overline{p'^2}$ to an equipartition value [Sarkar *et al.* 1991]:

$$\tilde{u}_1 \frac{\partial \overline{p'^2}}{\partial x_1} = - \frac{\overline{p'^2} - p_e^2}{\tau_a}, \quad (4.24b)$$

where the acoustic time scale τ_a is

$$\tau_a = \frac{M_t \tau}{\sqrt{54(1 + M_t^2/3)}} \quad (4.25a)$$

($\tau = \bar{\rho} q^2 / \epsilon^I$ denotes the turbulence time scale), and the equilibrium value p_e^2 is

$$\frac{p_e^2}{\bar{\rho}^2 q^2 \bar{c}^2} = \frac{\alpha M_t^2 + \beta M_t^4}{1 + \alpha M_t^2 + \beta M_t^4}. \quad (4.25b)$$

$\alpha = 1$ and $\beta = 2$ were chosen to best match the DNS results for highly compressible turbulence [Blaisdell *et al.* 1990]. The expression (4.25b) combines two assumptions: (1) the equilibrium ratio of compressible to solenoidal turbulent kinetic energy is

$$q_C^2 / q_I^2 = \alpha M_t^2 + \beta M_t^4,$$

and (2) in equilibrium, the compressible potential and kinetic energies are in equipartition,

$$\overline{p_C^2} = \bar{\rho}^2 q_C^2 \bar{c}^2.$$

Zeman [1991b] and Durbin and Zeman [1991] proposed modifications for (4.24a) and (4.24b) to account for the effect of the mean strain rate as

$$\overline{p' u''_{i,i}} = - \frac{1}{2} \frac{\tilde{u}_1}{\bar{\rho} \bar{c}^2} \frac{\partial \overline{p'^2}}{\partial x_1} - \frac{\overline{p'^2}}{\bar{p}} \frac{\partial \tilde{u}_1}{\partial x_1} \quad (4.26a)$$

and

$$\tilde{u}_1 \frac{\partial \overline{p'^2}}{\partial x_1} = -\frac{\overline{p'^2} - p_e^2}{\tau_a} - 2(\gamma + c_d) \overline{p'^2} \frac{\partial \tilde{u}_i}{\partial x_i}, \quad (4.26b)$$

where $c_d = (5 - 3\gamma)/12$.

As shown in Figures 4.29(a) and (b), the model in (4.26a) appears to be very accurate.

Figure 4.30 shows an evaluation of (4.26b) using DNS data. The closure equation for $\overline{p'^2}$ was found to be inadequate throughout the domain. The equilibrium pressure variance p_e^2 which best matches the upstream and downstream evolution of $\overline{p'^2}$, was found to be 0.3 times the expression given in (4.24b), and the result is also shown in the figure. Zeman assumed that the pressure variance $\overline{p'^2}$ is the *compressible potential energy*, and relaxes to the equilibrium compressible pressure variance p_e^2 . Investigation of the simulation database of decaying compressible turbulence [Lee *et al.* 1991b] showed that the contribution of the incompressible pressure is appreciable even in fairly compressible turbulence with $M_t \simeq 0.5$. For a flow with lower M_t , the incompressible pressure comprises the major portion of the pressure fluctuations. Therefore, the assumption behind the expression for p_e^2 given in (4.25b) is invalid except for highly compressible turbulence. For the range of parameters studied in this work, compressibility effects are not significant anywhere except in the shock zone.

Sarkar [1991] has also proposed a model for the pressure-dilatation correlation using the DNS database of isotropic turbulence and sheared homogeneous turbulence. He developed his model using the statistics in the fully developed stage where turbulent kinetic energy decays (isotropic turbulence) or grows (sheared turbulence) in time. Taulbee and Van Osdol [1991] proposed a single expression for the sum of the pressure-dilatation correlation and compressible dissipation, $\overline{p' u''_{i,i}} + \epsilon^C$, and tuned model parameters to match the experimental data in a boundary layer and a mixing layer. Both models were unable to predict the present observation of reversible energy transfer from mean thermal energy into turbulent kinetic energy in the absence of mean strain rate behind a shock.

The pressure transport term, $-(\overline{p'u_1''})_{,1}$, was identified to be the driving mechanism for the rapid evolution of the velocity fluctuations downstream of the shock wave. Assuming the isentropic relation between thermodynamic fluctuations, the pressure velocity correlation can be expressed as

$$-\overline{p'u_1''} = -\frac{\gamma\bar{p}}{\bar{\rho}}\overline{\rho'u_1''} = -\bar{c}^2\overline{\rho'u_1''}. \quad (4.27a)$$

The accuracy of this assumption is checked in Figure 4.31(a), which shows that the use of isentropic thermodynamic relations in (4.27a) is satisfactory throughout the domain. Therefore, modeling of the pressure transport can be reduced to that of the turbulent mass flux, $\overline{\rho'u_1''}$. Taulbee *et al.* [1991] developed a model transport equation for $\overline{\rho'u_1''}$ using Morkovin's hypothesis. However, as was shown in section 4.1.4 applicability of the Morkovin's hypothesis in the absence of mean temperature gradient is questionable. Zeman [1991b] proposed a model rate equation for $\overline{\rho'u_1''}$ as

$$\tilde{u}_1 \frac{\partial \overline{\rho'u_1''}}{\partial x_1} = -\frac{\overline{\rho'u_1''}}{\tau_a} - R_{11} \frac{\partial \bar{\rho}}{\partial x_1} - \overline{\rho'u_1''} \frac{\partial \tilde{u}_1}{\partial x_1}, \quad (4.27b)$$

which drives the mass flux fluctuation to zero except near the shock, on the fast acoustic time scale τ_a . The accuracy of the model in (4.27b) is checked in Figure 4.31(b) which shows that it qualitatively represents the behavior downstream of the shock wave. However, there are differences in the peak position and its magnitude.

To gain further insight into the physics of the turbulent mass flux $\overline{\rho'u_1''}$ downstream of the shock, several different scalings were examined. The best scaling is based on the assumption that the correlation between the density and velocity fluctuations is composed mainly from acoustic waves. The streamwise distance and the turbulent mass flux are scaled as

$$\frac{x_1/\tilde{u}_1}{\lambda_2/\bar{c}} \quad \text{and} \quad \frac{\overline{\rho'u_1''}}{\bar{\rho} \bar{c} M_t^2}, \quad (4.28)$$

respectively. Figure 4.32(a) and (b) show the unscaled and the scaled turbulent mass flux terms for different upstream conditions and shock strengths ($M_1^U =$

1.10, 1.20), respectively. The match in amplitudes and length scales of the turbulent mass fluxes from different simulations is significantly improved by the scaling (4.28), which suggests that the rapid evolution of TKE may have been caused by the propagation of acoustic waves which are generated during the interaction.

4.2 Modification of a Shock Wave

4.2.1 Statistics of a Shock Wave

The characteristics of the shock wave— shock wave thickness and shock front distortion— vary with time due to the effect of upstream turbulence. The peak compression $\theta_{\min}(x_2, x_3, t)$ inside the shock wave along the mean streamlines is used as a measure of the shock wave strength. (The \min is taken along the x_1 -direction for each x_2 and x_3 . θ_{\min} is not necessarily confined to a plane, however for clarity its “stretched” version on a plane will be presented.) Figure 4.33 shows a typical contour plot of $\theta_{\min}(x_2, x_3, t)$. (Dashed contours denote values with larger than the corresponding laminar value at the same upstream Mach number.) The average peak compression is found to decrease from the peak compression of the laminar shock wave by about 10%. The peak compression varies widely across the transverse plane, which is reflected in the large value of the ratio between the *rms* and the mean values of the peak compression, $(\theta_{\min})_{\text{rms}}/|\overline{\theta_{\min}}| = 0.42$.

Figures 4.34(a) and (b) show the probability density function (PDF) of the peak compression inside the shock wave. The flow tends to have frequent events of large compression. This trend is clearly shown in Fig. 4.34(b), where the probability of large compression zones is higher than the Gaussian distribution by several orders of magnitudes. This is confirmed by the skewness and flatness values of the PDF, -0.81 and 11.0 , respectively.

The statistics of the shock front distortion were estimated by LIA in Section 2.2. The shock wave front in the simulated field, however, is not clearly defined, because in the numerical simulations the shock wave spans over several grid points. The

pressure half-rise point was chosen to be the shock front position, $\xi(x_2, x_3, t)$. In other words,

$$\xi(x_2, x_3, t) = \left\{ \xi \mid p(\xi, x_2, x_3, t) = \frac{p_L^U + p_L^D}{2} \right\}, \quad (4.29)$$

where p_L denotes the pressure in the laminar shock wave which was shown in Figure 4.1 to be near the mean turbulent value. This designator is very well-defined and remains relatively noise-free for the cases with weak upstream turbulence. In order to check the sensitivity of the shock front statistics to the special choice of the designator, the contour plot of the shock wave position based on the pressure half-rise point was compared with that based on the density half-rise point in Figures 4.35(a) and (b). The difference between the *rms* shock distortions obtained by the two methods is always less than 1% of the predicted *rms* values.

Figure 4.36 shows the scaled *rms* displacement of the shock front from different simulations. The scaling suggested by LIA was found to collapse the simulation data reasonably well. The LIA prediction of the shock front displacement is dependent on the shape of the spectrum, especially on the low wave number part. The *rms* displacements of the shock front from the simulation are systematically lower than the LIA prediction based on the energy spectrum (2.1) and higher than that based on the von Kármán energy spectrum (2.2). This can be attributed to the shape of the upstream spectrum in the simulation: As the spectrum develops from the inflow spectra (3.32) or (2.1), it loses energy at small wave numbers and gains energy at large wave numbers. The scaled shock front displacement is smaller for the higher upstream turbulence level.

Figure 4.37 shows the scaled *rms* shock front inclination angle in the x_2 -direction, $\sigma_2 = \partial\xi/\partial x_2$. LIA predicts the *rms* shock front inclination angle to be independent of the upstream energy spectrum shape. The statistics from the simulation are in fair agreement with the LIA predictions. As the fluctuation Mach number of the simulation increases, the simulation result deviates further from the linear prediction (Note that an infinitesimal fluctuation Mach number is one of the assumptions for valid application of the linear analysis).

Shock front curvature profiles obtained from the simulation was too noisy to permit any decisive conclusion except for case C where the shock wave is resolved best. The *rms* values of the scaled shock front curvature

$$\frac{\tilde{u}_1 \kappa_2}{u' k_o}$$

range from 1.86 to 2.03, while the LIA prediction with spectrum (2.1) is 1.41 for $M_1^U = 1.20$.

4.2.2 Instantaneous Fields

Instantaneous density fields at a typical $x_1 - x_2$ plane from the cases D and F, are given in Figures 4.38(a) and (b): Figure 4.38(a) is for a weak upstream turbulence ($M_1^U = 1.20, M_t = 0.057$) and Figure 4.38(b) is for a relatively intense turbulence ($M_1^U = 1.05, M_t = 0.10$). The overlaid contour lines near the center of the figures are iso-compression (same $u_{i,i}$) lines. Figure 4.38(a) shows a clear shock front across which significant increase in density is noticed. For the more intense upstream turbulence (Figure 4.38(b)), the shape of the shock front is more distorted. The variation of peak compressions inside the shock wave in transverse directions becomes stronger for the more intense upstream turbulence. The variation in the visual thickness of the shock wave is also larger for the stronger upstream turbulence. Low density regions are often found behind the mean shock position for flows with $M_t > M_1^U - 1$.

By comparing Figures 4.33 and 4.35(a), we found a moderate correlation between the peak compression and the shock front distortion: the peak compression is larger for the shock wave pushed downstream relative to the mean position by upstream turbulence and weaker for the one pulled upstream. Figures 4.39(a) and (b) show the profiles of dilatation along the x_1 -direction for the cases D and F, respectively. The strength of the shock wave (or the peak compression in the shock) varies widely from one streamline to another. For the case of strong upstream turbulence (Figure 4.39(b)), the structure of the shock wave is significantly modified: multiple peaks in compression along streamlines (e.g., \diamond) are noticeable. Each compression peak has a strength comparable to that of the laminar shock wave. Sometimes, a shock wave is replaced by a series of compression waves (e.g., \times).

Figures 4.40(a) and (b) show the pressure profiles along the x_1 -direction. For relatively weak upstream turbulence, pressure rises monotonically from the upstream

to the downstream value. On the other hand, for strong upstream turbulence, patterns of the pressure rise are varied: rapid monotonic rise, slow monotonic rise and multiple-staged rise.

Figure 4.41 shows the streamwise Mach number in a x_1x_2 -plane near the shock wave for case A. The streamwise Mach number is a good representative of the upstream shock normal Mach number in cases where $\sigma_2 < 10^\circ$. The drops in the streamwise Mach number across the shock wave along the x_1 -direction are more or less uniform: the higher upstream Mach numbers correspond to the higher downstream Mach numbers, and vice versa. For a shock wave fixed in space, however, higher upstream Mach number M_1^U would correspond to lower downstream Mach number M_1^D , as

$$(M_1^D)^2 = \frac{1 + \frac{\gamma-1}{2}(M_1^U)^2}{\gamma(M_1^U)^2 - \frac{\gamma-1}{2}}. \quad (4.30)$$

The uniform Mach number drop for different upstream Mach numbers implies that the local fluctuating shock wave speed tends to be in phase with the upstream Mach number—positive for higher Mach numbers and negative for lower Mach numbers, so that the effective shock-normal Mach numbers are more or less uniform across the transverse plane. The nonuniformity in the upstream Mach number is smoothed out by the fact that the local shock wave speed (ξ, t) tends to be in phase with that of the fluctuating velocity (Section 2.2).

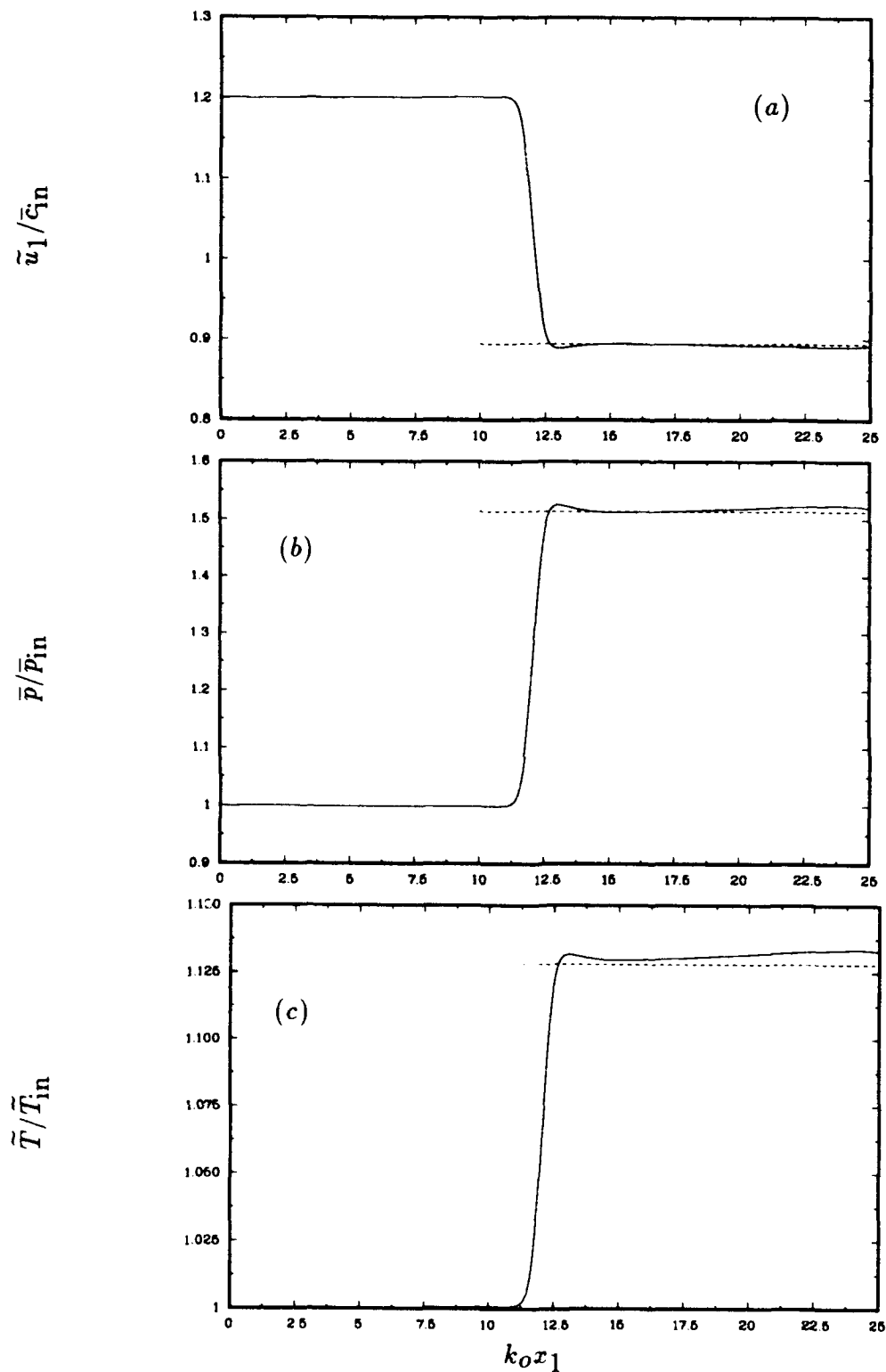


FIGURE 4.1. Evolution of mean quantities across the shock wave for case A: (a) streamwise velocity, (b) pressure, (c) temperature. (Dashed lines denote the laminar downstream values.)

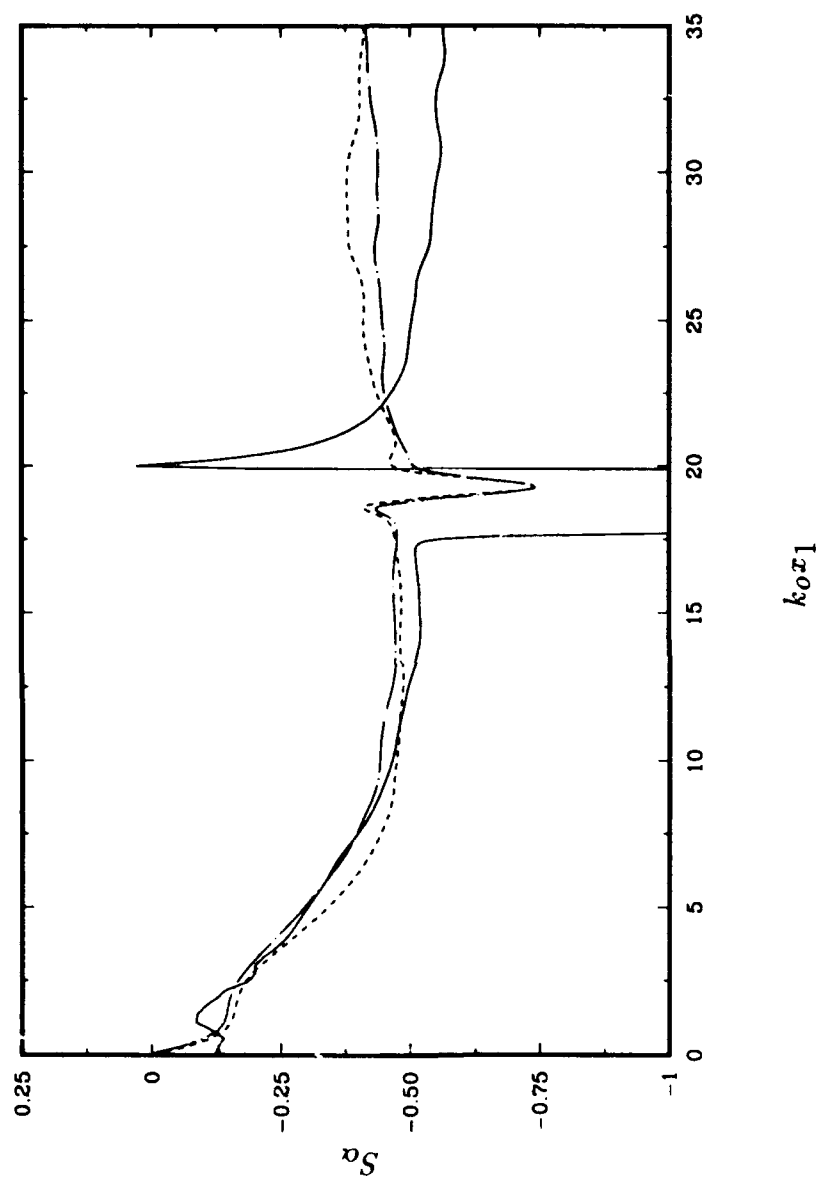


FIGURE 4.2. Evolution of velocity derivative skewnesses for case C: — S_1 , - - - S_2 , - · - S_3 .

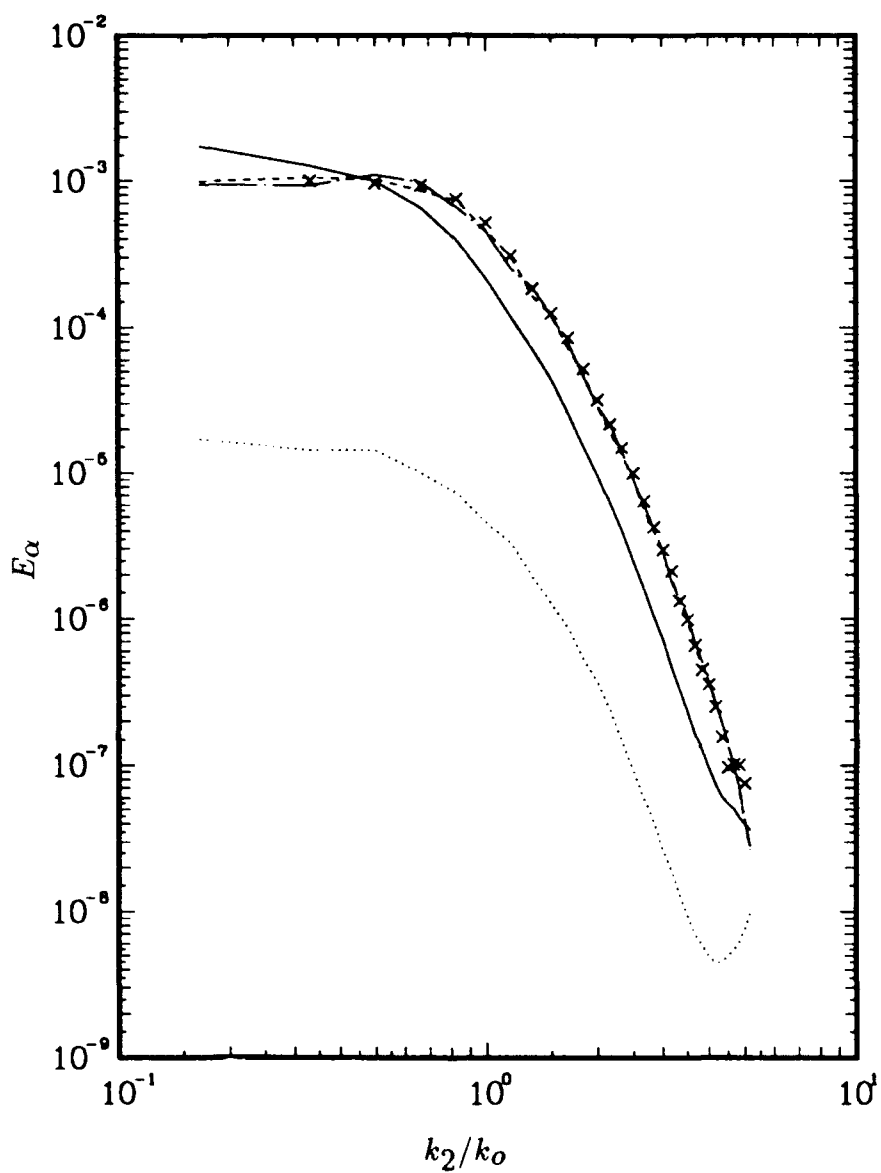


FIGURE 4.3. One dimensional power spectra upstream of the shock wave for case C at $k_0 x_1 = 15.8$: — E_2 , ---- E_1 , —·— E_3 , E_ρ , × E_1 from E_2 using isotropy relation, (4.6).

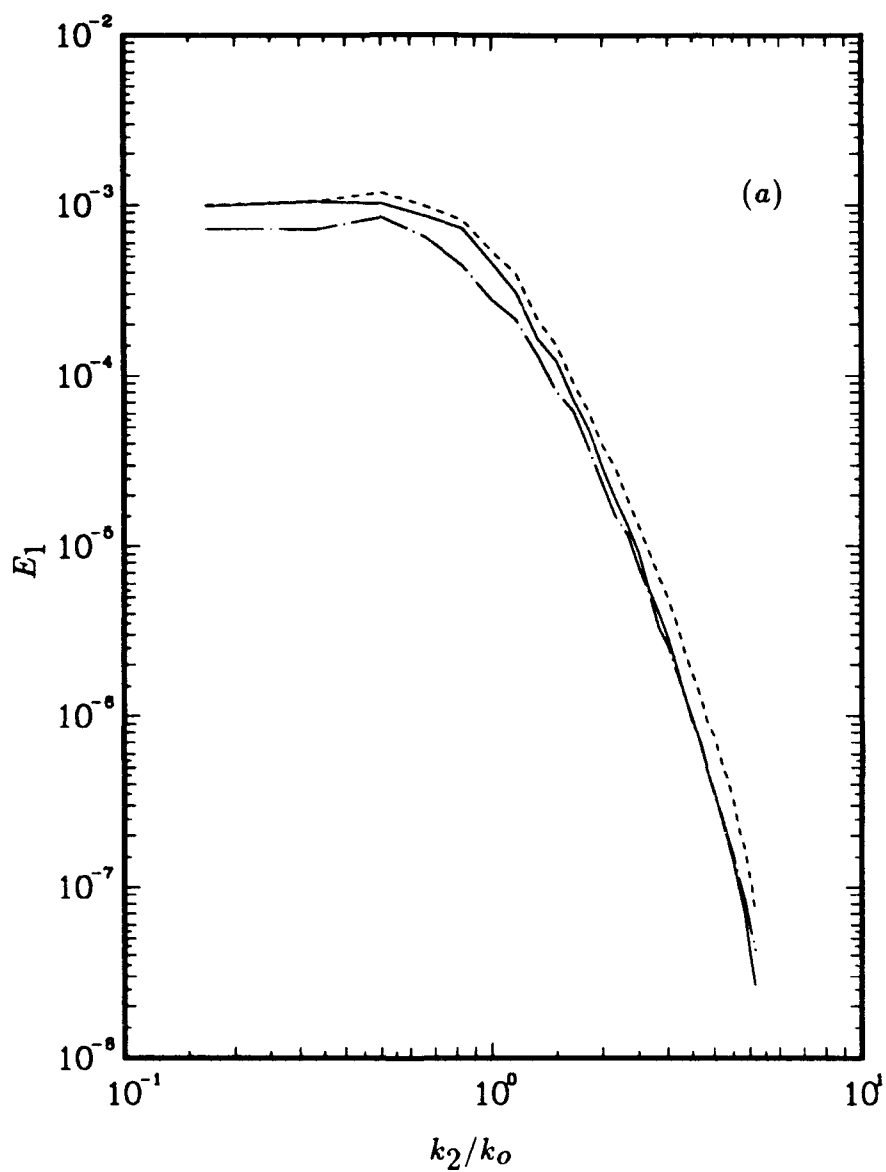


FIGURE 4.4. Evolution of the energy spectra of (a) streamwise velocity, (b) transverse velocity, and (c) density fluctuation for case C: — upstream($k_0x_1 = 15.8$), ---- downstream($k_0x_1 = 21.9$), - - - at exit boundary($k_0x_1 = 37.7$).

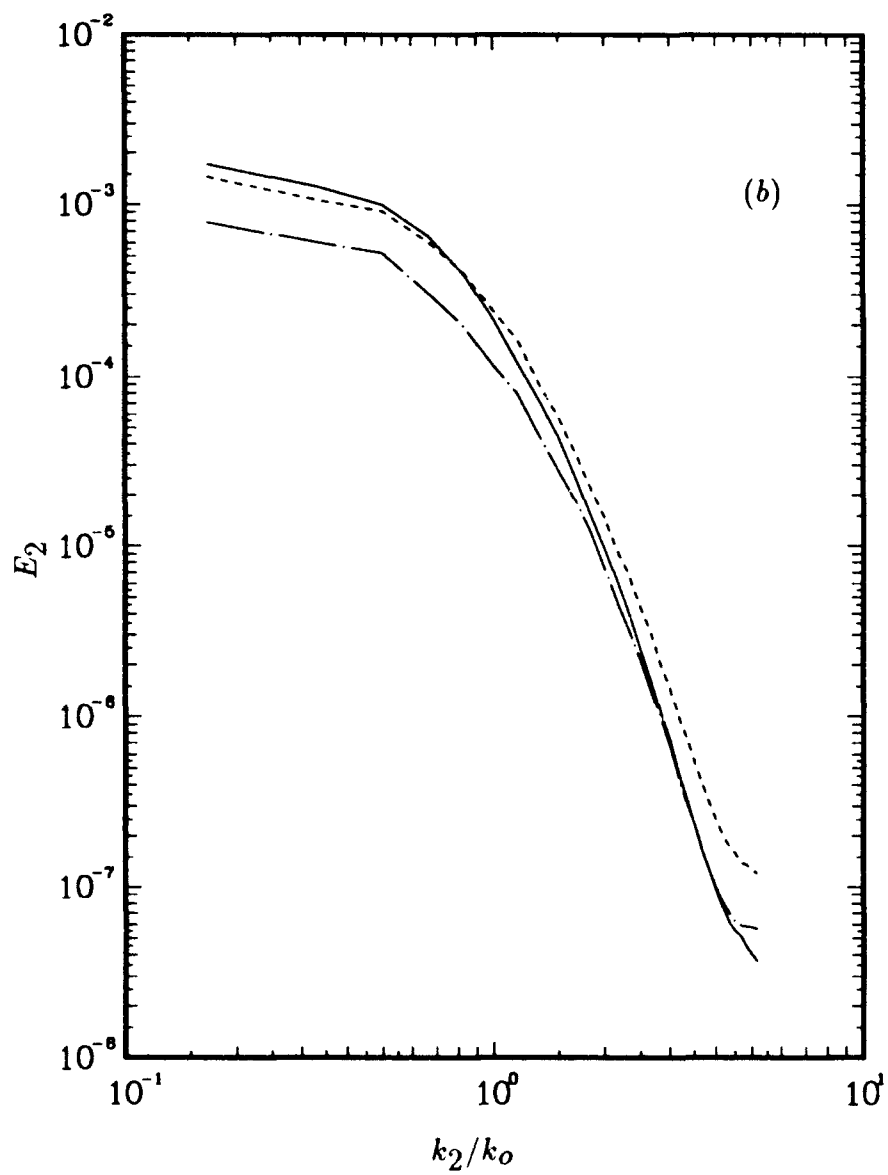


FIGURE 4.4. continued.

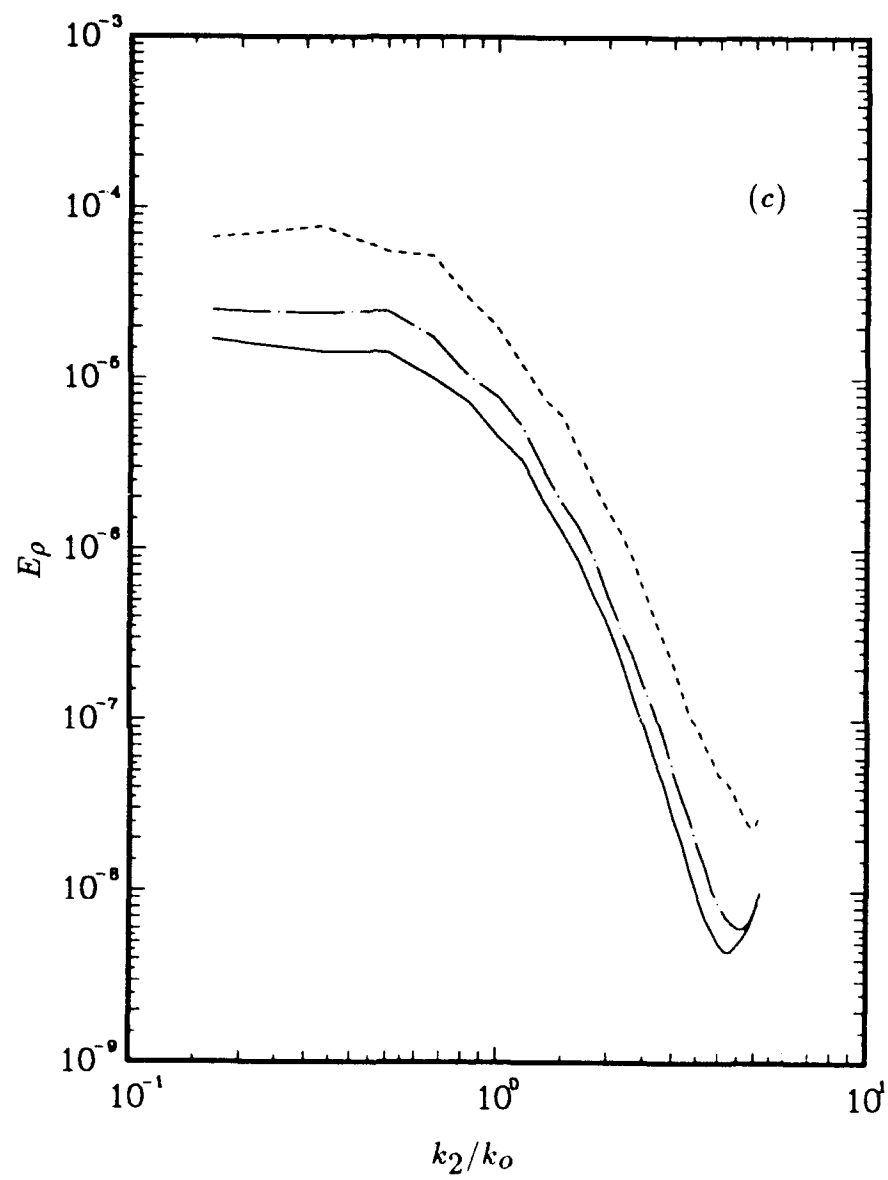


FIGURE 4.4. continued.

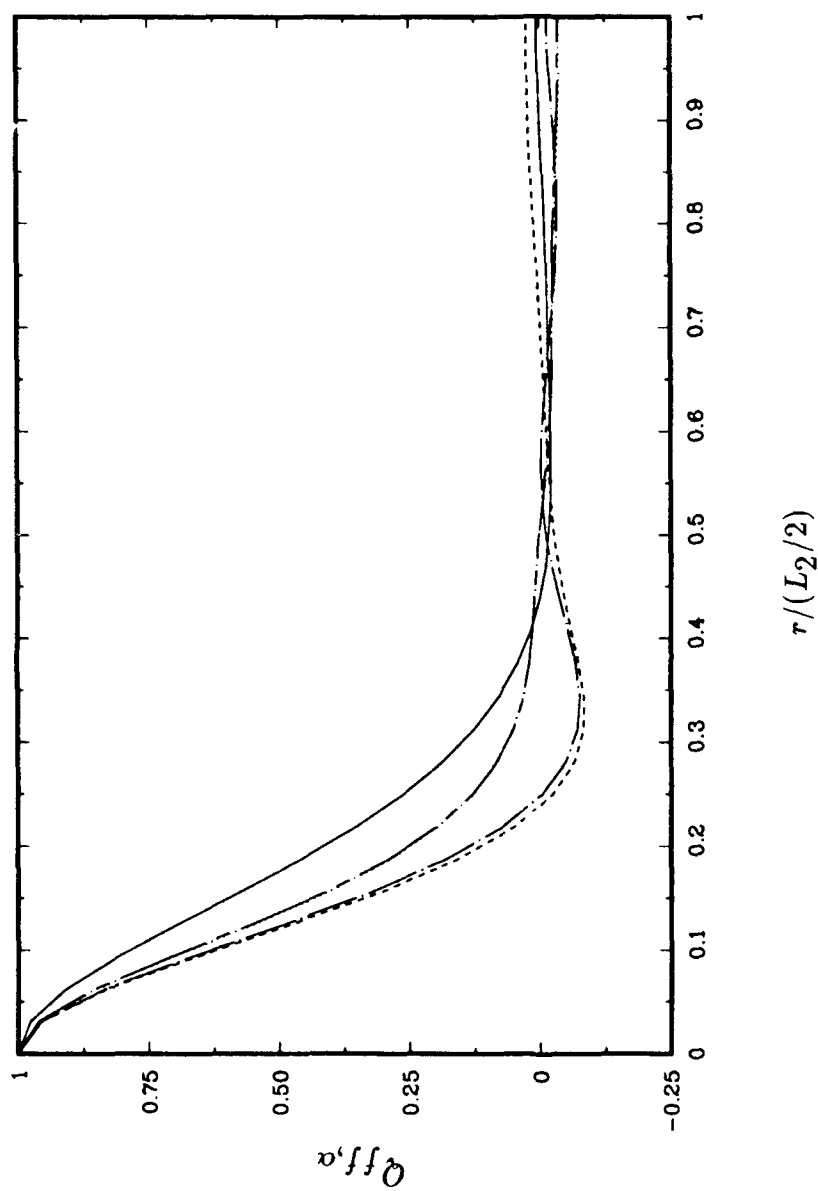


FIGURE 4.5. Two point correlations upstream of the shock wave ($k_0 x_1 = 9.07$) for case A, where the mean shock position is $k_0 x_1 = 12.6$: — $Q_{22,2}$, --- $Q_{11,2}$, $Q_{33,2}$, - · - · - $Q_{\rho\rho,2}$, - - - - $Q_{pp,2}$.

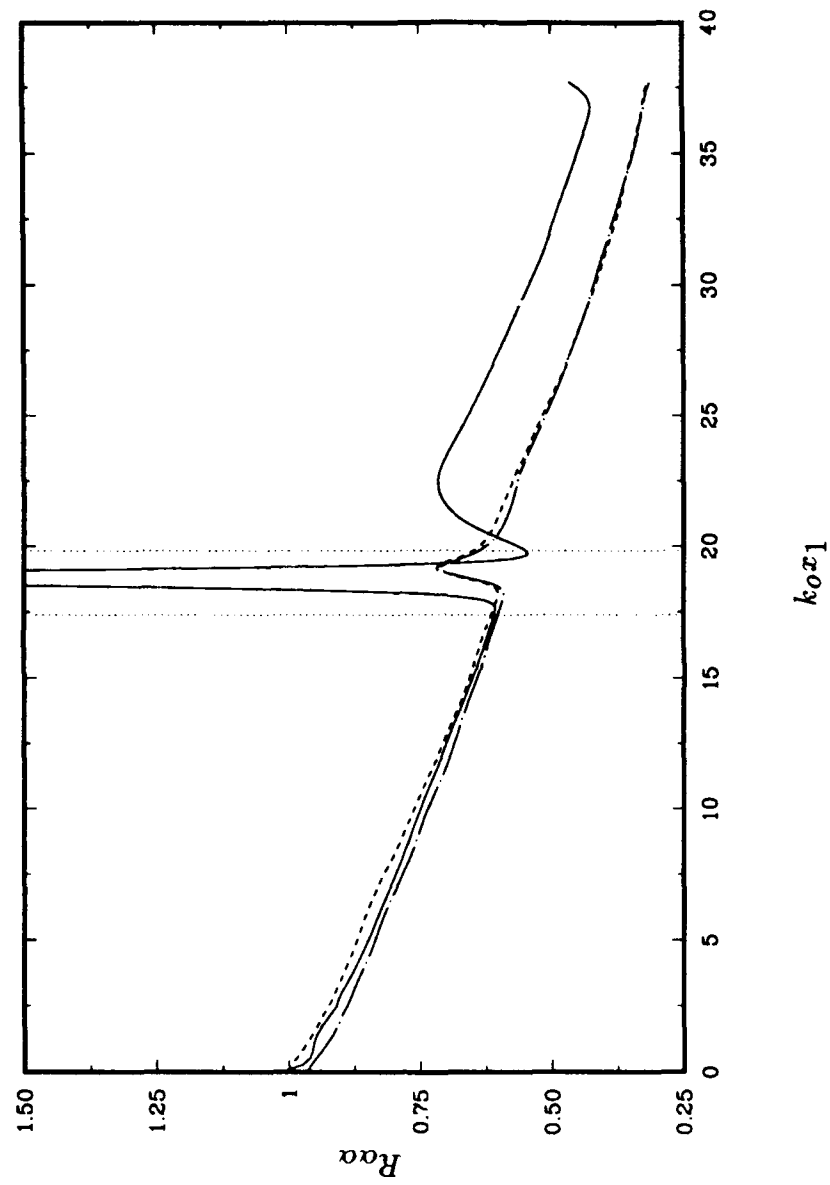


FIGURE 4.6. Evolution of the normal components of the Reynolds stress tensor, $R_{\alpha\alpha}$ for case C: — R_{11} , --- R_{22} , - · - R_{33} . (Vertical dotted lines denote the boundaries of shock intermittency.)

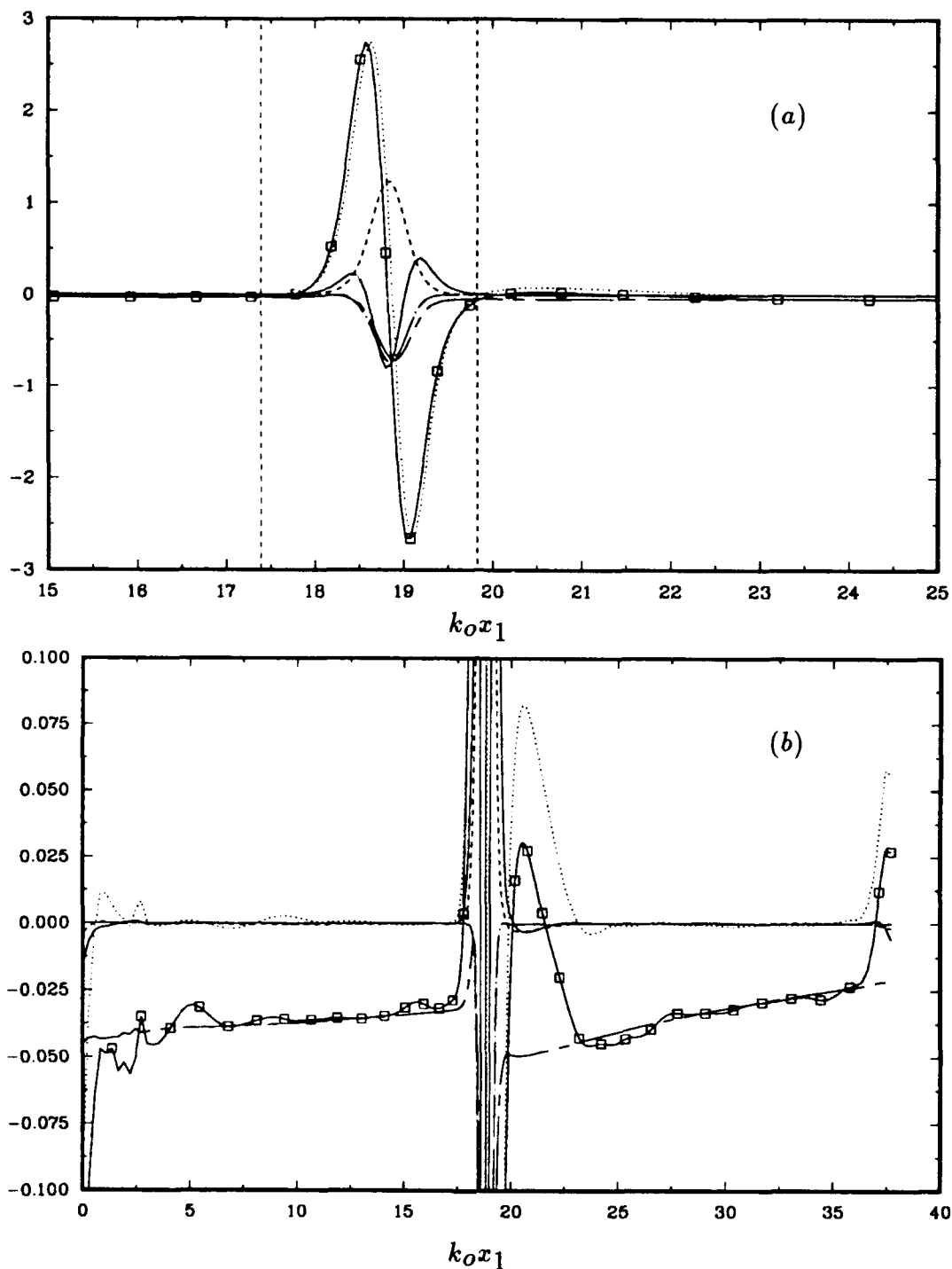


FIGURE 4.7. Budget of terms (scaled with $\rho_0 c_0 u_0^2 k_0$) in the turbulent kinetic energy transport equation for case C. (a) near the shock wave and (b) in the entire domain: —□— convection(I), ---- production by the mean strain(II), —·— production by mass flux fluctuation(III), pressure work(IV), —— turbulent transport(V), --- viscous dissipation and transport(VI). (Vertical dashed lines denote the boundaries of shock intermittency.)

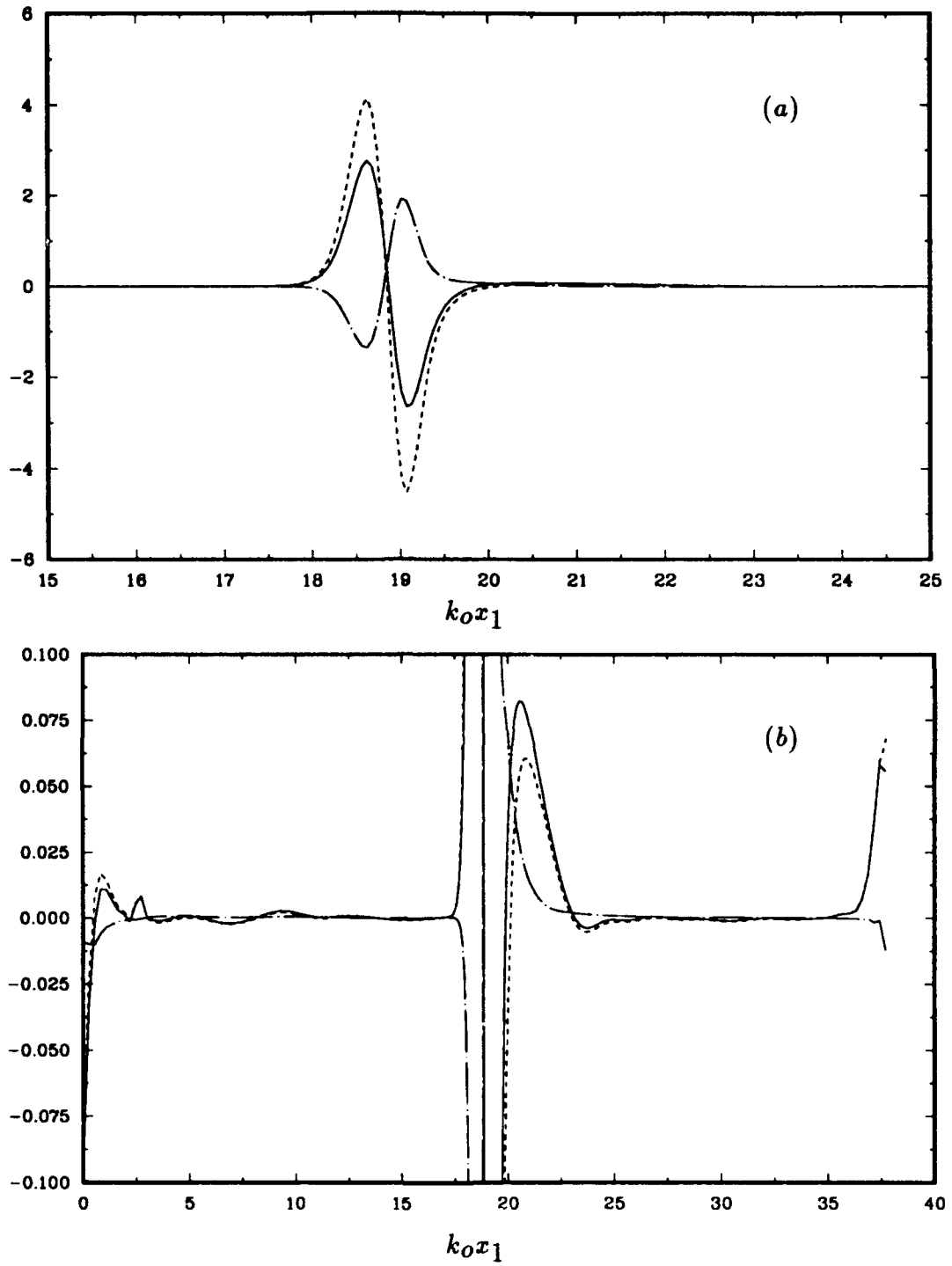


FIGURE 4.8. Decomposition of the pressure work term (scaled with $\rho_0 c_0 u_0^2 k_0$) for case C. (a) near the shock wave and (b) in the entire domain: — $-\overline{p'_{,i} u''_i}$, ---- $-(\overline{p' u''})_{,i}$, -.- $+\overline{p' u''}_{,i}$.

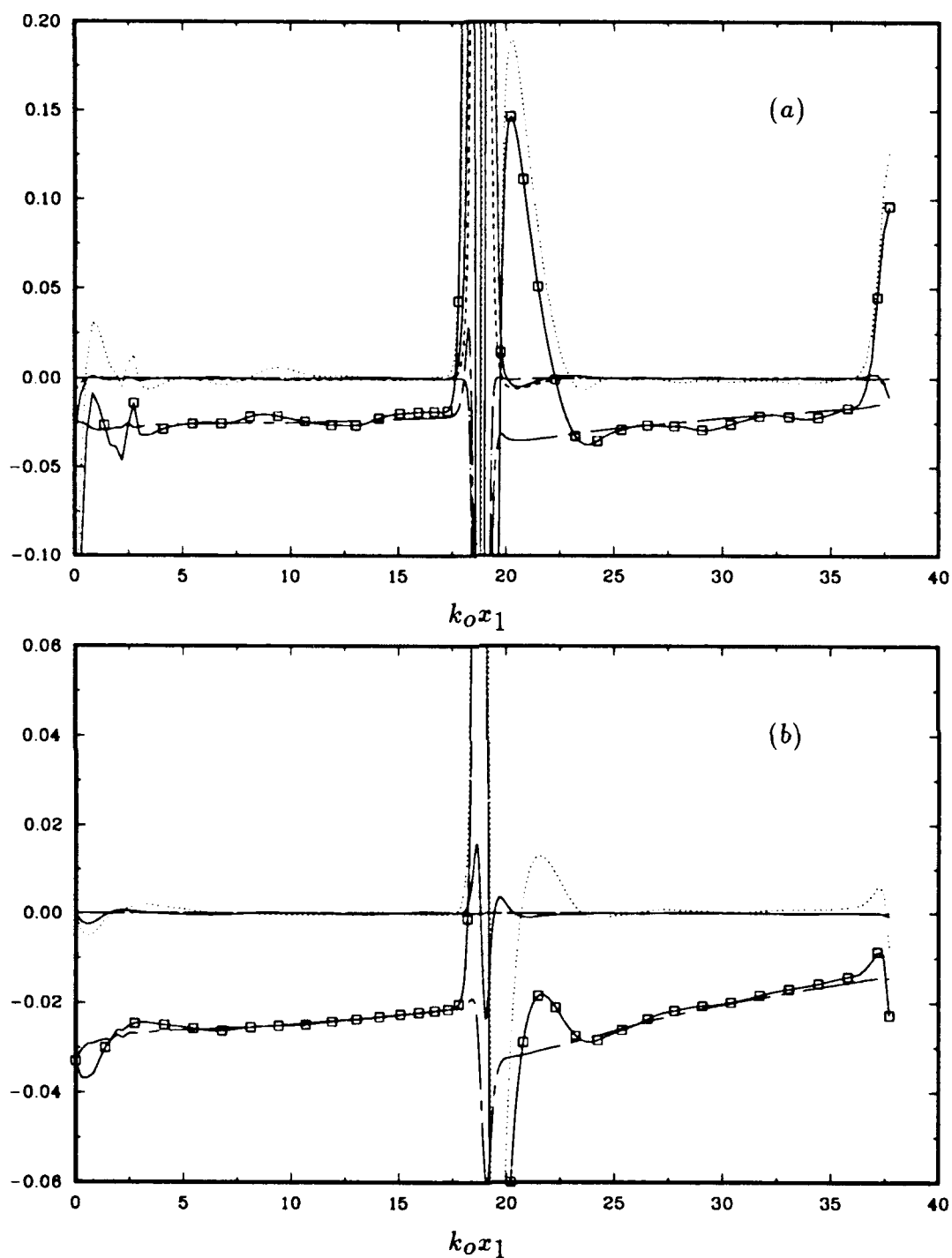


FIGURE 4.9. Budget of terms (scaled with $\rho_0 c_0 u_0^2 k_0$) in the transport equation of Reynolds stresses, (a) R_{11} and (b) R_{22} , for case C: \square — convection(I), ---- production by the mean strain(II), —·— production by mass flux fluctuation(III), pressure work(IV), ——— turbulent transport(V), --- viscous dissipation and transport(VI).

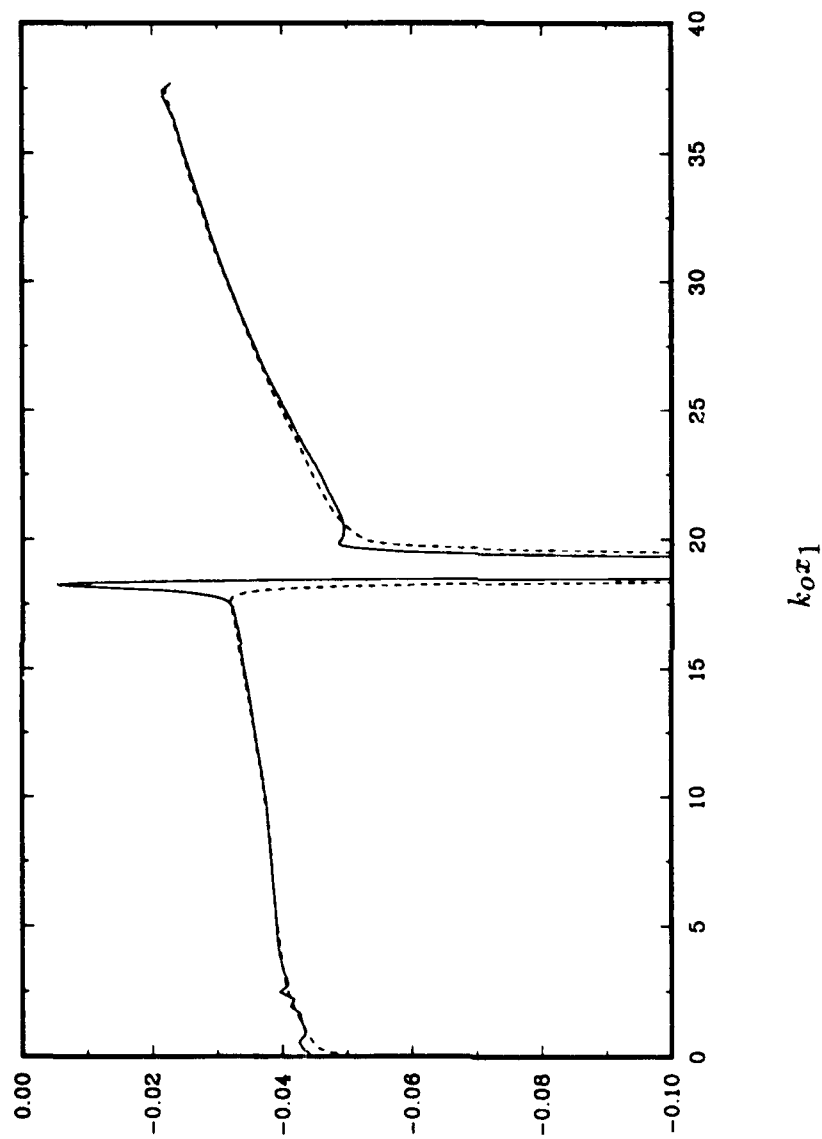


FIGURE 4.10. Approximation of the viscous term (scaled with $\rho_0 c_0 u_0^2 k_0$) for case C: — $-u''_i \tau_{ik,k}$, ---- $-\overline{\mu \left(\overline{\omega'_i \omega'_i} + \frac{4}{3} \overline{\theta'^2} \right)}$.

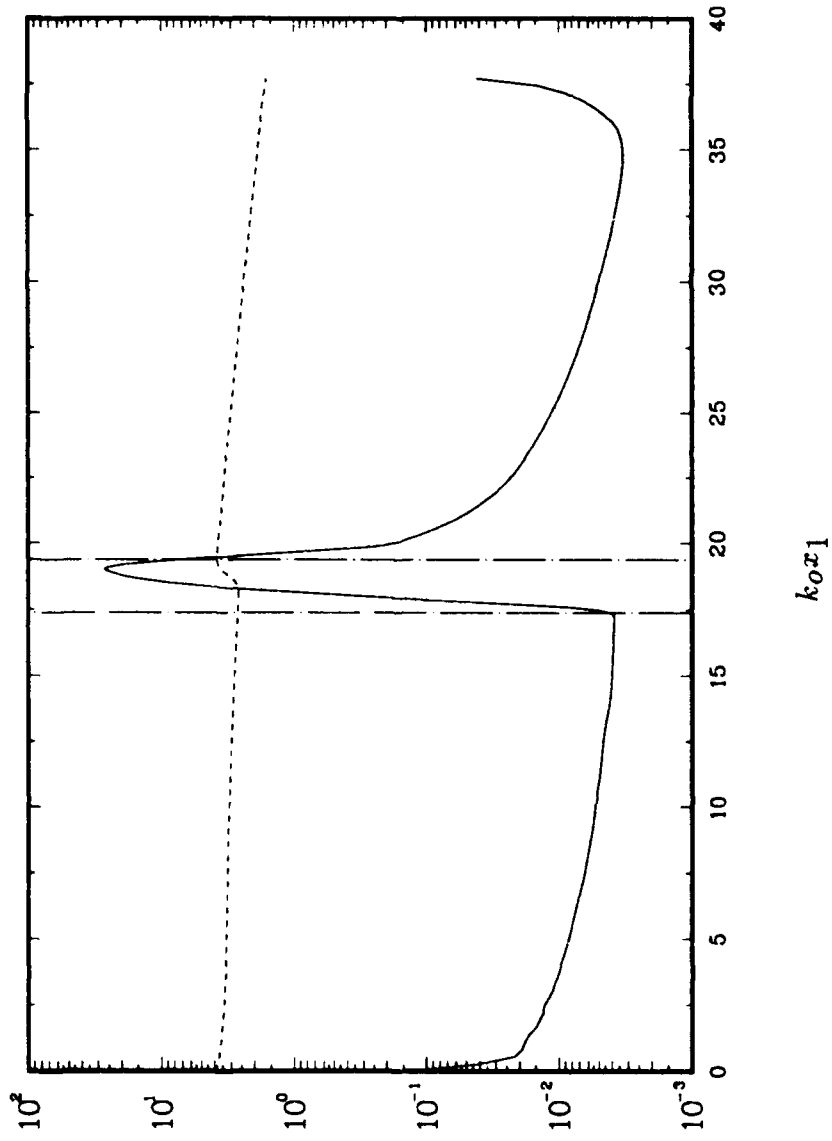


FIGURE 4.11. Variances of dilatation and vorticity for case C: — $\overline{u'_{i,i}{}^2}/(u_0 k_0)^2$, --- $\overline{\omega'_i \omega'_i}/(u_0 k_0)^2$. (Vertical lines denote the boundaries of shock intermittency.)

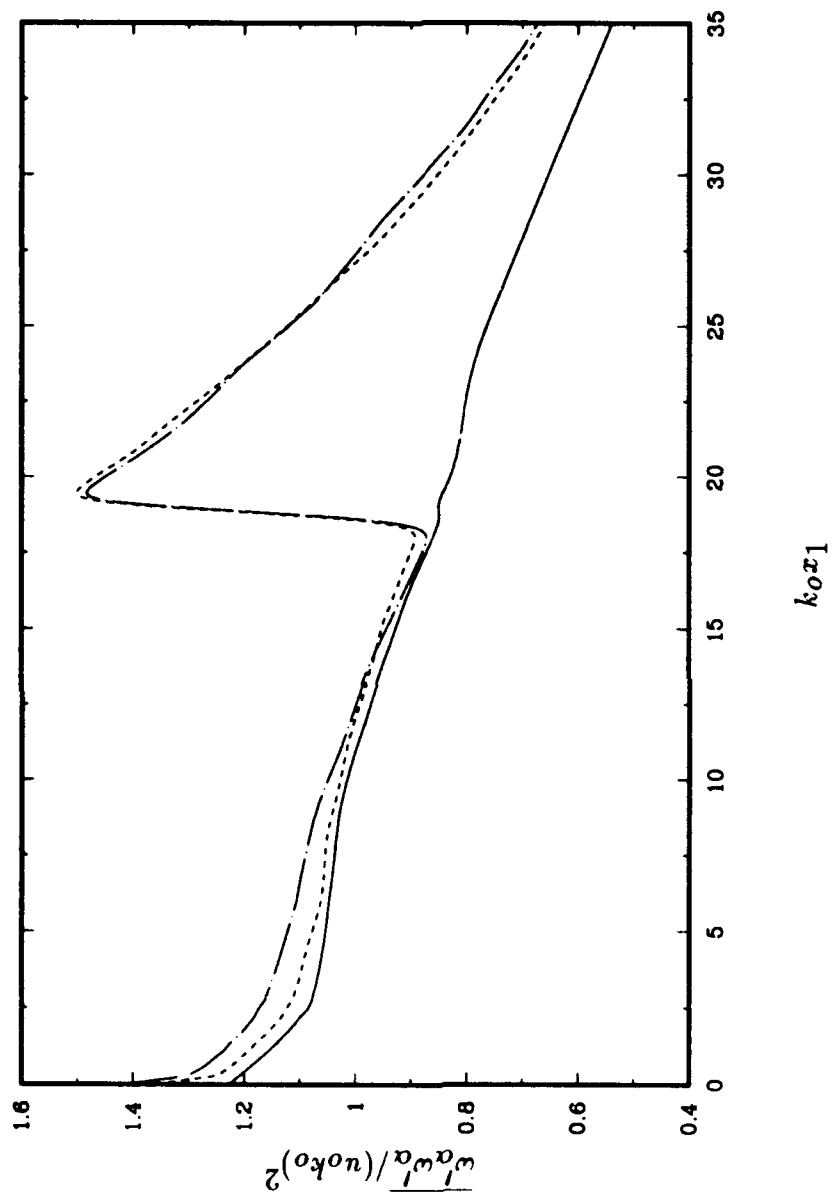


FIGURE 4.12. Evolution of components of vorticity for case C ($Re_T = 84.8$): — ω_1 , ---- ω_2 , - · - ω_3 .

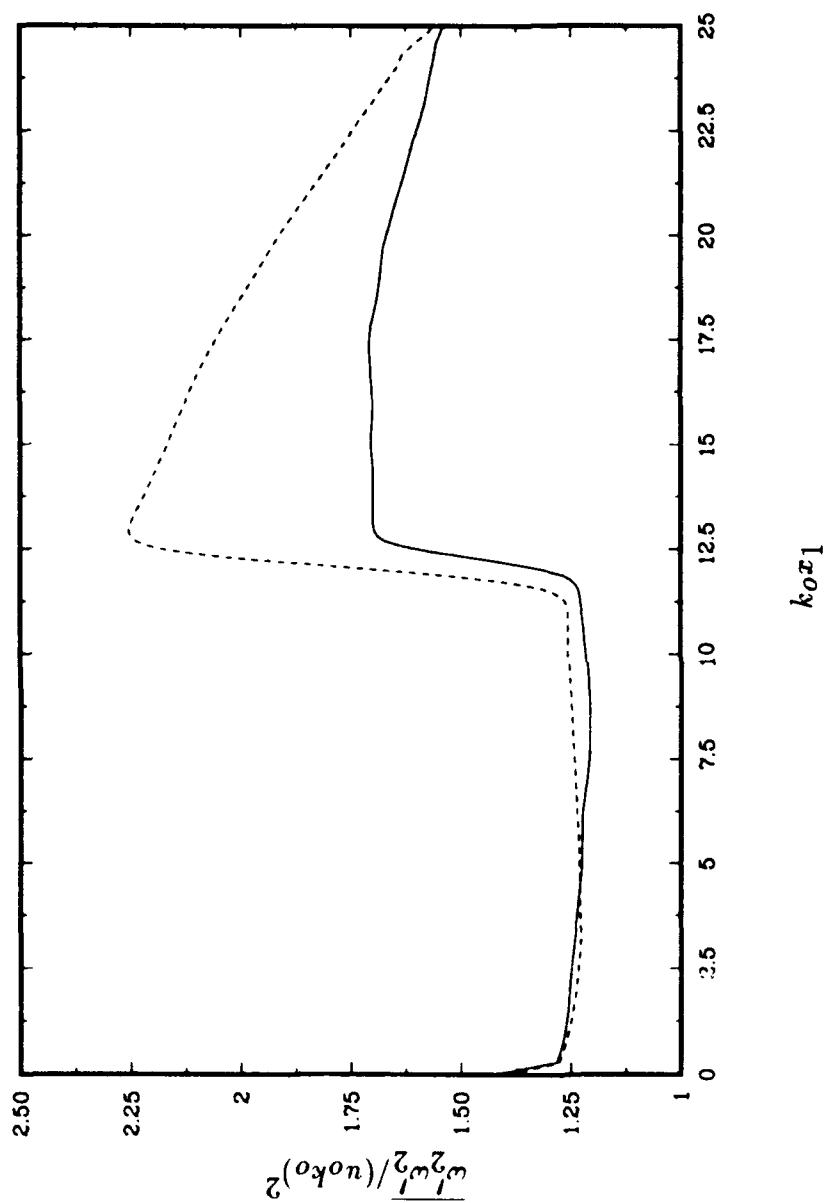


FIGURE 4.13. Evolution of a transverse component of vorticity for different shock strengths: — $M_1^U = 1.10$ (case E), ---- $M_1^U = 1.20$ (case A).

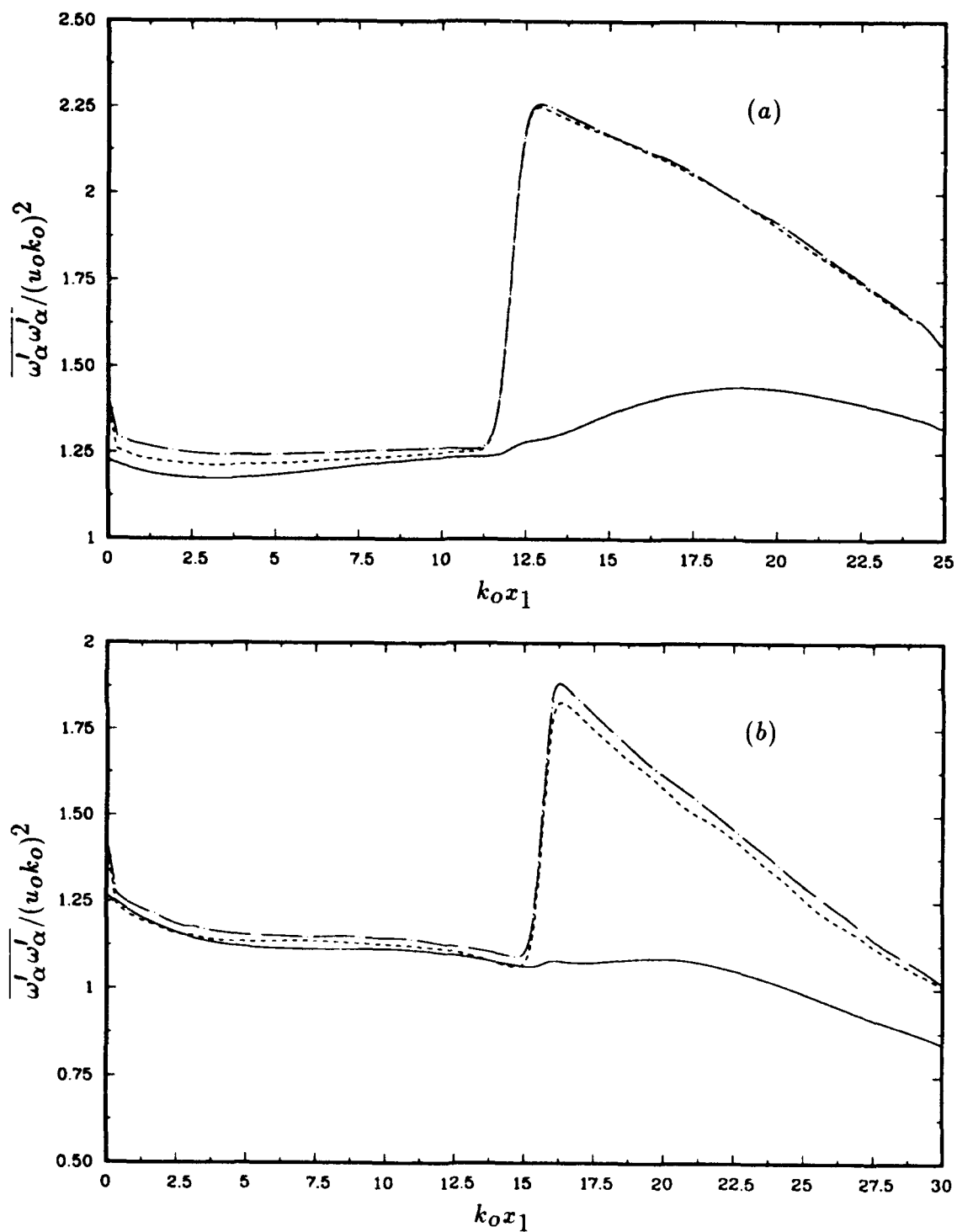


FIGURE 4.14. Evolution of vorticity for different turbulence Reynolds numbers, (a) $Re_T = 240$ (case A) and (b) $Re_T = 133$ (case B): — ω_1 , ---- ω_2 , - - - ω_3 .

(c)

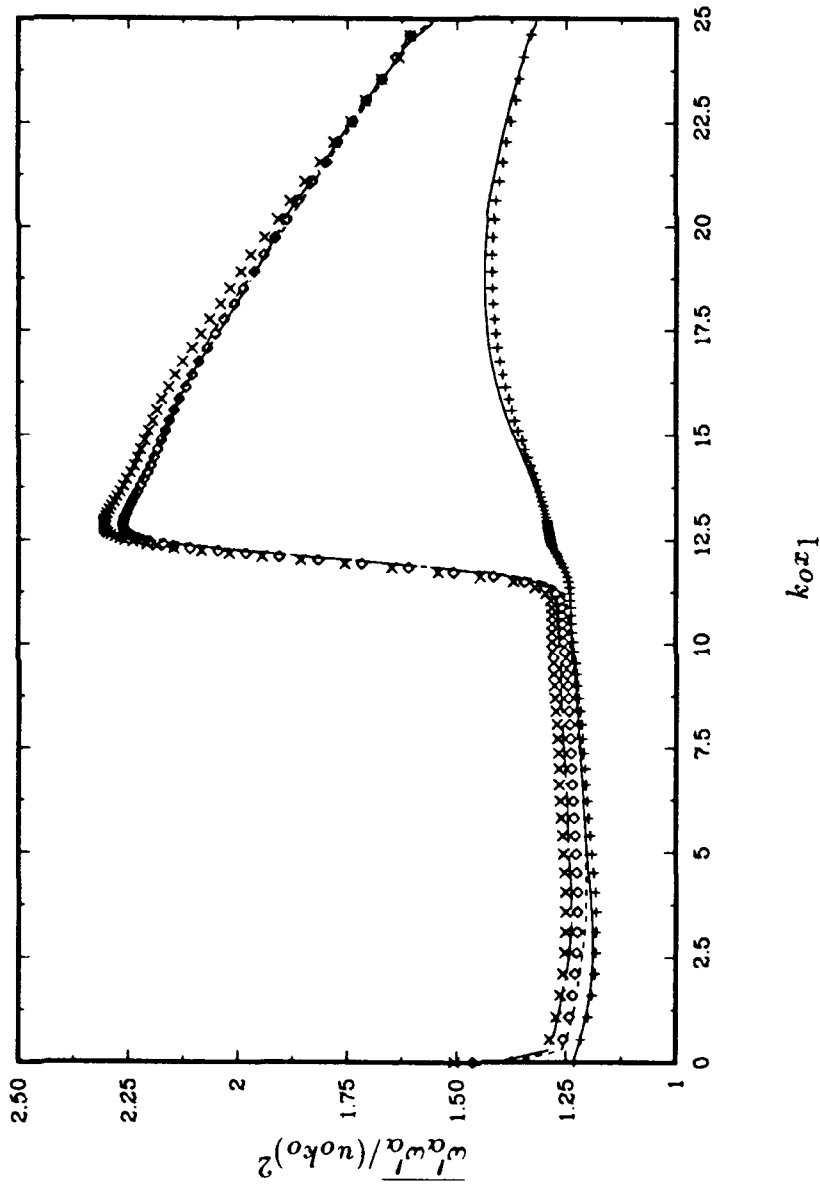


FIGURE 4.14(c). Comparison of vorticity evolutions for $Re_T = 240$: lines from the simulation with $129 \times 64 \times 64$ — ω_1 , - - - ω_2 , — ω_3 ; symbols from the simulation with $97 \times 48 \times 48 + \omega_1$, $\times \omega_2$, $\diamond \omega_3$.

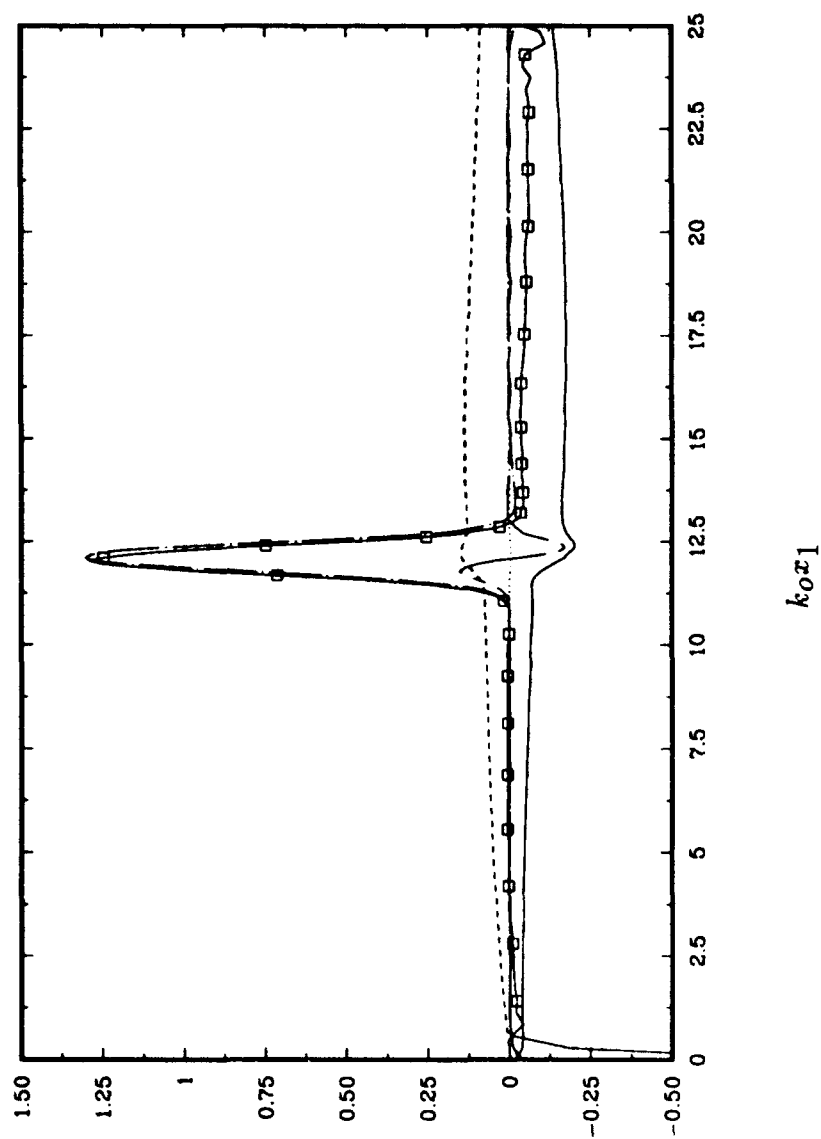


FIGURE 4.15. Budget of terms (scaled with cou_o^2/k_o) in the transport equation of $\overline{\omega_2'^2}$ for case A: \square — convection(I), - - - stretching(II+III), — · — baroclinic torque(VI), viscous dissipation and transport(VIII), ——— vorticity-dilatation(IV+V), ——— turbulent transport(VII).

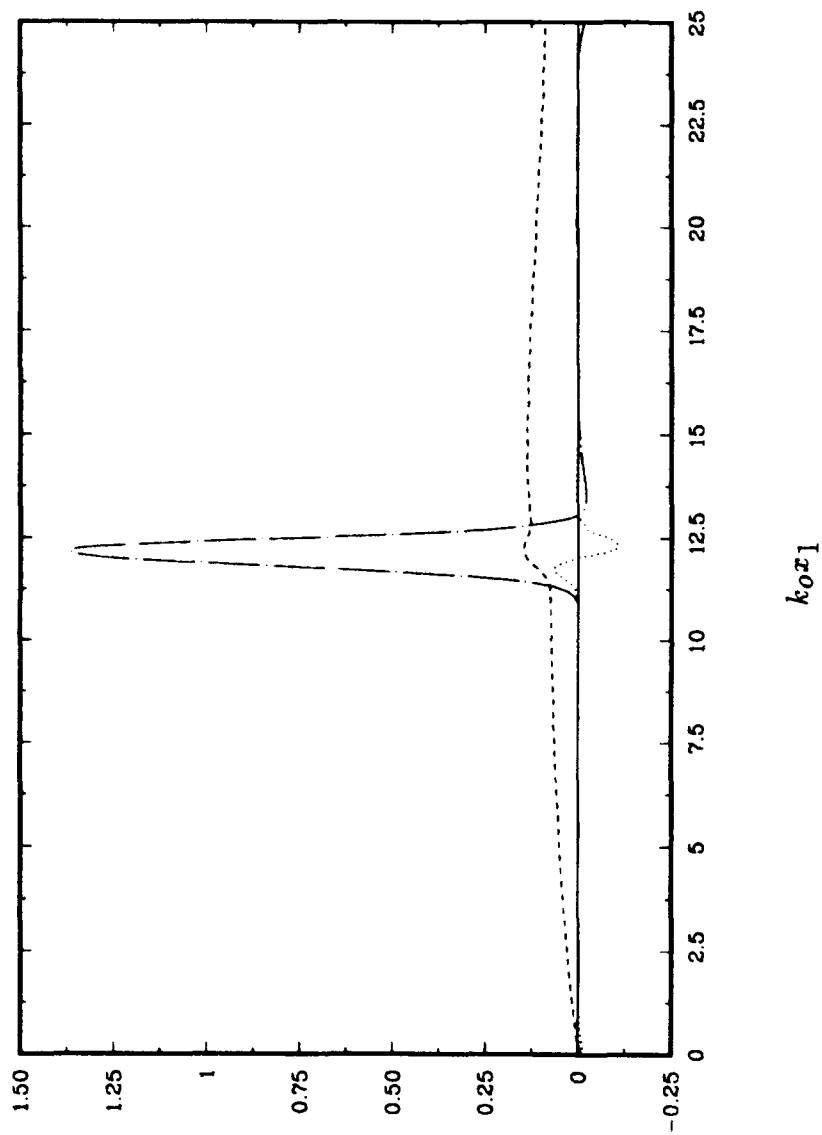


FIGURE 4.16. Production of vorticity by the mean and turbulent strain rates (scaled with $c_0 u_0^2 / k_0$) in the transport equation of $\overline{\omega'^2_2}$ for case A: — stretching by the mean flow(II), --- stretching by the turbulence(III), — · — compression by the mean flow(IV), compression by the turbulence(V).

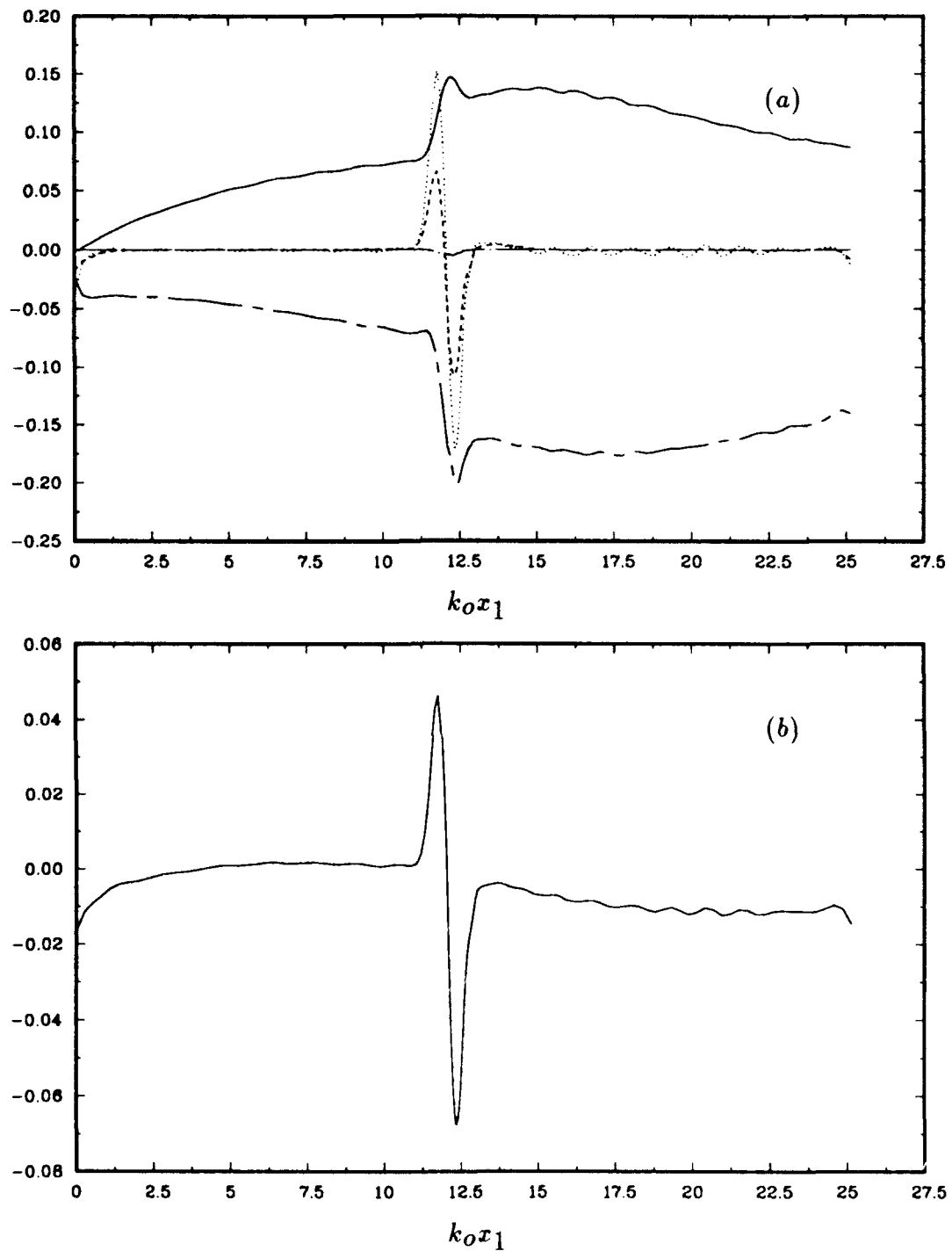


FIGURE 4.17. Individual (a) and total effects (b) of nonlinear terms (scaled with $c_0 u_0^2 k_0$) in the transport equation of $\overline{\omega_2'^2}$ for case A. In Figure 4.17(a): — stretching(III), ---- vorticity-compression(V), - · - baroclinic torque(VI), transport(VII), - - - viscous dissipation and transport(VIII).

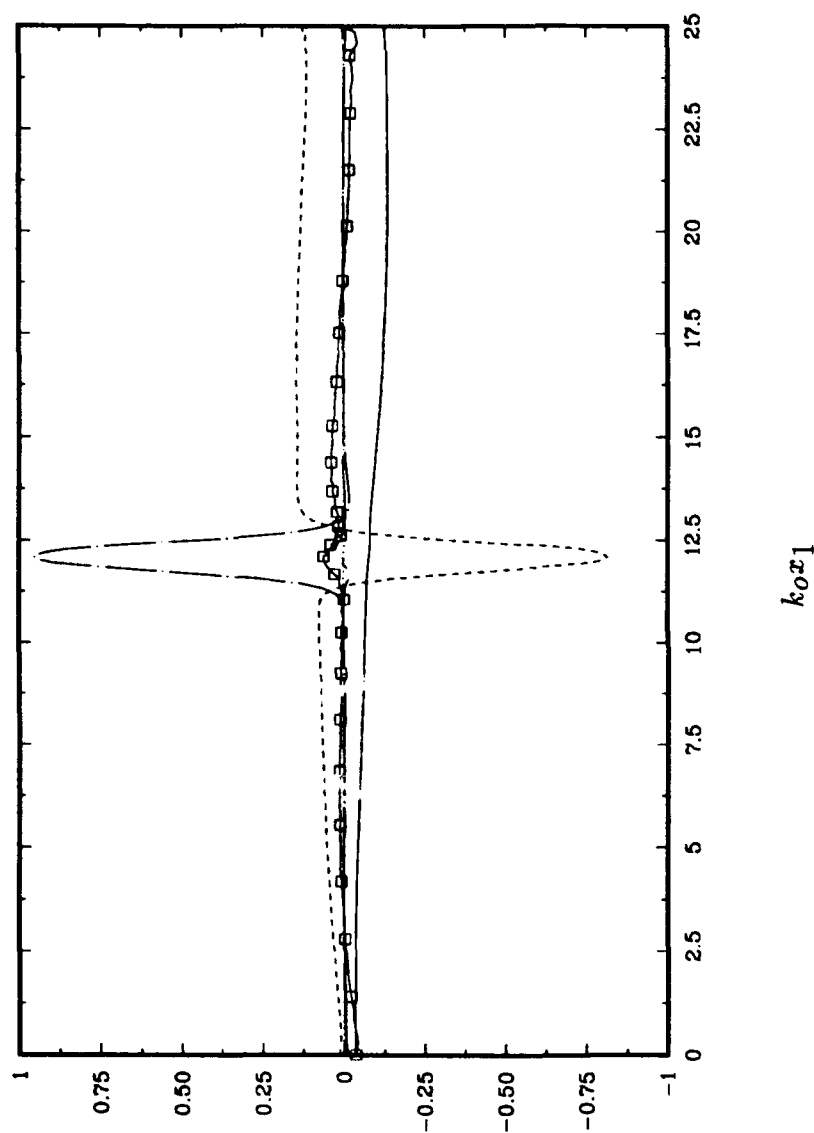


FIGURE 4.18. Budget of terms (scaled with cou_0^2/k_0) in the transport equation of $\omega_1'^2$ for case A, $Re_T = 240$: — convection(I), - - - stretching(II+III), — · — vorticity-compression(IV+V), baroclinic torque(VI), - - - - turbulent transport(VII), ——— viscous dissipation and transport(VIII).

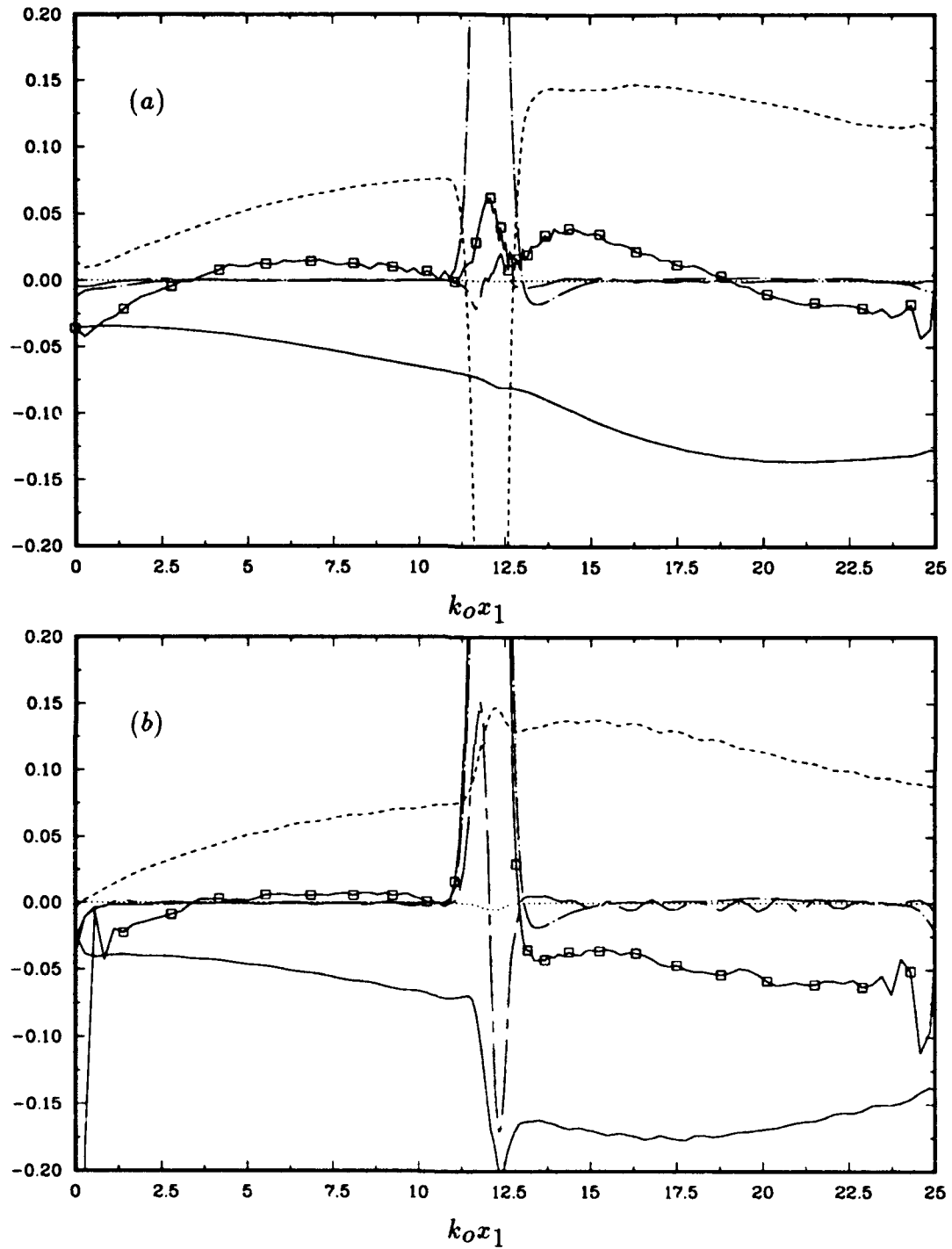


FIGURE 4.19. Budget of terms (scaled with $cou_0^2 k_0$) in the transport equation of (a) $\overline{\omega_1'^2}$ ($Re_T = 240$), (b) $\overline{\omega_2'^2}$ ($Re_T = 240$), (c) $\overline{\omega_1'^2}$ ($Re_T = 84.8$), and (d) $\overline{\omega_2'^2}$ ($Re_T = 84.8$): \square — convection(I), ---- stretching(II+III), — vorticity-compression(IV+V), baroclinic torque(VI), --- turbulent transport(VII), — viscous dissipation and transport(VIII).

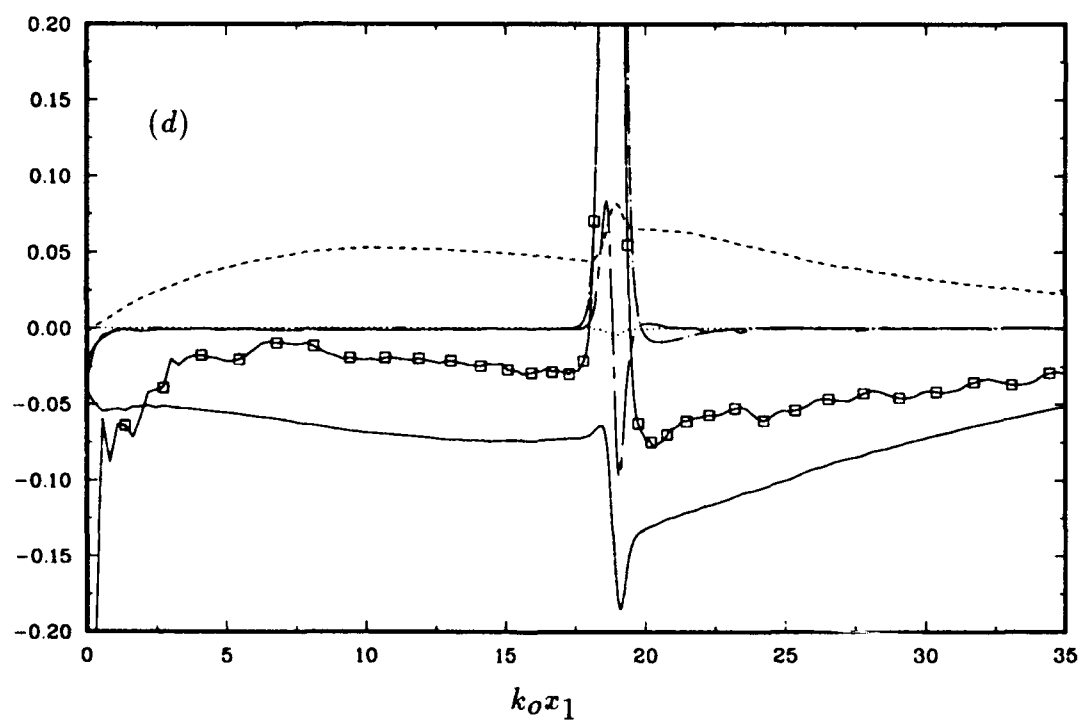
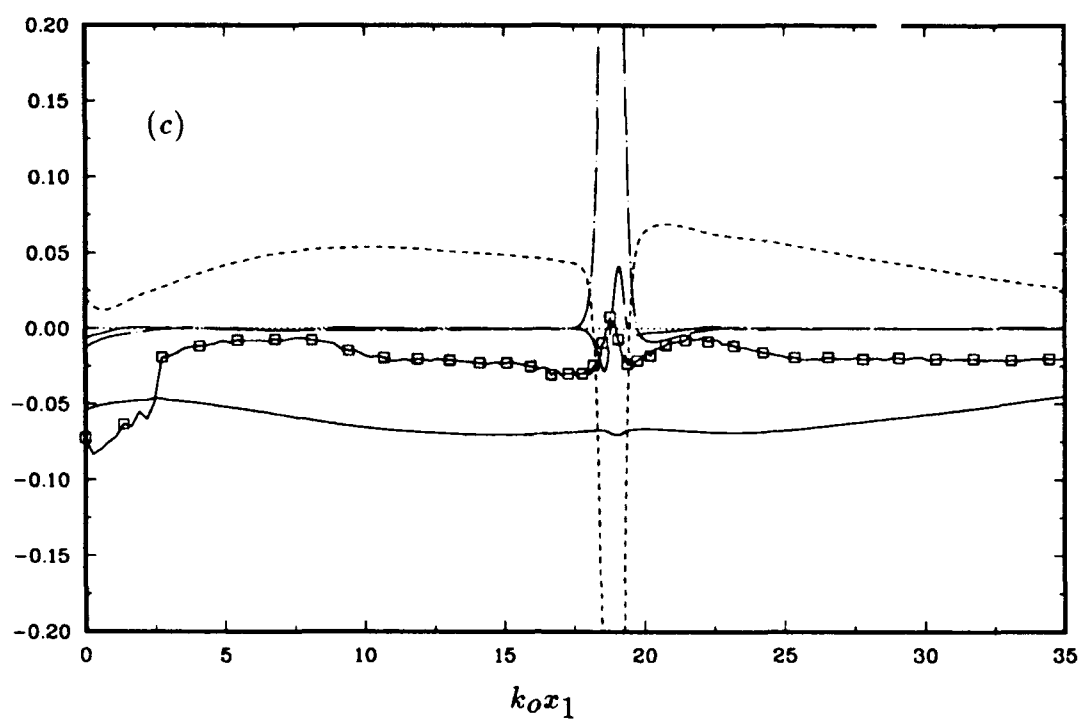


FIGURE 4.19. continued.

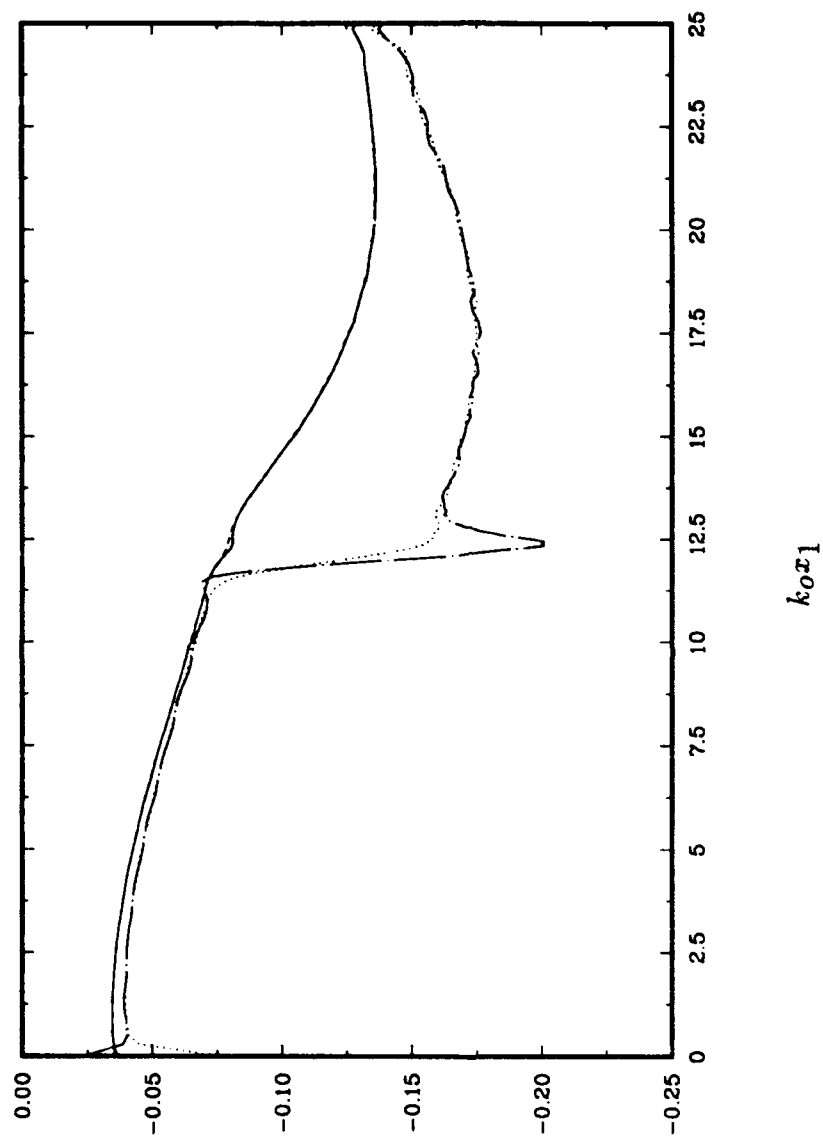


FIGURE 4.20. Approximation of the viscous term by the homogeneous dissipation (scaled with $c_0 u_0^2 / k_0$) in transport equations of $\omega_1'^2$ and $\omega_2'^2$ for case A: — Φ_1 , --- Φ_1^H , - · - Φ_2 , Φ_2^H .

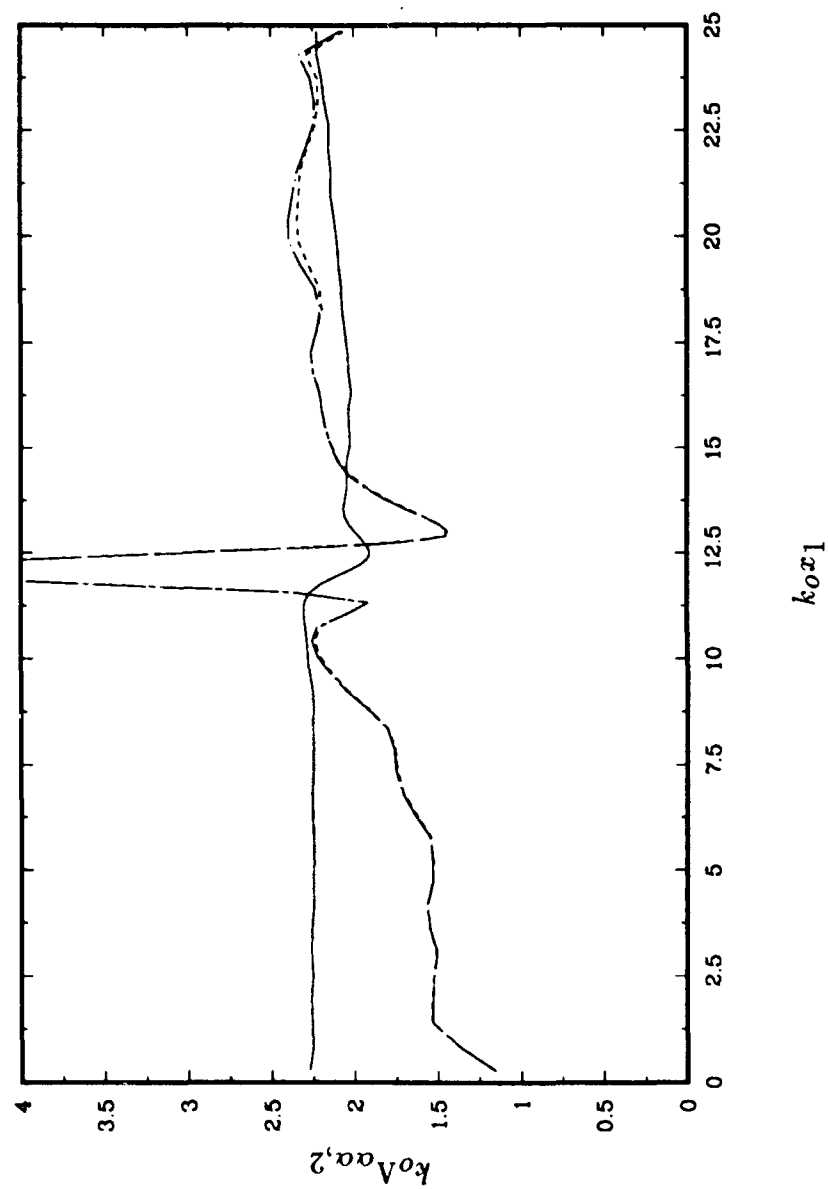


FIGURE 4.21. Evolution of integral scales defined in (4.7) for case A: — $\Lambda_{22,2}$, --- $\Lambda_{pp,2}$, — · — $\Lambda_{\rho\rho,2}$.

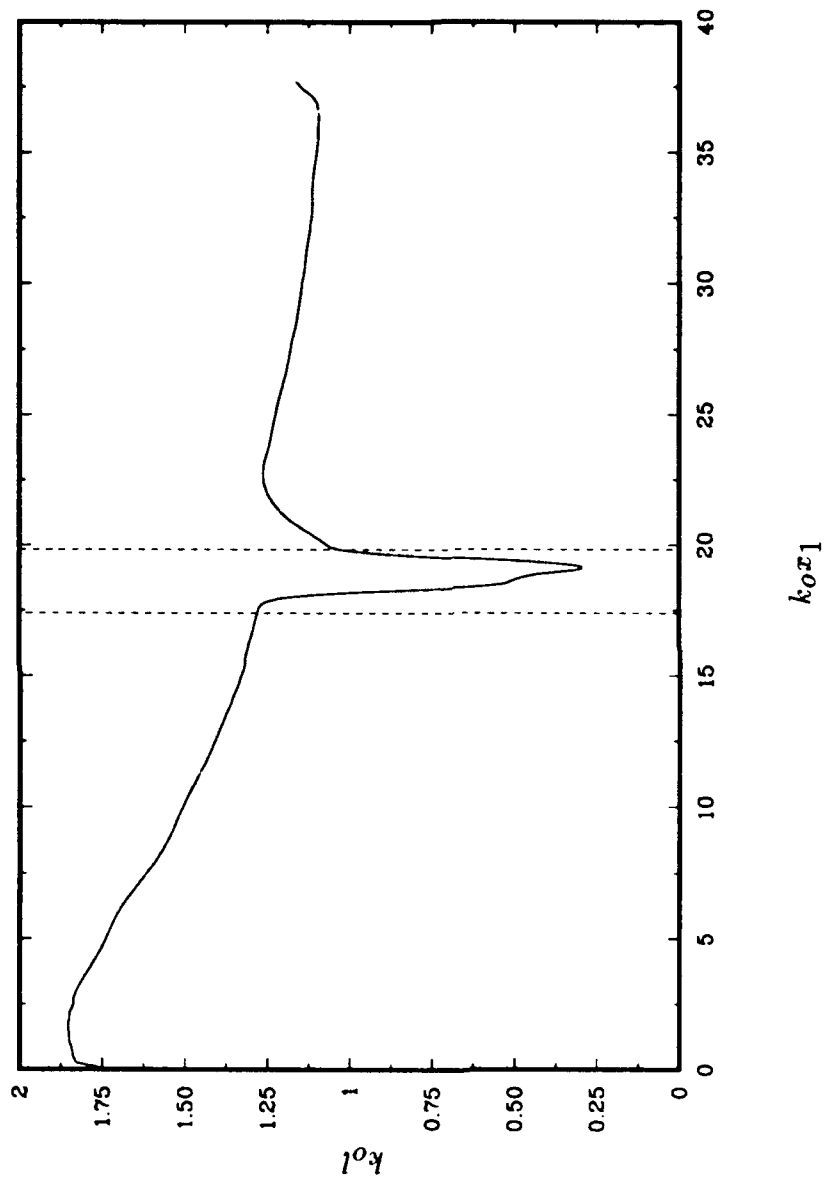


FIGURE 4.22. Evolution of the turbulence length scale defined in (4.17) for case C. (Vertical lines denote the boundaries of shock intermittency.)

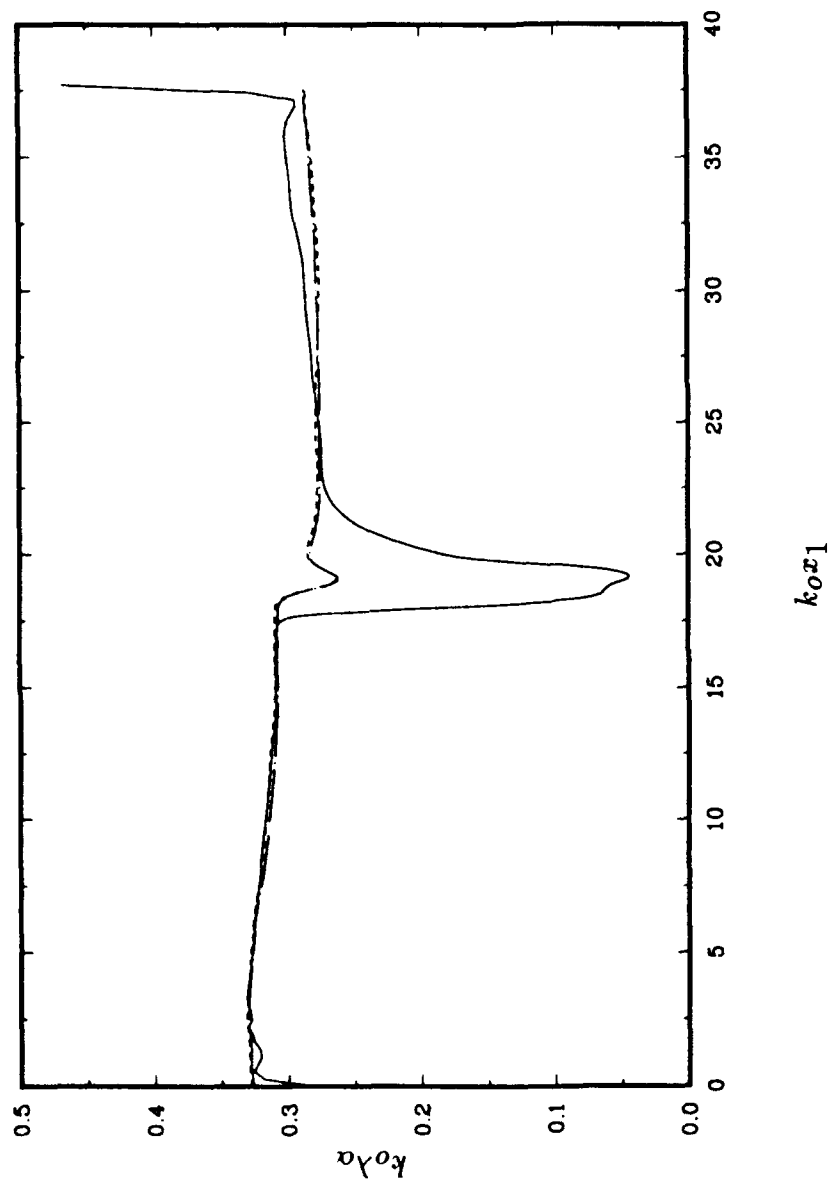


FIGURE 4.23. Evolution of Taylor microscale for case C: — λ_1 , ---- λ_2 , - · - λ_3 .

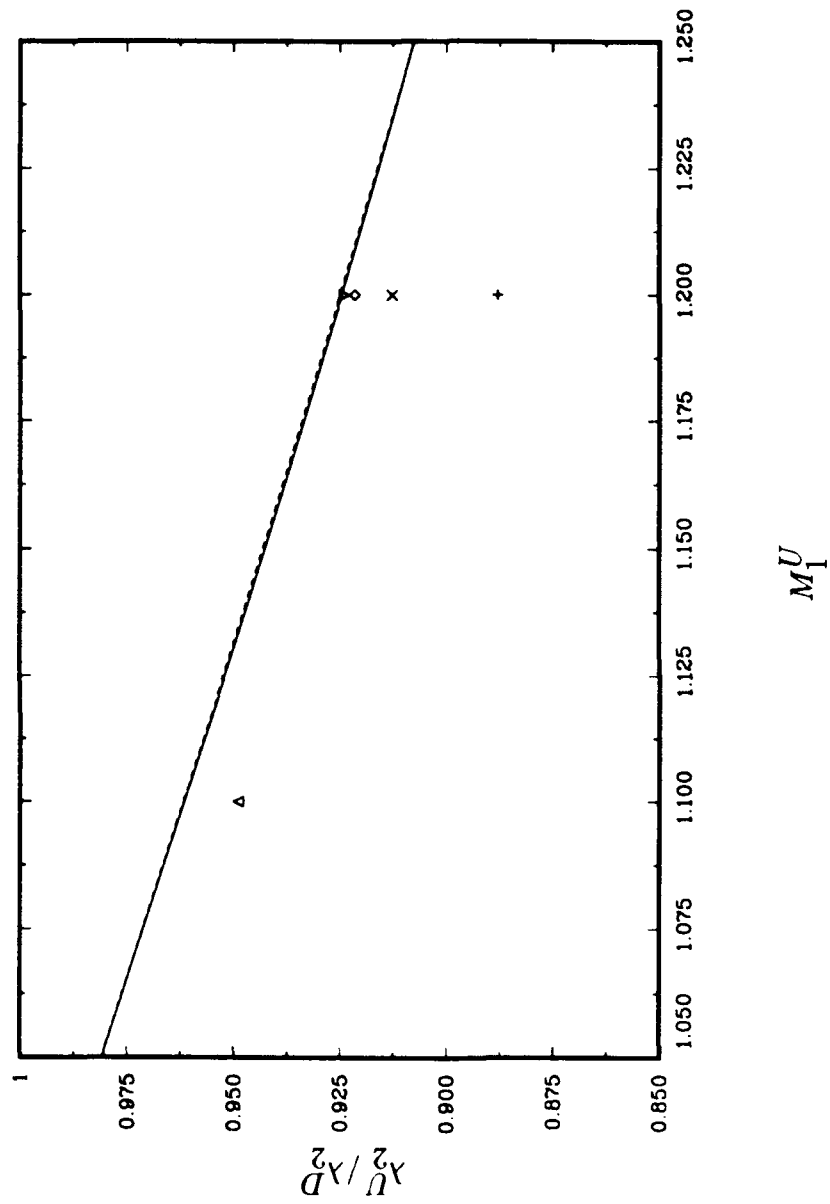


FIGURE 4.24. Comparison of the transverse Taylor microscale change across the shock wave with linear predictions:
 — LIA, --- RDT, + case A, x case B, \diamond case C, v case D, \triangle case E.

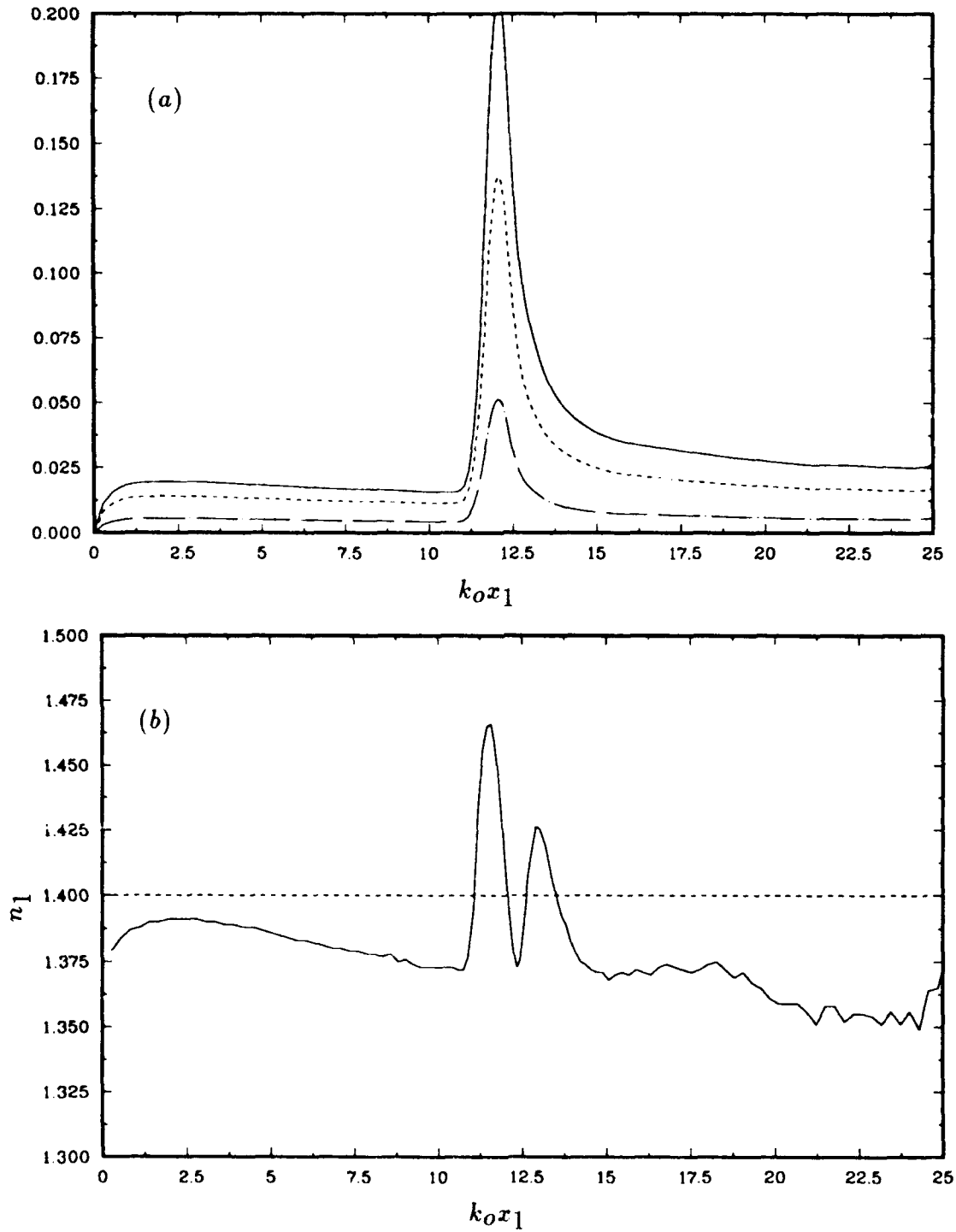


FIGURE 4.25. Evolutions of (a) rms values of thermodynamic properties and (b) the polytropic exponent n_1 for case A. For (a): — p_r/\bar{p}_{in} , ---- $\rho_r/\bar{\rho}_{in}$, — — T_r/\bar{T}_{in} .

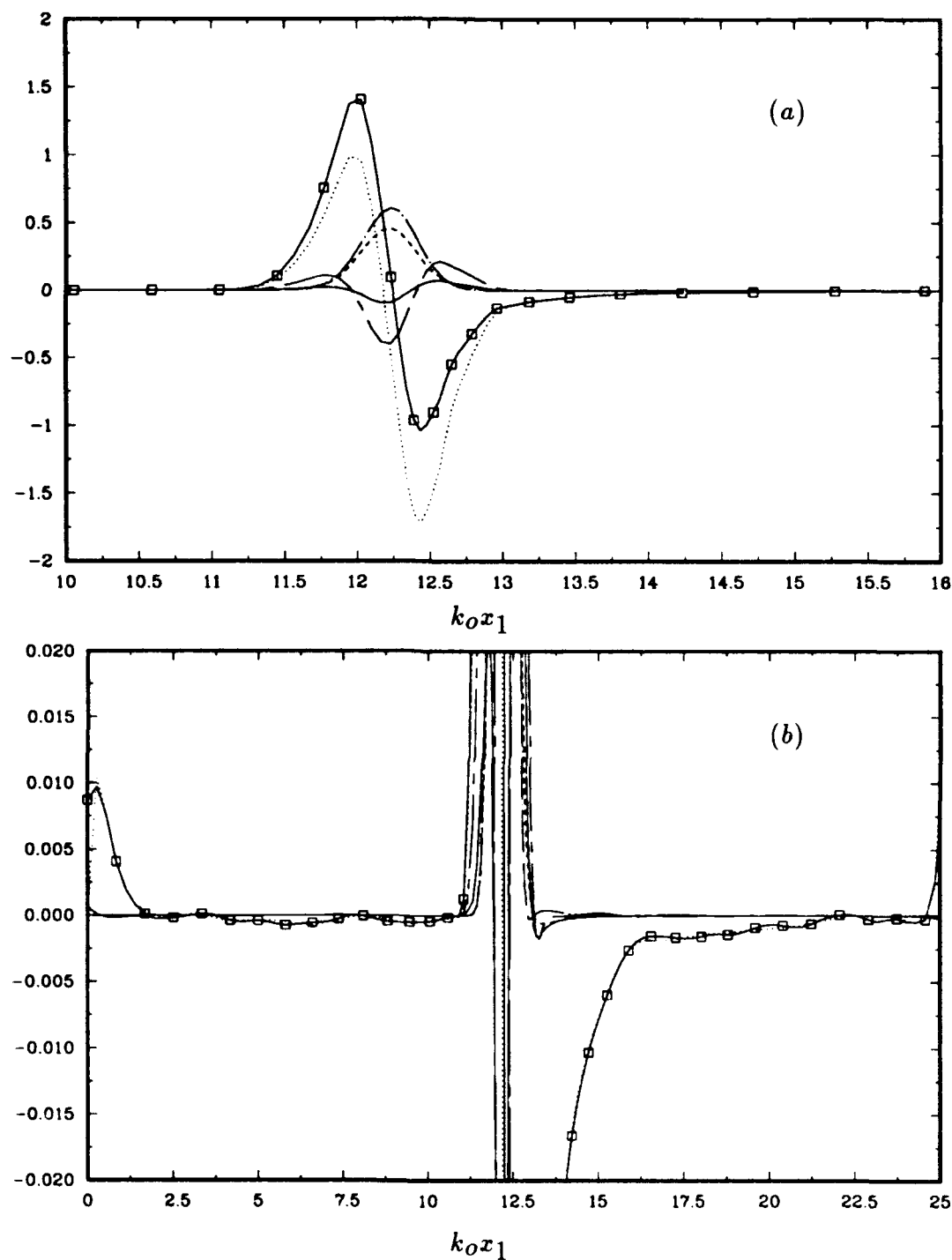


FIGURE 4.26. Budget of terms (scaled with $(\rho_0 M_t)^2 c_0 k_0$) in the transport equation of $\overline{\rho'^2}$ for case A: (a) in the shock zone, (b) in the entire domain. —□— convection(I), ---- production by the mean dilatation(II), — · — production by the mean density gradient(III), turbulent density-dilatation correlation(IV), ——— turbulent density squared-dilatation correlation(V), --- turbulent transport(VI).

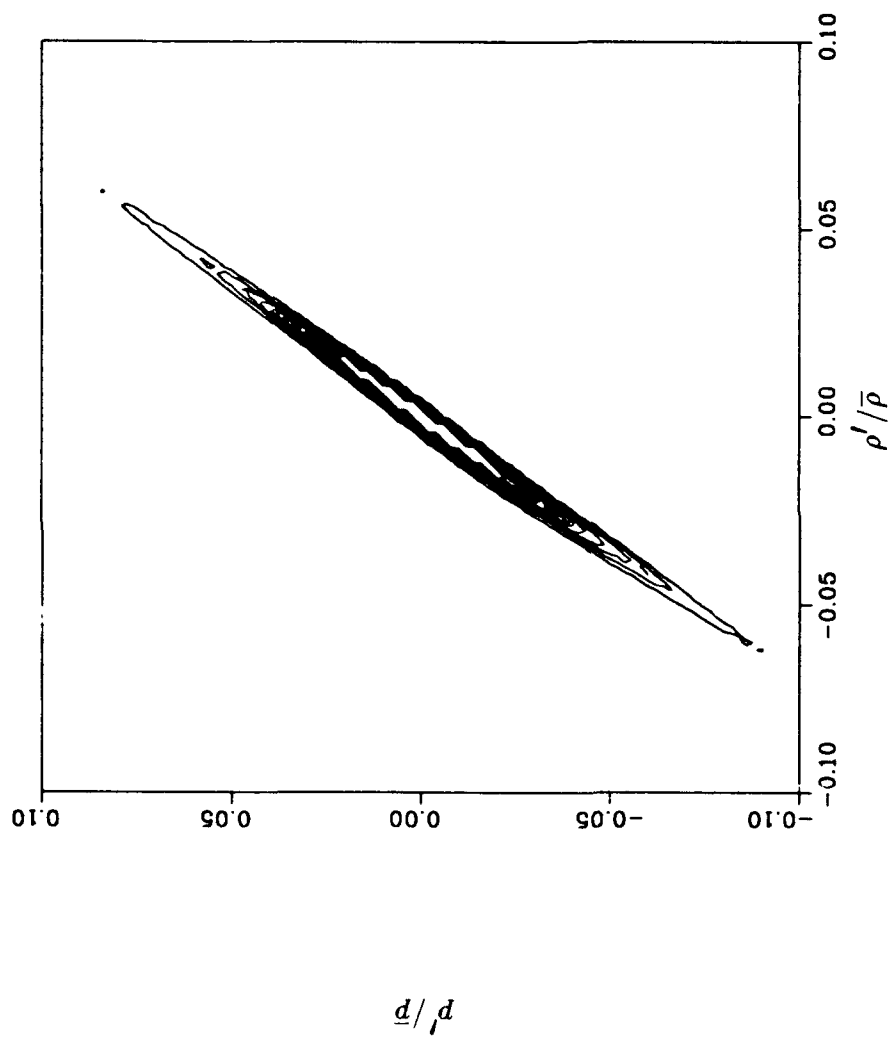


FIGURE 4.27. Joint probability function of scaled pressure and density fluctuations for case C.

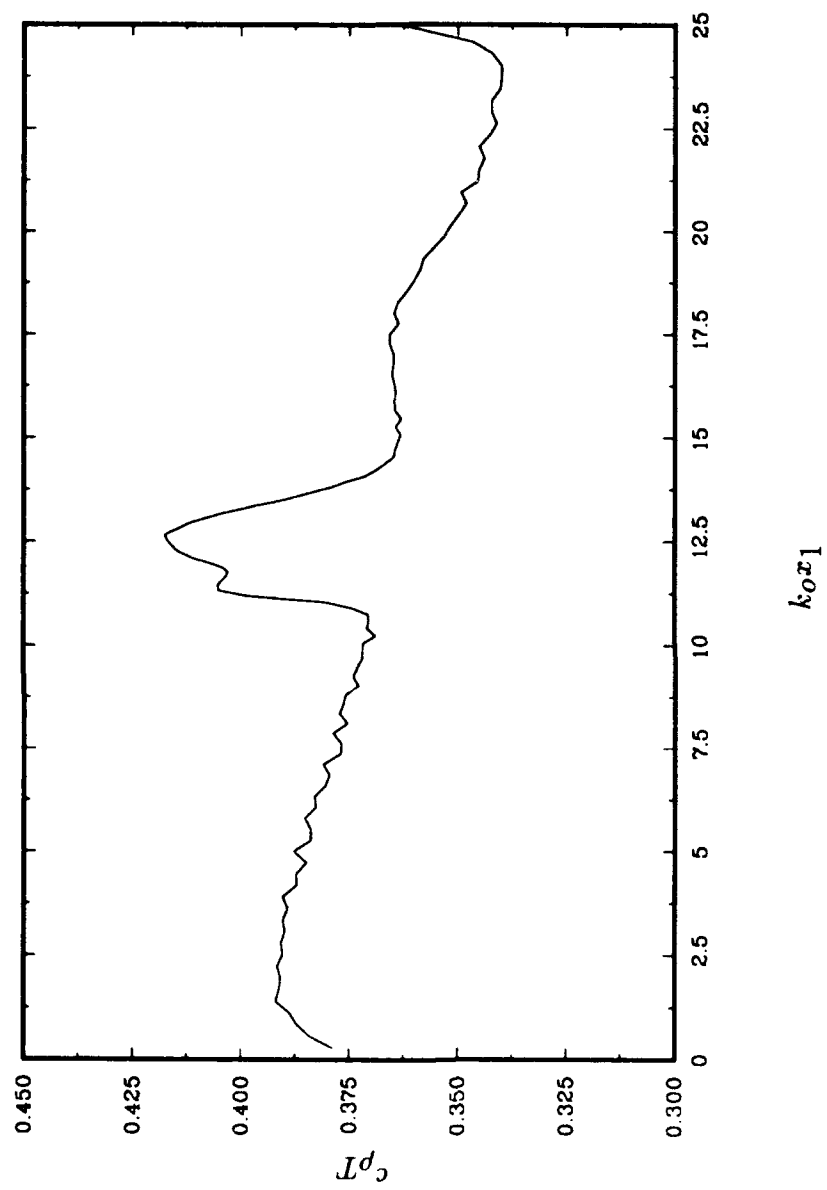


FIGURE 4.28. Evolution of the correlation coefficient $c_{\rho T}$ between density and temperature fluctuations for case A.

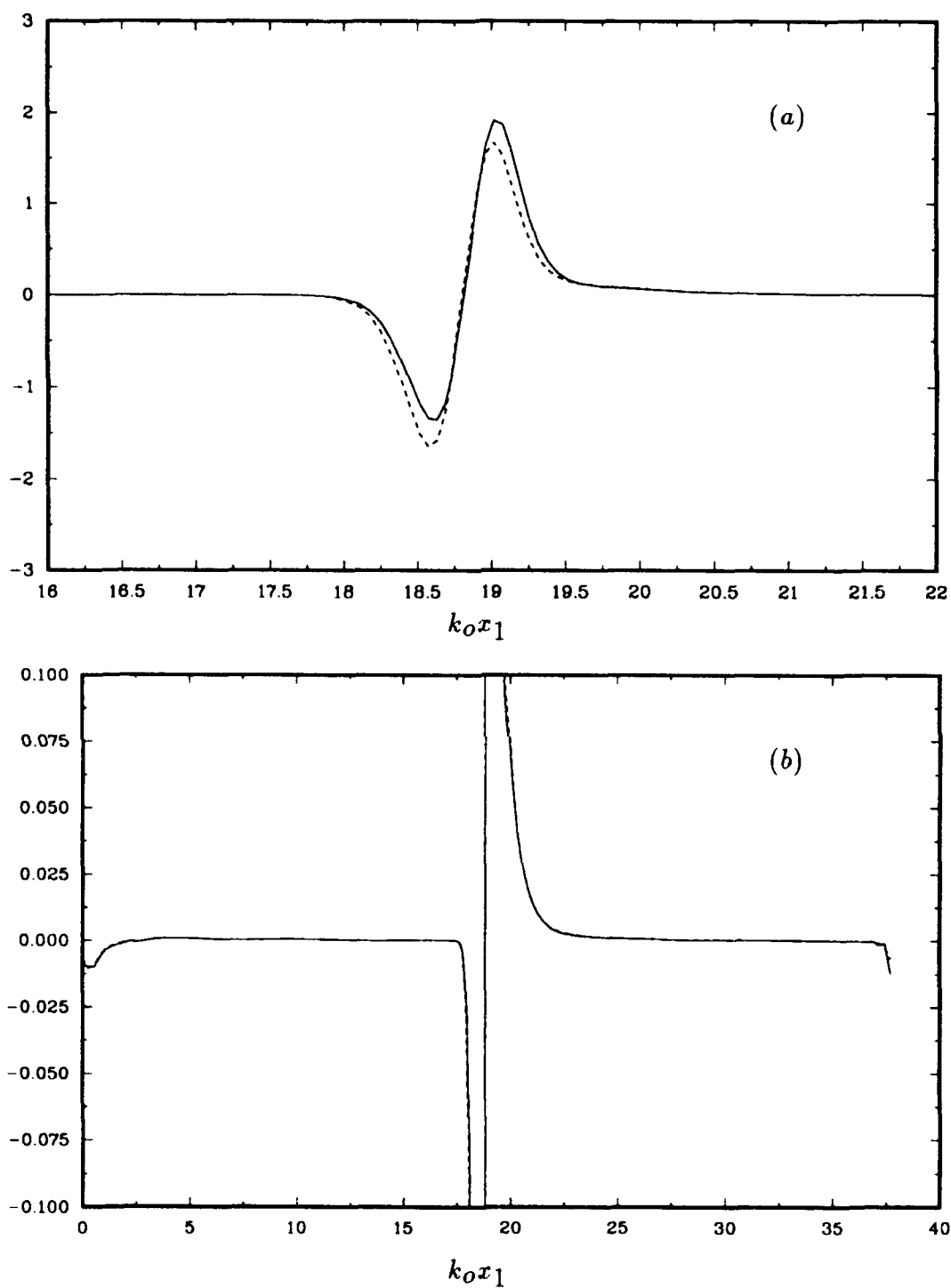


FIGURE 4.29. Evaluation of the Durbin and Zeman's [1991] modeling idea for $\overline{p'u''_{i,i}}$. (a) near the shock and (b) in the entire domain for case C: — LHS, ---- RHS.

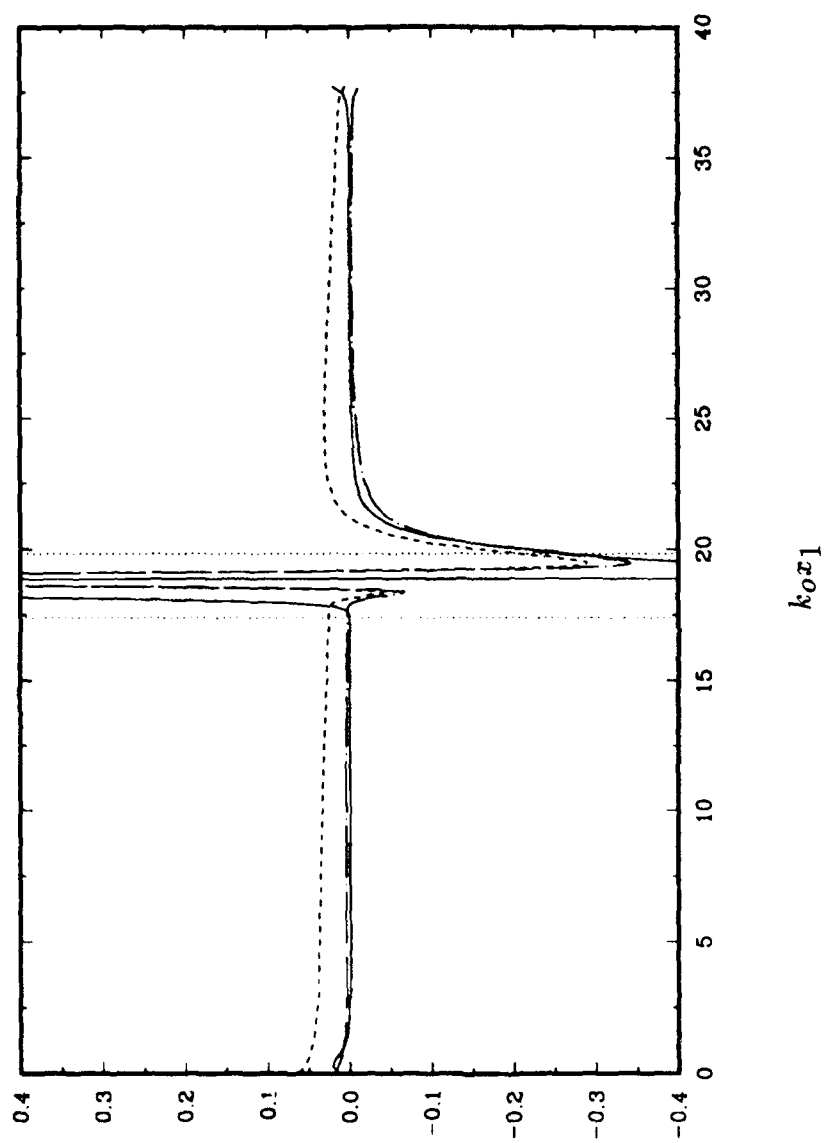


FIGURE 4.30. Evaluation of the model for case C: — LHS of (4.26b), --- RHS of (4.26b), — RHS of (4.26b) with p_e^2 replaced by 0.3 times the expression in (4.25b). (Vertical dotted lines denote the boundaries of shock intermittency.)

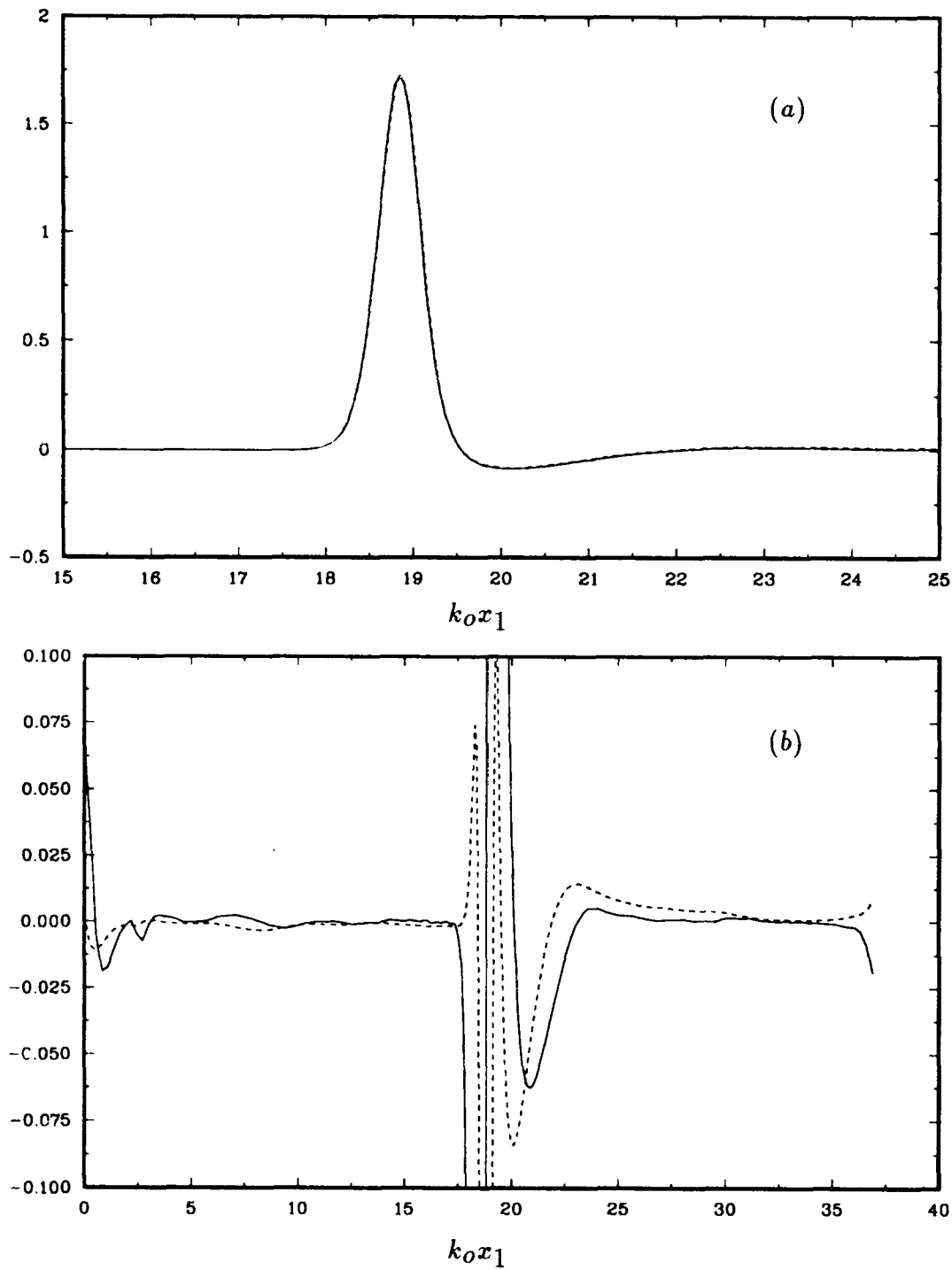


FIGURE 4.31. Evaluation of the models (4.27) for $-(\overline{p'u_1''})_{,1}$ for case C: (a) approximation in terms of $\overline{\rho'u_1''}$ (— LHS of (4.27a), ---- RHS of (4.27a)); (b) transport of $\overline{\rho'u_1''}$ (— LHS of (4.27b), ---- RHS of (4.27b)).

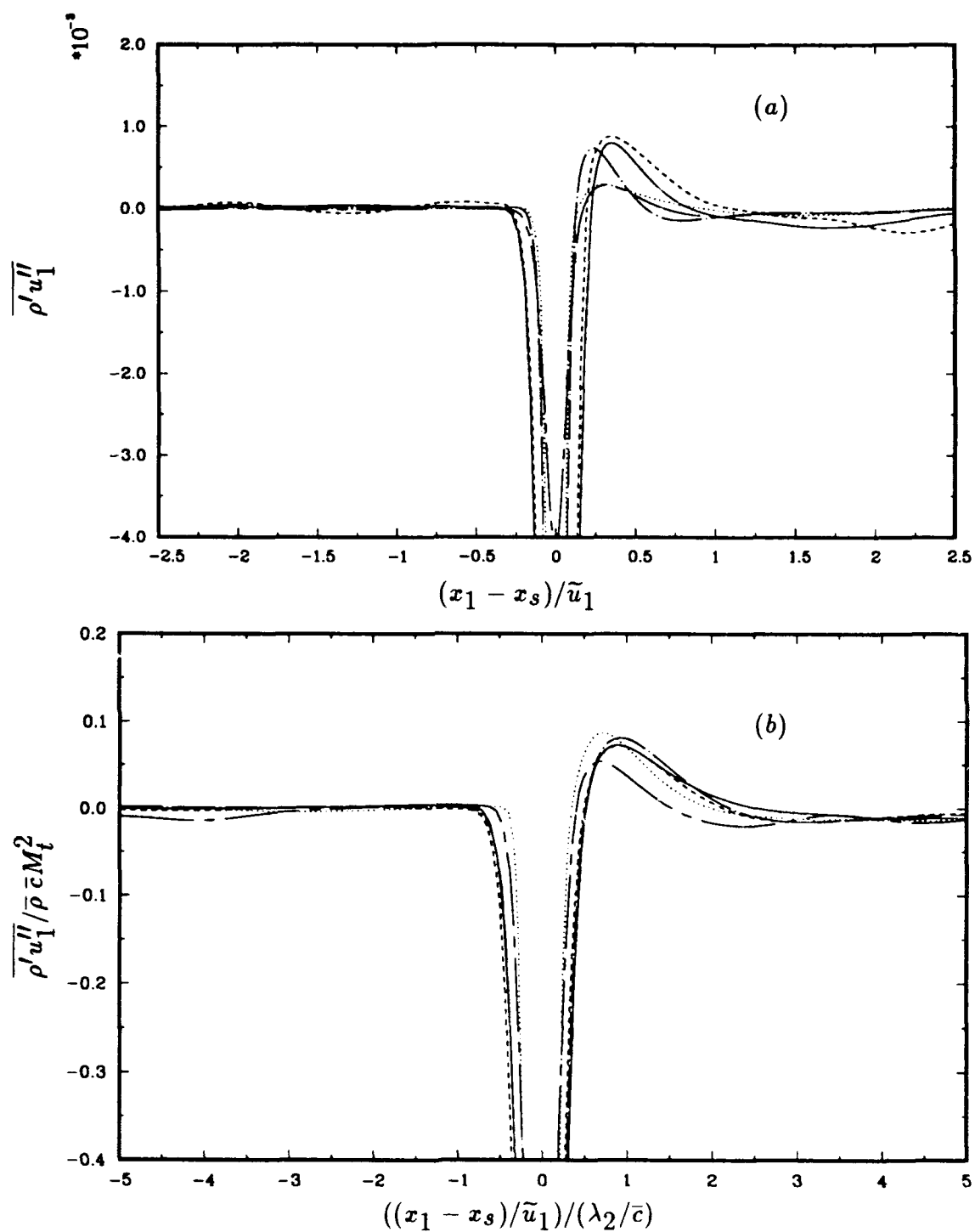


FIGURE 4.32. Unscaled (a) and scaled (b) turbulent mass fluxes (x_s is the position for peak negative turbulent mass flux): — case A, ---- case B, —·— case C, case D, ——— case E.

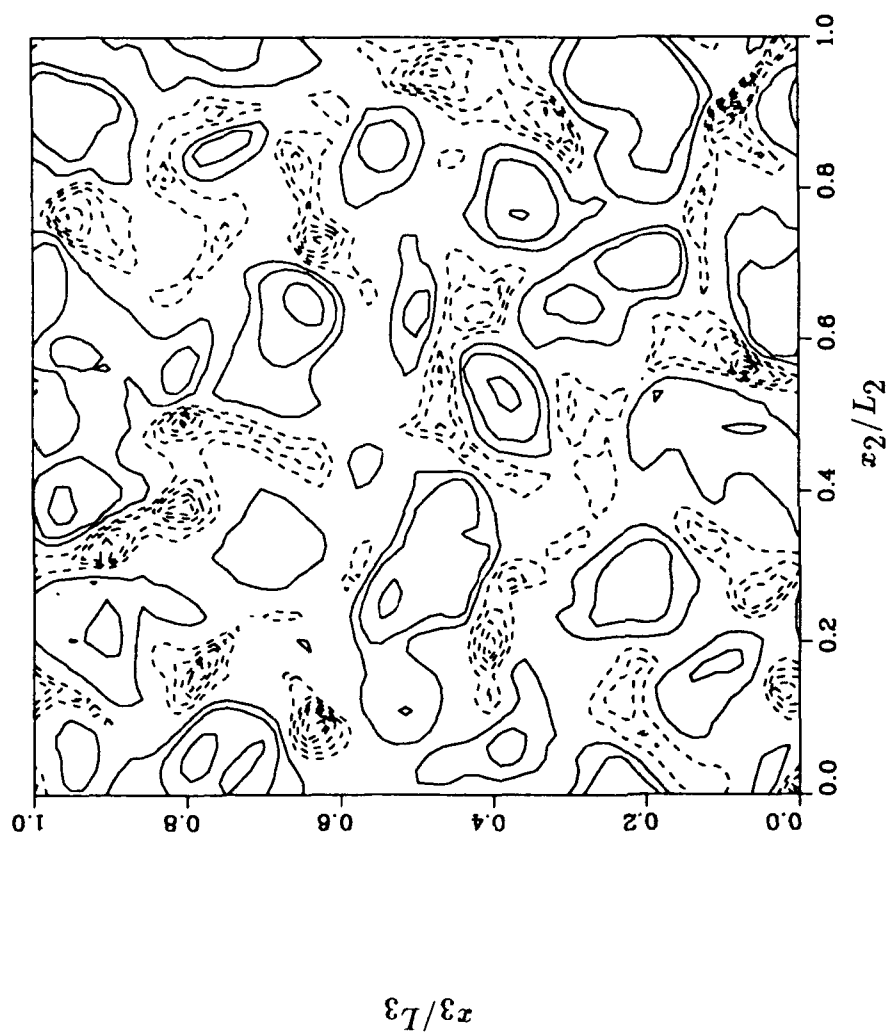


FIGURE 4.33. Contour plot for the peak negative dilatation inside the shock wave (θ_{\min}) along the mean streamlines for case C: solid lines denote weaker compression and dashed lines indicate stronger compression than that for the laminar shock wave, $\theta = -8.1$. Increment between lines, $\Delta\theta_{\min} = 2.0$.

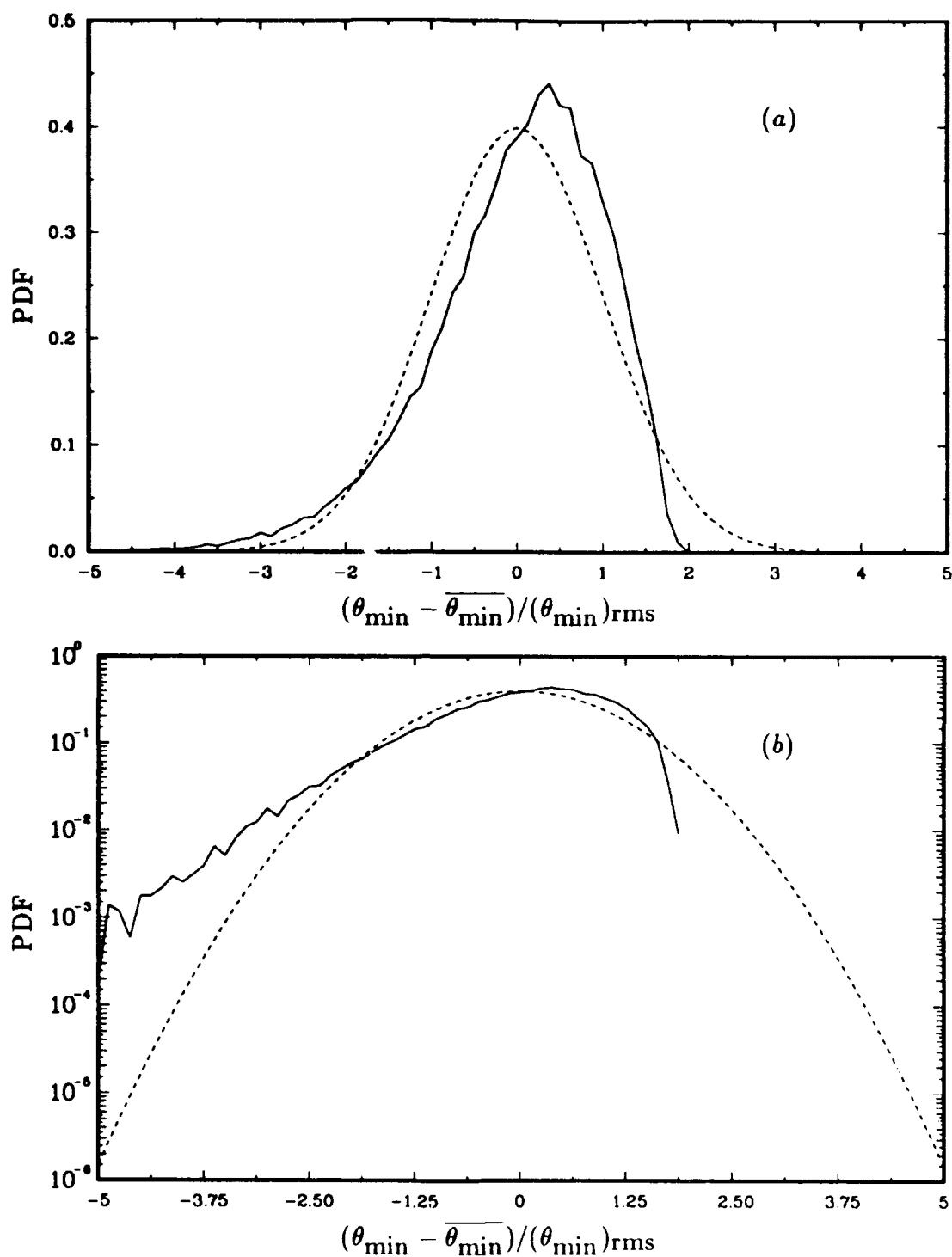


FIGURE 4.34. Probability density function for the peak negative dilatation in (a)linear-linear and (b)linear-logarithmic coordinates for case C: — PDF of θ_{\min} , ---- PDF of a Gaussian distribution.

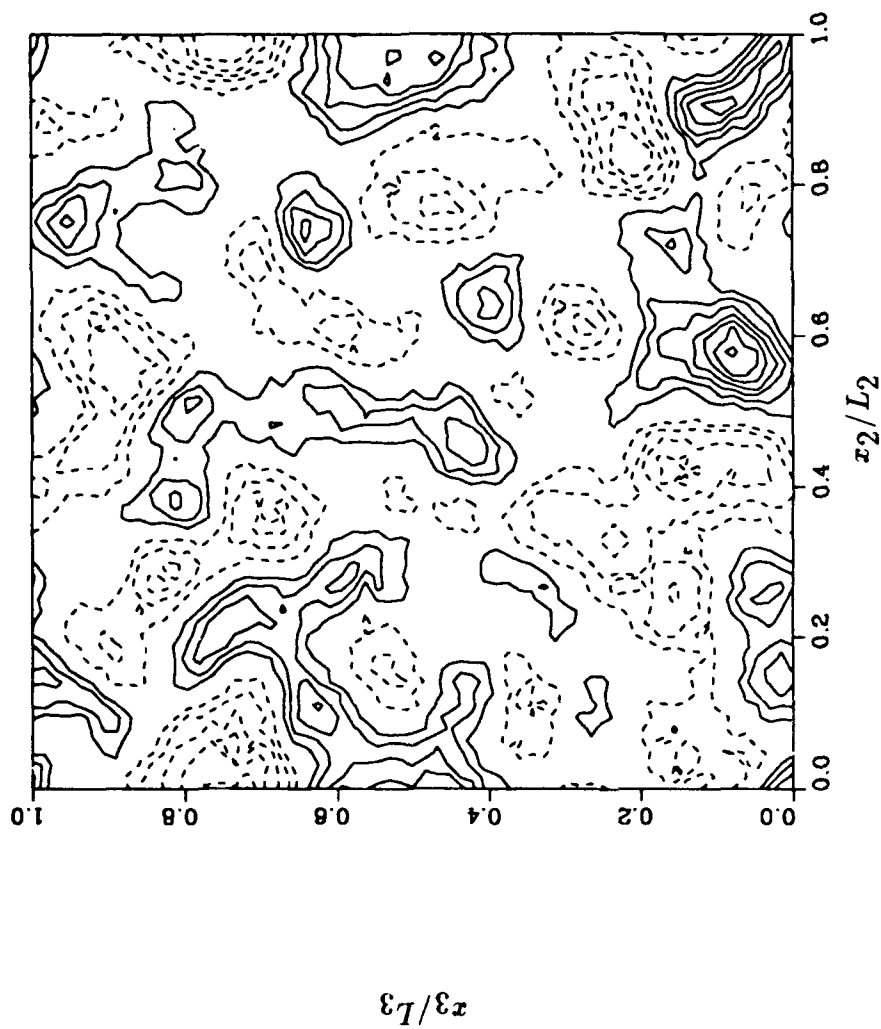


FIGURE 4.35. Contour plot for the shock front distortion based on (a) the pressure half-rise and (b) the density half-rise point for case C. Solid lines denote the shock front pushed downstream and dashed lines denote the shock front pulled upstream.

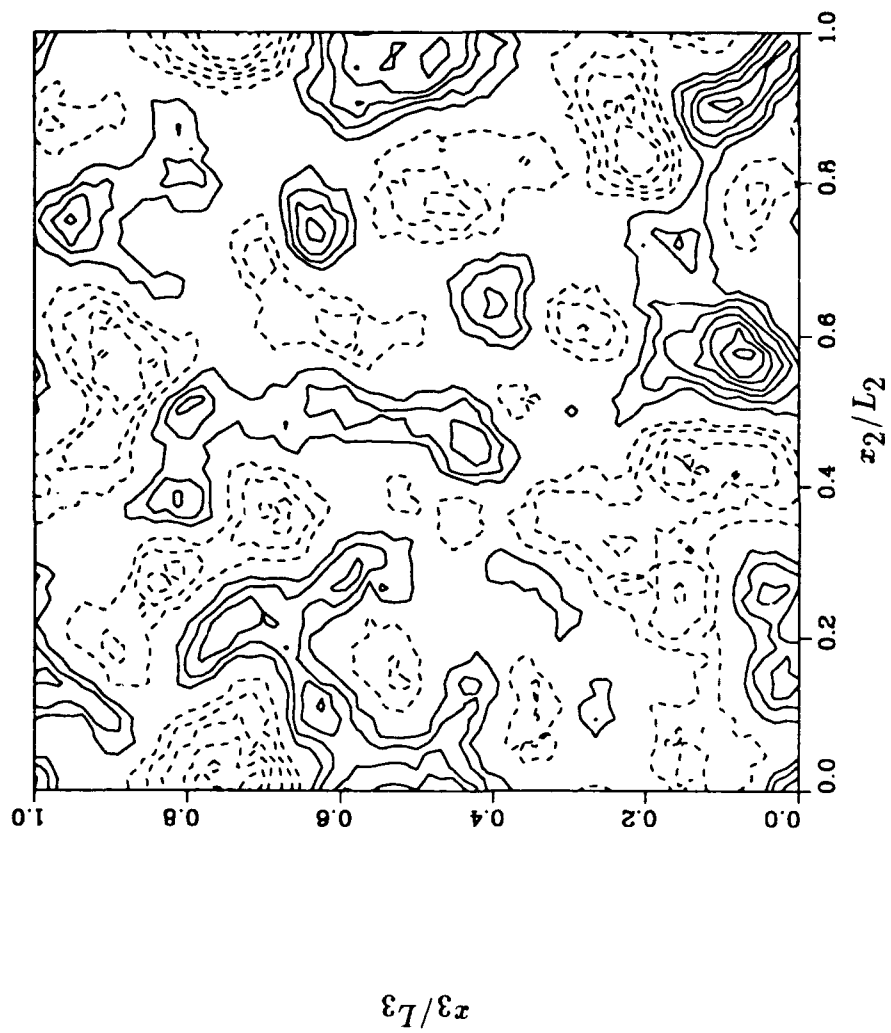


FIGURE 4.35. (continued from the previous page)

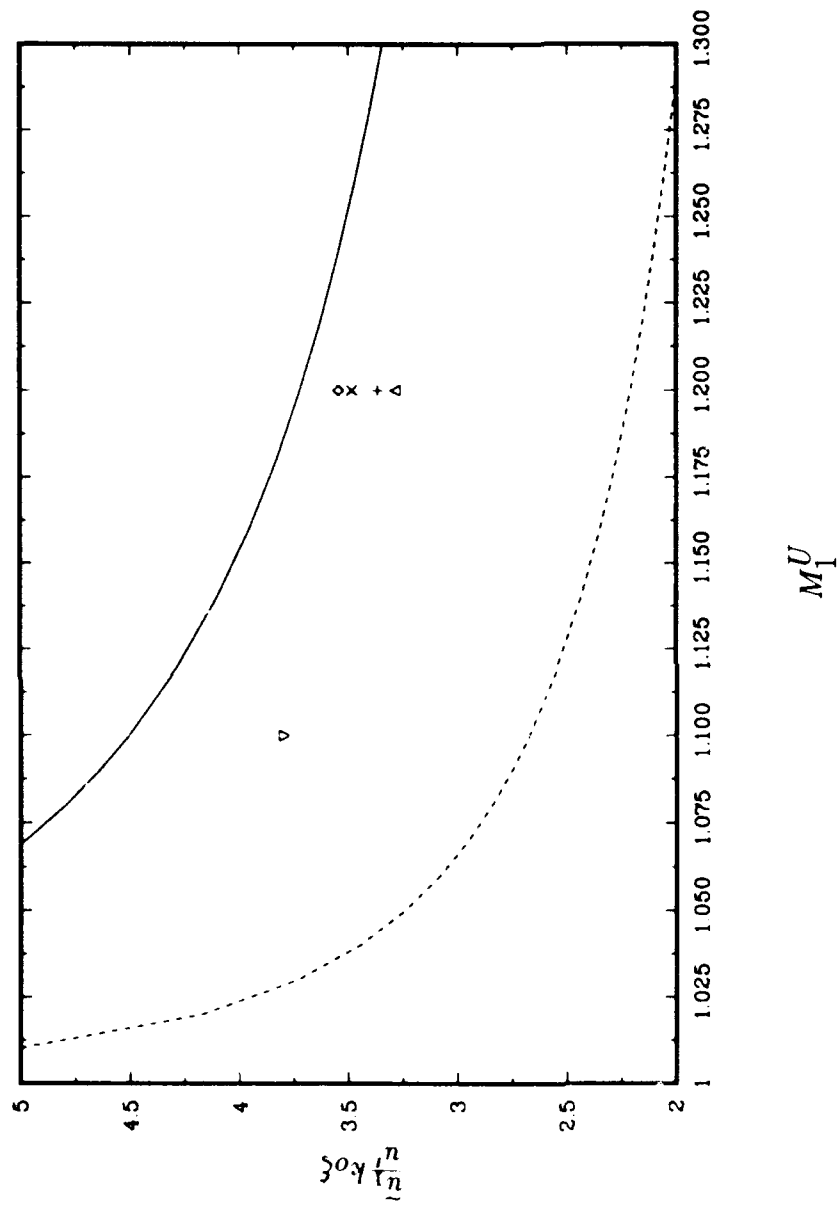


FIGURE 4.36. Comparison of scaled *rms* displacements of the shock front from different simulations with LIA predictions: — LIA with spectrum (2.1), - - - LIA with von Kármán spectrum, \diamond case A, \times case B, \triangle case C, ∇ case D, ∇ case E.

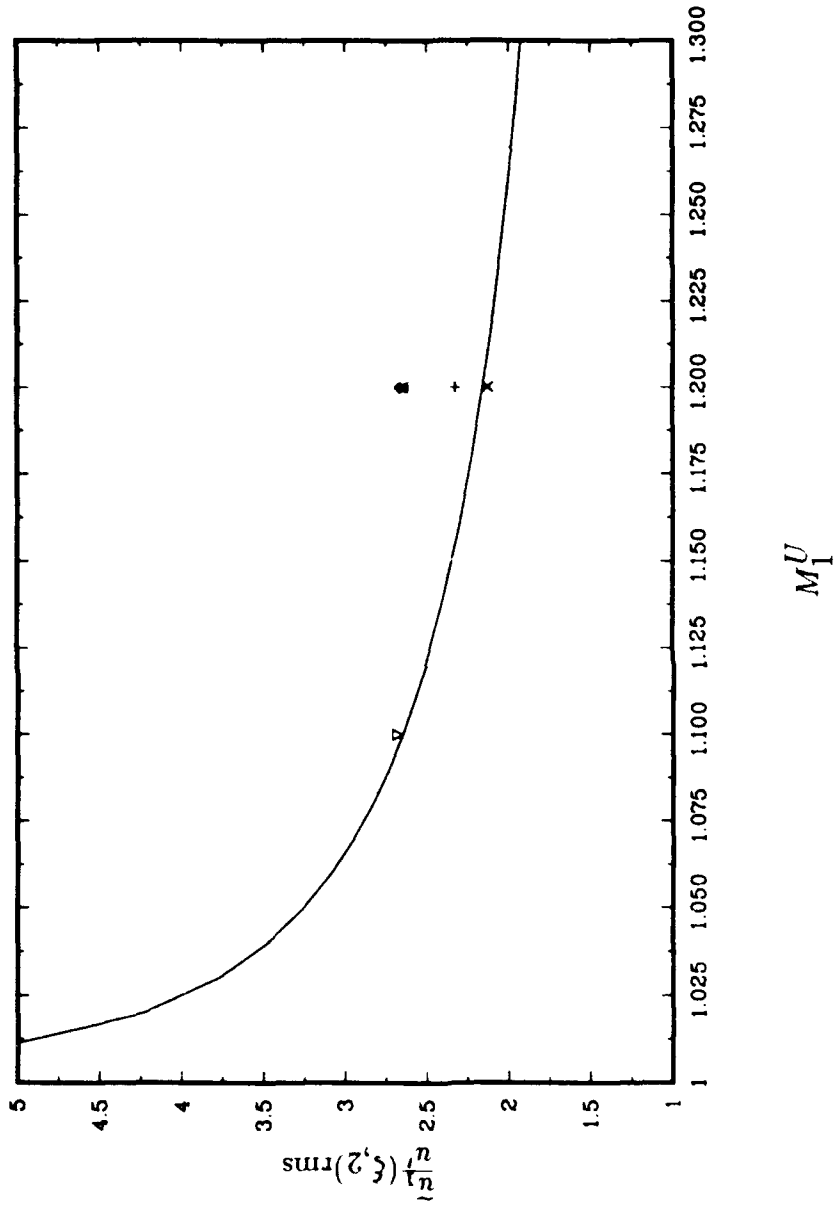


FIGURE 4.37. Comparison of scaled rms shock front slopes from different simulations with LIA predictions:
 — LIA with spectrum (2.1), - - - LIA with von Kármán spectrum, Δ case A, \times case B, \diamond case C, ∇ case D,
 ∇ case E.

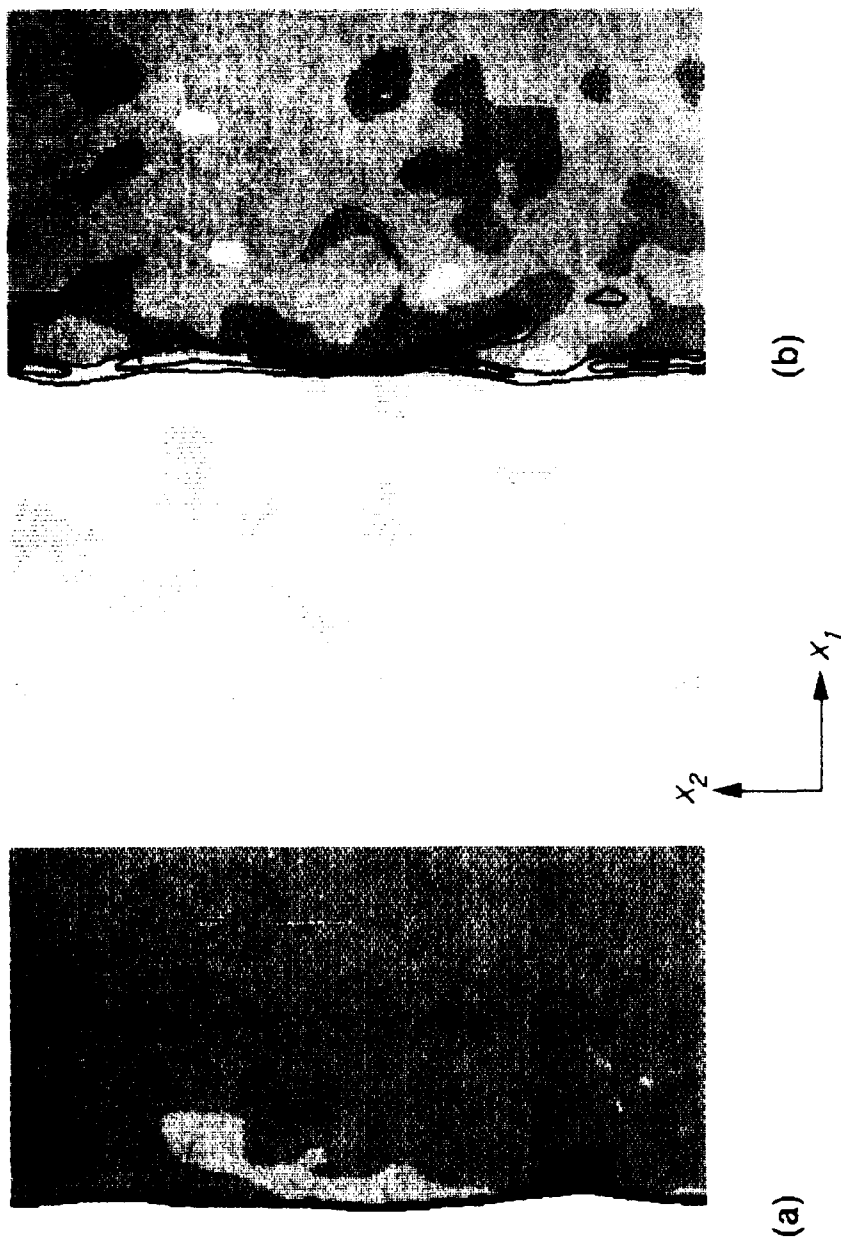


FIGURE 4.38. Instantaneous density fields in typical $x_1 x_2$ -planes for (a) case D and (b) case F. The overlaid thick lines near the center of the figure are iso-compression lines.

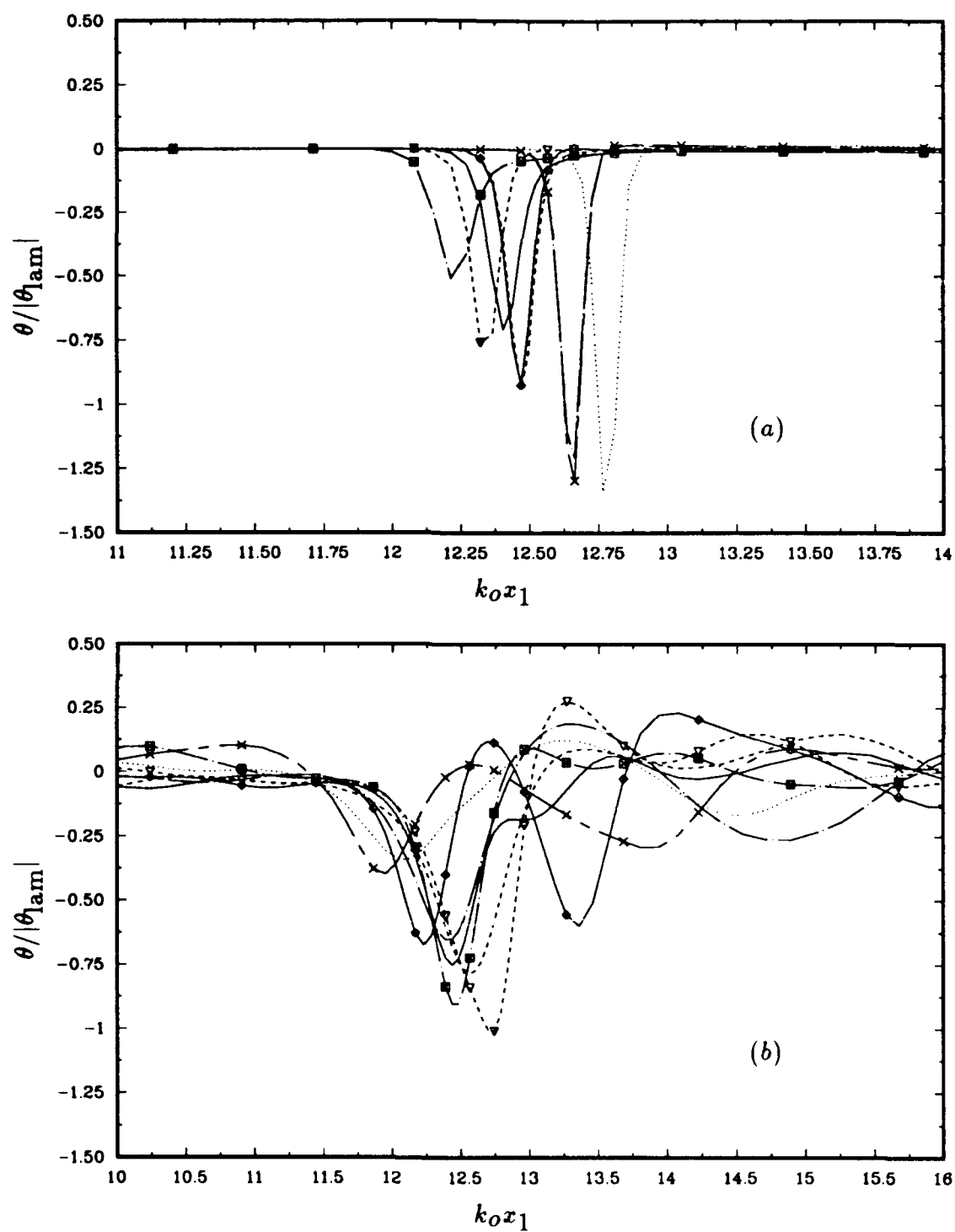


FIGURE 4.39. Profiles of dilatation along the mean streamlines for (a) case D and (b) case F.

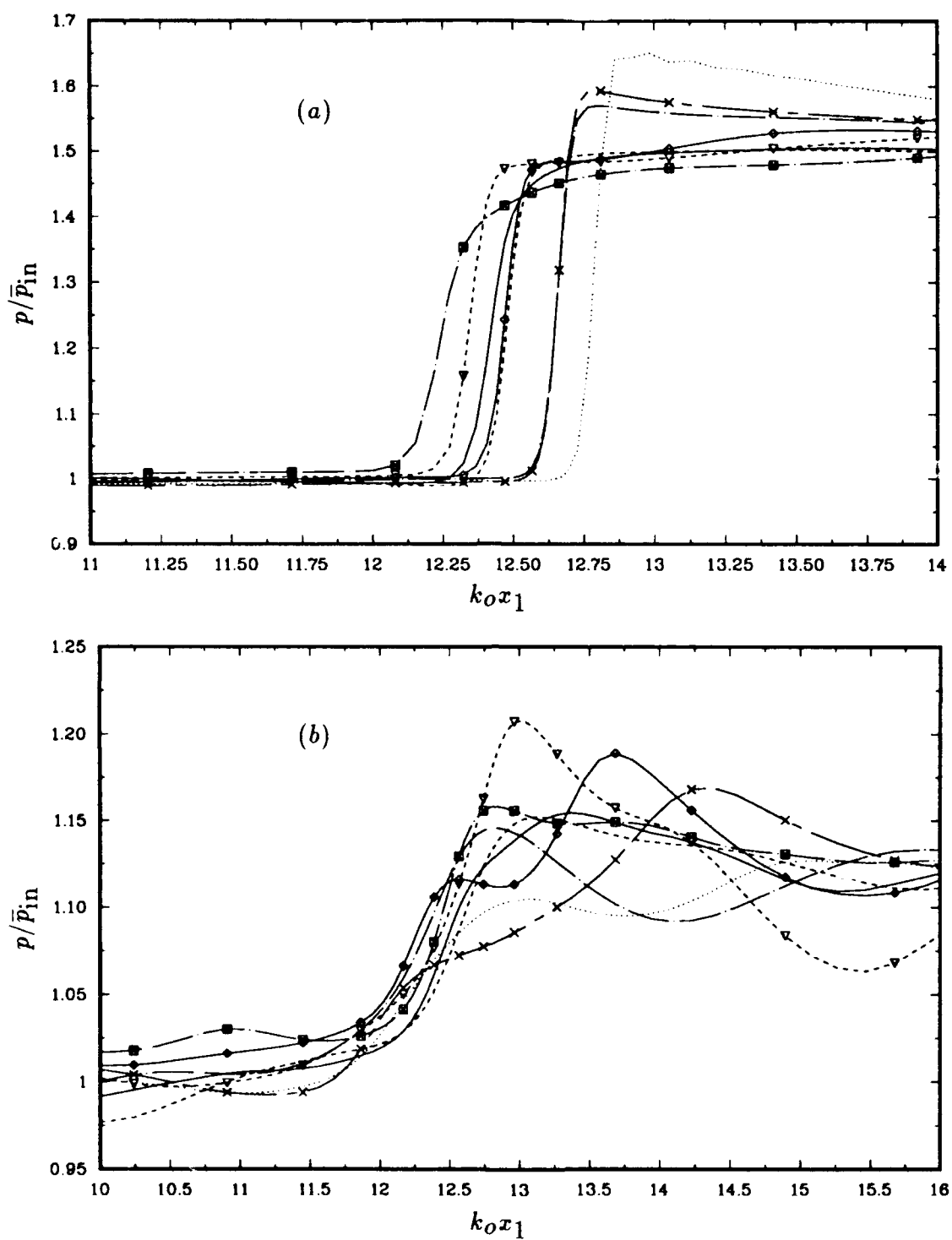


FIGURE 4.40. Profiles of pressure along the mean streamlines for (a) case D and of (b) case F.

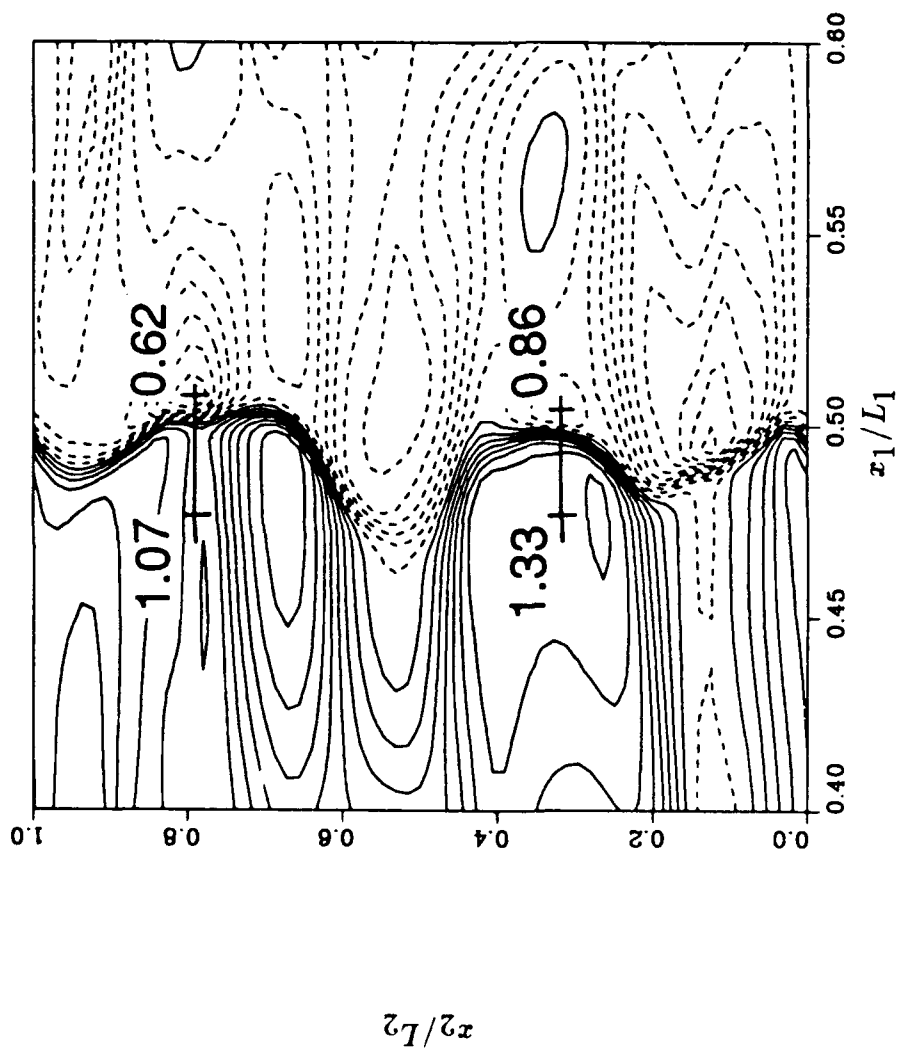


FIGURE 4.41. Contour plot for the streamwise Mach number for case A. Solid lines denote supersonic condition, and dashed lines denote subsonic condition. Increment between lines $\Delta M_1 = 0.05$.

CHAPTER 5

CONCLUSIONS AND RECOMMENDATIONS

This work has been concerned with a numerical study of the interaction of turbulence with a shock wave. The methods used were linear analyses (RDT and LIA) and direct numerical simulation of the compressible Navier Stokes equations. Linear analyses were used to predict modifications in turbulence statistics in passage through the shock and shock front statistics. In direct numerical simulation, the full equations were solved by an explicit code, with the spatial derivative evaluated by a modified Padé scheme. A summary of conclusions is provided below, followed by recommendations for future work. Conclusions are divided into three main areas: spatially decaying turbulence, turbulence modification by shock turbulence interaction, and shock wave modification by the interaction.

Spatially Decaying Turbulence

A method of generating stochastic inflow boundary conditions with prescribed spectrum was developed. Turbulence intensity, *rms* vorticity, and velocity derivative skewness factor compare favorably with those from the temporal simulation. However, the statistics of dilatation show significant departure from those obtained in the temporal simulation. Because of this difference, caution must be exercised in using periodic (or temporal) simulation databases to examine compressibility-driven quantities such as dilatation dissipation and pressure dilatation correlation. Turbulence statistics from spatially evolving simulations with low compressibility effects are also found to be in agreement with the experimental data.

Turbulence Modification by Shock Turbulence Interaction

The simulations and linear analyses of shock turbulence interaction show that the normal components of the Reynolds stresses, $R_{\alpha\alpha}$, are enhanced across the shock wave. The stress amplifications are larger for the stronger shock waves within the range of Mach numbers in the simulation, $1.05 \leq M_1^U \leq 1.20$. LIA, however,

predicts less amplification of the streamwise turbulence intensity for the stronger shock waves when $M_1^U \geq 2.0$, a range beyond that of the present simulations.

The simulations show a rapid evolution of $R_{\alpha\alpha}$ immediately behind the shock wave, including an increase in value just downstream. LIA, on the other hand, predicts that $R_{\alpha\alpha}$ monotonically decays from its post-shock value to the far-field value. The budget of the TKE transport equation revealed that the pressure work term $-\overline{u_i'' p_i'}$ is responsible for this rapid evolution. By decomposing the pressure work term into the pressure-dilatation correlation $\overline{p' u_{i,i}''}$ and the pressure transport $-(\overline{p' u_i''})_{,i}$ term, it was found that the pressure transport is the main contributor to the pressure work term. Therefore, rapid evolution of TKE is caused mainly by the redistribution of turbulent kinetic energy in the streamwise direction at the early stages of relaxation from compression.

The simulations and linear analyses show that the *rms* of the transverse vorticity components are amplified and that the streamwise vorticity is not influenced by the interaction. The amplifications are larger for stronger shock waves. The amplification of the transverse vorticity components predicted by the simulations are in excellent agreement with those of linear analyses for $M_t < M_1^U - 1$. For $M_t > M_1^U - 1$, the vorticity amplification obtained from the simulation is significantly less than the estimates of the linear analyses. Examination of the budget of $\overline{\omega_\alpha'^2}$ revealed that the vorticity-compression, $\overline{\omega_\alpha'^2 s_{ii}}$, is the main contributor to the transverse vorticity amplification during the interaction. In most cases, the baroclinic torque is at least two orders of magnitude smaller than the vorticity-compression term in the interaction zone.

Turbulent length scales decrease through the interaction. Linear analyses predict the amplification of one-dimensional energy spectra during the interaction, both in frequency and wave number space. In the frequency spectrum, amplification is larger for the smaller frequencies. In the wave number spectrum, however, amplification is larger at the larger wave numbers. More enhancement at the smaller scales leads to a decrease in turbulence length scales. Numerical simulations confirmed that the energy spectrum is amplified more at the larger wave numbers, whereas turbulence length scales are decreased through the interaction.

We investigated the relations between the fluctuations in pressure, density, and temperature by the use of the simulation results. Morkovin's hypothesis was tested and found inaccurate. Instead, the relations between properly scaled *rms* property fluctuations are very close to isentropic at least for turbulence passing through a weak shock wave, $M_1^U \leq 1.20$. Isentropic relations are satisfied even for the instantaneous fluctuations throughout the flow field including the shock wave.

Shock Wave Modification by Shock Turbulence Interaction

Due to the nonuniformity of upstream turbulence, the shock wave has a time-dependent distorted front and nonuniform thickness in the transverse directions. For the simulations with $M_t < M_1^U - 1$, shock waves have well-defined fronts with single compression peaks in the streamwise direction.

Through LIA, it was found that the shock front distortion scales with the upstream integral length scale and turbulence intensity. We also found that the local shock front inclination angle scales only with upstream turbulence intensity, and the shock front curvature is scaled with turbulence intensity and the inverse of the Taylor microscale. All scaling factors depend only on the shock strength. The statistics of the shock front obtained by the simulations are in fair agreement with the LIA predictions.

Through LIA, local shock wave speed was found to scale with the upstream fluctuating velocity. Instantaneous flow fields from the simulations showed that the velocity jump across the shock wave, or the shock wave strength, is more or less uniform in the transverse directions: The shock wave moves upstream for lower velocity, and moves downstream for higher velocity of the approaching flow, thus reducing the variation in the effective shock-normal Mach number.

For a simulation with $M_t > M_1^U - 1$, shock waves no longer have well-defined fronts in the transverse directions. Low density regions are often found behind the mean shock position, and shock wave thickness varies quite widely in transverse directions. Along the streamwise direction, multiple peaks in dilatation and pressure are found, which are similar to those observed in the experiments of a very

weak shock wave interacting with a highly inhomogeneous medium [Hesselink *et al.* 1988].

A comprehensive quantitative data base has been generated which may be used to develop and test turbulence models and to further study the physics of shock/turbulence interaction.

Recommendations for Future Research

Direct numerical simulation of shock/turbulence interaction is a new area of research, and many questions remain to be answered. From our work, we recommend the following directions for future research.

Interactions with Significant Acoustic or Entropy Fluctuations

In this work, upstream turbulence conditions in the simulations were restricted to quasi-incompressible states. It is also important to study the interaction of a shock wave both with highly compressible turbulence and with flows of large density variations.

Towards Turbulent Boundary Layer Interaction with a Shock Wave

The logical next step towards understanding of shock/turbulent boundary layer interaction is to study interaction of homogeneous turbulence under a mean shear with a shock wave. Through this study, one can investigate the effect of a shock wave on turbulence anisotropy and Reynolds shear stress.

Large-Eddy Simulation of Shock Turbulence Interaction

Direct numerical simulation of shock turbulence interaction is restricted to low Reynolds numbers and weak shock waves by the resolution requirements of the shock wave structure. Subgrid-scale models have been actively under development [Erlebacher *et al.* 1990, Moin *et al.* 1991] for the large-eddy simulation of compressible turbulence. For shock turbulence interaction, the ratio of the turbulence length scale $l = \rho q^3/\epsilon$ to the shock wave thickness δ_s is

$$\frac{l}{\delta_s} \sim \frac{Re_T}{M_t},$$

typically $O(10^3)$ - $O(10^4)$ or larger in practical flows where $Re_T > 1000$. Since the cost of resolving the shock wave structure in large-eddy simulation is prohibitive, one needs a subgrid-scale model for the shock wave effect on turbulence [Zeman 1991b], as well as for the effect of small scale turbulence on the large scales. Another possible option is to use a shock capturing technique [Yee 1987, Harten *al.* 1987] without any subgrid-scale model of the shock wave effect. Careful tests of these ideas can be made by using the data obtained in the present work via linear analyses and direct numerical simulations.

APPENDIX A

RAPID DISTORTION THEORY

Rapid Distortion Theory (hereafter RDT) is applied to study the response of turbulence quantities to one-dimensional compression due to a shock wave. The state of homogeneous turbulence changes significantly when it is subjected to mean strain, but the nonlinearity of the governing equations makes it impossible to develop a rigorous theory of turbulence under straining process. For cases where nonlinear effects are not significant, however, one can solve the exact linearized equations.

When the time scale of turbulence, q^2/ϵ , is long compared to that of the mean deformation ($|S|q^2/\epsilon \gg 1$), the turbulence has no time to interact with itself. Thus, we need not consider the nonlinear terms in the governing equations involving products of fluctuation quantities, and we can obtain the linear RDT equations. The viscous terms are linear and can be included in the analysis, but are often neglected and will be here for simplicity. RDT for one-dimensional compression is applied to study the response of turbulence during its passage through a shock wave. In the following, a brief review of the RDT procedure is given for one-dimensional compression [Lee and Reynolds 1985, Lee 1989].

We consider turbulence subject to a rapid irrotational strain, where density is uniform throughout the field but allowed to vary in time. Since the mean flow is assumed to be irrotational, we use the principal axes of strain rate tensor as axes of reference so that the mean velocity field is

$$U_{\alpha,\beta}(t) = S_{\alpha\beta}(t) = \Gamma_{\alpha}(t)\delta_{\alpha\beta}. \quad (A.1)$$

Using the equation of continuity, we can then express the evolution of density $\rho(t)$ in the form

$$\rho(t) = \rho_o \exp \left[- \int_0^t S_{ii}(t') dt' \right], \quad (A.2)$$

where $\rho_0 = \rho(0)$ and the trace of mean strain rate tensor S_{ii} signifies the expansion rate (or the compression rate) of the mean flow field.

The turbulent momentum equation in the RDT is given by

$$\frac{\partial u_i}{\partial t} + U_j \frac{\partial u_i}{\partial x_j} = -S_{ij}u_j - \frac{1}{\rho} \frac{\partial p}{\partial x_i}, \quad (A.3)$$

and the equation of continuity is unchanged. The dynamical equation for the fluctuating vorticity ω becomes

$$\frac{\partial \omega_i}{\partial t} + U_j \frac{\partial \omega_i}{\partial x_j} = \omega_j S_{ij}^* - \frac{2}{3} S_{ij} \omega_i, \quad (A.4)$$

where

$$S_{ij}^* = S_{ij} - \frac{1}{3} S_{kk} \delta_{ij} \quad (A.5)$$

is the deviatoric component of the mean strain rate tensor. The first term on the right hand side of (A.4) represents the production of vorticity due to stretching by the incompressible mean strain rate S_{ij}^* . The second term indicates reduction of vorticity by isotropic expansion (or increase by compression).

We impose periodic boundary conditions and represent homogeneous turbulence in terms of Fourier series. The dependence of U_j on the position \mathbf{x} in (A.3) and (A.4), however, poses problems with this approach. To remove this, we use a deforming coordinate system [Rogallo 1981] which follows the mean flow:

$$\xi_\alpha = \frac{x_\alpha}{e_\alpha}, \quad \tau = t, \quad (A.6)$$

where the factor e_α is the total strain in the α -direction defined as

$$e_\alpha(t) = \exp \left[\int_0^t \Gamma_\alpha(t') dt' \right]. \quad (A.7)$$

In the deforming coordinates, the vorticity equation becomes

$$\frac{\partial \omega_\alpha}{\partial \tau} = \tilde{\Gamma}_\alpha \omega_\alpha, \quad (A.8)$$

where

$$\tilde{\Gamma}_\alpha = \Gamma_\alpha - \Gamma_o, \quad \Gamma_o = S_{ii} = \Gamma_1 + \Gamma_2 + \Gamma_3 \quad (A.9)$$

are the reduced strain rate and the dilatation rate, respectively. The solution of (A.8) is

$$\frac{\omega_\alpha(\xi, \tau)}{\rho(\tau)} = e_\alpha \frac{\omega_\alpha(\xi, 0)}{\rho_o} \quad \text{or} \quad \omega_\alpha(\xi, \tau) = \tilde{e}_\alpha \omega_\alpha(\xi, 0). \quad (A.10)$$

Here, $\omega_\alpha(\xi, 0)$ is the initial value of $\omega_\alpha(\xi, \tau)$, and

$$\tilde{e}_\alpha = \frac{e_\alpha}{e_o}, \quad e_o = e_1 e_2 e_3 = \frac{\rho_o}{\rho} \quad (A.11)$$

are the reduced total strain in the α -direction and the dilatational total strain, respectively. Note that $e_o = 1$ for an incompressible mean flow field.

Since we have the solution (A.10) for the vorticity evolution in an explicit form, it is easy to obtain the history of turbulence statistics in terms of the initial values and total strains. Thus, the evolution of the vorticity correlation tensor at time τ is

$$V_{\alpha\beta}(\tau) = \tilde{e}_\alpha \tilde{e}_\beta V_{\alpha\beta}(0), \quad (A.12)$$

where

$$V_{\alpha\beta}(0) = \overline{\omega_\alpha(\xi, 0) \omega_\beta(\xi, 0)}. \quad (A.13)$$

The velocity field can be deduced from the vorticity field. In the transformed coordinates, the Poisson equation for the velocity is

$$\tilde{\nabla}^2 u_1 = \frac{1}{e_3} \frac{\partial \omega_2}{\partial \xi_3} - \frac{1}{e_2} \frac{\partial \omega_3}{\partial \xi_2}, \quad (A.14)$$

where the transformed Laplace operator is

$$\tilde{\nabla}^2 = \frac{1}{e_1^2} \frac{\partial^2}{\partial \xi_1^2} + \frac{1}{e_2^2} \frac{\partial^2}{\partial \xi_2^2} + \frac{1}{e_3^2} \frac{\partial^2}{\partial \xi_3^2}. \quad (A.15)$$

The equations for u_2 and u_3 can be obtained by permuting the indices. The solution is obtained using Fourier expansions,

$$\begin{aligned}\omega_i &= \sum_{\kappa_n} \hat{\omega}_i(\kappa_n, \tau) e^{-i\kappa_n \xi_n} \\ u_i &= \sum_{\kappa_n} \hat{u}_i(\kappa_n, \tau) e^{-i\kappa_n \xi_n},\end{aligned}\tag{A.16}$$

where κ_α is the Fourier wave number vector in the deforming reference frame, $\kappa_\alpha = e_\alpha k_\alpha$ (k_α is the wave number vector in the undeformed reference frame).

The solution for \hat{u}_1 is

$$\hat{u}_1 = \frac{i}{\chi^2} \left(\frac{\kappa_3 \hat{\omega}_2}{e_3} - \frac{\kappa_2 \hat{\omega}_3}{e_2} \right),\tag{A.17}$$

where

$$\chi^2 = \frac{\kappa_1^2}{e_1^2} + \frac{\kappa_2^2}{e_2^2} + \frac{\kappa_3^2}{e_3^2}.$$

The other components can be found by permutation of the indices.

Using (A.17), we find the velocity spectrum in κ -space to be

$$E_{11}(\kappa, \tau) = \frac{1}{\chi^2} \left[\left(\frac{\kappa_3}{e_3} \right)^2 H_{22}(\kappa, \tau) + \left(\frac{\kappa_2}{e_2} \right)^2 H_{33}(\kappa, \tau) - 2 \left(\frac{\kappa_2}{e_2} \right) \left(\frac{\kappa_3}{e_3} \right) H_{23}(\kappa, \tau) \right],\tag{A.18}$$

where $H_{ij}(\kappa, \tau)$ is the vorticity spectrum in κ -space, and the relation $H_{23} = H_{32}$ is used. The vorticity spectrum at a later time is obtained in terms of its initial spectrum as

$$H_{\alpha\beta}(\kappa, \tau) = H_{\alpha\beta}(\kappa, 0) \tilde{e}_\alpha \tilde{e}_\beta.\tag{A.19}$$

The initial vorticity can be expressed in terms of initial velocities in the Fourier space as

$$\widehat{\omega}_l(\kappa, 0) = -i\epsilon_{lmn}\kappa_m\widehat{u}_n(\kappa, 0). \quad (\text{A.20})$$

Therefore, we can represent the initial vorticity spectrum $H_{ij}(\kappa, 0)$ in terms of the initial velocity spectrum $E_{ij}(\kappa, 0)$, for example,

$$H_{11}(\kappa, 0) = \kappa_2^2 E_{33}(\kappa, 0) + \kappa_3^2 E_{22}(\kappa, 0) - 2\kappa_2\kappa_3 E_{23}(\kappa, 0), \quad (\text{A.21})$$

where the relation $E_{23} = E_{32}$ was used.

Using the relations (A.17), (A.19), and (A.20), we can obtain the evolution of the velocity spectrum during a rapid irrotational strain.

As a special case of irrotational strain, we consider one-dimensional compression in the x_1 -direction, where

$$e_1 = \frac{\rho_0}{\rho}, \quad e_2 = e_3 = 1, \quad (\text{A.22})$$

and

$$\tilde{e}_1 = 1, \quad \tilde{e}_2 = \tilde{e}_3 = e_1^{-1}. \quad (\text{A.23})$$

Vorticity components in the x_2 and x_3 directions are amplified by a factor of density increase during the rapid compression, while vorticity in the x_1 -direction stays the same. These relations hold regardless of the specific form of the initial spectrum. In general, amplifications of Reynolds stresses do depend on the shape of the spectrum. However, for an isotropic initial turbulence, amplifications of Reynolds stresses are again independent of the initial spectrum: for example, to compute $\overline{u_1'^2}$, triple integration of (A.18) in κ space, using (A.20) and a general form of the vorticity spectrum for an isotropic turbulence,

$$H_{ij}(\kappa, 0) = \frac{E(\kappa, 0)}{4\pi\kappa^2}(\kappa^2\delta_{ij} - \kappa_i\kappa_j), \quad (\text{A.24})$$

gives

$$\begin{aligned}
\overline{u_1'^2} &= \int_{-\infty}^{\infty} \int_{-\infty}^{\infty} \int_{-\infty}^{\infty} E_{11}(\kappa, \tau) d\kappa_1 d\kappa_2 d\kappa_3 \\
&= \frac{1}{4\pi} \int_0^{\infty} E(\kappa, 0) d\kappa \int_0^{2\pi} \int_0^{\pi} \frac{\tilde{\kappa}_3^2(1 - \tilde{\kappa}_2^2) + \tilde{\kappa}_2^2(1 - \tilde{\kappa}_3^2) + 2\tilde{\kappa}_2^2\tilde{\kappa}_3^2}{[(\tilde{\kappa}_1/e_1)^2 + \tilde{\kappa}_2^2 + \tilde{\kappa}_3^2]^2} \sin \theta d\phi d\theta,
\end{aligned} \tag{A.25}$$

where

$$\tilde{\kappa}_1 = \frac{\kappa_1}{\kappa} = \cos \theta, \quad \tilde{\kappa}_2 = \frac{\kappa_2}{\kappa} = \sin \theta \cos \phi, \quad \tilde{\kappa}_3 = \frac{\kappa_3}{\kappa} = \sin \theta \sin \phi.$$

The result is independent of κ . Note that $\int E(\kappa, 0) d\kappa = q_o^2/2$, where $E(\kappa, 0)$ is the initial energy spectrum function and $q_o^2 = \overline{u_i' u_i'}$ at $t = 0$.

The same result can be obtained by properly scaling the RDT result for turbulence under *incompressible* axisymmetric expansion. The one-dimensional compression can be decomposed into isotropic compression $S_{kk}\delta_{ij}/3$ (or density change) and incompressible axisymmetric expansion S_{ij}^* as

$$\begin{aligned}
S_{ij} &= S_{kk}\delta_{ij}/3 + S_{ij}^* \\
&= \begin{pmatrix} \Gamma_1/3 & 0 & 0 \\ 0 & \Gamma_1/3 & 0 \\ 0 & 0 & \Gamma_1/3 \end{pmatrix} + \begin{pmatrix} 2\Gamma_1/3 & 0 & 0 \\ 0 & -\Gamma_1/3 & 0 \\ 0 & 0 & -\Gamma_1/3 \end{pmatrix}. \tag{A.26}
\end{aligned}$$

The total strain can be accordingly decomposed:

$$\mathbf{e} = e_o^{1/3} \mathbf{e}^* = (\rho_o/\rho)^{1/3} \mathbf{e}^*, \tag{A.27}$$

where

$$\mathbf{e}^* = (e_1^*, e_2^*, e_3^*) \tag{A.28}$$

is the incompressible total strain vector (i.e., $e_1^* e_2^* e_3^* = 1$) and

$$e_o = e_1 e_2 e_3 = \rho_o/\rho \tag{A.29}$$

is the total dilatation.

Using (A.10) and (A.20), the Fourier amplitude of velocity fluctuations under one-dimensional compression (A.17) can be expressed as

$$\hat{u}_1(\kappa, \mathbf{e}) = \frac{1}{e_o \chi^2} \left[\left(\frac{e_3}{e_2} \kappa_2^2 + \frac{e_2}{e_3} \kappa_3^2 \right) \hat{u}_{1o} - \frac{e_3}{e_2} \kappa_1 \kappa_2 \hat{u}_{2o} - \frac{e_2}{e_3} \kappa_1 \kappa_3 \hat{u}_{3o} \right], \quad (\text{A.30})$$

where $\chi^2 = \kappa_1^2/e_1^2 + \kappa_2^2/e_2^2 + \kappa_3^2/e_3^2$, and \hat{u}_o is the initial Fourier amplitude. Expressions for the other two components are obtained by cyclic interchange of indices.

By using the decomposition (A.26), the Fourier amplitude of turbulent velocity in (A.30) can be expressed as a product of the isotropic dilatation and incompressible contributions:

$$\hat{\mathbf{u}}(\kappa, \mathbf{e}) = (\rho/\rho_o)^{1/3} \hat{\mathbf{u}}^*(\kappa, \mathbf{e}^*), \quad (\text{A.31})$$

where from (A.30), the incompressible part $\hat{\mathbf{u}}^*$ is given by,

$$\hat{u}_1^*(\kappa, \mathbf{e}^*) = \frac{1}{\chi^{*2}} \left[\left(\frac{e_3^*}{e_2^*} \kappa_2^2 + \frac{e_2^*}{e_3^*} \kappa_3^2 \right) \hat{u}_{1o} - \frac{e_3^*}{e_2^*} \kappa_1 \kappa_2 \hat{u}_{2o} - \frac{e_2^*}{e_3^*} \kappa_1 \kappa_3 \hat{u}_{3o} \right], \quad (\text{A.32})$$

with $\chi^{*2} = \kappa_1^2/e_1^{*2} + \kappa_2^2/e_2^{*2} + \kappa_3^2/e_3^{*2}$. The appearance of the total dilatation as a common factor in all components of the velocity amplitude implies that the anisotropy in a turbulent flow is not affected by isotropic compression of the mean flow.

The energy spectrum tensor after one-dimensional compression is expressed as

$$E_{ij}(\kappa, \mathbf{e}) = (\rho/\rho_o)^{2/3} E_{ij}^*(\kappa, \mathbf{e}^*), \quad (\text{A.33})$$

where E_{ij}^* is the energy spectrum tensor of turbulence subject to incompressible axisymmetric compression.

The RDT result for turbulence under one-dimensional compression can be obtained by *scaling* the RDT result of turbulence under *incompressible* axisymmetric expansion (see (A.33)).

APPENDIX B

LINEAR INTERACTION THEORY

Some aspects of the interaction of turbulence with a shock wave are amenable to linear analysis. A fluctuating quantity in a compressible flow can be decomposed into acoustic, entropy, and vorticity waves [Kovasznay 1953]. Linear interaction analysis (hereafter LIA) of a shock wave with various linear plane waves were performed by Ribner[1953], Moore[1953], Kerrebrock[1956], Chang[1957], and McKenzie and Westphal[1968]. In general, whenever any one of these waves passes through a shock, it generates the other two waves downstream. In this work, we follow the methodology of Ribner, where the main interest is confined to the interaction of vorticity waves with a shock. In the following, a brief description of Ribner's analysis is given first, followed by its application to the analysis of shock-turbulence interaction.

B.1 Description of LIA— Ribner's Analysis

Ribner formulated the interaction of a plane vorticity wave with a shock wave as a boundary-value problem for the flow in the region downstream of the shock. The governing partial differential equation for small-perturbation rotational flow was derived as an extension of Sears' work [1950], boundary conditions on the velocity components just behind the shock were obtained from the oblique-shock relations, and finally the rotation term in the governing equation was evaluated in terms of gradients of entropy and total enthalpy with the use of the entropy change across the shock. The initially unknown distortion of the shock wave was taken into account in the boundary conditions and the rotation term by assuming it to be sinusoidal with initially undetermined amplitude and phase.

B.1.1 Formulation of the Boundary-Value Problem

The inclined plane sinusoidal shear wave is schematically shown in Figure B.1. The flow is viewed in a plane perpendicular to the shock and to the wave fronts. The wave is supposed to be convected downstream by the mean flow with velocity U_A (most variables in this Appendix are used exclusively, and those commonly used are listed in the Nomenclature section). The passage through the shock is evidently

an unsteady process, since the intercepts of the inclined shear wave with the shock wave move downward along the shock front.

A plane oblique sinusoidal shear wave may accompany a perturbation velocity component normal to the plane of the figure. This velocity component, however, is parallel everywhere to the shock and is unaffected as the shear wave passes through; this component also has no effect on the shock wave and, therefore, is excluded in the following analysis without any loss of generality. In the following analysis, the plane shear wave is assumed to propagate in the x_1x_2 -plane.

If an observer moves downward along the shock with a speed V , the flow has an apparent upward velocity component V . The observer speed V is to be chosen such that the resultant mean velocity (in the observer's frame of reference) is aligned with the velocity in the disturbance wave, that is, $V = U_A \tan \theta$. The process appears to the observer as an interaction of a steady sinusoidal shear flow with an oblique shock wave. Thus, by properly choosing the frame of reference, the original unsteady flow problem has been reduced to an equivalent steady flow problem.

The analysis is aimed at calculating the flow field downstream of the shock produced by the passage of a sinusoidal shear flow through the equivalent oblique shock. Because of the nonuniform upstream velocity field, the shock wave is corrugated and introduces vorticity downstream of the shock wave. If the upstream disturbance wave is weak, the downstream velocity perturbations are also weak compared to the mean velocity, so that a linearized treatment of the flow field is feasible.

Ribner derived the governing partial differential equation for small-perturbation compressible rotational flow with gradients in entropy and stagnation enthalpy. In the transformed coordinates, or in the observer's frame of reference shown in Figure B.2, the governing equation is expressed as

$$(1 - M^2)\psi_{\zeta\zeta} + \psi_{\eta\eta} = -\Omega \quad (B.1)$$

($\psi_{\zeta\zeta} = \partial^2\psi/\partial\zeta^2$ and $\psi_{\eta\eta} = \partial^2\psi/\partial\eta^2$). Using Crocco theorem [Thompson 1984], we have

$$\Omega = -\frac{1}{W} \left(\frac{\partial H}{\partial \eta} - T \frac{\partial s}{\partial \eta} \right),$$

where ζ is the distance in the streamwise direction, η is the distance in the perpendicular direction, W is the streamwise velocity, M is the corresponding Mach number, H is the stagnation enthalpy, s is the entropy, T is the temperature, Ω is the vorticity, and ψ is a perturbation stream function defined as:

$$\partial\psi/\partial\eta = w_\zeta, \quad -(1 - M^2)\partial\psi/\partial\zeta = w_\eta, \quad (B.2)$$

where w_ζ and w_η are the perturbation velocities in ζ and η direction, respectively. The final flow pattern depends crucially on whether W is subsonic or supersonic, which depends on the Mach number corresponding to U_A and on the wave inclination, θ .

The boundary conditions just downstream of the shock are obtained by applying the Rankine-Hugoniot relations across the perturbed shock wave. By geometry shown in Figure B.3, the mean velocity components normal and tangential to the undisturbed shocks are, respectively,

$$U_A = W_A \cos \theta, \quad V = W_A \sin \theta.$$

The shear wave provides a perturbation w_A to W_A , and causes indirectly a perturbation $\sigma(x_2)$ to the shock wave inclination which is defined as

$$\tan \sigma = \frac{\partial \xi}{\partial x_2},$$

whose magnitude is yet to be determined. The effect of σ is equivalent to an increment in θ . The associated perturbations to U_A and V are

$$dU_A = (W_A + w_A) \cos(\theta + \sigma) - W_A \cos \theta, \quad dV = (W_A + w_A) \sin(\theta + \sigma) - W_A \sin \theta.$$

Assuming that σ and w_A/W_A are small, we can express the perturbations as

$$dU_A = w_A \cos \theta - \sigma W_A \sin \theta, \quad dV = w_A \sin \theta + \sigma W_A \cos \theta. \quad (B.3)$$

The change in shock-normal velocity across the shock wave is given by Rankine-Hugoniot relations as

$$\frac{U_A}{U} = \frac{\frac{\gamma+1}{2}(U_A/a_A)^2}{1 + \frac{\gamma-1}{2}(U_A/a_A)^2}.$$

Assuming the upstream sound speed, $a_A = \text{constant}$, the change in the downstream shock-normal velocity due to the change in the upstream shock-normal velocity is given by

$$\frac{dU}{U} = -\frac{dU_A}{U_A} \left(1 - 2\frac{\gamma-1}{\gamma+1}m \right), \quad (B.4)$$

where $m = U_A/U$.

On the downstream side of the shock, the perturbation of the velocity in the ζ direction, $W = U \cos \theta' + V \sin \theta'$, is

$$w_\zeta = (U + dU) \cos(\theta' + \sigma) + (V + dV) \sin(\theta' + \sigma) - W, \quad (B.5a)$$

and the perturbation velocity in the η direction is

$$w_\eta = -(U + dU) \sin(\theta' + \sigma) + (V + dV) \cos(\theta' + \sigma), \quad (B.5b)$$

where,

$$\theta' = \tan^{-1}(m \tan \theta). \quad (B.5c)$$

Dividing both sides of (B.5a) and (B.5b) by U , expanding trigonometric identities using the assumption of small perturbations, and relating dU/U and dV/U to w_A/W_A by the use of (B.3) and (B.4), one gets

$$\begin{aligned} \frac{w_\zeta}{U} &= -\left(\frac{w_A}{W_A} - \frac{\sigma}{m} \tan \theta' \right) \left(1 - 2\frac{\gamma-1}{\gamma+1}m \right) \cos \theta' + \left(\frac{w_A}{W_A} \tan \theta' + m\sigma \right) \sin \theta' \\ \frac{w_\eta}{U} &= \left(\frac{w_A}{W_A} - \frac{\sigma}{m} \tan \theta' \right) \left(1 - 2\frac{\gamma-1}{\gamma+1}m \right) \sin \theta' + \left(\frac{w_A}{W_A} \tan \theta' + m\sigma \right) \cos \theta' - \sigma \sec \theta'. \end{aligned} \quad (B.6)$$

This is the general form of the boundary conditions for the governing equation (B.1) downstream of the shock wave.

In the present analysis, the perturbation w_A is a sinusoidal disturbance velocity (associated with the incident shear wave) parallel to W_A ,

$$\frac{w_A}{W_A} = \epsilon \cos k\eta_A$$

where k is the wave number and η_A is perpendicular to W_A . The corresponding argument for the refracted shear wave involves η and an altered wave number k' . The wave length of the disturbance should match along the shock front, that is, $k_2 = k'_2$. But $k_2 = k \cos \theta$ and $k'_2 = k' \cos \theta'$, and along the shock $\cos \theta = \eta_A/x_2$ and $\cos \theta' = \eta/x_2$. Therefore,

$$k\eta_A = k'\eta$$

and

$$\frac{w_A}{W_A} = \epsilon \cos k'\eta \quad (B.7)$$

along the shock. By geometry (Figure B.1), $k \cos \theta = k' \cos \theta'$. Since the disturbance is sinusoidal, the shock inclination σ is expected to be sinusoidal. For generality, a phase shift is allowed for, so that σ can be assumed to have the form

$$\sigma = \epsilon(a_S \cos k'\eta + b_S \sin k'\eta). \quad (B.8)$$

Substitution of (B.8) into the general form of the boundary conditions (B.6), yields the final form of the boundary conditions. The boundary conditions imposed by the shock wave on the perturbation velocity components parallel to ζ and η , immediately behind the shock wave are

$$\begin{aligned} \frac{w_\zeta}{\epsilon U} = & \left[\frac{a_S}{m} \left(1 - 2\frac{\gamma-1}{\gamma+1}m + m^2 \right) \sin \theta' - \left(1 - 2\frac{\gamma-1}{\gamma+1}m \right) \cos \theta' + \frac{\sin^2 \theta'}{\cos \theta'} \right] \cos k'\eta \\ & + \left[\frac{b_S}{m} \left(1 - 2\frac{\gamma-1}{\gamma+1}m + m^2 \right) \sin \theta' \right] \sin k'\eta \end{aligned}$$

$$\begin{aligned} \frac{w_\eta}{\epsilon U} = & \left[-\frac{a_S}{m} \left(1 + \frac{3-\gamma}{\gamma+1} m \right) \frac{\sin^2 \theta'}{\cos \theta'} + a_S(m-1) \cos \theta' + 2 \left(1 - \frac{\gamma-1}{\gamma+1} m \right) \sin \theta' \right] \cos k' \eta \\ & + \left[-\frac{b_S}{m} \left(1 + \frac{3-\gamma}{\gamma+1} m \right) \frac{\sin^2 \theta'}{\cos \theta'} + b_S(m-1) \cos \theta' \right] \sin k' \eta, \end{aligned} \quad (B.9)$$

respectively. In (B.8), the parameters a_S and b_S governing the shock inclination σ are undetermined.

For the solution of the governing equation (B.1), the vorticity term Ω on the right-hand side must be evaluated for the region behind the shock wave. Downstream of the shock, the stagnation enthalpy H and the entropy s (and hence the vorticity) are constant along streamlines, and in the linear theory the streamlines are approximated by lines of constant η . Thus, $\partial H / \partial \eta$ and $\partial s / \partial \eta$ may be evaluated at the shock and the result also holds downstream for the same η .

The total enthalpy upstream and at the shock is

$$\begin{aligned} H &= c_p T_A + \frac{1}{2} (W_A + w_A)^2 \\ &\simeq c_p T_A + \frac{1}{2} W_A^2 \left(1 + \frac{2w_A}{W_A} \right). \end{aligned}$$

Hence, along the shock

$$\frac{\partial H}{\partial \eta} = W_A^2 \frac{\partial}{\partial \eta} \left(\frac{w_A}{W_A} \right). \quad (B.10)$$

The entropy upstream of the shock is constant by virtue of the assumption of constant pressure and density there. The entropy change across the shock is given in terms of the upstream velocity by

$$\begin{aligned} s - s_A &= \frac{R}{\gamma - 1} \times \\ &\log \left\{ \left[\frac{2\gamma}{\gamma + 1} M^2 \cos^2 \theta + \frac{\gamma - 1}{\gamma + 1} \right] \left[\frac{(\gamma - 1) M^2 \cos^2 \theta + 2}{(\gamma + 1) M^2 \cos^2 \theta} \right]^\gamma \right\} \end{aligned}$$

[Thompson 1984]. Differentiating and expanding the above expression under the assumption of small perturbations gives

$$\frac{\partial s}{\partial \eta} = \frac{U^2}{T}(m-1)^2 \frac{\partial}{\partial \eta} \left(\frac{w_A}{W_A} - \sigma \tan \theta \right) \quad (B.11)$$

along the shock.

Substitution of (B.10) and (B.11) into the governing equation (B.1) yields

$$(1 - M^2)\psi_{\zeta\zeta} + \psi_{\eta\eta} = U m^2 \frac{\cos \theta'}{\cos^2 \theta} \frac{\partial}{\partial \eta} \left(\frac{w_A}{W_A} \right) - U \cos \theta' (m-1)^2 \frac{\partial}{\partial \eta} \left(\frac{w_A}{W_A} - \sigma \tan \theta \right), \quad (B.12)$$

where the right-hand side is evaluated along the shock ($x_1 = 0$) and expressed as function of η alone.

Substitution of (B.7) and (B.8) for w_A/W_A and σ for the sinusoidal form of the upstream disturbances converts (B.12) into

$$(1 - M^2)\psi_{\zeta\zeta} + \psi_{\eta\eta} = U \epsilon \left\{ -k' \left[\sec \theta' + 2(m-1) \cos \theta' + a_S \frac{(m-1)^2}{m} \sin \theta' \right] \sin k' \eta + k' b_S \frac{(m-1)^2}{m} \sin \theta' \cos k' \eta \right\}, \quad (B.13)$$

where the relation $\tan \theta' = m \tan \theta$ is used to eliminate θ . Equation (B.13) is the partial differential equation governing the flow downstream of the shock subject to the boundary conditions (B.9), which are

$$w_\zeta = \frac{\partial \psi}{\partial \eta}, \quad w_\eta = -(1 - M^2) \frac{\partial \psi}{\partial \zeta}.$$

B.1.2 Solutions to the Problem

The nature of the governing equation (B.13) depends on the sign of $(1 - M^2)$: for flows with $M < 1$ the partial differential equation is elliptic, and for flows with $M > 1$ it is hyperbolic. In the following, therefore, two different sets of solutions to (B.13) are presented.

Solution when Flow Downstream of the Shock is Subsonic, $M < 1$

The governing differential equation (B.13) can be written in abbreviated form as

$$\beta_w^2 \psi_{\zeta\zeta} + \psi_{\eta\eta} = -k' U \epsilon (A_S \sin k' \eta - B_S \cos k' \eta), \quad (B.14)$$

where

$$\begin{aligned} A_S &= \sec \theta' + 2(m-1) \cos \theta' + a_S \frac{(m-1)^2}{m} \sin \theta' \\ B_S &= b_S \frac{(m-1)^2}{m} \sin \theta' \\ \beta_w^2 &= 1 - M^2. \end{aligned} \quad (B.15)$$

A particular solution to (B.14) is

$$\psi_P = U \epsilon \left(\frac{A_S}{k'} \sin k' \eta - \frac{B_S}{k'} \cos k' \eta \right). \quad (B.16)$$

A homogeneous solution is

$$\begin{aligned} \psi_C &= U \epsilon e^{-\frac{k' \beta_w}{\beta^2} (\zeta \cos \theta' - \eta \sin \theta')} \cos \theta' \\ &\times \left\{ c' \cos \left[\frac{k' \cos \theta'}{\beta^2} (\zeta \sin \theta' + \beta_w^2 \eta \cos \theta') \right] + d' \sin \left[\frac{k' \cos \theta'}{\beta^2} (\zeta \sin \theta' + \beta_w^2 \eta \cos \theta') \right] \right\}, \end{aligned} \quad (B.17)$$

where c' and d' are the constants of integration, and $\beta^2 = 1 - U^2/a^2$.

The complete solution for the perturbation stream function $\psi = \psi_P + \psi_C$ contains four undetermined parameters, a_S, b_S, c' , and d' which are to be determined by matching velocity components, $w_\zeta = \partial\psi/\partial\eta$ and $w_\eta = -\beta_w^2 \partial\psi/\partial\zeta$ at the shock wave ($\zeta = 0$) using boundary conditions (B.9).

$$\begin{aligned} a_S &= m \frac{C_S E_S + D_S F_S}{C_S^2 + D_S^2}, & b_S &= m \frac{C_S F_S - D_S E_S}{C_S^2 + D_S^2}, \\ c' &= \frac{1}{k' \beta^2 \cos \theta'} \left(\frac{a_S}{m} D_S - F_S \right), & d' &= \frac{1}{k' \beta^2 \cos \theta'} \frac{b_S}{m} D_S, \end{aligned} \quad (B.18)$$

where

$$\begin{aligned} C_S &= \left(\frac{\gamma-1}{\gamma+1} + \frac{3-\gamma}{\gamma+1} m \right) \tan \theta' - \left[(m-1)^2 + \frac{2(m-1)}{\gamma+1} \right] \sin \theta' \cos \theta' \\ D_S &= \frac{\beta_w}{\beta^2} (m-1) \left[1 + (m-1) \cos^2 \theta' \right] \\ E_S &= 2 \left(1 - \frac{\gamma-1}{\gamma+1} m \right) + 2(m-1) \frac{\beta_w^2 \cos^2 \theta'}{\beta^2} \\ F_S &= \frac{\beta_w}{\beta^2} \left[2(m-1) \sin \theta' \cos \theta' \right]. \end{aligned} \quad (B.19)$$

Solution when Flow Downstream of the Shock is Supersonic, $M > 1$

The particular solution to (B.13) is the same as that for $M < 1$, which is

$$\psi_P = \frac{U \epsilon A_S}{k'} \sin k' \eta,$$

where the fact that the final solution yields $b_S = 0$ (and hence $B_S = 0$) is used to delete B_S term at the outset.

The complementary solution satisfying (B.13) has the general form of

$$\psi_C = f(\zeta + \beta_w \eta) + g(\zeta - \beta_w \eta),$$

where $\beta_w^2 = M^2 - 1$. The function f represent Mach waves inclined downward by the Mach angle μ_M from the ζ -axis and the function g represents Mach waves inclined upward by the same angle. For upstream shear waves with inclination $0 \leq \theta \leq \pi/2$, the g -family of Mach waves represent disturbances overtaking the shock wave from behind (propagating upstream). However, its propagation toward upstream beyond the shock wave is unphysical, since the Mach waves can only propagate with the speed of sound of the medium relative to the mean flow speed while the upstream mean flow speed is always supersonic, $W_A/a_A > 1$: Therefore, g -function must be zero for upstream shear waves with inclination $0 \leq \theta \leq \pi/2$. For the same reason, f -function must be zero for upstream shear waves with inclination $\pi/2 \leq \theta \leq \pi$. In the following, the discussion is limited to the specified range $0 \leq \theta \leq \pi/2$ due to the symmetry.

From (B.9) with $b_S = 0$, the function f reduces to

$$f \sim \sin[\alpha(\zeta + \beta_w \eta)].$$

Along the shock front, where $\zeta = \eta \tan \theta'$,

$$\alpha(\zeta + \beta_w \eta) = k' \eta.$$

A suitable complementary function is therefore

$$\psi_C = \frac{U \epsilon c''}{k'} \sin \frac{k'(\zeta + \beta_w \eta)}{\beta_w + \tan \theta'},$$

where c'' is a constant of integration.

The complete solution for the perturbation stream function is

$$\psi = \psi_P + \psi_C = \frac{U \epsilon}{k'} \left[A_S \sin k' \eta + c'' \sin \frac{k'(\zeta + \beta_w \eta)}{\beta_w + \tan \theta'} \right], \quad (B.20)$$

where the two arbitrary parameters a_S (occurring in A_S of (B.15)) and c'' remain to be determined. These two parameters are determined by matching velocity components derived from (B.20) with the boundary conditions given in (B.9). The resulting expressions for the parameters are

$$a_S = m \frac{C'_S + G_S F'_S}{E'_S + G_S D'_S}, \quad c'' = \frac{1}{\beta_w \cos \theta'} \left(\frac{a_S}{m} D'_S - F'_S \right), \quad (B.21)$$

where

$$\begin{aligned} C'_S &= 2 \frac{\gamma - 1}{\gamma + 1} m - 2[1 + (m - 1) \cos^2 \theta'] \\ D'_S &= (m - 1)[1 + (m - 1) \cos^2 \theta'] \\ E'_S &= (m - 1)^2 \sin \theta' \cos \theta' - \left(1 + \frac{3 - \gamma}{\gamma + 1} m \right) \tan \theta' \\ F'_S &= 2(m - 1) \sin \theta' \cos \theta' \\ G_S &= \frac{1 - \beta_w \tan \theta'}{\beta_w + \tan \theta'} = \tan(\mu_M - \theta') \end{aligned} \quad (B.22)$$

with the Mach angle $\mu_M = \cot^{-1} \beta_w$.

B.1.3 Summary and Discussion

The interaction of a plane shear wave and a shock wave is schematically shown in Figure 2.1. The method of predicting the flow field downstream of the shock wave, produced by convection of an oblique sinusoidal shear wave through the shock, has been briefly described. In this section, the main results are summarized in more compact form, and are simplified to help the geometrical interpretation.

Criterion on M

Although the streamwise velocity U downstream of the specified normal shock is always subsonic, the nature of the flow depends primarily on the streamwise

velocity in the transformed frame of reference (Figures B.2 and 2.1), which may be subsonic or supersonic. Two forms of the solution for all flow quantities thus appear: one for the subsonic range $M < 1$ and the other for the supersonic range $M > 1$. Since M depends on the initial Mach number U_A/a_A and the inclination angle θ , the equation for the dividing line $M = 1$ gives a relation between the critical value of θ and the upstream Mach number U_A/a_A as

$$\theta_{cr} = \pm \tan^{-1} \sqrt{\frac{(\gamma + 1)(m - 1)}{2m^2}}, \quad (B.23)$$

where $m = U_A/U$ is determined by U_A/a_A .

For waves incident at angles less than the critical angle, a pressure wave generated at time t catches up with that generated at time $t + \delta t$, because the upstream shear wave travels along the shock wave slower than the pressure wave generated: $U_A^2 \tan^2 \theta < a^2 - U^2$. Note that the upstream shear wave travels with the velocity $U_A \tan \theta$ along the shock wave, and the generated pressure wave propagates radially outward with the speed of sound a relative to the mean flow speed, U . In this case, pressure waves are superposed onto each other, and disable each pressure wave from propagating independently, resulting in an exponential attenuation in the shock-normal direction. For waves incident at angles larger than the critical angle, the pressure waves generated at different times propagate independently from the others, because $U_A^2 \tan^2 \theta > a^2 - U^2$.

Downstream Velocity Field

By using (B.2), for $M < 1$,

$$\begin{aligned} \frac{w_\zeta}{|w_A|} &= S \cos[k'_2(x_2 - x_1 \tan \theta') + \delta_s] + \Pi(x_1) \cos[k'_2(x_2 - x_1 \tan \theta'') + \delta_p] \\ \frac{w_\eta}{|w_A|} &= \beta_w \Pi(x_1) \sin[k'_2(x_2 - x_1 \tan \theta'') + \delta_p], \end{aligned} \quad (B.24)$$

where $|w_A| = \epsilon W_A$ is the amplitude of the upstream sinusoidal velocity and

$$k'_2 = k' \cos \theta' = k \cos \theta$$

$$S = \frac{\cos \theta}{m} \sqrt{A_S^2 + B_S^2}$$

$$\Pi(x_1) = \frac{\cos \theta}{m} \frac{\sqrt{c_S^2 + d_S^2}}{\beta} e^{-x_1 k'_2 \beta_w / \beta^2}$$

$$\delta_s = \tan^{-1} \left(\frac{-B_S}{A_S} \right)$$

$$\theta'' = -\tan^{-1} \frac{\bar{U}^2 \tan \theta'}{\beta^2}$$

$$\delta_p = \tan^{-1} \frac{c_S \beta_w - d_S \tan \theta'}{d_S \beta_w + c_S \tan \theta'}$$

with $c_S = c' k' \beta_w \cos \theta'$, $d_S = d' k' \beta_w \cos \theta'$. The functions A_S and B_S are given by (B.15), and a_S, b_S, c' , and d' are the constants of integration given in (B.18).

For $M > 1$,

$$\begin{aligned} \frac{w_\zeta}{|w_A|} &= S \cos k'_2(x_2 - x_1 \tan \theta') + \Pi \cos k'_2(x_2 - x_1 \tan \theta'') \\ \frac{w_\eta}{|w_A|} &= \beta_w \Pi \cos k'_2(x_2 - x_1 \tan \theta''), \end{aligned} \quad (B.25)$$

where,

$$S = \frac{\cos \theta}{m} A_S$$

$$k'_2 = k' \cos \theta' = k \cos \theta$$

$$\Pi = \frac{\cos \theta}{m} c_S \frac{\sin \mu_M}{\cos(\theta' - \mu_M)}$$

$$\begin{aligned}\theta'' &= \theta' - \mu_M \\ \mu_M &= \cot^{-1} \beta_w\end{aligned}$$

with $c_S = c'' \beta_w \cos \theta'$. The function A_S is still given by (B.15), and a_S and c'' are evaluated in (B.21).

The cosine in the first terms of (B.24) and (B.25) are constant along lines $x_2 - x_1 \tan \theta' = \text{constant}$, which are inclined at an angle θ' with the horizontal and are thus parallel to the ζ -axis. Since w_ζ is parallel to ζ and w_η is parallel to η , the first terms represent contribution to the vorticity wave.

The remaining terms in (B.24) and (B.25) involving the factor Π correspond to an irrotational velocity field, or potential flow. If derivation is traced backward, the Π -terms are found to originate from the complementary solution, which is a solution with zero vorticity, $\Omega = 0$. These remaining terms in (B.24) and (B.25) represent contributions from pressure waves. For the case $M > 1$, this pressure wave propagates in the form of Mach waves with the speed of sound relative to the stream velocity. For the case $M < 1$, the resultant pressure pattern does not propagate with the speed of sound, but it can be represented as a superposition of cylindrical sound waves which individually propagate with sonic speed. The resultant perturbation velocity attenuates exponentially with the distance from the shock wave, x_1 (see (B.24)).

Shock Wave Perturbation

From (B.8), the local perturbation in the shock inclination angle can be represented as

$$\sigma = \epsilon(a_S \cos k'_2 x_2 + b_S \sin k'_2 x_2),$$

where a_S and b_S are evaluated in (B.18) for $M < 1$ and (B.21) for $M > 1$ ($b_S = 0$ for $M > 1$).

At any point along the shock, x_2 , the local shock deflection ξ from the plane $x_1 = 0$ is obtained by integration of the slope $\sigma \simeq \partial \xi / \partial x_2$:

$$\begin{aligned}\xi &= \int \sigma dx_2 \\ &= |w_A| \frac{\sqrt{a_S^2 + b_S^2}}{kU_A} \cos(k'_2 x_2 + \delta_{sh})\end{aligned}\quad (B.26)$$

where $\delta_{sh} = \tan^{-1}(a_S/b_S)$ is the phase shift.

For a given wave length, the amplitude of this sinusoidal corrugation in the shock wave is proportional to the factor $\sqrt{a_S^2 + b_S^2}$ and also to the upstream turbulence intensity.

B.2 Application of LIA to Shock-Turbulence Interaction

Homogeneous turbulence can be represented as a spectrum of waves with random orientations and wave lengths. In a solenoidal (or incompressible) velocity field, a velocity vector in Fourier space is perpendicular to its corresponding wave number vector due to the continuity constraint. (Any incompressible velocity field can be decomposed only into vorticity waves.) The velocity vector corresponding to a vorticity wave in the Fourier space meets this constraint, as is schematically shown in Figure 2.1. When turbulence is convected into a shock, the individual vorticity waves are abruptly altered producing acoustic and entropy waves downstream of the shock. This process is schematically shown in Figure 2.1. The amplitude and wave length of downstream waves can be related to those of the upstream vorticity wave through linear theory. Therefore, given the upstream statistics of a solenoidal turbulence field, we can obtain its downstream turbulence statistics.

B.2.1 Turbulence Modification

An upstream vorticity wave is associated with a velocity field which can be decomposed into three velocity components in cylindrical coordinates as shown in Figure 2.1. Each velocity component can be represented in terms of Fourier coefficients as

$$du_i = d\hat{u}_i \exp(ik \cdot x), \quad (B.27)$$

where the wave number vector \mathbf{k} lies in the x_1, r -plane, making an angle θ with the r -axis. The velocity of the refracted vorticity wave can also be expressed as

$$du_1' = d\hat{u}_1' \exp(i\mathbf{k}' \cdot \mathbf{x}), \quad (B.28)$$

where \mathbf{k}' is the new wave number vector, making an angle θ' with the r -axis. The radial components of \mathbf{k}' and \mathbf{k} are equal, and the dependence of \mathbf{k}' on \mathbf{k} is expressed through the dependence of θ' on θ :

$$\theta' = \tan^{-1}(m \tan \theta), \quad (B.29)$$

where $m = J^{-1} > 1$ is the density ratio across the shock wave.

Amplitudes of downstream velocity components associated with the *vorticity* wave can be related to those of upstream velocity components as

$$\begin{aligned} d\hat{u}_1' &= X d\hat{u}_1, \\ d\hat{u}_r' &= Y d\hat{u}_r, \\ d\hat{u}_\phi' &= d\hat{u}_\phi, \end{aligned} \quad (B.30)$$

where

$$X = Sc^{i\delta} \frac{\cos \theta'}{\cos \theta}, \quad Y = Sc^{i\delta} \frac{\sin \theta'}{\sin \theta}. \quad (B.31)$$

Here, we have used (B.24) with

$$w_A = \frac{u_A}{\cos \theta} \quad \text{and} \quad w_\zeta = \frac{u_1}{\cos \theta'}.$$

Interaction of a vorticity wave with a shock also generates an acoustic wave downstream of the shock. For a small inclination angle θ of the upstream vorticity wave, this acoustic wave attenuates exponentially with the distance from the shock. On the other hand, for inclinations greater than a certain critical value θ_{cr} , the acoustic wave propagates without attenuation.

The *acoustic* velocity field can be expressed in the form

$$du_1'' = d\hat{u}_1'' \exp(i\mathbf{k}'' \cdot \mathbf{x}), \quad (B.32)$$

where \mathbf{k}'' is the wave number vector, making an angle θ'' with the r -axis. Again the radial component matches that of \mathbf{k} . The amplitude of downstream velocity components associated with the acoustic wave can be related to those of upstream velocity components as

$$\begin{aligned} d\hat{u}_1'' &= \Xi d\hat{u}_1, \\ d\hat{u}_r'' &= \Gamma d\hat{u}_r, \\ d\hat{u}_\phi'' &= 0, \end{aligned} \quad (B.33)$$

where

$$\begin{aligned} \Xi &= \Pi e^{i\delta_p} \frac{\cos \theta' - e^{in\pi/2} \beta_w \sin \theta'}{\cos \theta} \\ \Gamma &= \Pi e^{i\delta_p} \frac{\sin \theta' + e^{in\pi/2} \beta_w \cos \theta'}{\sin \theta} \end{aligned} \quad (B.34)$$

with $n = 1$ for $0 \leq \theta \leq \theta_{cr}$ and $n = 0$ for $\theta_{cr} \leq \theta \leq \pi/2$. That is, the transfer functions in (B.31) and (B.34) are valid for both subsonic and supersonic cases with the appropriate choices of δ_s and δ_p .

Turbulence components in the Cartesian coordinates are obtained using the relations

$$du_2 = du_r \cos \phi - du_\phi \sin \phi, \quad du_3 = du_r \sin \phi + du_\phi \cos \phi, \quad (B.35)$$

and conversely

$$du_r = du_2 \cos \phi + du_3 \sin \phi, \quad du_\phi = -du_2 \sin \phi + du_3 \cos \phi. \quad (B.36)$$

The same relations apply to the downstream velocity components du' and du'' . Using (B.30) and (B.33) - (B.36), we can represent downstream waves in terms of the amplitude and wave number of the corresponding upstream wave. Upstream and downstream vorticity waves represented in (B.27) and (B.28) can be related as

$$\begin{aligned}
d\hat{u}'_1 &= X d\hat{u}_1, \\
d\hat{u}'_2 &= Y d\hat{u}_r \cos\phi - d\hat{u}_\phi \sin\phi, \\
d\hat{u}'_3 &= Y d\hat{u}_r \sin\phi + d\hat{u}_\phi \cos\phi.
\end{aligned} \tag{B.37}$$

The velocity fields of the corresponding acoustic wave downstream of the shock is expressed in (B.32), where

$$\begin{aligned}
d\hat{u}''_1 &= \Xi d\hat{u}_1, \\
d\hat{u}''_2 &= \Gamma d\hat{u}_r \cos\phi, \\
d\hat{u}''_3 &= \Gamma d\hat{u}_r \sin\phi.
\end{aligned} \tag{B.38}$$

The quantity $u_i(\mathbf{x})$ can be obtained from the Fourier transform as

$$\begin{aligned}
u_i(\mathbf{x}) &= \int du_i(\mathbf{k}, \mathbf{x}) \\
&= \int \exp(i\mathbf{k} \cdot \mathbf{x}) d\hat{u}_i(\mathbf{k}),
\end{aligned} \tag{B.39}$$

where the triple integration is extended over $(-\infty, \infty)$ in each component of $\mathbf{k} = (k_1, k_2, k_3)$. By defining

$$d\hat{u}_i(\mathbf{k}) = \hat{u}_i(\mathbf{k}) d\mathbf{k}, \tag{B.40}$$

we can rewrite (B.39) as

$$u_i(\mathbf{x}) = \int \hat{u}_i(\mathbf{k}) \exp(i\mathbf{k} \cdot \mathbf{x}) d\mathbf{k}. \tag{B.41}$$

If the field is homogeneous, the two-point correlation, $\overline{u_i(\mathbf{x})u_j(\mathbf{x}')}$ can be represented as

$$\overline{u_i(\mathbf{x})u_j(\mathbf{x}')} = \int \int \exp[i(\mathbf{k} \cdot \mathbf{x} + \mathbf{l} \cdot \mathbf{x}')] \overline{\hat{u}_i(\mathbf{k})\hat{u}_j(\mathbf{l})} d\mathbf{k} d\mathbf{l}, \tag{B.42}$$

where the triple integrations are extended over $(-\infty, \infty)$ in each component of \mathbf{k} and \mathbf{l} , and the overline $\overline{(\cdot)}$ means the average over an ensemble. By the use of the orthogonality of the Fourier modes, (B.42) can be rewritten as

$$\overline{u_i(\mathbf{x})u_j(\mathbf{x}')}\overline{=} \int \exp(i\mathbf{k} \cdot \mathbf{r}) \overline{\hat{u}_i(\mathbf{k})\hat{u}_j^*(\mathbf{k})}d\mathbf{k}, \quad (B.43)$$

where $\mathbf{r} = \mathbf{x}' - \mathbf{x}$, $\hat{u}_j^*(\mathbf{k})$ is the complex conjugate of $\hat{u}_j(\mathbf{k})$. The energy spectrum tensor $E_{ij}(\mathbf{k})$, the spectral density of $\overline{u_i u_j}$, is defined as

$$E_{ij}(\mathbf{k}) = \overline{\hat{u}_i(\mathbf{k})\hat{u}_j^*(\mathbf{k})} \quad (B.44)$$

so that

$$\overline{u_i u_j} = \int E_{ij}(\mathbf{k})d\mathbf{k}. \quad (B.45)$$

In order to predict the changes in the second-order turbulence statistics through the interaction, we multiply both sides of (B.37) by their complex conjugates and add the last two, resulting in

$$\begin{aligned} d\hat{u}'_1 d\hat{u}_1'^* &= |X|^2 d\hat{u}_1 d\hat{u}_1^*, \\ d\hat{u}'_2 d\hat{u}_2'^* + d\hat{u}'_3 d\hat{u}_3'^* &= |Y|^2 d\hat{u}_r d\hat{u}_r^* + d\hat{u}_\phi d\hat{u}_\phi^*. \end{aligned} \quad (B.46)$$

From geometry (see Figure 2.1),

$$\begin{aligned} d\hat{u}_r &= d\hat{u}_1 \tan\theta, \\ d\hat{u}_r^* &= d\hat{u}_1^* \tan\theta, \end{aligned} \quad (B.47)$$

and also from the coordinate transformation (B.35) we have,

$$d\hat{u}_r d\hat{u}_r^* + d\hat{u}_\phi d\hat{u}_\phi^* = d\hat{u}_2 d\hat{u}_2^* + d\hat{u}_3 d\hat{u}_3^*. \quad (B.48)$$

Thus, using relations (B.40), (B.45), and (B.48), the ensemble average of (B.46) can be expressed as

$$\begin{aligned}\overline{\widehat{u}'_1 \widehat{u}'_1^*} dk' &= |X|^2 \overline{\widehat{u}_1 \widehat{u}_1^*} dk, \\ (\overline{\widehat{u}'_2 \widehat{u}'_2^*} + \overline{\widehat{u}'_3 \widehat{u}'_3^*}) dk' &= (|Y|^2 - 1) \tan^2 \theta \overline{\widehat{u}_1 \widehat{u}_1^*} dk + (\overline{\widehat{u}_2 \widehat{u}_2^*} + \overline{\widehat{u}_3 \widehat{u}_3^*}) dk. \quad (B.49)\end{aligned}$$

If operations similar to those performed on (B.37) are applied to (B.38), we get

$$\begin{aligned}\overline{\widehat{u}''_1 \widehat{u}''_1^*} dk'' &= |\Xi|^2 \overline{\widehat{u}_1 \widehat{u}_1^*} dk, \\ (\overline{\widehat{u}''_2 \widehat{u}''_2^*} + \overline{\widehat{u}''_3 \widehat{u}''_3^*}) dk'' &= |\Gamma|^2 \tan^2 \theta \overline{\widehat{u}_1 \widehat{u}_1^*} dk. \quad (B.50)\end{aligned}$$

The mean-square velocity components associated with vorticity waves follow directly from integration of the spectral density. Integration of both sides of (B.49) yields

$$\begin{aligned}\overline{u_1'^2} &= \int |X|^2 E_{11}(\mathbf{k}) d\mathbf{k}, \\ \overline{u_2'^2} + \overline{u_3'^2} &= \overline{u_1^2} + \overline{u_2^2} + \int (|Y|^2 - 1) \tan^2 \theta E_{11}(\mathbf{k}) d\mathbf{k}. \quad (B.51)\end{aligned}$$

Similarly, integration of (B.50) yields the mean-square fluctuating velocity components in acoustic waves:

$$\begin{aligned}\overline{u_1''^2} &= \int |\Xi|^2 E_{11}(\mathbf{k}) d\mathbf{k}, \\ \overline{u_2''^2} + \overline{u_3''^2} &= \int |\Gamma|^2 \tan^2 \theta E_{11}(\mathbf{k}) d\mathbf{k}. \quad (B.52)\end{aligned}$$

Thus, the mean-square velocity fluctuations behind the shock are given in terms of those ahead of the shock, the single-wave transfer functions X, Y, Ξ , and Γ , and the longitudinal spectral density, $E_{11}(\mathbf{k})$. Note that the single-wave transfer functions are functions of k and θ , where $k = |\mathbf{k}|$.

Due to the interaction of turbulence with a shock wave, aerodynamic noise is produced behind the shock wave in the form of fluctuating pressure, p' . The fluctuating acoustic pressure is related to the velocity fluctuation as

$$p' = -\rho W w_P$$

or

$$\frac{p'}{p^D} = -\gamma M^2 \frac{w_P}{W}, \quad (B.53)$$

where w_P is the ζ -component of the perturbation velocity associated with the pressure fluctuation, and p^D is the mean downstream pressure. (B.53) can be recognized as the linearized Bernoulli equation applied to the velocity in the acoustic wave.

Substituting for M and W , and using (B.24) and (B.25) for w_P without vorticity wave contribution, (B.53) results in

$$\frac{p'}{p^D} = -\frac{|w_A|}{U_A} \frac{2\gamma m}{(\gamma+1)m - (\gamma-1)} \frac{\Pi}{\cos \theta'} \cos[k'_2(x_2 - x_1 \tan \theta'') + \delta_p], \quad (B.54)$$

where downstream pressure wave is expressed in terms of the shock strength for the corresponding upstream vorticity wave ($U_A = U_1$). (B.54) can be interpreted as the relation between the Fourier coefficients of the downstream pressure wave and upstream velocity fluctuations:

$$\frac{\hat{p}}{p^D} = -\frac{\hat{u}_1 / \cos \theta}{U_1} \frac{2\gamma m}{(\gamma+1)m - (\gamma-1)} \frac{\Pi}{\cos \theta'} \exp(i\delta_p), \quad (B.55)$$

where \hat{p} and \hat{u}_1 are the Fourier coefficients of the pressure and streamwise velocity fluctuations, respectively. Pressure fluctuations can be calculated using the relation:

$$\overline{p'^2} = \int \hat{p}(\mathbf{k}) \hat{p}^*(\mathbf{k}) d^3 \mathbf{k}, \quad (B.56)$$

where \hat{p}^* is the complex conjugate of \hat{p} .

Following a similar procedure, we can relate the downstream power spectra to the upstream power spectra, and all their derived quantities of interest (such as two-point correlations, turbulence length scales, and dissipation rate) to their upstream counterparts.

B.2.2 Shock Front Distortion

The local perturbation in the shock front inclination angle σ in (B.8) can be considered as the shock inclination when r -axis in Figure 2.1 coincides with x_2 -axis. In general, the shock wave inclinations in x_1x_2 and x_1x_3 -planes, σ_2 and σ_3 respectively, can be expressed as

$$\sigma_2 = \sigma \cos \phi \quad \text{and} \quad \sigma_3 = \sigma \sin \phi.$$

By the use of (B.8), $\underline{\sigma} = (\sigma_2, \sigma_3)$ can be written as

$$\begin{aligned} \underline{\sigma} &= \nabla_h \xi \\ &= |\hat{\sigma}| \frac{\mathbf{k}_h}{|\mathbf{k}_h|} \exp[i(\mathbf{k}_h \cdot \mathbf{x}_h + \delta_{sh})], \end{aligned} \quad (B.57)$$

where

$$|\hat{\sigma}| = \frac{\hat{u}_1}{U_1} \sqrt{a_S^2 + b_S^2}, \quad (B.58)$$

$\nabla_h = (\partial/\partial x_2, \partial/\partial x_3)$, $\mathbf{k}_h = (k_2, k_3)$, $\mathbf{x}_h = (x_2, x_3)$, ξ is the local shock front displacement from the mean shock position; $U_1 (= U_A)$ is the mean upstream flow speed.

For isotropic turbulence, variances of the local inclination angles are related by:

$$\begin{aligned} \overline{\sigma^2} &= \overline{\sigma_2^2} + \overline{\sigma_3^2} \\ &= 2\overline{\sigma_2^2}. \end{aligned} \quad (B.59)$$

Using (B.57), (B.58) and (B.59), we can express the variance $\overline{\sigma_2^2}$ for an isotropic upstream turbulence as

$$\begin{aligned}
\overline{\sigma_2^2} &= \frac{1}{2} \overline{\sigma^2} \\
&= \frac{1}{2} \int \overline{\widehat{\sigma} \widehat{\sigma}^*} dk \\
&= \frac{1}{2U_1^2} \int \overline{\widehat{u}_1 \widehat{u}_1^*} (a_S^2 + b_S^2) dk,
\end{aligned} \tag{B.60}$$

where $\overline{\widehat{u}_1 \widehat{u}_1^*} = E_{11}(\mathbf{k})$ and triple integration is extended over the wave number space. We can evaluate this integral numerically in the spherical coordinate system defined as

$$k_1 = k \sin \theta, \quad k_2 = k \cos \theta \cos \phi, \quad k_3 = k \cos \theta \sin \phi, \tag{B.61}$$

and

$$d\mathbf{k} = k^2 \cos \theta \, d\phi d\theta dk. \tag{B.62}$$

In this coordinate system, $E_{11}(\mathbf{k})$ can be expressed as

$$E_{11}(k, \theta, \phi) = \frac{E(k)}{4\pi k^2} \cos^2 \theta, \tag{B.63}$$

where

$$\int E(k) dk = \frac{q^2}{2} = \frac{3}{2} u_o^2, \tag{B.64}$$

and u_o is the *rms* of the velocity fluctuations in one direction.

Now (B.60) can be rewritten as

$$\begin{aligned}
\overline{\sigma_2^2} &= \frac{1}{2U_1^2} \int_0^\infty \int_0^\pi \int_0^{2\pi} \frac{E(k)}{4\pi k^2} \cos^2 \theta (a_S^2 + b_S^2) k^2 \cos \theta d\phi d\theta dk \\
&= \frac{1}{2U_1^2} \int_0^\infty E(k) dk \int_0^{\pi/2} (a_S^2 + b_S^2) \cos^3 \theta d\theta \\
&= \frac{3}{4} \left(\frac{u_o}{U_1} \right)^2 \int_0^{\pi/2} (a_S^2 + b_S^2) \cos^3 \theta d\theta,
\end{aligned} \tag{B.65}$$

where symmetry in θ is used in the evaluation of the integral. Note that the result of the integration is independent of the specific form of the upstream energy spectrum, $E(k)$. Since the remaining integral is only a function of the upstream Mach number, the variance of the shock inclination angle is dependent only on turbulence intensity and the Mach number upstream of the shock wave.

Using (B.57), the local shock displacement ξ in (B.26) can be expressed as:

$$\xi = \frac{1}{ik_h} |\hat{\sigma}| \exp[i(\mathbf{k}_h \cdot \mathbf{x}_h + \delta_{sh})]. \quad (B.66)$$

The local shock front curvature in the x_2 direction, $\kappa_2 = \partial^2 \xi / \partial x_2^2$, can be obtained by differentiation of (B.57) as

$$\kappa_2 = i \frac{k_2^2}{k_h} |\hat{\sigma}| \exp[i(\mathbf{k}_h \cdot \mathbf{x}_h + \delta_{sh})]. \quad (B.67)$$

Using (B.58) and (B.66), and following the same procedure which was used to determine the variance of the local shock inclination angle, we can obtain the variance of the local shock displacement:

$$\begin{aligned} \overline{\xi^2} &= \frac{1}{U_1^2} \int_0^\infty \int_0^\pi \int_0^{2\pi} \frac{E(k)}{4\pi k^2} \cos^2 \theta \frac{1}{k^2 \cos^2 \theta} (a_S^2 + b_S^2) k^2 \cos \theta d\phi d\theta dk \\ &= \frac{1}{U_1^2} \int_0^\infty \frac{E(k)}{k^2} dk \int_0^{\pi/2} (a_S^2 + b_S^2) \cos \theta d\theta. \end{aligned} \quad (B.68)$$

Using (B.58) and (B.67), we find the variance of the shock front curvature in the x_2 direction to be

$$\begin{aligned} \overline{\kappa_2^2} &= \frac{1}{2U_1^2} \int_0^\infty \int_0^\pi \int_0^{2\pi} \frac{E(k)}{4\pi k^2} \cos^2 \theta (k^2 \cos^2 \theta \cos^4 \phi) (a_S^2 + b_S^2) k^2 \cos \theta d\phi d\theta dk \\ &= \frac{3}{16U_1^2} \int_0^\infty k^2 E(k) dk \int_0^{\pi/2} (a_S^2 + b_S^2) \cos^5 \theta d\theta. \end{aligned} \quad (B.69)$$

Note that variances of shock front displacement and shock front curvature are dependent on the shape of the upstream turbulence spectrum as well as on the mean flow Mach number and turbulence intensity upstream of the shock wave.

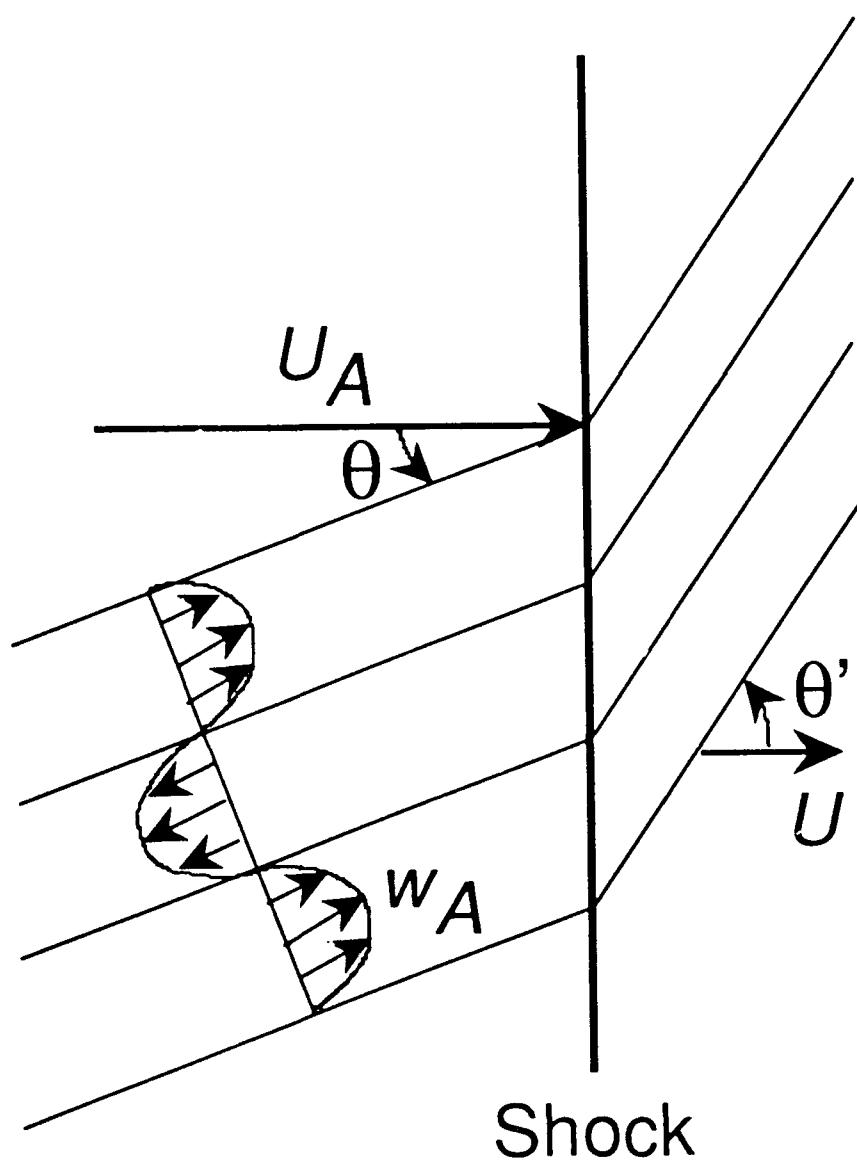


FIGURE B.1. Convection of plane oblique sinusoidal shear wave through the shock wave.

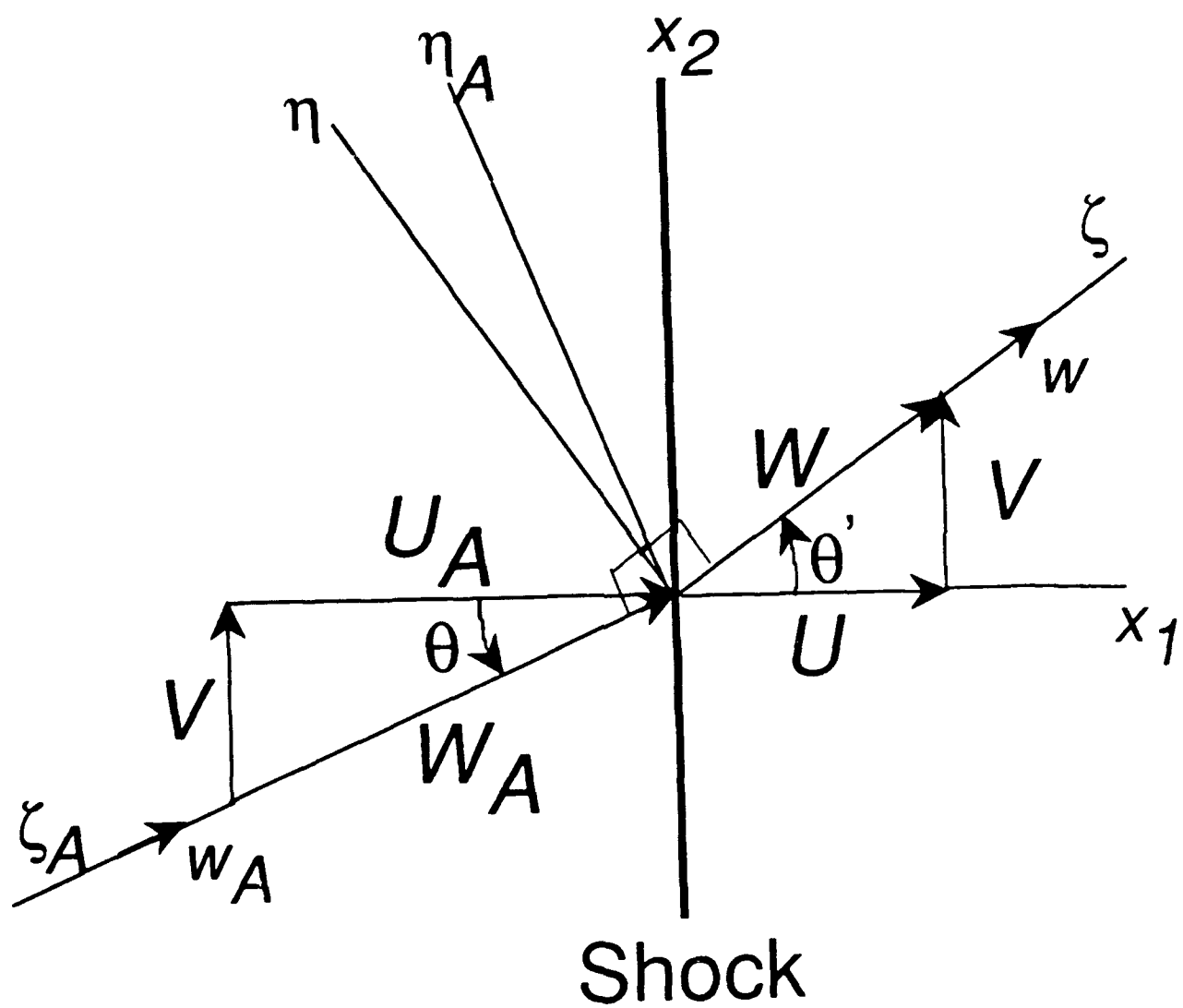


FIGURE B.2. Symbols and coordinate systems used in LIA.

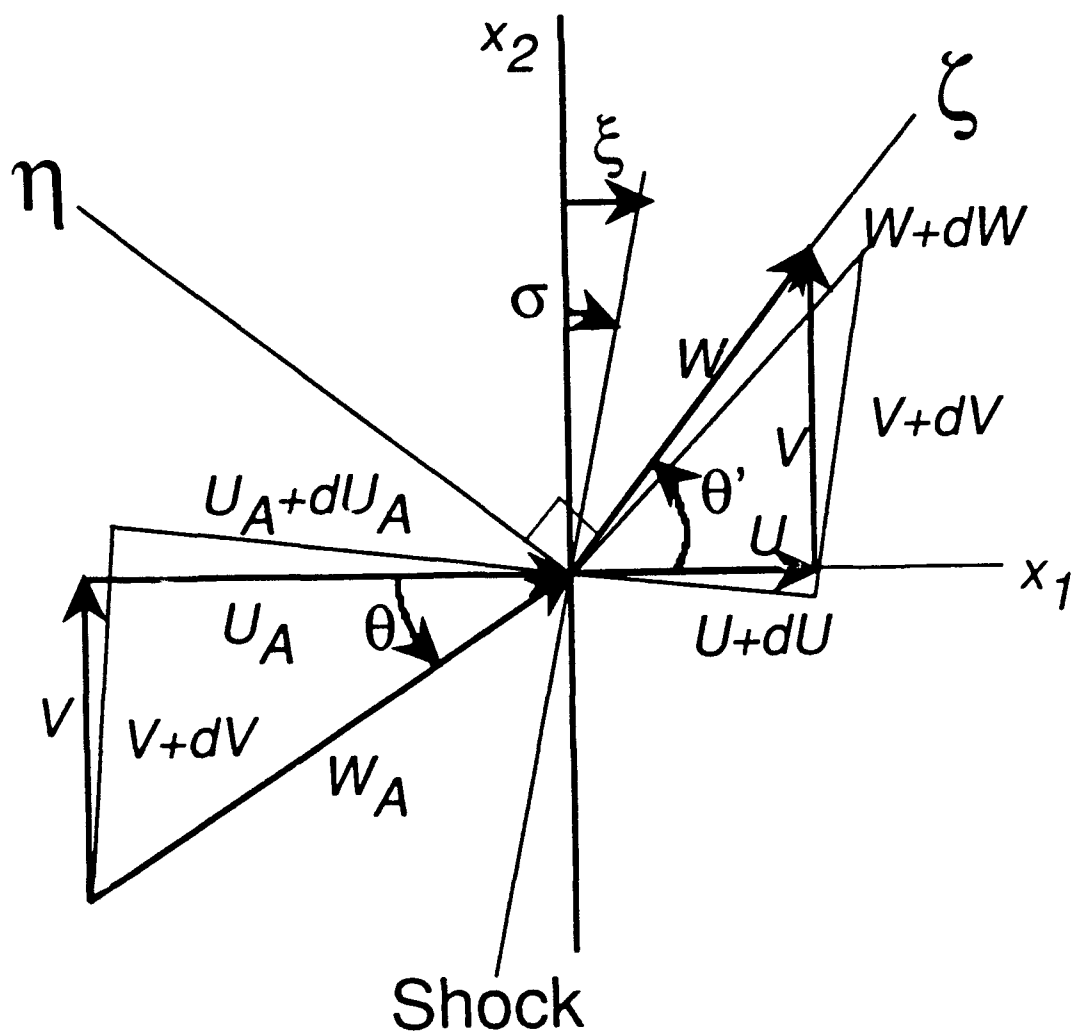


FIGURE B.3. Geometrical relations across the shock, with and without perturbation σ in the shock inclination angle.

APPENDIX C

REMOVAL OF ALIASING ERRORS IN SIMULATION OF COMPRESSIBLE FLOWS

In computational fluid mechanics aliasing errors arise from the non-linear terms. The product of two quantities resolved on a mesh of size N results in a function with higher frequency components that can not be resolved on the mesh. These components are then "aliased" back in the computational mesh and contaminate the solution. Aliasing errors have been reported to lead to inaccurate simulations [Kim *et al.* 1987, Spalart 1988].

In a simulation of incompressible Navier-Stokes equations, aliasing errors are produced from the product of two velocity components in the convective term. (For simplicity, we only consider the one-dimensional problem and choose the Fourier collocation method as the numerical differentiation scheme.) A real function defined on N grid points can be represented with $N/2$ complex Fourier coefficients. The multiplication of two variables generates contributions up to the wave number N which is beyond the resolution limit. These contributions lead to aliasing errors. Since we know the exact origin and destination of aliasing errors we can remove them. First, we expand the wave number domain from $(-N/2 + 1, N/2)$ to $(-3N/4 + 1, 3N/4)$ with zero Fourier coefficients for the expanded modes. Multiplication is then performed in the physical space with the expanded grid. The result is then Fourier transformed and the additional modes are eliminated.

In a simulation of compressible Navier-Stokes equations using conservative variables, aliasing errors arise from both multiplication and division operations. Division is necessary to get the velocity components and temperature from the conservative variables. Removal of aliasing errors stemming from multiplication is possible in an analogous manner as in the incompressible case. However, we can not remove all aliasing errors explicitly, since division distributes the aliasing error throughout the wave number domain.

Good spatial resolution is helpful to minimize the effect of aliasing, since the aliasing errors are not significant for a well-resolved flow [Canuto *et al.* 1988]. Using a numerical scheme which conserves physically important quantities, such

as mass, kinetic energy, and total energy, helps to control the *instability* resulting from aliasing error [Feiereisen *et al.* 1981, Blaisdell *et al.* 1990].

In the following, we propose a procedure for alias-free simulations of compressible turbulence. The main difficulty in controlling aliasing errors stems from the division by density to yield velocity components and temperature from conservative variables. If the equation for the specific volume is solved instead of the density equation for mass conservation, we can multiply by the specific volume wherever division by density is needed. The equation for the specific volume, $v = 1/\rho$, is:

$$\frac{\partial v}{\partial t} = v^2 \frac{\partial(\rho u_i)}{\partial x_i}. \quad (C.1)$$

The remaining equations are the momentum and energy equations in conservative forms. The velocities and temperature are obtained from the conservative variables using

$$u_i = v (\rho u_i) \quad T = \gamma v \left[E_T - v \frac{(\rho u_k)(\rho u_k)}{2} \right]. \quad (C.2)$$

The equation of state, (3.17), can be recast as

$$pv = \frac{(\gamma - 1)}{\gamma} T. \quad (C.3)$$

Another possible source of aliasing errors is the non-integer power law dependence of viscosity on temperature. The effect of this error on the solution remains to be investigated.

APPENDIX D

DIRECT NUMERICAL SIMULATIONS OF SPATIALLY EVOLVING TURBULENCE

Most direct or large eddy simulations of turbulent flows have been performed with periodic boundary conditions [Rogallo and Moin 1984]. Direct or large eddy simulations of flows in complex geometries require "turbulent" conditions at the inflow boundary.

This Appendix presents a method of generating inflow turbulence with a prescribed power spectrum. The results from simulations of spatially decaying turbulence are then compared with those from the corresponding temporal simulation to validate the method. The method is also validated by comparison with the experimental data for decaying isotropic turbulence in the regime where the energy spectrum undergoes a self-similar decay [Ling and Huang 1970].

D.1 Method of Generating Inflow Turbulence

For simplicity, we consider a turbulent flow evolving in the x_1 direction, the mean flow direction, homogeneous in coordinates x_2, x_3 , and statistically stationary in time. At the entrance ($x_1 = 0$) of the computational domain, the energy spectrum of a flow variable, E_{ff} , is prescribed in terms of frequency and two transverse wave numbers. The Fourier coefficients, $\hat{f}(k_2, k_3, \omega, t)$, are prescribed by the equation

$$\hat{f}(k_2, k_3, \omega, t) = \sqrt{E_{ff}(k_2, k_3, \omega)} \exp[i\phi_r(k_2, k_3, \omega, t)], \quad (D.1)$$

where ϕ_r is the phase factor and $i = \sqrt{-1}$. The functional dependence of ϕ_r on time, as well as on frequency and wave numbers, is necessary so that the signal generated is not periodic in time. The variable t in \hat{f} denotes an element of the ensemble of realizations. In our scheme, ϕ_r is changed only once in a given time interval, T_r , at a random instance by a random amount, $\Delta\phi_r$, where $|\Delta\phi_r|$ is bounded by a prescribed value, $\Delta\phi_{\max}$. The randomized temporal dependence of each phase, $\phi_r(k_2, k_3, \omega, t)$, is shown schematically in Figure D.1. Because the phases are time-dependent, the generated signal is not continuous and the frequency spectrum of the turbulence signal generated only approximates the target spectrum, $E_{ff}(k_2, k_3, \omega)$. The frequency and amplitudes of the random phase shifts determine the smoothness of

the generated signal. If this temporal dependence is weakened, the approximation of the target spectrum improves, but the generated signal also approaches a temporally periodic signal. The fluctuation signal, $f(x_2, x_3, t)$, is obtained by Fourier transforms in the homogeneous directions (i.e., x_2 and x_3) followed by a sum over all frequencies. The turbulence signal at the inflow plane is prescribed by adding the fluctuation signal, $f(x_2, x_3, t)$, to the mean flow profile, $F(x_2, x_3)$. One can easily generalize this method to create inhomogeneous "turbulence" as well.

The approximation of the target spectrum depends on the choices $T_r^* = \omega_o T_r / 2\pi$ and $\Delta\phi_{\max}^* = \Delta\phi_{\max} / 2\pi$, where ω_o is the frequency of the peak energy. The sensitivity of the approximation to T_r^* and $\Delta\phi_{\max}^*$ is shown in Figure D.2. The target spectrum, $E_{ff}(\omega)$, is of the form $\omega^4 \exp[-2(\omega/\omega_o)^2]$. As the temporal dependence of the random phase increases (small T_r^* and large $\Delta\phi_{\max}^*$), the approximation of the target spectrum worsens. The region of disagreement is localized in the non-energetic frequencies. In the high ω range, the spectrum has a ω^{-2} tail. Figure D.3 shows typical turbulence signals generated at the inflow.

D.2 Simulation of Spatially Decaying Turbulence

The first part of this section demonstrates the performance of the spatial simulation and compares it with a corresponding temporal simulation. In the second part, direct numerical simulation results are compared with the experimental data.

D.2.1 Comparison with Temporal Simulation Results

The method of generating inflow turbulence described in Section II is used to conduct simulations of spatially decaying compressible isotropic turbulence. The governing equations are the continuity equation, three momentum equations, and the energy equation, along with the equation of state. We assume the fluid to be an ideal gas ($\gamma = 1.4$) with zero bulk viscosity. Viscosity is assumed to have power-law dependence on temperature, $\frac{\mu}{\mu_o} = (\frac{T}{T_o})^{0.76}$, while the Prandtl number, Pr , is kept constant at 0.70. Special attention is given to ensure numerical conservation of mass, kinetic energy, and total energy in the inviscid limit. We approximate spatial derivatives by a compact finite-difference scheme [Lele 1990], which has spectral-like resolution as well as sixth-order formal accuracy. Time advancement is done explicitly by a third-order Runge-Kutta method. Periodic boundary conditions

are used in the x_2 and x_3 directions. The mean streamwise velocity, U_1 , is kept supersonic and uniform for the most rigorous application of the outflow boundary conditions. In the example presented, the mean inflow Mach number, $M_1 = U_1/c$, is 2.0 (c is the speed of sound). Simulations conducted for subsonic inflow yield essentially the same results. Inflow turbulence is generated with zero density and temperature fluctuations, with a three-dimensional energy spectrum given by

$$E(k) \sim k^4 \exp[-2(k/k_o)^2]. \quad (D.2)$$

The inflow fluctuation Mach number $M_t = q/c$ ($q = \sqrt{u'_i u'_i}$, where u'_i is a fluctuation from the ensemble averaged velocity) and the turbulence Reynolds number based on the Taylor microscale, $Re_\lambda = u_o \lambda_1 / \nu$, constitute two independent parameters of the simulation, where u_o is the *rms* fluctuation in a velocity component. We consider several cases with the inflow fluctuation Mach numbers $M_t = 0.519, 0.346, 0.173$ and $Re_\lambda = 25.0$. The size of the computational domain is 2π in each direction with 64 grid points. Thus, the computational wave numbers are integers, and we use the energy peak wave number, $k_o = 4$, in prescribing the inflow spectrum. For comparison, a corresponding computation of temporally decaying turbulence [Lee *et al.* 1991b] is conducted with the initial fluctuation Mach number and Reynolds number $M_t = 0.346$ and $Re_\lambda = 25.0$, respectively. Taylor's hypothesis is used to convert the downstream distance from the inflow boundary in the spatial simulation into the evolution time, *i.e.*, $t = x_1/U_1$.

Figure D.4 shows evolution of velocity derivative skewness, which is a measure of inertial nonlinearity of turbulence. Skewness varies with compressibility as well as turbulence Reynolds number [Tavoularis *et al.* 1978, Erlebacher *et al.* 1990], having a value of about -0.4 to -0.6 for isotropic turbulence at $Re_\lambda \sim 25$. Turbulence may therefore be considered realistic beyond time $t/\tau_t = 0.4$, where the turbulence time scale is defined as $\tau_t = \lambda/u_o$. The development of the velocity derivative skewness for the spatially decaying turbulence compares favorably with that for the temporally decaying turbulence.

Figures D.5(a) and D.5(b) present comparisons between spatial and temporal simulations for one-dimensional spectra of vorticity and dilatation as a function of the transverse wave number k_2 . The vorticity spectra agree closely, while the dilatation spectra show some differences.

The evolution of turbulent kinetic energy is shown in Figure D.6. The turbulent kinetic energy in the spatial simulation compares favorably with that in the temporal simulation. The same kind of agreement is obtained in the evolution of *rms* vorticity and turbulence Reynolds number. These agreements contrast with a systematic difference in the statistics of dilatation. Close comparisons are generally found for the statistics dominated by the incompressible part of turbulence [Moyal 1952], whereas the statistics dominated by the flow compressibility tend to differ. The level of *rms* dilatation of the spatial simulation when $M_t = 0.346$ is lower than the corresponding temporal simulation by 15 percent.

The deviation in the dilatation statistics may be attributed to two causes. Firstly, disturbances in incompressible turbulence are generally advected at the mean flow speed, U_1 , while fluctuations in compressible turbulence are convected at different speeds, U_1 , $U_1 + c$, and $U_1 - c$. Hence, for statistics dominated by compressibility the use of Taylor's hypothesis may be inaccurate. Secondly, as Figure D.5(b) illustrates, the level of the dilatation spectrum for low wave numbers is higher in the temporally decaying flow than in the spatially decaying flow. This higher level of compressibility in the temporal simulation may be attributed to the inability of the periodic boundary conditions to freely radiate the acoustic waves generated by turbulence. The existence of one freely radiating boundary (outflow boundary) in the spatial simulation lowers the overall intensity of acoustic waves trapped in the domain. Because of this difference, caution must be exercised in using periodic (or temporal) simulation databases to examine compressibility-driven quantities such as dilatation dissipation and pressure dilatation correlation.

D.2.2 Comparison with Experimental Data

Ling and Huang [1970] found the isotropic turbulence decay between microscale Reynolds numbers 3 and 30 to be self-similar. At low Reynolds numbers the energy and dissipation scales overlap so that there is only a single characteristic length scale. Domaradzki and Rogallo [1990] confirmed this finding through direct numerical simulation of temporally decaying incompressible turbulence by showing that the three-dimensional energy spectra, $E(k)$, at different times can be collapsed using the Taylor microscale as the characteristic length scale. We initialized a direct

numerical simulation of spatially decaying isotropic turbulence with the normalized inflow energy spectrum given by Ling and Huang [1970] as

$$E^*(k^*) = \alpha k^*(1 + k^*) \exp(-k^*), \quad (D.3)$$

where k^* is the magnitude of the normalized wave number, $\mathbf{k}^* = (k_1^*, k_2^*, k_3^*)$, with $k_i^* = k_i \alpha \sqrt{\nu(t - t_o)}$, $\alpha = 3.162$, $E^* = E(k) \sqrt{\nu(t - t_o) / u_1'^2}$, and $t = x_1 / U_1$ and t_o are the decay time and the virtual origin of the decay time, respectively.

The corresponding one-dimensional energy spectrum is

$$E_1^*(k_1^*) = \alpha \exp(-k_1^*). \quad (D.4)$$

The self-similarity of normalized spectra in (D.3) and (D.4) is based on the assumption that turbulent kinetic energy and all the relevant turbulence length scales evolve like t^{-2} and $t^{1/2}$, respectively.

In the simulation of the experimental conditions, we follow the same numerical procedures as in Section D.2.1. The mean streamwise Mach number, fluctuation Mach number, and Reynolds number at the inflow are $M_1 = 1.20$, $M_t = 0.173$, and $Re_\lambda = 15.0$, respectively. The size of the computational domain is 2π in each direction with 64 grid points, and the energy spectrum peaks at $k = 4$. An incoming fluid particle passes through the computational domain in time, $t = 2.5\tau_t$, where $\tau_t = \lambda / u_o$.

Normalized one-dimensional spectra at different downstream positions are shown in Figure D.7. Spectra collapse onto the experimental results with some deviation at small wave numbers because of the limited sample size. It was experimentally² observed that turbulent kinetic energy decays like $(x_1 - x_o)^{-2}$, i.e.,

$$\frac{q^2}{q_o^2} = \left(\frac{-x_o}{x_1 - x_o} \right)^2, \quad (D.5)$$

where $q_o^2/2$ is the turbulent kinetic energy at inflow (i.e., $x_1 = 0$) and $x_o / U_1 \tau_t = -4.2$ in the simulation. Figure D.8 compares the turbulent kinetic energy decay in the simulation with that expressed by (D.5). The evolution of turbulent kinetic

energy in the numerical simulation is in excellent agreement with the experimental data.

We have developed a method of generating inflow turbulence fluctuations for spatially developing turbulence computations. Using this method we performed direct numerical simulation of spatially evolving isotropic turbulence. The computed incompressible turbulence statistics are in excellent agreement with those from the corresponding temporal simulation and the experimental data. The algorithm for generating inflow turbulence is by no means unique. The significant result is that one apparently can compute spatially developing turbulence with the accuracy typical of present temporally evolving simulations.

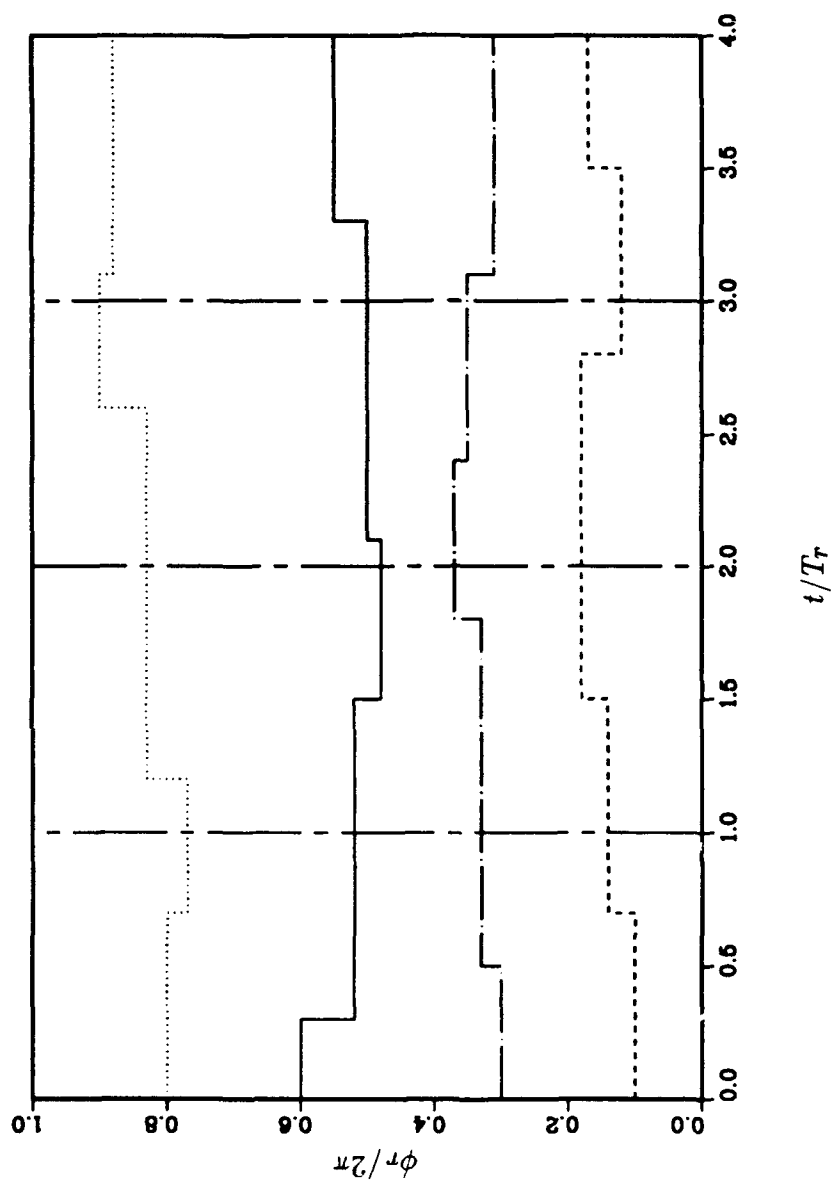


FIGURE D.1. Schematic plot of randomized temporal dependence of phases. Lines represent the phase factor at different wave numbers and frequencies.

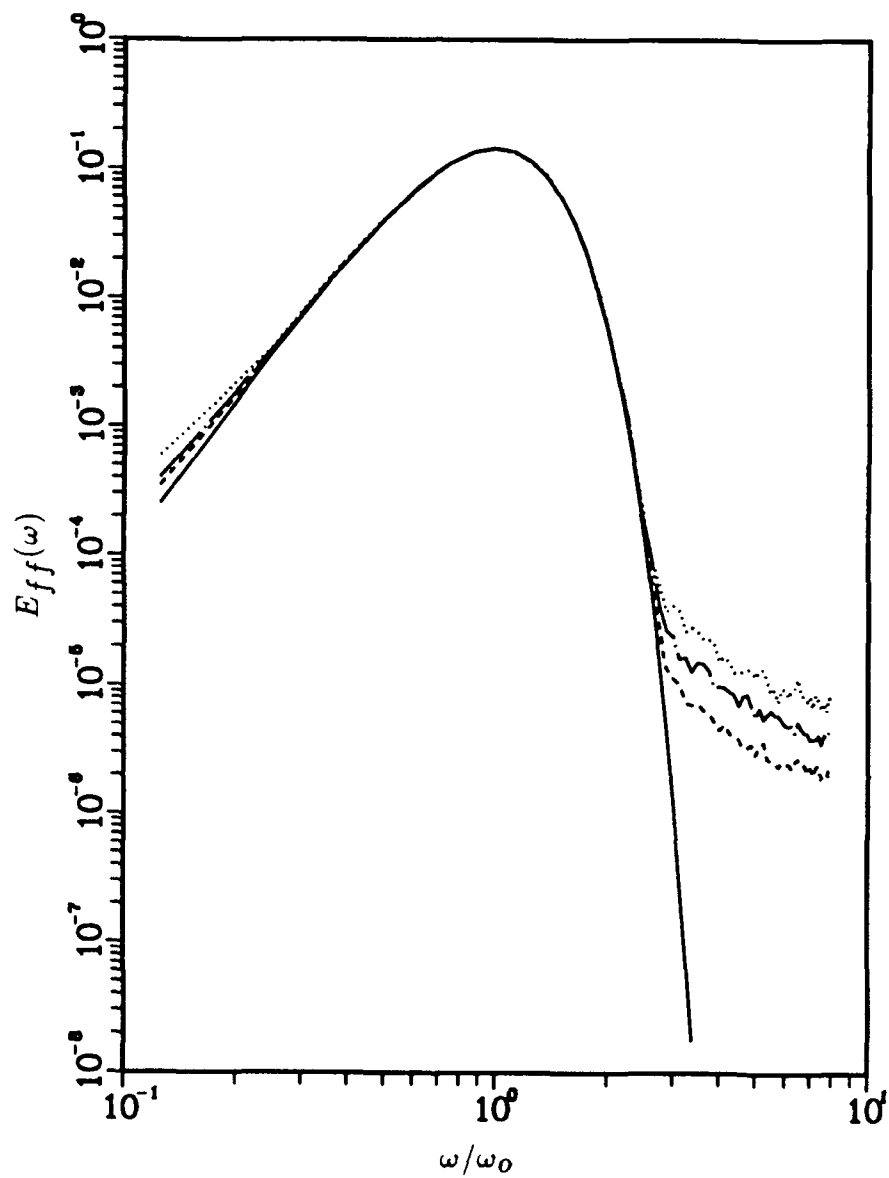


FIGURE D.2. Approximation of the spectrum by signals with time-dependent random phases: — target spectrum, ---- $T_r^* = 2, \Delta\phi_{\max}^* = 1/20$, - - - $T_r^* = 2, \Delta\phi_{\max}^* = 1/10$, $T_r^* = 1, \Delta\phi_{\max}^* = 1/20$.

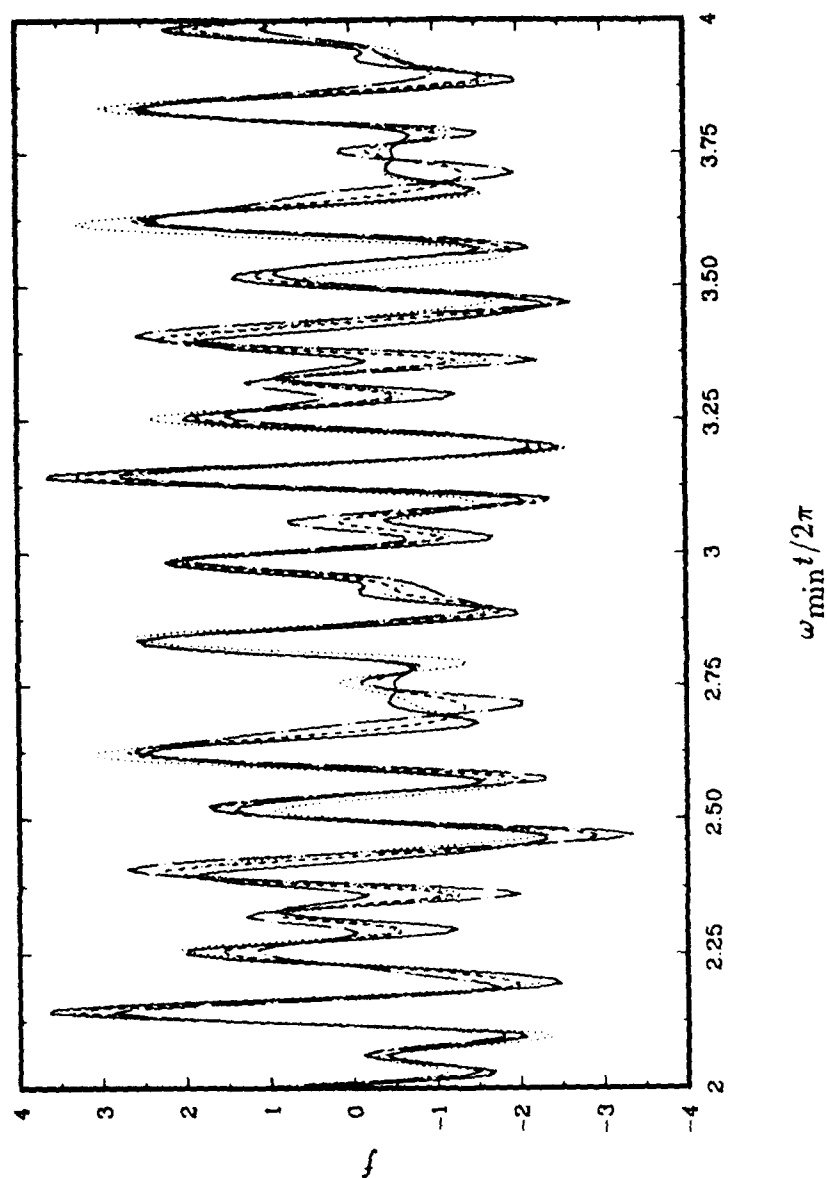


FIGURE D.3. Time history of typical turbulence signals at the inflow ($\omega_0/\omega_{\min} = 8$): — periodic signal, --- $T_r^* = 2, \Delta\phi_{\max}^* = 1/20$, - - - $T_r^* = 1/10, \Delta\phi_{\max}^* = 1/20$.

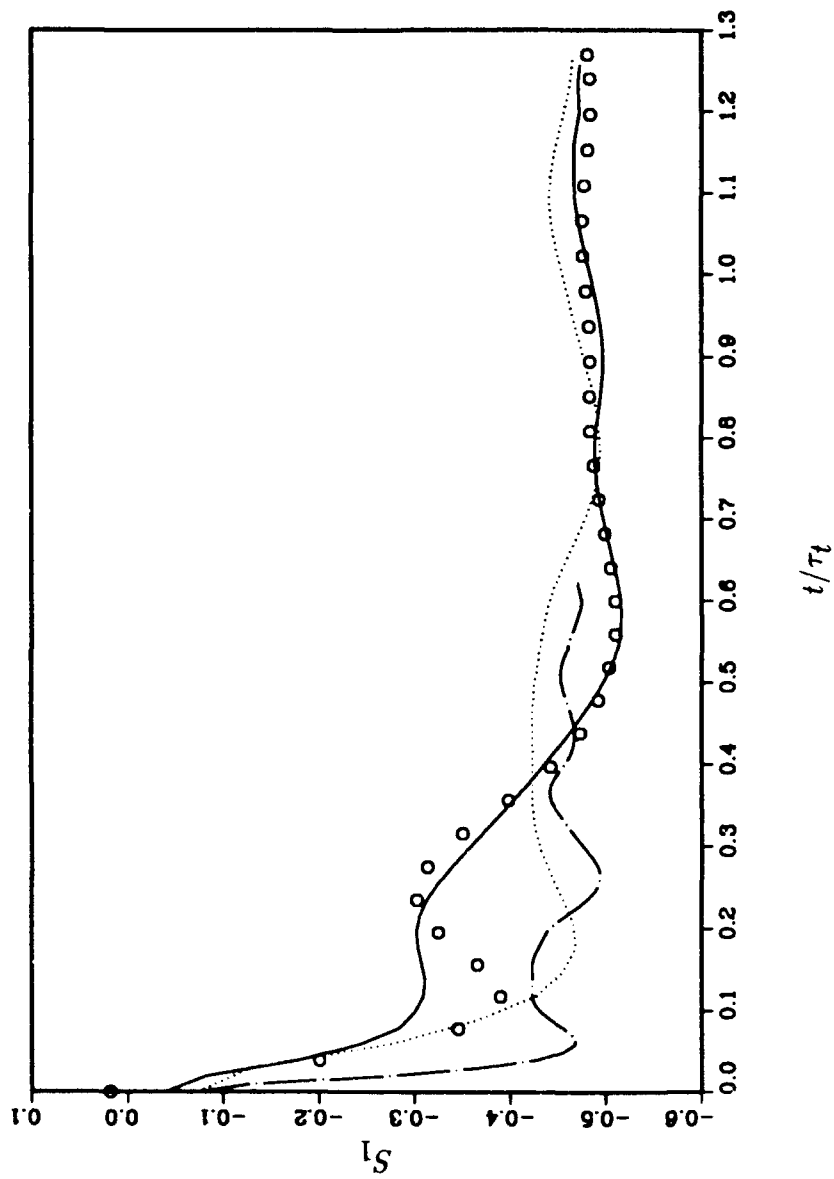


FIGURE D.4. Evolutions of velocity derivative skewness, symbol: temporal simulation with $M_t = 0.346$, spatial simulations $M_t = 0.519$, — $M_t = 0.346$, — — $M_t = 0.173$.

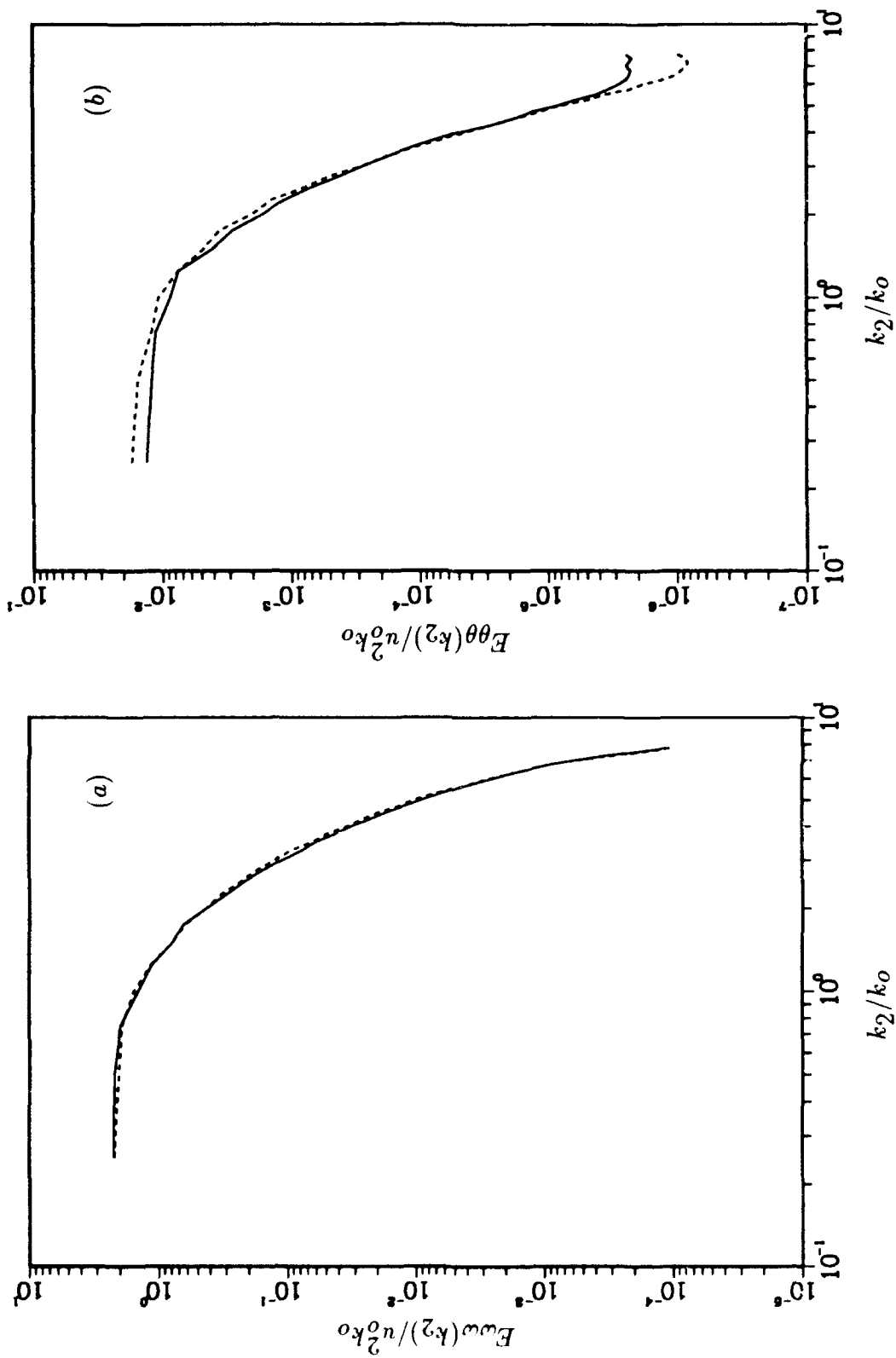


FIGURE D.5. Comparison of one-dimensional spectra of (a) vorticity and (b) dilatation at $t/\tau_l = 0.67$: — spatial, --- temporal.

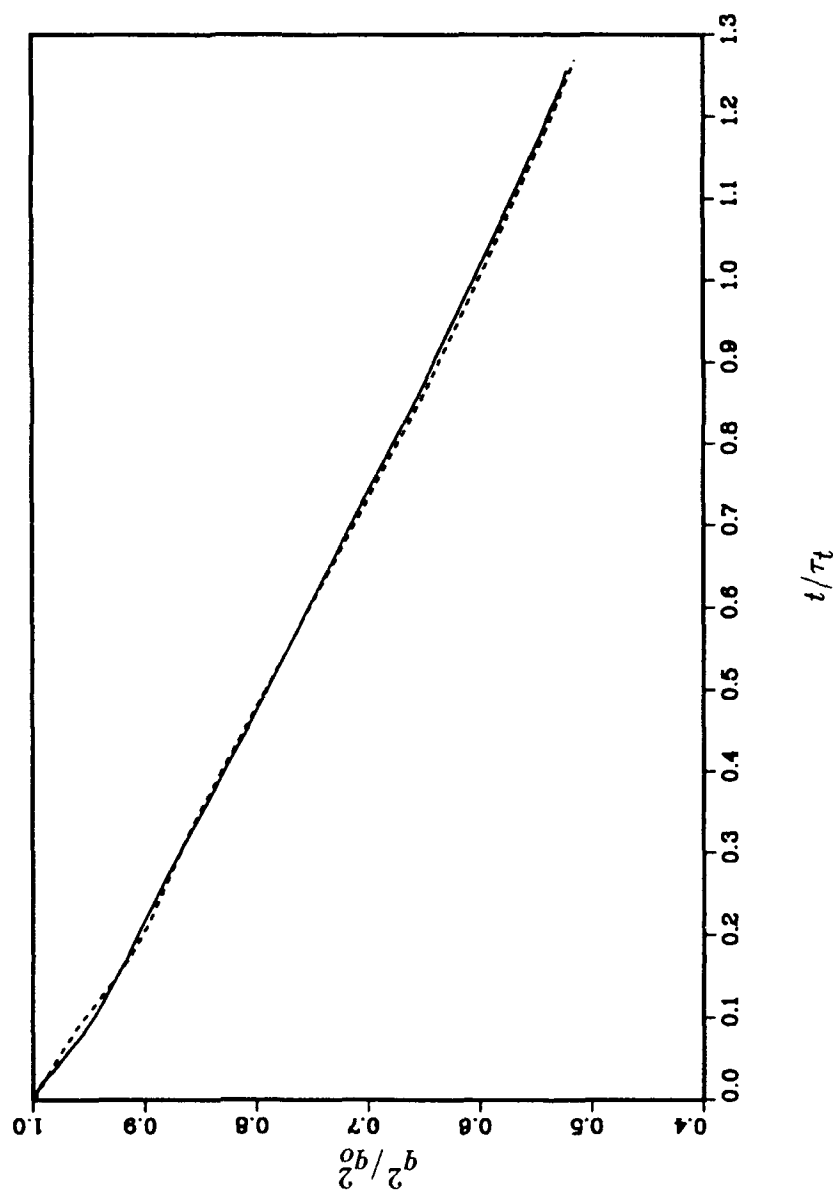


FIGURE D.6. Comparison of turbulent kinetic energy evolution: — spatial, - - - temporal.

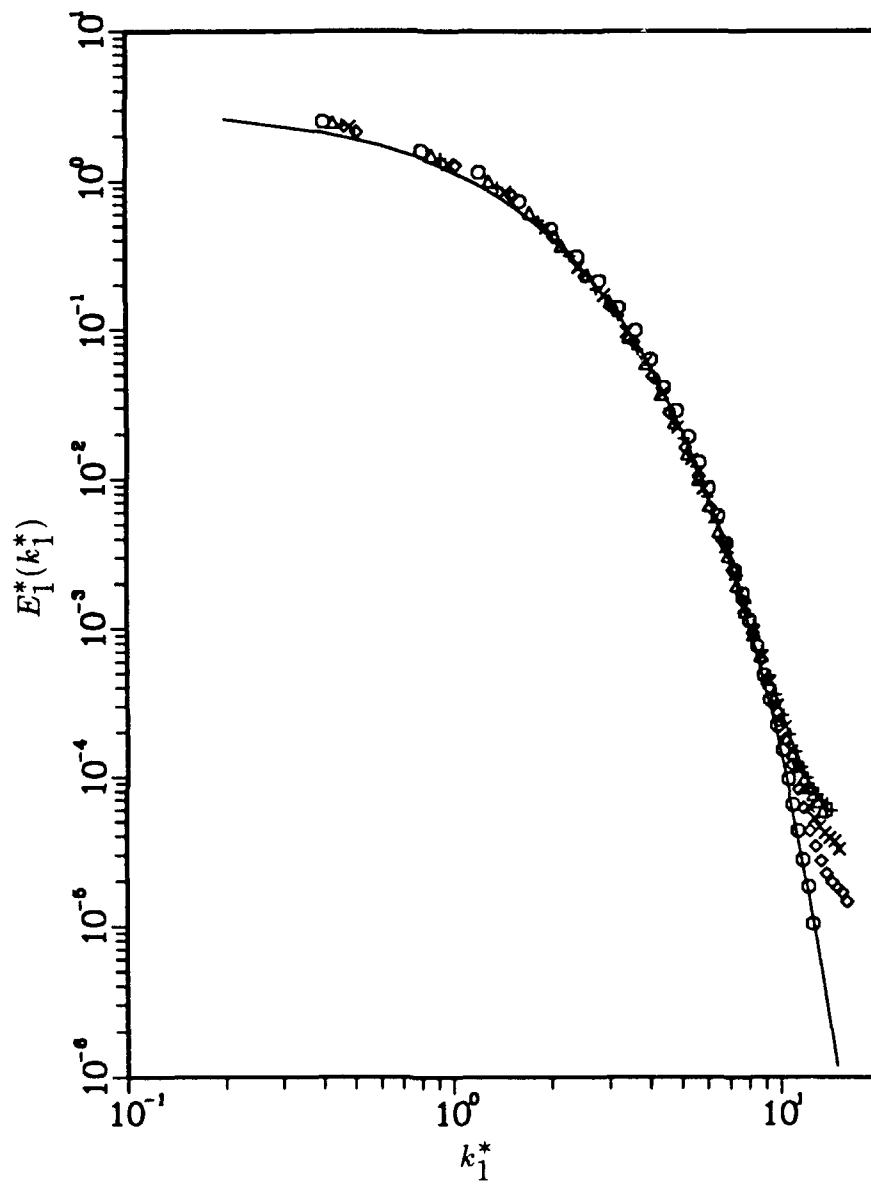


FIGURE D.7. Comparison of the normalized energy spectrum of Ling and Huang [1970] given by (D.4) (solid line) and the energy spectra obtained in the simulation at five different positions (symbols): \circ , $x_1 = 0$; \triangle , $x_1 = \pi/2$; $+$, $x_1 = \pi$; \times , $x_1 = 3\pi/2$, and \diamond , $x_1 = 2\pi$.

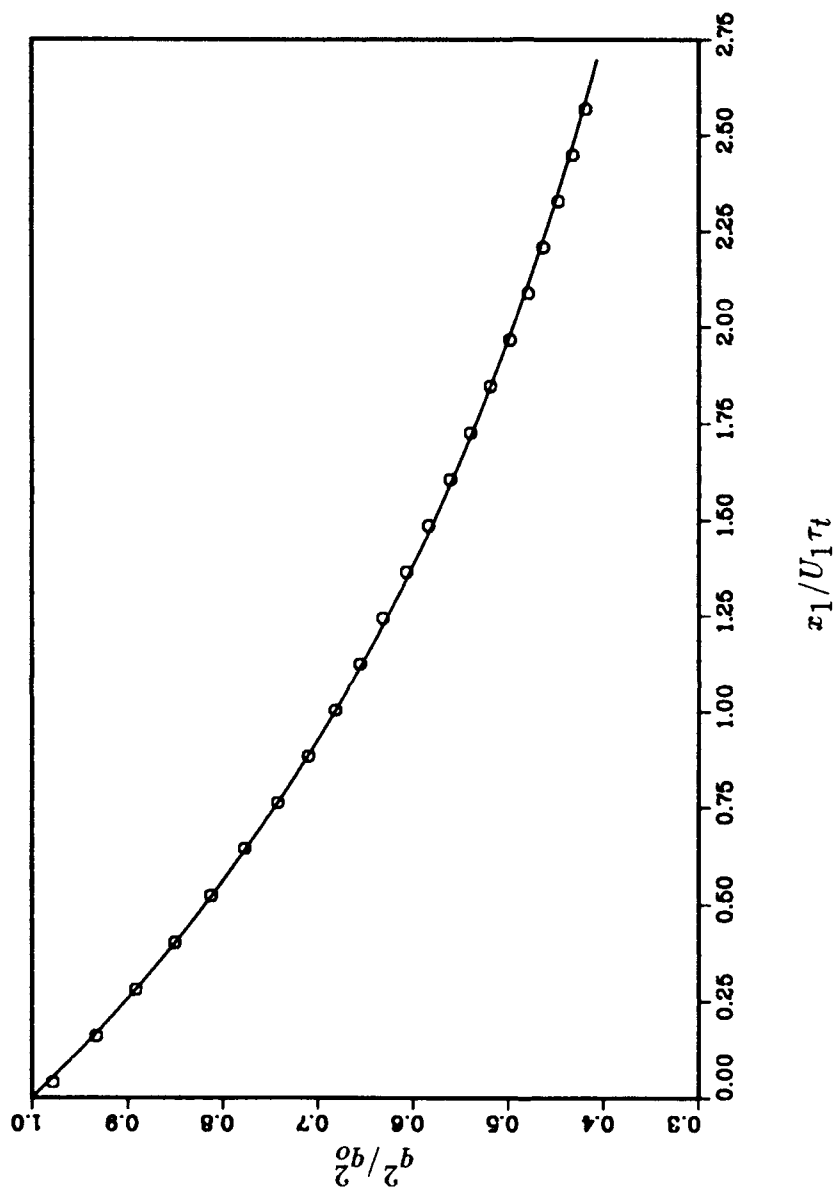


FIGURE D.8. Comparison of turbulent kinetic energy decay (symbol) with (D.5) (solid line).

APPENDIX E

PARAMETER LIMITATIONS FOR DIRECT NUMERICAL SIMULATION OF SHOCK TURBULENCE INTERACTION

In our direct numerical simulations of shock turbulence interaction, we have required the resolution of all the relevant scales of turbulence and the shock wave. The resolution requirement for incompressible turbulence is far better established than that of compressible turbulence. For weakly compressible turbulence with $M_t < 0.2$ where there are no significant compressibility effects on turbulence, resolution requirements for compressible turbulence is comparable to that of incompressible turbulence. Some simulations of compressible turbulence at very high M_t [Kida *et al.* 1990, Blaisdell *et al.* 1990, Sarkar *et al.* 1991] were not successful in resolving changes of the flow variables across the eddy shocklets. Since their main interests were to study the effect of compressibility on turbulence evolution, resolving the eddy shocklets may not have been a critical factor. In this study we investigated the effect of turbulence on the shock wave structure as well as the effect of a shock wave on turbulence. Therefore, proper resolution of the shock wave is necessary for accurate results. Limitations on the availability of computer resources leads to limitations on the choice of physical parameters in the simulation, Re_λ , M_1^U and M_t .

E.1 Requirements for Resolution and Sample Size

As shown in Section 3.3.1, proper resolution of the shock wave structure requires a grid distribution which places at least three points inside the shock wave whose thickness δ_s is defined by

$$\delta_s = \frac{\Delta U_1}{|(dU_1/dx_1)_{\min}|}.$$

Thus, $\delta_s \geq 3(\Delta x_1)_{\min}$, where $(\Delta x_1)_{\min}$ is the typical streamwise grid spacing near the shock wave. For weak shock waves, the shock thickness δ_s is estimated as

$$\delta_s = \frac{8}{3} \frac{\nu}{c(M-1)} \quad (E.1)$$

[Thompson 1984], where ν and c are the upstream kinematic viscosity and speed of sound, and M is the maximum instantaneous upstream Mach number, $M \simeq M_1^U + M_t$, where M_t is the fluctuation Mach number at the inflow.

In the numerical simulation, artificial turbulence generated at the inflow evolves into "realistic" turbulence as it approaches the shock wave. In Appendix D, evolution of artificial inflow turbulence into realistic turbulence was found to take place in a distance which determines the minimum streamwise computational box size upstream of the shock wave. Using the results of Appendix D and applying Taylor's hypothesis, we get the following relation:

$$\frac{t}{\tau_t} = \frac{x_1/U_1}{\lambda/u_o} > 0.4, \quad (E.2)$$

where λ is the longitudinal Taylor microscale, and $\tau_t = \lambda/u_o$ is a turbulence time scale. Therefore, the minimum streamwise computational box size upstream of the shock wave L_1^U is

$$L_1^U = \frac{0.4\lambda}{u_o/U_1}, \quad (E.3)$$

where u_o/U_1 is the streamwise turbulence intensity at the inflow. The streamwise distance downstream of the shock wave, L_1^D was chosen to be the same as L_1^U . The streamwise computational box size L_1 can now be expressed as

$$L_1 = L_1^U + L_1^D = \frac{0.8\lambda}{u_o/U_1}.$$

This relation can be rewritten as

$$L_1 = \frac{0.46\lambda}{M_t/M_1^U}, \quad (E.4)$$

using the definitions of M_t and M_1^U

$$M_t = \frac{q}{c} = \sqrt{3} \frac{u_o}{c}, \quad M_1^U = \frac{U_1^U}{c}.$$

In order to eliminate the contamination of long-time-averaged statistics across the shock, the mean shock front should not drift in space. As the upstream fluctuation Mach number, M_t , becomes comparable to $M_1^U - 1$, the mean shock drift speed increases. Therefore, the fluctuation Mach number should be bounded by $M_1^U - 1$.

Compressible turbulence of $M_t < 0.2$ does not contain eddy shocklets [Lee *et al.* 1991b] and can be resolved by a grid similar to that in incompressible turbulence at the same Reynolds number. In our simulations turbulence Mach number is always lower than 0.2 except possibly just behind the shock wave.

The size of the computational domain and the number of grid points in transverse directions are determined to satisfy the requirements of sample size and resolution of turbulence. Based on the form of inflow turbulence spectrum given in (3.32), the integral scale $\Lambda_{22,2}$ defined in (4.7), the longitudinal Taylor microscale λ , and the Kolmogorov length scale η_K are, respectively,

$$\begin{aligned} k_o \Lambda_{22,2} &= \sqrt{2\pi} \\ k_o \lambda &= 2 \end{aligned} \tag{E.5}$$

$$k_o \eta_K = \left(\frac{16}{15} \right)^{1/4} Re_\lambda^{-1/2},$$

where Re_λ is Taylor microscale Reynolds number defined in (4.1).

To have a sufficient sample of large scale structures, the computational box in the transverse directions were chosen to be larger than about ten integral scales,

$$L_2 = L_3 \geq 10 \Lambda_{22,2}. \tag{E.6}$$

To resolve the smallest scale of turbulence which is comparable to η_K , we chose the mesh size in the transverse direction as

$$\Delta x_2 = \Delta x_3 \leq 2\eta_K$$

[Lee and Reynolds 1985], or using (E.5)

$$k_o \Delta x_2 = 0.508 Re_\lambda^{-1/2}. \quad (E.7)$$

Using the expression for η_K in (E.5), the ratio of the cutoff wave number k_c to the energy peak wave number k_o can be expressed as

$$\frac{k_c}{k_o} \geq \frac{\pi}{2} Re_\lambda^{1/2}, \quad (E.8)$$

where the relation

$$k_c = \frac{\pi}{L_2} N_2 \quad (E.9)$$

is used (N_2 is the number of grid points in the x_2 direction). Combining this with (E.5), (E.6), (E.8) and (E.9), the number of grid points in the transverse directions can be expressed as

$$N_2 = N_3 \geq 12 Re_\lambda^{1/2}. \quad (E.10)$$

The number of grid points in the transverse directions according to (E.10) satisfies the requirements of sample size and fine scale resolution.

A non-uniform mesh is used in the streamwise direction. The minimum mesh size to resolve the shock wave is obtained from (E.1) as

$$k_o(\Delta x_1)_{\min} = \frac{16}{9\sqrt{3}} \frac{M_t}{Re_\lambda} \frac{1}{M_1^U + M_t - 1}.$$

The maximum streamwise mesh spacing is equal to the mesh spacing in the transverse directions.

Turbulence statistics are obtained with averaging over a time t such that

$$\frac{u_o t}{\lambda} \geq 4,$$

and the maximum time step of the simulation is determined by the numerical stability condition of

$$CFL = \frac{(U_1 + c)\Delta t}{(\Delta x_1)_{\min}},$$

where CFL is the Courant-Friedrichs-Lewy number. Since the smallest grid spacing is in the x_1 -direction, the total number of time steps required in each simulation N_t is estimated to be

$$N_t = \frac{t}{\Delta t} \geq \frac{4\sqrt{3}}{CFL} \frac{\lambda}{(\Delta x_1)_{\min}} \frac{M_1^U + 1}{M_t}. \quad (E.11)$$

By using $\delta_s \geq 3(\Delta x_1)_{\min}$, (E.1), (E.5), (E.8) and (E.9), one can rewrite (E.11) as

$$N_t \geq \frac{13.5}{CFL} \frac{Re_\lambda}{M_t^2} (M_1^U + M_t - 1) (M_1^U + 1). \quad (E.12)$$

In the present study with the choice of parameters given in Table 4.1, the number of time steps ranges from 10,000 to 30,000.

The separation between the typical turbulence length scale and the shock wave thickness requires a large grid stretching in the streamwise direction. Furthermore, acoustic waves should be accurately resolved in the region occupied by the shock wave, which excludes the possibility of using an implicit time advancement to take a large time increment. Explicit time advancement with a small time increment is the main reason for the large CPU time required for direct numerical simulation of realistic shock/turbulence interaction.

In a three-dimensional direct numerical simulation, storage of all the flow variables in the core requires a large memory. On the Cray Y-MP/832, this problem is alleviated by using the Solid State Device (SSD) I/O. In the present computations, the SSD I/O takes about 15% of the total CPU time used.

The code performance is about 130 megaflops with $129 \times 64 \times 64$ grid points, and uses about 45 CPU seconds of Cray Y-MP/832 for each time step. It takes about 100 to 200 CPU hours of Cray Y-MP/832 to obtain adequate turbulence statistics for one case.

E.2 Limitations of the Physical Parameters: Re_λ, M_1^U, M_t

To discuss the limitations of the physical parameters, we use as a reference the simulated case: $Re_\lambda = 25.0$, $M_1^U = 1.20$, and $M_t = 0.173$. In realistic problems

with shock/turbulence interaction, the turbulence Reynolds number is higher, and the shock strength is usually stronger with a wider range of M_t .

Increase in the Reynolds number, Re_λ , results in an increase in the number of grid points (ref. (E.10)) in all directions which leads to an increase in the CPU time per time step. Increasing the upstream Mach number, M_1^U , requires a larger grid stretching ratio in the streamwise direction due to the increased scale separation between turbulence and the shock wave (ref. (E.1)) and more CPU time per time step. Increasing the Mach number to $M_1^U = 1.40$ requires at least twice the CPU time required for the reference case.

Lowering the upstream fluctuation Mach number, M_t , with fixed upstream turbulence length scale requires a longer computational box size in the streamwise direction (ref. (E.4)), which leads to the increase of the number of grid points. Higher M_t requires more grid points in the streamwise direction to resolve the instantaneous shock wave structure (ref. (E.1)). The upper limit of M_t is usually set by the condition of shock stationarity, $M_t < M_1^U - 1$.

As shown in Table 4.1, the ranges of inflow parameters used in the simulations were

$$\begin{aligned} 16 &\leq Re_\lambda \leq 25, \\ 1.05 &\leq M_1^U \leq 1.20, \\ 0.087 &\leq M_t \leq 0.173. \end{aligned}$$

APPENDIX F

TURBULENCE STATISTICS IN KINEMATIC OSCILLATION OF A PLANE SHOCK WAVE

In the interaction of turbulence with a shock wave, the shock front is distorted and undergoes an oscillatory movement. The oscillation of the shock front produces an intermittent time history of the flow variables at a fixed point in a reference frame fixed at the mean shock position, and it leads to overprediction of turbulence statistics (see Section 4.1 and [Debieve *et al.* 1986]). This large fluctuation (which is not turbulence) is driven by the upstream turbulence, and undergoes rapid viscous decay since its time and length scales are small.

In order to identify the effects of the shock oscillation on turbulence statistics, a plane shock wave was moved back and forth in a sinusoidal fashion in the streamwise direction, and the budget of terms in the R_{11} equation in (4.9) was computed. The profiles of the flow variables across the shock wave were obtained as the laminar solution of the one-dimensional Navier-Stokes equations for $M_1^U = 1.20$ (see Section 3.2.2 for more details on the solution procedure). And the solution $U = (\rho, u_1, p)^T$ is expressed in terms of the relative position with respect to the shock center position x_s as $(x_1 - x_s)/\delta_s$, where δ_s is the shock thickness. The oscillatory movement of the shock wave is emulated by externally driving the shock wave to move back and forth in time as

$$x_s(t) = x_s(0) + \alpha_s \delta_s f(t), \quad (F.1)$$

where $\alpha_s \delta_s$ is the spatial amplitude of the oscillation, and $f(t)$ is a periodic function with $\overline{f(t)} = 0$. Statistical samples were taken at fixed points x_1^S , which were apart by about a tenth of the shock thickness. The flow variables at a sampling point near the shock wave vary in time due to changes in the relative positions with respect to the shock wave. The sampling points far away from the shock wave are not affected by the shock wave oscillation. The sampling time interval was chosen so that 100 samples were taken per oscillation period of the shock wave. The statistics were not found to be sensitive to the choice of the parameter, α_s , and the function, $f(t)$. In the following, a sinusoidal function is used for $f(t)$ with $\alpha_s = 0.25$.

Figure F.1 shows the statistics of the streamwise velocity, dilatation, pressure, density, and temperature. As found in Section 4.2, all the statistics peak inside the zone of shock oscillation. The peak values were also comparable to those from the direct numerical simulation (see Figures 4.4 and 4.24).

Figure F.2 shows the budget of terms in the R_{11} equation. The behaviors of all the terms in the equation were found to be consistent with those computed from the direct numerical simulations (see Figure 4.8(a)). The pressure work term, $-\overline{u_1'' p'_{,1}}$, was found to be the dominant term inside the shock wave.

Figure F.3 shows the decomposition of the pressure work term into the pressure transport term, $-(\overline{p' u_1''})_{,1}$, and the pressure-dilatation correlation, $\overline{p' u_{1,1}''}$. Again, behaviors of the two decomposed terms are in agreement with the results from the simulations (see Figure 4.7(a)).

It can be concluded that the large levels of fluctuations in the shock zone in the direct numerical simulations were mainly due to the oscillatory movement of a plane shock wave.

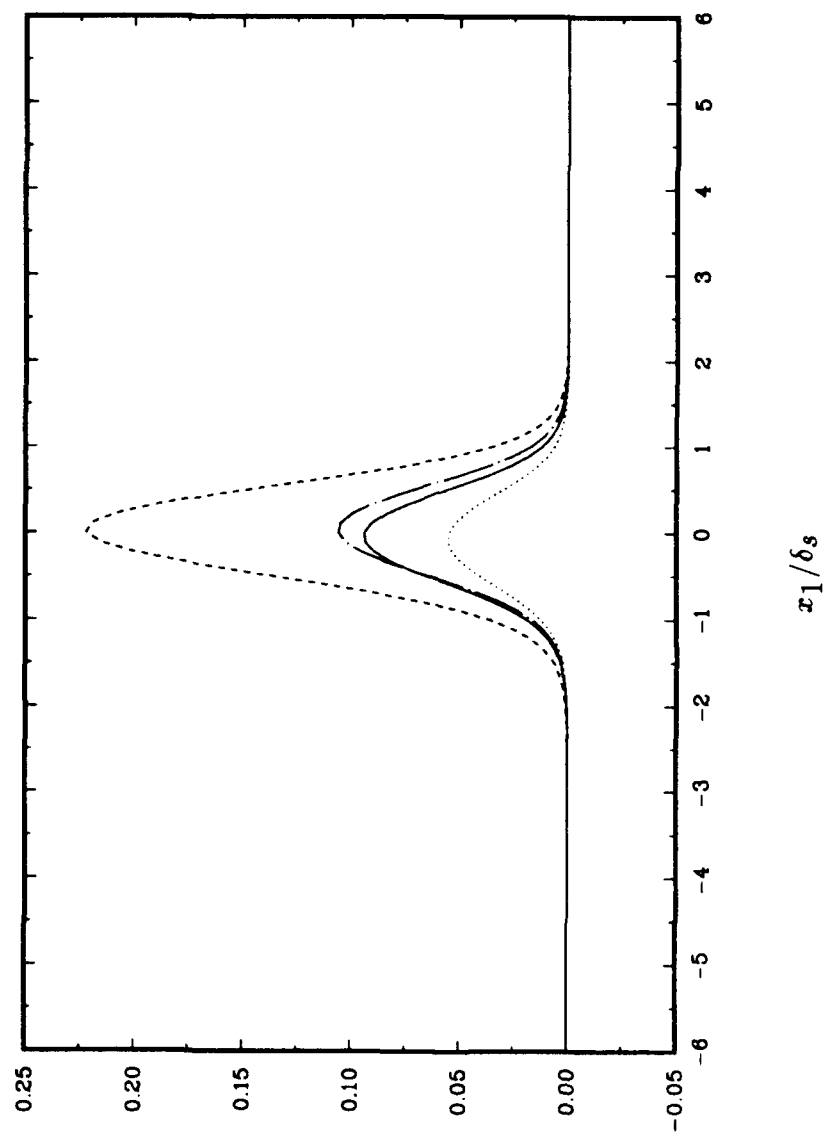


FIGURE F.1. Effects of kinematic shock wave oscillation on turbulence statistics: — u_{rms} , ---- ρ_{rms} , T_{rms} .

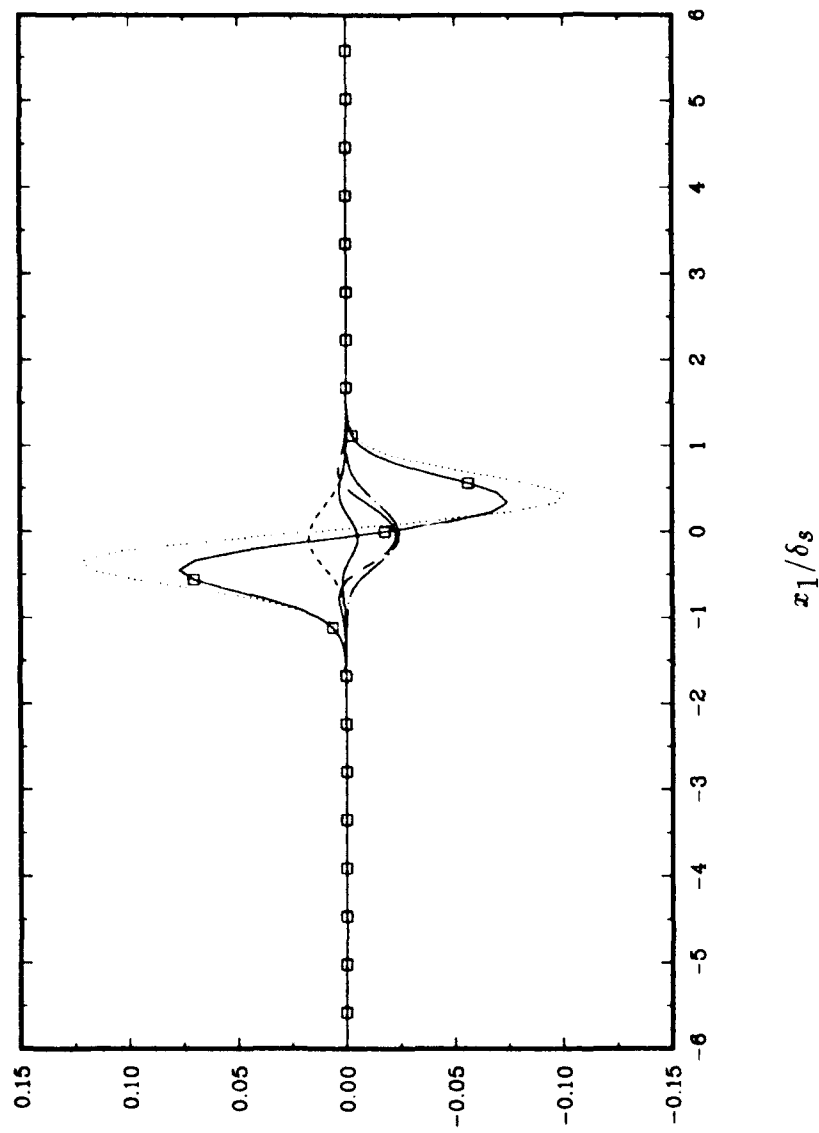


FIGURE F.2. Effects of kinematic shock wave oscillation on the budget of terms in the transport equation for R_{11} : —□— convection, --- production by the mean strain, -.- production by mass flux fluctuation, pressure work, ---- turbulent transport, - - - - viscous dissipation and transport.

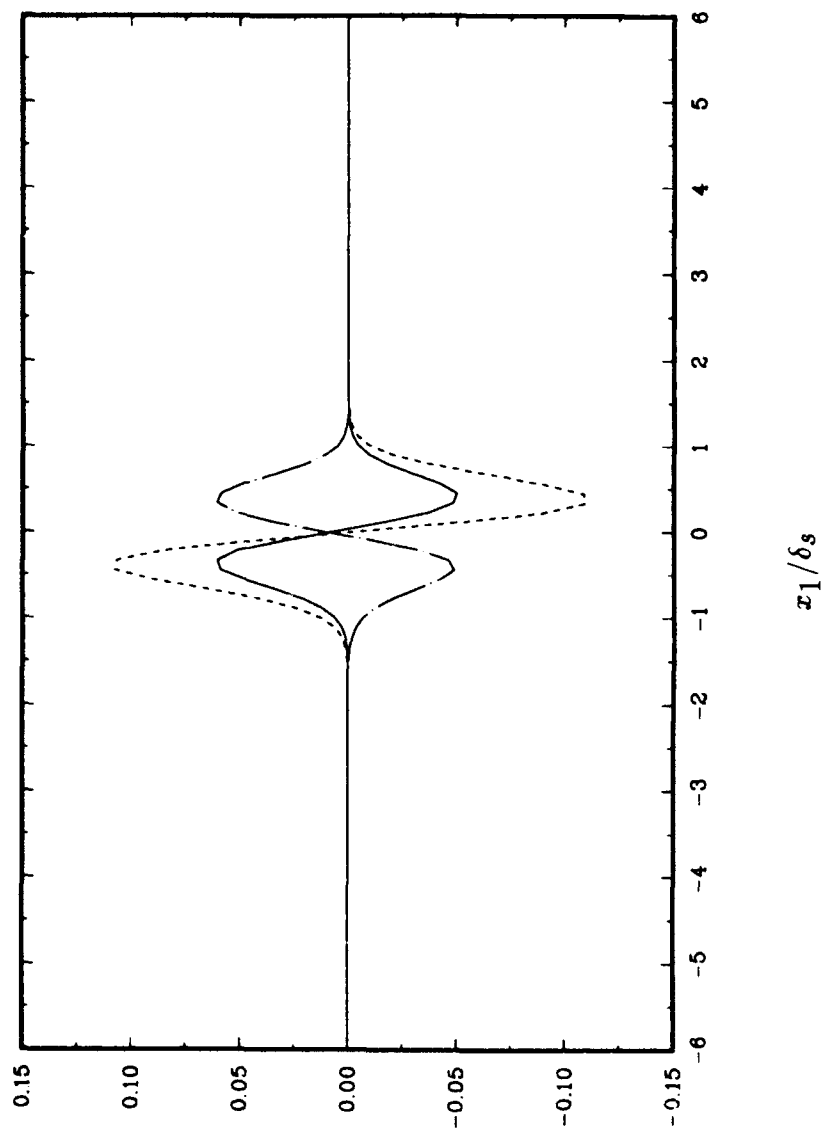


FIGURE F.3. Effects of kinematic shock wave oscillation on the pressure-work term decomposition: — $-\overline{p'_{,1}u''_1}$,
 ---- $-(\overline{p'u''_1})_{,1}$, - · - $\overline{p'u''_{1,1}}$.

APPENDIX G

EFFECT OF A REFINED OUTFLOW BOUNDARY CONDITION

As described in Section 3.2.4, Thompson's non-reflecting boundary condition [1987] was used in the present work. This boundary condition was successful in suppressing the reflection of nonphysical acoustic waves in test problems, where the vortical and entropy waves were passed through the outflow boundary (see Section 3.3.2). However, in the simulations of shock wave turbulence interaction, the statistics which are associated with acoustic waves, such as pressure work (Figure 4.6(b)) and dilatation (Figure 4.10), show anomalous behaviors near the outflow boundary. In order to assess the extent of influence of downstream boundary conditions on turbulence evolution, the more refined boundary conditions of Giles [1990] were implemented and turbulence statistics from these computations were compared with those using Thompson's boundary conditions. In this Appendix, a brief description of Giles' boundary condition is given first, followed by a comparison of the statistics using Giles' boundary condition with those using Thompson's boundary condition.

G.1 Description of Giles' Boundary Condition

The original derivation of Giles' boundary condition is based on the analysis of the linearized Euler equations; here the viscous terms were added. We begin with Giles' analysis on the three-dimensional Euler equations which can be written in terms of the primitive variables as

$$\frac{\partial U}{\partial t} + A \frac{\partial U}{\partial x_1} + B \frac{\partial U}{\partial x_2} + C \frac{\partial U}{\partial x_3} = 0, \quad (G.1)$$

where $U = (\delta\rho, \delta u_1, \delta u_2, \delta u_3, \delta p)^T$,

$$A = \begin{pmatrix} u_1 & \rho & 0 & 0 & 0 \\ 0 & u_1 & 0 & 0 & 1/\rho \\ 0 & 0 & u_1 & 0 & 0 \\ 0 & 0 & 0 & u_1 & 0 \\ 0 & \gamma p & 0 & 0 & u_1 \end{pmatrix} \quad (G.2)$$

$$B = \begin{pmatrix} u_2 & 0 & \rho & 0 & 0 \\ 0 & u_2 & 0 & 0 & 0 \\ 0 & 0 & u_2 & 0 & 1/\rho \\ 0 & 0 & 0 & u_2 & 0 \\ 0 & 0 & \gamma p & 0 & u_2 \end{pmatrix} \quad (G.3)$$

and

$$C = \begin{pmatrix} u_3 & 0 & 0 & \rho & 0 \\ 0 & u_3 & 0 & 0 & 0 \\ 0 & 0 & u_3 & 0 & 0 \\ 0 & 0 & 0 & u_3 & 1/\rho \\ 0 & 0 & 0 & \gamma p & u_3 \end{pmatrix}. \quad (G.4)$$

The elements of the vector U represent perturbations from uniform flow conditions, and the matrices A , B , and C are evaluated using uniform flow conditions. We consider wave-like solutions of the form

$$U(x_1, x_2, x_3, t) = \exp[i(k_1 x_1 + k_2 x_2 + k_3 x_3 - \omega t)]u^R, \quad (G.5)$$

where u^R is a constant column vector. Substituting this into the differential equation (G.1), we obtain

$$(-\omega I + k_1 A + k_2 B + k_3 C)u^R = 0, \quad (G.6)$$

which has a nontrivial solution, provided that

$$\det(-\omega I + k_1 A + k_2 B + k_3 C) = 0. \quad (G.7)$$

The vector u^R is also an eigenvector of the matrix

$$H = A^{-1}(-\omega I + k_1 A + k_2 B + k_3 C) \quad (G.8)$$

corresponding to the eigenvalue k_1 .

Suppose that the differential equation is to be solved in the domain $x_1 < L_1$, and one wants to construct boundary conditions at $x_1 = L_1$ to minimize or ideally prevent the reflection of outgoing waves. At the boundary $x_1 = L_1$, U can be decomposed into a sum of Fourier modes with different values of k_2, k_3 , and ω . Consider a single wave with particular choice of k_2, k_3 , and ω . In this case, the most general form for U is

$$U(L_1, x_2, x_3, t) = \left[\sum_n a_n u_n^R e^{i(k_1)_n L_1} \right] e^{i(k_2 x_2 + k_3 x_3 - \omega t)}, \quad (G.9)$$

where $(k_1)_n$ is one of the roots of the dispersion relation for the given values of k_2, k_3 , and ω , and u_n^R is the corresponding right eigenvector.

The ideal nonreflecting boundary condition would specify $a_n = 0$ for each n that corresponds to an incoming wave. The construction of such a boundary condition requires the vector v^L , which is an eigenvector of H^T . It is well known from linear algebra that the eigenvectors of H and H^T corresponding to different eigenvalues are orthogonal, that is,

$$(v_m^L)^T u_n^R = 0, \quad (G.10)$$

where v_m^L and u_n^R are the left and right eigenvectors corresponding to different solutions $(k_1)_m$ and $(k_1)_n$ of the dispersion relation, (G.7).

At the boundary, $x_1 = L_1$, orthogonality leads to

$$\begin{aligned} (v_n^L)^T U &= (v_n^L)^T \left[\sum_m a_m u_m^R e^{i(k_1)_m L_1} \right] e^{i(k_2 x_2 + k_3 x_3 - \omega t)} \\ &= a_n \left[(v_n^L)^T u_n^R \right] e^{i(k_1)_n L_1} e^{i(k_2 x_2 + k_3 x_3 - \omega t)}. \end{aligned} \quad (G.11)$$

Therefore, an equivalent specification of nonreflecting boundary condition is

$$(v_n^L)^T U = 0 \quad (G.12)$$

for each n corresponding to an incoming mode.

In principle, these exact boundary conditions can be implemented in a numerical method. The problem is that, in general, v_n^L depends on $l_2 = k_2/\omega$ and $l_3 = k_3/\omega$, and the implementation would involve Fourier transforms in x_2 and x_3 and Laplace transform in t . Computationally, this is both difficult and expensive to implement. In the following, an approximation used for general situations is described.

A sequence of approximate, nonreflecting boundary conditions can be obtained by expanding v_n^L in a Taylor series as a function of l_2 and l_3 as

$$v_n^L(l_2, l_3) = v_n^L(0, 0) + l_2 \frac{\partial v_n^L}{\partial l_2}(0, 0) + l_3 \frac{\partial v_n^L}{\partial l_3}(0, 0) + O(l_2^2, l_2 l_3, l_3^2). \quad (G.13)$$

The first-order approximation, obtained by keeping only the leading term, gives Thompson's boundary condition. The second-order approximation is,

$$\left(v_n^L(0, 0) + \frac{k_2}{\omega} \frac{\partial v_n^L}{\partial l_2}(0, 0) + \frac{k_3}{\omega} \frac{\partial v_n^L}{\partial l_3}(0, 0) \right)^T U = 0. \quad (G.14)$$

Multiplying by $-i\omega$ and replacing ik_2, ik_3 , and $i\omega$ by $\partial/\partial x_2, \partial/\partial x_3$, and $-\partial/\partial t$, respectively, gives

$$(v_n^L)^T(0, 0) \frac{\partial U}{\partial t} - \frac{\partial (v_n^L)^T}{\partial l_2}(0, 0) \frac{\partial U}{\partial x_2} - \frac{\partial (v_n^L)^T}{\partial l_3}(0, 0) \frac{\partial U}{\partial x_3} = 0. \quad (G.15)$$

This is a local boundary condition of the same differential order as the governing equations. These boundary conditions are only approximately nonreflecting and may produce nonphysical reflections of outgoing waves for which l_2 and/or l_3 are far from zero.

Using (G.2)-(G.4), the dispersion relation (G.7) for the system of equations, (G.1), can be written as

$$(u_1 k_1 + u_2 k_2 + u_3 k_3 - \omega)^3 \left[(u_1 k_1 + u_2 k_2 + u_3 k_3 - \omega)^2 - c^2(k_1^2 + k_2^2 + k_3^2) \right] = 0. \quad (G.16)$$

Three of the five roots are identical, i.e.,

$$(k_1)_{1,2,3} = \frac{\omega - u_2 k_2 - u_3 k_3}{u_1}. \quad (G.17)$$

For $u_1 > 0$, these correspond to right-travelling waves.

The other two roots are

$$(k_1)_4 = \frac{(\omega - u_2 k_2 - u_3 k_3)(-u_1 + cD)}{c^2 - u_1^2} \quad (G.18)$$

and

$$(k_1)_5 = \frac{(\omega - u_2 k_2 - u_3 k_3)(-u_1 - cD)}{c^2 - u_1^2}, \quad (G.19)$$

where

$$D = \sqrt{1 - (c^2 - u_1^2)(k_2^2 + k_3^2)/(\omega - u_2 k_2 - u_3 k_3)^2}. \quad (G.20)$$

For $0 < u_1 < c$, which corresponds to subsonic flow normal to the boundary, the fifth root is a left-travelling wave, provided the correct branch of the complex square root function is used in defining D . (D is defined as the positive root for $D^2 > 0$ and as the one with negative imaginary part otherwise, so that it represents a left-travelling wave with finite amplitude.) This wave is of interest in implementing Giles' boundary condition at the subsonic outflow boundary. The left null-vector defined in (G.9) for $(k_1)_5$, which correspond to an upstream travelling pressure wave, is

$$(v_5^L)^T = (0, \rho c(-\omega + u_2 k_2 + u_3 k_3), -\rho c u_1 k_2, -\rho c u_1 k_3, (\omega - u_2 k_2 - u_3 k_3)I). \quad (G.21)$$

The second-order approximation of (G.21) in the form of (G.15) is

$$(0, -\rho c, 0, 0, 1) \frac{\partial U}{\partial t} - (0, \rho c u_2, -\rho c u_1, 0, -u_2) \frac{\partial U}{\partial x_2} - (0, \rho c u_3, 0, -\rho c u_1, -u_3) \frac{\partial U}{\partial x_3} = 0. \quad (G.22)$$

For convenience of implementation and for comparison with Thompson's boundary condition, we define one-dimensional characteristic variables,

$$\mathbf{c} = (c_1, c_2, c_3, c_4, c_5)^T,$$

as

$$\mathbf{c} = \begin{pmatrix} -c^2 & 0 & 0 & 0 & 1 \\ 0 & 0 & \rho c & 0 & 0 \\ 0 & 0 & 0 & \rho c & 0 \\ 0 & \rho c & 0 & 0 & 1 \\ 0 & -\rho c & 0 & 0 & 1 \end{pmatrix} U \quad (G.23)$$

and

$$U = \begin{pmatrix} -1/c^2 & 0 & 0 & 1/(2c^2) & 1/(2c^2) \\ 0 & 0 & 0 & 1/(2\rho c) & -1/(2\rho c) \\ 0 & 1/(\rho c) & 0 & 0 & 0 \\ 0 & 0 & 1/(\rho c) & 0 & 0 \\ 0 & 0 & 0 & 1/2 & 1/2 \end{pmatrix} \mathbf{c}. \quad (G.24)$$

We can express the boundary condition (G.22) using a characteristic variable as

$$\frac{\partial c_5}{\partial t} + (0, u_1, 0, 0, u_2) \frac{\partial \mathbf{c}}{\partial x_2} + (0, 0, u_1, 0, u_3) \frac{\partial \mathbf{c}}{\partial x_3} = 0. \quad (G.25)$$

The corresponding expression for Thompson's boundary condition is

$$\frac{\partial c_5}{\partial t} + (0, c, 0, 0, u_2) \frac{\partial \mathbf{c}}{\partial x_2} + (0, 0, c, 0, u_3) \frac{\partial \mathbf{c}}{\partial x_3} = 0, \quad (G.26)$$

which simply replaces the velocity u_1 in (G.25) with c .

The actual boundary conditions used in the present code were those given by (G.22) with viscous terms added. The implementation of Thompson's boundary conditions also included the viscous terms.

G.2 Comparison of Turbulence Statistics

The code used in the present study was modified to include the more accurate Giles' boundary condition instead of Thompson's boundary condition. One of the saved fields for the case A which used Thompson's boundary condition was used as the initial field. Except for the outflow boundary condition, the same algorithm was used. After a transient period, statistical samples of flow variables were accumulated. Turbulence statistics are compared with those from case A which are computed from samples taken for exactly the same time interval.

Figure G.1 compares the evolution of mean square vorticity for the two different outflow boundary conditions. The difference is negligible throughout the domain which indicates that the improved boundary conditions for removing acoustic wave reflections have virtually no effect on the evolution of vortical waves.

Figure G.2 compares the evolution of the streamwise velocity fluctuations. The anomalous increase towards the outflow boundary is reduced by applying Giles' boundary condition. This improved behavior is, however, localized near the outflow boundary and does not affect the evolution of turbulence downstream of the shock.

Apparently, the anomalous behavior of the streamwise velocity fluctuations near the outflow boundary is caused by the pressure work term (see Figure 4.8(a)). Figure G.3 compares the statistics of pressure work term, $-\overline{p'_i u''_i}$ in the TKE transport equation. The sudden increase in the pressure work term towards the outflow boundary is reduced by half by using Giles' boundary condition instead of Thompson's boundary condition. This improvement is also localized near the outflow boundary.

As shown in Figure 4.10, the variance of the fluctuating dilatation increases by a factor of 10 near the outflow boundary due to nonphysical reflection of acoustic waves. Figure G.4 shows the improvement resulting from removing the acoustic wave reflection by the use of Giles' boundary condition.

In conclusion, Thompson's boundary condition used in the present study is found to be acceptable because reflections of acoustic waves at the outflow boundary do not appear to affect turbulence statistics downstream of the shock.

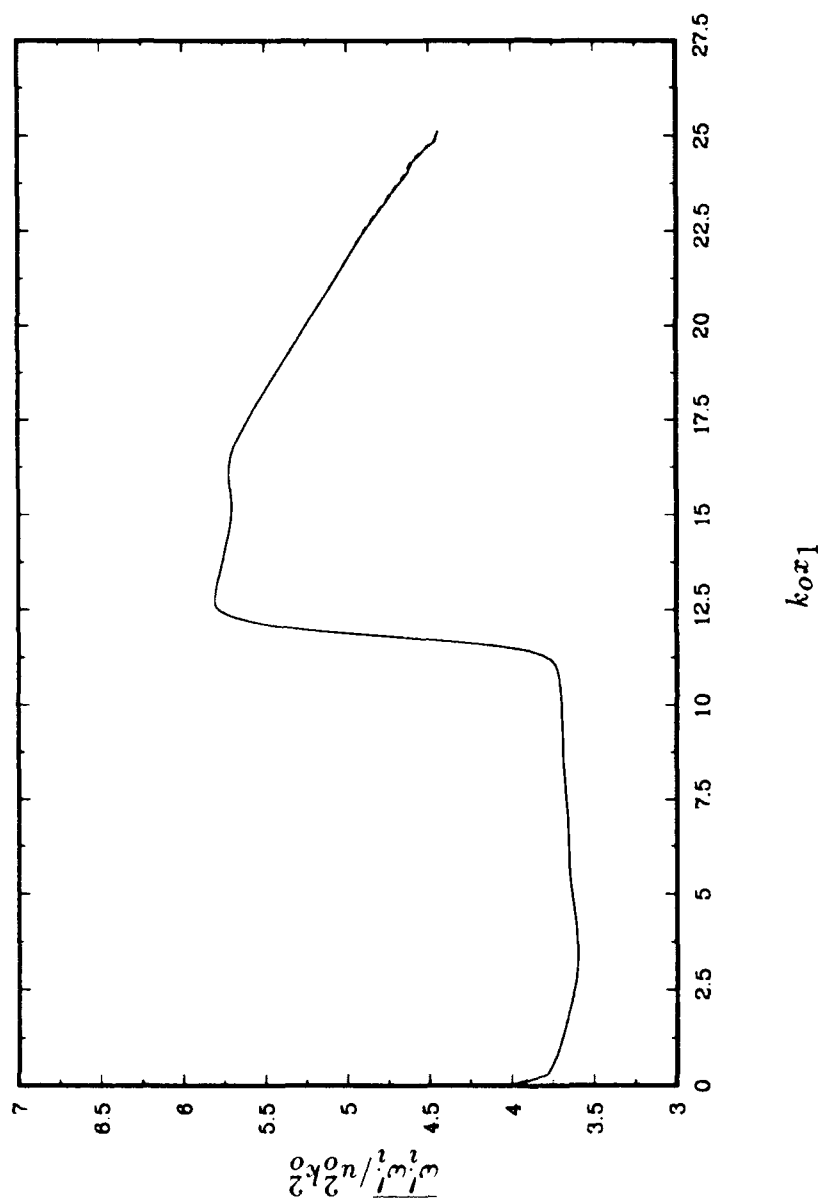


FIGURE G.1. Effect of boundary conditions on the evolution of the vorticity variance $\overline{\omega_i'^2}$ for case A: — Giles BC, ---- Thompson BC.

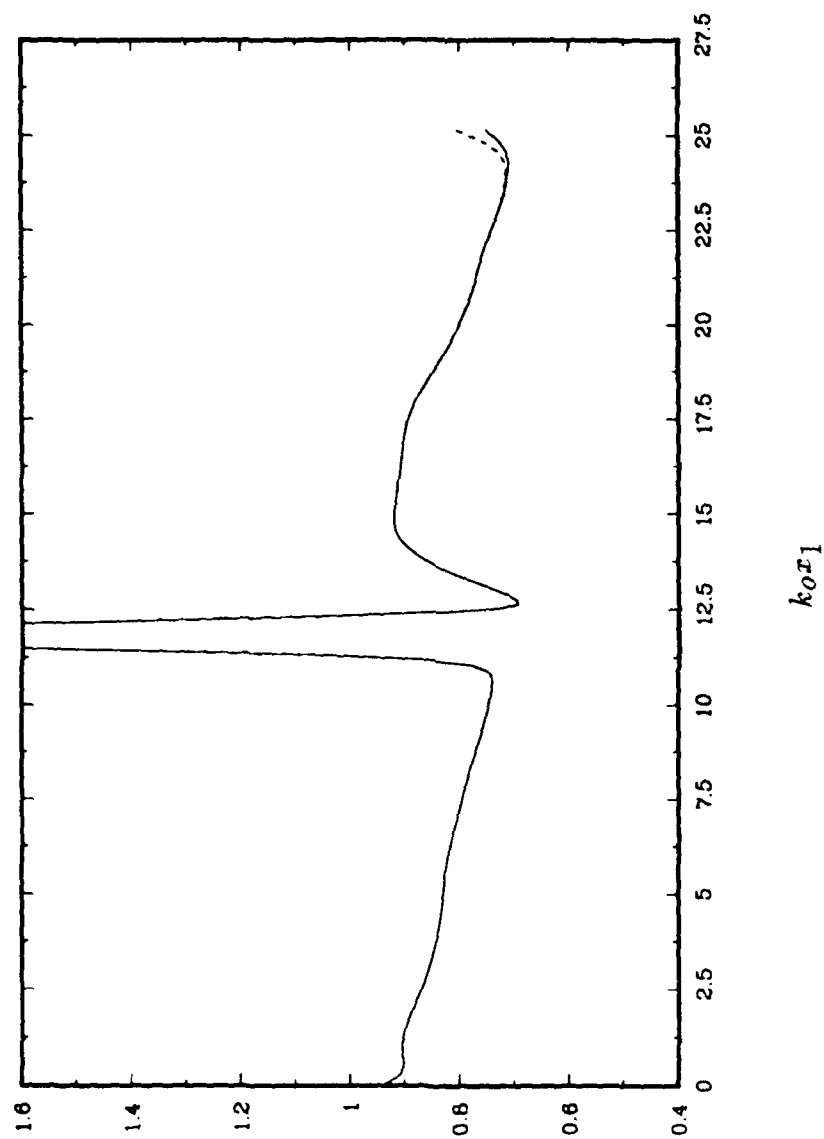


FIGURE G.2. Effect of boundary conditions on the evolution of R_{11} for case A: — Giles BC, ---- Thompson BC.

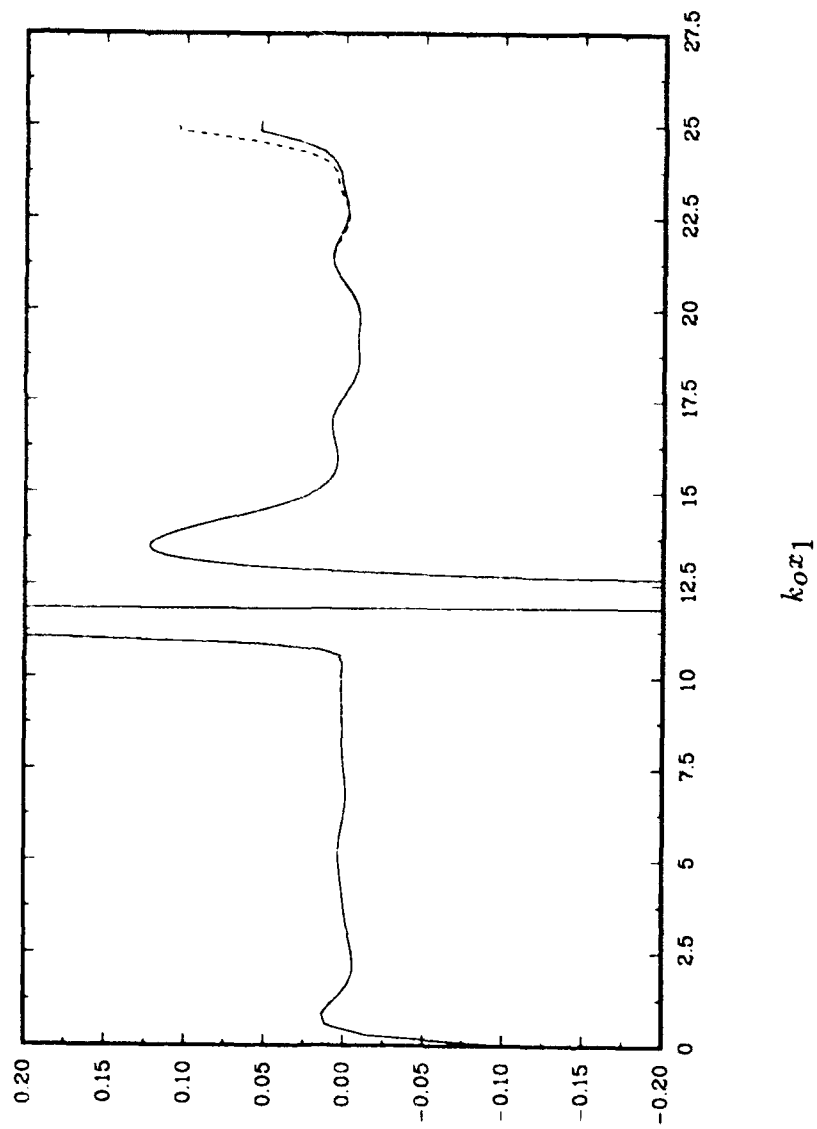


FIGURE G.3. Effect of boundary conditions on the evolution of the pressure-work $-p'_t u''_t$ for case A: ——— Giles BC, - - - - Thompson BC.

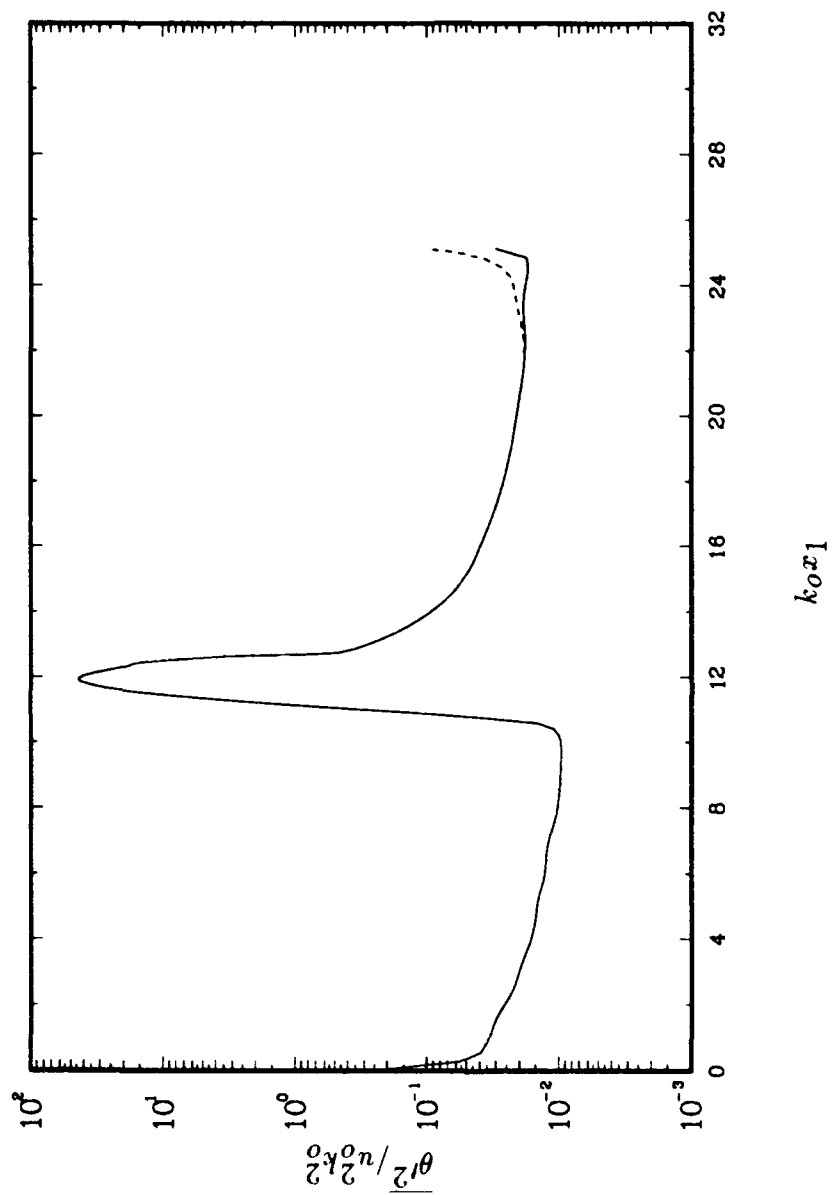


FIGURE G.4. Effect of boundary conditions on the evolution of the dilatation variance $\overline{\theta'^2}$ for case A: — Giles BC, ---- Thompson BC.

APPENDIX H

DRIFT IN THE SHOCK POSITION AND THE OUTFLOW CONDITION

In our numerical setup, there is no external mechanism to fix the position of the shock wave. From numerical experiments with a one dimensional shock wave interacting with a sinusoidal entropy wave, we found that poor resolution of the shock and a high amplitude fluctuation lead to the shock movement. If the shock wave drifts in the streamwise direction, the inflow mean Mach number is not the true upstream Mach number of the system. Moreover, the statistics obtained at a fixed point in space become contaminated because the relative distance to the shock wave is changing in time. The drift of the shock wave position in time is represented as the mismatch of the upstream and downstream mass fluxes in the chosen reference frame of the simulation, which reflects the fact that the mean turbulent shock propagation speed is different from the specified laminar shock propagation speed. The shock drift speed can be related to the mass flow rate difference by integrating the continuity equation in time and space, as

$$\int \int \int [\rho(t) - \rho(t_o)] dx_1 dx_2 dx_3 = - \int_{t_o}^t \int \int [(\rho u_1)^D - (\rho u_1)^U] dx_2 dx_3 dt. \quad (H.1)$$

The left side of (H.1) can be expressed in terms of the mean shock drift speed U_s as

$$\int \int \int [\rho(t) - \rho(t_o)] dx_1 dx_2 dx_3 = -(\bar{\rho}^D - \bar{\rho}^U) U_s L_2 L_3 (t - t_o), \quad (H.2)$$

which represents the mass decrease in the computational domain due to the mean drift of the shock wave (The shock wave drift in the $+x_1$ direction leads to a decrease of the total mass in the computational domain). The statistically averaged quantity $\bar{\rho}$ is defined as

$$\bar{\rho} = \frac{\int_{t_o}^t \int \int \rho dx_2 dx_3 dt}{L_2 L_3 (t - t_o)}.$$

The right side of (H.1) can be rewritten in terms of the statistically averaged quantities as

$$-\int_{t_o}^t \int \int [(\rho u_1)^D - (\rho u_1)^U] dx_2 dx_3 dt = -(\overline{\rho u_1}^D - \overline{\rho u_1}^U) L_2 L_3 (t - t_o). \quad (H.3)$$

Using (H.1) - (H.3), the mean shock drift speed can be obtained as

$$U_s = \frac{\overline{\rho u_1}^D - \overline{\rho u_1}^U}{\overline{\rho}^D - \overline{\rho}^U}. \quad (H.4)$$

Figure H.1 shows the mismatch in the mass fluxes across the shock wave for the worst case among the simulations. The shock drift speed in this case is about 0.7% of the average upstream speed.

Since the flow variables at the outflow boundary are not explicitly specified, they may drift in time. For the simulations of subsonic inflow-outflow condition, Poinso *et al.* [1990] proposed to add an extra term to Thompson's boundary condition in order to force the exit pressure to relax to an equilibrium pressure. Figure H.2 shows the time history of the mean exit pressure over three eddy turnover times. The drift in the mean exit pressure is about 0.2% of the mean exit pressure, which is not significant. Therefore, no modifications were introduced to the Thompson boundary condition at the outflow.

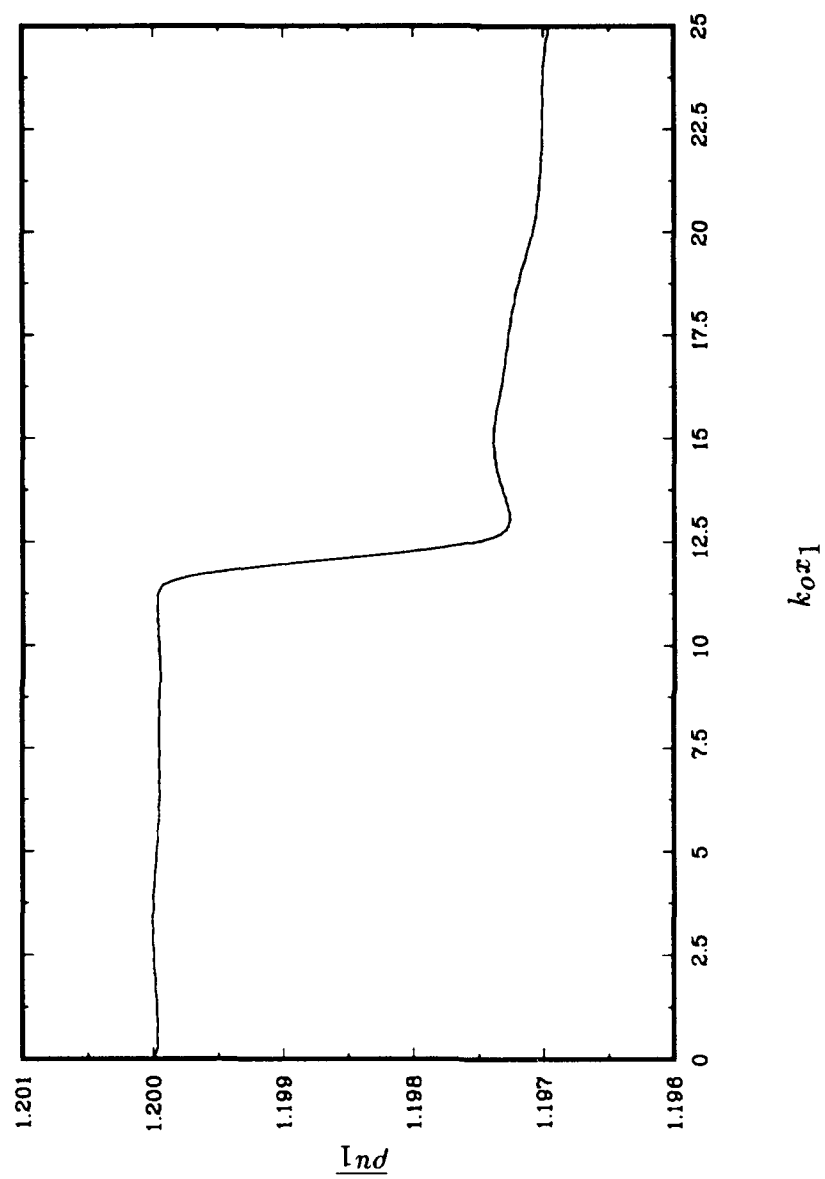


FIGURE H.1. Mass flowrate across the shock wave for case A.

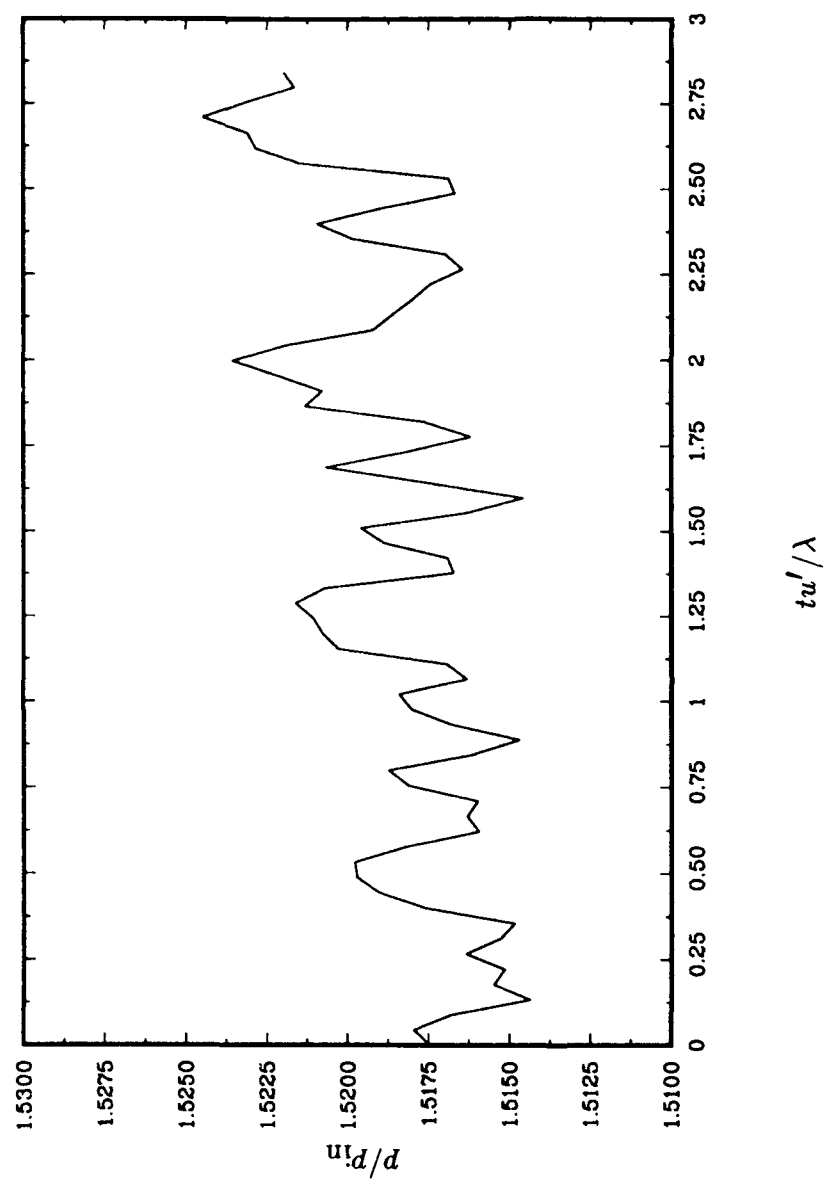


FIGURE H.2. Time history of the mean exit pressure for case A.

REFERENCES

- ANDERSON, D. A., J. C. TANNEHILL, & R. H. PLETCHER 1984 *Computational Fluid Mechanics and heat Transfer*, MacGraw-Hill, New York.
- ANDREOPOULOS, J. & K.-C. MUCK 1987 Some New Aspects of the Shock-Wave Boundary Layer Interaction in Compression Ramp Corner. *J. Fluid Mech.* **180**, 405-428.
- ANYIWO, J. C. & D. M. BUSHNELL 1982 Turbulence Amplification in Shock-Wave Boundary-Layer Interaction. *AIAA Journal* Vol. 20, No. 7, 893-899.
- BLAISDELL, G. A., MANSOUR, N. N. & W. C. REYNOLDS 1990 Numerical Simulations of Compressible Homogeneous Turbulence. *Report No. TF-50*. Department of Mechanical Engineering, Stanford University, Stanford, CA.
- BRADSHAW, P. 1977 Compressible Turbulent Shear Layers. *Ann. Rev. Fluid Mech.* **9**, 33-54.
- BUELL, J. C. & P. HUERRE 1988 Inflow/Outflow Boundary Conditions and Global Dynamics of Spatial Mixing Layers. *Center for Turbulence Research Proceedings of the Summer Program 1988*, Stanford/NASA Ames, CA.
- CANUTO, C., M. Y. HUSSAINI, A. QUARTERONI, & T. A. ZANG 1988 *Spectral Methods in Fluid Dynamics*, Springer-Verlag, Berlin.
- CHANG, C.-T., 1957 Interaction of a Plane Shock and Oblique Plane Disturbances with Special Reference to Entropy Waves. *J. Aero. Sci.*, Vol. 24, Sep. 1957, 675-682.
- COLEMAN G. N. & N. N. MANSOUR 1991 Simulation and Modeling of Homogeneous Compressible Turbulence under Isotropic Mean Compression. *Eighth Symposium on Turbulent Shear Flows*, Munich, September 9-11, 1991.
- DEBIEVE, F.-R., H. GOUIN, & J. GAVIGLIO 1982a Evolution of the reynolds Stress Tensor in a Shock Wave-Turbulence Interaction. *Indian Journal of Technology*, Vol. 20, March 1982, 90-97.
- DEBIEVE, F.-R., H. GOUIN, & J. GAVIGLIO 1982b Momentum and Temperature Fluxes in a Shock Wave-Turbulence Interaction. In *Structure of Turbulence in Heat and Mass Transfer* edited by Z. P. Zarić, Hemisphere, New York.

- DEBIEVE, J. F. & J. P. LACHARME 1986 A Shock-Wave/Free Turbulence Interaction. In *Turbulent Shear Layer/Shock wave Interactions* edited by J. Détery, Springer, Berlin.
- DOLLING, D. S. & C. T. OR 1985 Unsteadiness of the Shock Wave Structure in Attached and Separated Compression Ramp Flows. *Experiments in Fluids*, **3**, 24-32.
- DOMARADZKI, J. A. & R. S. ROGALLO 1990 Local Energy Transfer and Non-local Interactions in Homogeneous, Isotropic Turbulence. *Phys. Fluids A*, **2**, 413-426.
- DURBIN, P. A. & O. ZEMAN 1991 Rapid Distortion Theory for Homogeneous Compressed Turbulence with Application to Modeling. *Center for Turbulence Research Manuscript* 127, Stanford University/NASA Ames, CA.
- DUSSAUGE, J. P., K.-C. MUCK & J. ANDREOPOULOS 1986 Properties of Wall Pressure Fluctuations in a Separated Flow over a Compression Ramp. In *Turbulent Shear Layer/Shock wave Interactions* edited by J. Détery, Springer, Berlin.
- DUSSAUGE, J. P. & J. GAVIGLIO 1987 The Rapid Expansion of a Supersonic Turbulent Flow: Role of Bulk Dilatation. *J. Fluid Mech.* **174**, 81-112.
- ERLEBACHER, G., M. Y. HUSSAINI, C. G. SPEZIALE & T. A. ZANG 1990 Toward the large-Eddy Simulation of Compressible Turbulent Flows. *ICASE Report* No. 90-76.
- FAVRE, A. 1965a Équations des Gaz Turbulents Compressibles I. *Journal Mécanique* Vol. 4, No. 3, 361-390.
- FAVRE, A. 1965b Équations des Gaz Turbulents Compressibles II. *Journal Mécanique* Vol. 4, No. 4, 391-421.
- FEIEREISEN, W. J., W. C. REYNOLDS & J. H. FERZIGER 1981 Numerical Simulations of a Compressible, Homogeneous, Turbulent Shear Flow. *Report No. TF-13*. Department of Mechanical Engineering, Stanford University, Stanford, CA.
- GILES, M. B. 1990 Nonreflecting Boundary Conditions for Euler Equation calculations. *AIAA Journal* Vol. 28, No. 12, 2050-2058.
- HARTEN, A., B. ENQUIST, S. OSHER & S. R. CHAKRAVARTHY 1987 Uniformly High Order Accurate Essentially Non-Oscillatory Schemes, III. *J. Comp. Phys.* **71**, 231-303.

- HESSELINK, L. & B. STURTVANT 1988 Propagation of Weak Shocks through a Random Medium. *J. Fluid Mech.* **196**, 513-553.
- HINZE, J. O. 1975 *Turbulence*, 2nd Edition, McGraw-Hill, New York.
- HONKAN, A. & J. ANDREOPOULOS 1990 Experiments in a Shock Wave/Homogeneous Turbulence Interaction. *AIAA Paper* No. 90-1647.
- HUSSAINI, M. Y., F. COLLIER & D. M. BUSHNELL 1986 Turbulence Alteration due to Shock Motion. In *Turbulent Shear Layer/Shock Wave Interactions* edited by J. Détery, Springer, Berlin.
- JACQUIN, L., E. BLIN & P. GEFFROY 1991 Experiments on Free Turbulence/Shock Wave Interaction *Eighth Symposium on Turbulent Shear Flows*, Munich, September 9-11, 1991.
- JAYARAM, M., M. W. TAYLOR & A. J. SMITS 1987 The Response of a Compressible Turbulent Boundary Layer to Short Regions of Concave Surface Curvature. *J. Fluid Mech.* **175**, 343-362.
- KELLER, J. & W. MERZKIRCH 1990 Interaction of a Normal Shock Wave with a Compressible Turbulent Flow. *Experiments in Fluids* **8**, 241-248.
- KERREBROCK, J. L. 1956 The Interaction of Flow Discontinuities with Small Disturbances in a Compressible Fluid. *Ph. D. Thesis*. California Institute of Technology.
- KIDA, S. & S. A. ORSZAG 1990 Enstrophy Budget in Decaying Compressible Turbulence. *Journal of Scientific Computing* Vol. 5, No. 1, 1-34.
- KIM, J., P. MOIN & R. D. MOSER 1987 Turbulence Statistics in Fully Developed Channel Flow at Low Reynolds Number. *J. Fluid Mech.* **177**, 133-166.
- KOVASZNAY, L. S. G. 1953 Turbulence in Supersonic Flow. *J. Aero. Sci.* Vol. 20, No. 10, 657-682.
- KUNTZ, D. W., V. A. AMATUCCI & A. L. ADDY 1987 Turbulent Boundary-Layer Properties Downstream of the Shock-Wave/Boundary-Layer Interaction. *AIAA Journal* Vol. 25, No. 5, 668-675.
- LAGERSTROM, P. A. 1964 *Theory of Laminar Flows* edited by F. K. Moore, Princeton University, New York, Vol.4, 183.
- LEE, M. J. 1989 Distortion of Homogeneous Turbulence by Axisymmetric Strain and Dilatation. *Phys. Fluids A*, **9**, 1541-1557.

- LEE, M. J. & W. C. REYNOLDS 1985 Numerical Experiment on the Structure of Homogeneous Turbulence. *Report No. TF-24*. Department of Mechanical Engineering, Stanford University, Stanford, CA.
- LEE, S., S. K. LELE & P. MOIN 1991a Direct Numerical Simulation and Analysis of Shock Turbulence Interaction. *AIAA Paper No. 91-0523*.
- LEE, S., S. K. LELE & P. MOIN 1991b Eddy-Shocklets in Decaying Compressible Turbulence. *Phys. Fluids A*, **3**, 657-664.
- LELE, S. K. 1990 Compact Finite Difference Schemes with Spectral-like Resolution. *Center for Turbulence Research Manuscript 107*, Stanford University/NASA Ames, CA.
- LING, S. C. & T. T. HUANG 1970 Decay of Weak Turbulence. *Phys. Fluids* **13**, 2912-2924.
- LIGHTHILL, M. J. 1953 On the Energy Scattered from the Interaction of Turbulence with Sound or Shock Waves. *Proc. Camb. Phil. Soc.* **49**, 531-551.
- LUMPKIN, F. E. III 1990 Development and Evaluation of Continuum Models for Translational-Rotational Nonequilibrium. *Ph. D. Thesis*. Stanford University.
- MEADOWS, K. R., A. KUMAR & M. Y. HUSSAINI 1991 Computational Study on the Interaction between a Vortex and a Shock Wave. *AIAA Journal* Vol. 29, No. 2, 174-179.
- McKENZIE, J. F. & K. O. WESTPHAL 1968 Interaction of Linear Waves with Oblique Shock Waves. *Phys. Fluids* **11**, 2350-2362.
- MOIN, P., K. SQUIRES, W. CABOT & S. LEE 1991 A Dynamic Subgrid-Scale Model for Compressible Turbulence and Scalar Transport. *Phys. Fluids A* **3**, 2746-2757.
- MOORE, F. K., 1953 Unsteady Oblique Interaction of a Shock Wave with a Plane Disturbances. *NACA TN-2879*. Also as *NACA Report 1165*.
- MORKOVIN, M. V. 1962 Effects of Compressibility on Turbulent Flows. *Mechanique de la Turbulence*, CNRS, Paris, 1962.
- MOYAL, J. E. 1952 The Spectra of Turbulence in a Compressible Fluid; Eddy Turbulence and Random Noise. *Proc. Camb. Phil. Soc.* **48**, 329-344.
- PICONE, J. M., E. S. ORAN, J. P. BORIS & T. R. YOUNG 1985 Theory of Vorticity Generation by Shock Wave and Flame Interactions. In *Dynamics of Shock*

- Waves, Explosions, and Detonations*, 429-448. American Institute of Aeronautics and Astronautics.
- POINSOT, T. J. & S. K. LELE 1990 Boundary Conditions for Direct Simulations of Compressible Viscous Reacting Flow. *Center for Turbulence Research Manuscript 102*, Stanford University/NASA Ames, CA.
- RIBNER, H. S. 1953 Convection of a Pattern of Vorticity through a Shock Wave. *NACA TN-2864*. Also as *NACA Report 1164*.
- RIBNER, H. S. 1954 Shock-Turbulence Interaction and the Generation of Noise. *NACA TN-3255*. Also as *NACA Report 1233*.
- RIBNER, H. S. 1969 Acoustic Energy Flux from Shock-Turbulence Interaction. *J. Fluid Mech.* **35**, 299-310.
- RIBNER, H. S. 1987 Spectra of Noise and Amplified Turbulence Emanating from Shock-Turbulence Interaction. *AIAA Journal* Vol. 25, No. 3, 436-442.
- ROGALLO, R. S. 1981 Numerical Experiments in Homogeneous Turbulence. *NASA Technical Memorandum* 81315.
- ROGALLO, R. S. & P. MOIN 1984 Numerical Simulation of Turbulent Flows. *Ann. Rev. Fluid Mech.*, **16**, 99-137.
- ROTMAN, D. 1991 Shock Wave Effects on a Turbulent Flow. *Phys. Fluids A*, **3**, 1792-1806.
- RUBESIN, M. W. 1976 A One-Equation Model of Turbulence for Use with the Compressible Navier-Stokes Equations. *NASA Technical Memorandum* X-73,128.
- SARKAR, S., G. ERLEBACHER, M. Y. HUSSAINI & H. O. KREISS 1991 The Analysis and Modeling of Dilatational Terms in Compressible Turbulence. *J. Fluid Mech.* **227**, 473-493.
- SARKAR, S. 1991 Modeling the Pressure-Dilatation Correlation. *ICASE Report* No. 91-42.
- SEARS, W. R. 1950 The Linear-Perturbation Theory for the Rotational Flow. *Jour. Math. and Phys.* Vol. 28, No. 9, 268-271.
- SETTLES, G. S., T. J. FITZPATRICK & S. M. BOGDONOFF 1979 Detailed Study of Attached and Separated Compression Corner Flowfields in High Reynolds Number Supersonic Flow. *AIAA Journal* Vol. 17, No. 6, 579-585.

- SELIG M. S., J. ANDREOPOULOS, K.-C. MUCK, J. P. DUSSAUGE & A. J. SMITS 1989 Turbulence Structure in a Shock Wave/Turbulent Boundary-Layer Interaction. *AIAA Journal* Vol.27, No. 7, 862-869.
- SHAPIRO, A. H. 1953 *The Dynamics and Thermodynamics of Compressible Fluid Flow*, The Roland Press, New York.
- SHERMAN, F. S. 1955 A Low-Density Wind-Tunnel Study of Shock-Wave Structure and Relaxation Phenomena in Gases. *NASA TN-3298*
- SMITS, A. J. & K.-C. MUCK 1987 Experimental Study of Three Shock Wave/Turbulent Boundary Layer Interactions. *J. Fluid Mech.* **182**, 294-314.
- SPALART, P. 1988 Direct Simulation of a Turbulent Boundary Layer up to $Re_\theta = 1410$. *J. Fluid Mech.* **187**, 61-98.
- TAULBEE, D. & J. VanOSDOL 1991 Modeling Turbulent Compressible Flows: The Mass Fluctuating Velocity and Squared Density. *AIAA Paper* No. 91-0524.
- TAVOULARIS, S., BENNETT, J.C. & CORRSIN, S. 1978 Velocity-Derivative Skewness in Small Reynolds Number, Nearly Isotropic Turbulence. *J. Fluid Mech.* **176**, 33-66.
- THOMPSON, K. W. 1987 Time Dependent Boundary Conditions for Hyperbolic Systems. *J. Comp. Phys.* **68**, 1-24.
- THOMPSON, P. A. 1984 *Compressible-Fluid Dynamics*, McGraw-Hill, New York.
- WRAY, A. A. 1986 Very Low Storage Time-Advancement Schemes. *Internal Report*, NASA-Ames Research Center, Moffett Field, CA.
- WRAY, A. A. 1988 Vectorial Manual. *Internal Report*, NASA-Ames Research Center, Moffett Field, CA.
- YEE, H.C. 1987 Upwind and Symmetric Shock-Capturing Schemes. *NASA Technical Memorandum* 89464.
- ZANG, T. A., M. Y. HUSSAINI & D. M. BUSHNELL 1984 Numerical Computations of Turbulence Amplification in Shock-Wave Interaction. *AIAA Journal* Vol. 22, No. 1, 13-21.
- ZEMAN, O. 1990 Dilatation Dissipation: The Concept and Application in Modeling Compressible Mixing Layers. *Phys. Fluids A* **3**, 178-188.
- ZEMAN, O. 1991a On the Decay of Compressible Isotropic Turbulence *Phys. Fluids A* **3**, 951-955.

ZEMAN, O. 1991b Compressible Turbulence Subject to Shear and Rapid Compression. *Eighth Symposium on Turbulent Shear Flows*, Munich, September 9-11, 1991.